Università degli Studi di Ferrara

DOCTORAL COURSE IN

PHYSICS

CYCLE XXXV

COORDINATOR

Prof. Luppi Eleonora

Advanced experimental techniques for SiPM characterization at cryogenic temperatures

Scientific-Disciplinary Sector (SDS): FIS/01

Ph.D. Candidate:
Giammaria Tommaso

Supervisor:
Tomassetti Luca

Years 2019/2023

Contents

Introduction

The main topic of this thesis is the characterization of silicon photomultipliers (SiPMs) in the context of the DUNE experiment, in particular for the ProtoDUNE-HD and DUNE-FD1 detectors, and the development of novel experimental setups and techniques to perform this task.

The chapter 1 is an overview of DUNE, as it describes the main features of the experiment and the underlying physics, the scientific program and finally the current plan for the DUNE beam and detector design.

The chapter 2 focuses on the first module of the Far Detector (DUNE-FD1), describing the general working principles of a LArTPC before entering the more technical topic of the DUNE-FD1 design. The chapter contains also a brief description of the ProtoDUNE experiment, in particular of the ProtoDUNE2-HD detector, which is a prototype of DUNE-FD1 with smaller LAr volume but full-scale fundamental components. Particular attention is given to the role of SiPMs in these detectors, which are the fundamental units of the LArTPCs photon detection system (PDS) in the current design plan.

The chapter 3 contains a detailed description of the SiPM fundamental properties and working principles, discussing both the mathematical model used to explain the physics of these sensors and the equivalent electric circuit used to describe their behaviour. The chapter includes also a review of the most important parameters involved in the SiPM characterization, and some of the possible procedures used to measure these parameters, with a particular attention to the ones important for the application of these sensors in DUNE.

The chapter 4 refers to the test campaign engaged by the DUNE PDS consortium (which is responsible for the DUNE and ProtoDUNE PDS design and development) to characterize a pool of SiPMs of different models, previously chosen for low-noise properties and cryogenic operation reliability. This campaign was aimed to down-select the best choice for ProtoDUNE-HD and DUNE-FD1 SiPM models and define the best working conditions to use them. The test campaign ended up in 2019 with the down-selection of two SiPM models, even if all the starting SiPM models are within the DUNE specifications.

The final chapter, chapter 5, outlines the second test campaign of the DUNE PDS consortium: quality assurance tests of a large number of SiPMs (of the selected models) for the entire ProtoDUNE2-HD and DUNE-FD1 productions, counting 6000 and 288000 sensors, respectively. The Ferrara and Bologna groups of the consortium designed and developed a specific apparatus (CACTUS) for this task, the apparatus is able to perform fast and automatized characterizations of SiPMs at LN_2 temperature (2021-2022). This experimental setup was used for the ProtoDUNE2-HD SiPM characterization campaign (6000 sensors, ended in September 2022), finding an out-of-specs rate below the 0.05%

level on the tested SiPMs, and is currently operating for the DUNEFD1-HD SiPM characterization campaign (288000 sensors).

After a first prototyping phase, the CACTUS system is now operative and fully calibrated in two different sites (Bologna and Ferrara Universities) since March 2022, and identical apparatuses are planned to be installed in other 3 facilities. These are the Milano Bicocca, Granada and Prague Universities, they will join the Ferrara and Bologna sites in the DUNEFD1-HD SiPM characterization campaign in 2023.

Chapter 1

The Deep Underground Neutrino Experiment

The *Deep Underground Neutrino Experiment* (DUNE) is a next-generation neutrino experiment which aims to measure with high precision the parameters governing the neutrino long-baseline oscillation patterns [1], as will be described in the following. In particular, it is designed to maximize the sensitivity to the ν_μ to ν_e oscillations, using both neutrino and antineutrino beams.

The experiment consists of a broadband, high-power neutrino beam peaked at $\approx 2.5\,\text{GeV}$ and a powerful Near Detector (ND) complex, both located at Fermi National Accelerator Laboratory, in Batavia, Illinois, plus a massive Far Detector (FD) located $\approx 1.5\,\text{km}$ (4850 ft) underground at the Sanford Underground Research Facility (SURF), in Lead, South Dakota, at a distance of 1285 km from the neutrino production point. The geographic locations of the two facilities are reported in figure 1.1, together with a sketch of the neutrino fluxes at the far site, while figure 1.2 shows the baseline trajectory in a satellite photo.

The neutrinos are produced using a proton beam in the energy range of $[60-120]\,\text{GeV}$ from the Fermilab's Main Injector. More precisely, the protons are guided onto a graphite target to interact with carbon nuclei producing, among other particles, charged pions. The neutrino beam is produced from the decay-in-flight of these charged pions, which are previously focused using a magnetic horn; this technique will be described more in detail in the subsection 1.3.1. The neutrinos cannot be focused directly by a magnetic (or electric) field since they have no electric charge, so the horn acts on the pion beam prior the decay, and the polarity of the horn focusing magnets can be reversed to switch from a muon neutrino beam to a muon antineutrino beam.

The FD is a massive *Liquid Argon Time Projection Chamber* (LArTPC) divided in four identically sized modules [5]. This technology is based on a LAr cryostat which is instrumented to detect the products of neutrino interactions with the Argon nuclei inside it. More precisely, it collects both the scintillation light and the charged particles produced in these interactions, providing particle ID and 3D track determination for each event. This technology will be described more in detail in the subsection 1.3.3, together with the design of the first FD module (DUNE-FD1).

The ND is a detector complex composed of both movable and steady elements, this will be used to detect the unoscillated neutrino flux as a reference for the study of the FD events. The movable

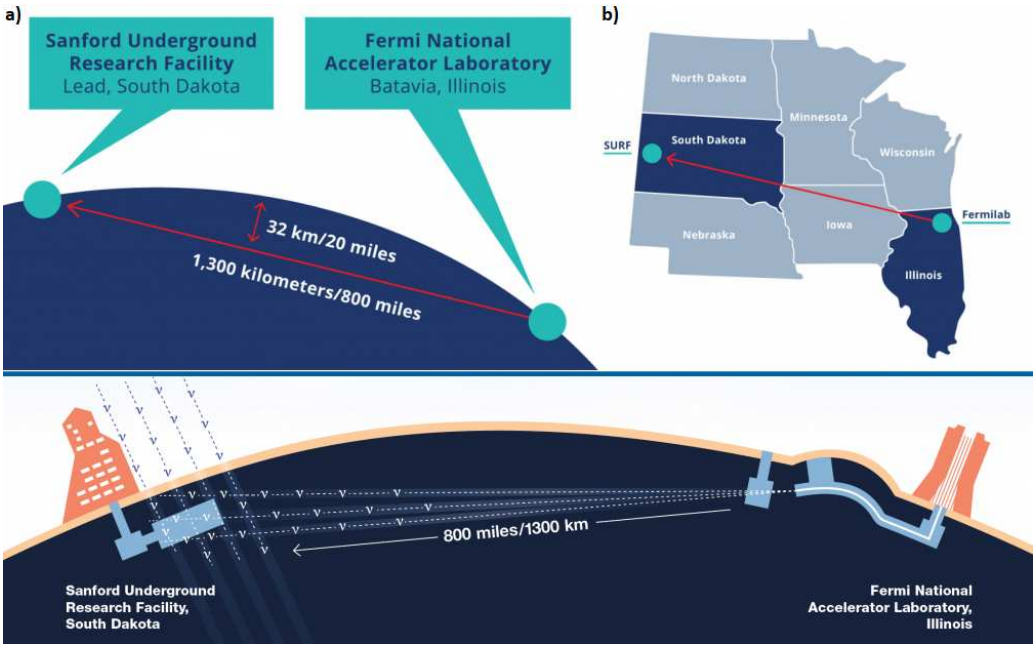

Figure 1.1: Top: sketch of both the near and far sites on the Earth's vertical section (a) and Geographic location of the two sites (b), from [2]. Bottom: sketch of the DUNE experiment, with a representation of the neutrino fluxes at the far site (neutrino beam from the right; atmospheric, solar and cosmic neutrinos in general from above), from [3].

Figure 1.2: Trajectory of the neutrino beam in the DUNE experiment marked on a satellite photo, from [4].

components can slide off the beam axis, in order to measure the flux in different energy (and intensity) spectrum conditions and characterize the neutrino beam with more precision. Some of the modules are argon-based detectors, this similarity with the FD permits to reduce the systematic uncertainties in the neutrino event detection. The single ND components will be described more in detail in the subsection 1.3.2.

1.1 DUNE physics

The gauge symmetry principle is one of the pillars of modern particle physics, since it establishes an unambiguous connection between the local gauge symmetries and the forces mediated by spin-1 particles. In the Standard Model (SM) of particle physics the strong, weak, and electromagnetic interactions are connected to the $SU(3)_C \times SU(2)_L \times U(1)_Y$ gauge symmetry group, where C stands for colour, L for left-handedness, and Y for hypercharge. This symmetry is spontaneously broken to $SU(3)_C \times U(1)_{EM}$, with $U(1)_{EM}$ coupling the electromagnetic charge[1], neutrinos are singlets of the $SU(3)_C \times U(1)_{EM}$ subgroup since they do not interact strongly nor electromagnetically. The (left-handed) neutrinos are part of the lepton doublets: the SM associates one neutrino for each charged lepton, ν_e, ν_μ, ν_τ. The $SU(2)_L$ gauge invariance dictates the form of weak neutral current (NC) interactions among neutrinos and of charged current (CC) interactions between neutrinos and their corresponding charged leptons, mediated by the Z^0 and $W^\pm$ bosons, respectively.

In the SM, the masses of the fermions are generated via a Yukawa coupling of the scalar Higgs doublet with a right-handed and left-handed fermion component, the former being a $SU(2)_L$ singlet, while the latter being part of a doublet, as mentioned above. For leptons, one can build this Yukawa term by coupling the left-handed lepton doublets with the right-handed charged lepton field, and after spontaneous symmetry breaking the charged lepton obtain non-zero masses [6]. This is the so-called *Higgs mechanism*, and it has been confirmed by the observation of the Higgs boson in 2012 [7, 8]. Since the SM does not contain right-handed neutrinos, this Yukawa interaction cannot be built, and the neutrinos result to be massless at the Lagrangian level: in order to add a mass to the neutrino, one must go beyond the SM.

As a matter of fact, neutrino mass terms can be constructed in different ways, but the theoretical models which are candidates to explain the neutrino masses are out of the scope of this thesis.

From the experimental point of view, the observation of flavour transitions in neutrino propagation in a variety of experiments has established beyond doubt that neutrinos do have non-zero masses, and also that lepton flavours are not symmetries of nature [9, 10]. The neutrino flavour oscillations have been already observed in atmospheric, solar, accelerator and nuclear reactor neutrinos, and all validate the massive neutrinos scenario. More precisely, the observed dependence of the flavour transition probabilities on the distance travelled by the neutrinos, and on their energy, confirms the mixing of massive neutrino states in weak charged current interactions as the responsible mechanism for flavour oscillations.

1.1.1 Neutrino flavour oscillations

The neutrino oscillation arises from mixing between the flavour and mass eigenstates of neutrinos, corresponding to the weak and gravitational interactions, respectively [11]. This phenomenon can be described as a rotation between the weak-interaction eigenstate basis (ν_e, ν_μ, ν_τ) and the mass eigenstates basis (ν_1, ν_2, ν_3). The transformations between basis states are expressed in the form of a complex unitary matrix, known as the *Pontecorvo – Maki – Nakagawa – Sakata* (PMNS)

[1] defined as the sum of weak isospin charge (third $SU(2)_L$ generator) and hypercharge

matrix, similarly to the mixing mechanism in the quark sector[2]. The PMNS matrix depends on four parameters: three mixing angles θ_{12}, θ_{23}, θ_{13} and a CP-violating phase δ_{CP}. As explained in the following, these parameters contribute to the determination of the probability amplitudes in neutrino oscillation phenomena.

The flavour oscillations of neutrinos can be qualitatively described as follows: a neutrino with defined flavour l ($l = e, \mu, \tau$) is produced from a weak CC interaction as a combination of the three mass eigenstates. The neutrino propagates through a distance L before participating another weak CC interaction, in which it can produce a different lepton l' with a certain (non-zero) probability. This oscillation probability depends on the two related mixing angles $\theta_{ll'}$, $\theta_{l'l}$, on the neutrino energy E and on the traveled distance L. The probability of neutrino oscillation among the l and l' weak-interaction eigenstates depends also on the squared mass difference $\Delta m^2{}_{ij} = m^2{}_i - m^2_j$ (with $i, j = 1, 2, 3$) of the related mass eigenstates. Furthermore, the CP violation results in different oscillation probabilities for neutrinos and antineutrinos, and the value of the related phase δ_{CP} is still unknown.

The three mass eigenstate scenario implies two independent mass-squared differences (for example Δm^2_{21} and Δm^2_{32}), and one of these two quantities is currently undefined. More precisely, the sign of the Δm^2_{32} is unknown, with a resulting ambiguity in the possible interpretations of experimental data. For this reason the so-called *neutrino mass hierarchy* (or *neutrino mass ordering*) question is still open, as sketched in figure 1.3.

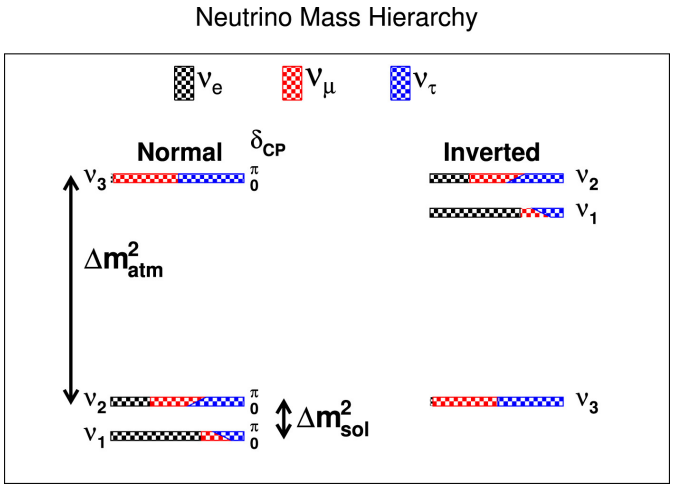

Figure 1.3: Sketch of the two possible neutrino mass orderings, referred to as normal ordering (left) and inverted ordering (right), from [6]. The current knowledge of neutrino oscillations does not permit to assess which scenario is the most probable.

The two possible ordering of the mass states configurations are known as *normal hierarchy* and *inverted hierarchy* (or ordering) and are equally probable in general.

From the experimental point of view, the intrinsic challenges related to the production and detection of tau neutrinos makes the oscillation modes $\nu_{\mu,e} \rightarrow \nu_{e,\mu}$ the most promising phenomena to search for experimental signatures of leptonic CP violation, and the theoretical model reported in the following refers to this particular case.

[2] Represented by the *Cabibbo – Kobayashi – Maskawa* (CKM) matrix

The $\nu_{\mu,\mathrm{e}} \rightarrow \nu_{\mathrm{e},\mu}$ oscillations that occur as the neutrinos propagate through the Earth's mantle are modified by the coherent forward scattering of electronic neutrinos on electrons in matter. More precisely, the energy and baseline dependence of the vacuum oscillation probabilities changes according to the sign of ${\Delta m_{31}}^2$ [12, 13]. This is known as the *Mikheyev – Smirnov – Wolfenstein* effect (MSW) or matter effect, and has already been observed in solar-neutrino oscillation experiments.

The matter effect simply stems from the presence of electrons (and absence of positrons) along the neutrino trajectory and it induces an asymmetry that adds to the CP asymmetry effect, but its magnitude also depends on the mass hierarchy [11].

The probability of $\nu_\mu \rightarrow \nu_\mathrm{e}$ oscillations through matter in a constant density medium can be written, at first order approximation, as [14]:

$$
\begin{gathered}
P(\nu_\mu \rightarrow \nu_e) \simeq P_{\mathrm{atm}} + 2\sqrt{P_{\mathrm{atm}}}\sqrt{P_{\mathrm{sol}}} cos(\Delta_{31} + \delta_{\mathrm{CP}}) + P_{\mathrm{sol}} = \\
sin^2\theta_{23} sin^2 2\theta_{13} \frac{sin^2(\Delta_{31} - aL)}{(\Delta_{31} - aL)^2} {\Delta^2}_{31} \\
+ sin 2\theta_{23} sin 2\theta_{13} sin 2\theta_{12} \frac{sin(\Delta_{31} - aL)}{(\Delta_{31} - aL)} \Delta_{31} \frac{sin(aL)}{(aL)} \Delta_{21} cos(\Delta_{31} \pm \delta_{\mathrm{CP}}) \\
+ cos^2\theta_{23} sin^2 2\theta_{12} \frac{sin^2(aL)}{(aL)^2} \Delta_{21}^2
\end{gathered}
$$

where

$$
a = \pm \frac{G_\mathrm{F} N_\mathrm{e}}{\sqrt{2}} \approx \pm \frac{1}{3500\,km} \left(\frac{\rho}{3.0 \frac{g}{cm^3}}\right)
$$

The P_{atm} and P_{sol} terms are the so-called *atmospheric* and *solar* probabilities, and the middle term is the interference between these two contributions[3]. G_F is the Fermi constant, N_e is the number density of electrons in the Earth, L is the baseline in km, E_ν is the neutrino energy in GeV and $\Delta_{\mathrm{ij}} \approx 1.267 {\Delta m_{\mathrm{ij}}}^2 \frac{L}{E_\nu}$. The presented formula takes into account both the CP violating phase and the MSW effect, represented by the terms δ_{CP} and a, respectively.

Both the δ_{CP} term and the $\pm$ signs in the equations are positive for $\nu_\mu \rightarrow \nu_\mathrm{e}$ oscillations and negative for $\bar{\nu}_\mu \rightarrow \bar{\nu}_\mathrm{e}$ oscillations, so the $\nu - \bar{\nu}$ asymmetry is introduced both by the CP violation and by the matter effect.

The sinusoidal form of $P(\nu_\mu \rightarrow \nu_e)$ implies that the related spectrum presents a series of maxima in correspondence of certain combinations of E, L and ${\Delta m_{\mathrm{ij}}}^2$ values, as visible in the plots reported in figure 1.4.

For long baselines it is possible to probe multiple oscillation maxima in the oscillation spectrum, if the neutrino flux covers a sufficiently wide range of energies; this will be described more in details in the next subsection.

1.1.2 Experimental requirements for measuring CP violation and MSW effect

In the DUNE experiment, the combination of baseline length and neutrino beam energy range was carefully selected to disentangle the contributions of MSW effect and CP violation on the oscillation spectra. More precisely, the factors related to these two effects have different magnitudes in the

[3] One of the approximations is $\Delta_{32} \pm \delta_{\mathrm{CP}} \simeq \Delta_{31} \pm \delta_{\mathrm{CP}}$

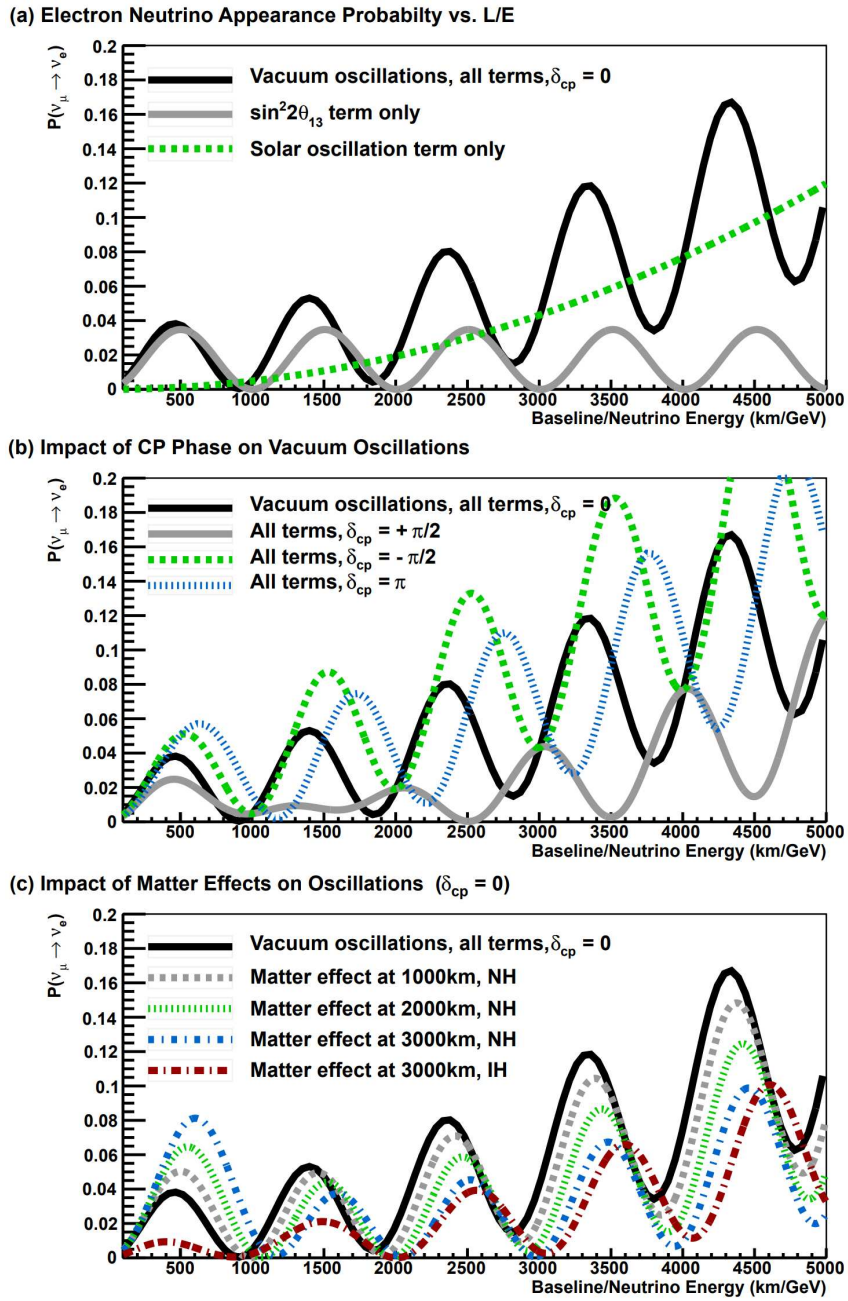

Figure 1.4: From [15]: The $\bar{\nu}_\mu \rightarrow \bar{\nu}_e$ oscillation probability as a function of L/E. The top graph (a) shows the full probability for vacuum oscillations with $\delta_{CP} = 0$, and also the separated contributions of the solar and atmospheric terms (the last denoted as $sin2\theta_{13}$). the middle graph (b) shows the full probability in vacuum for different values of δ_{CP}. The bottom graph (c) shows the full oscillation probability in matter, assuming constant density, for different baselines and with $\delta_{CP} = 0$.

DUNE energy-baseline conditions, with the resulting possibility to unambiguously measure both the neutrino mass ordering and the CP violating phase δ_{CP} with the same data set.

The figures 1.5 and 1.6 show the electron and anti-electron neutrino appearance probabilities as functions of both the baseline and the neutrino energy, and for different possible values of δ_{CP}. More precisely, figure 1.5 reports the normal ordering case, while figure 1.6 refers to the inverted ordering

scenario.

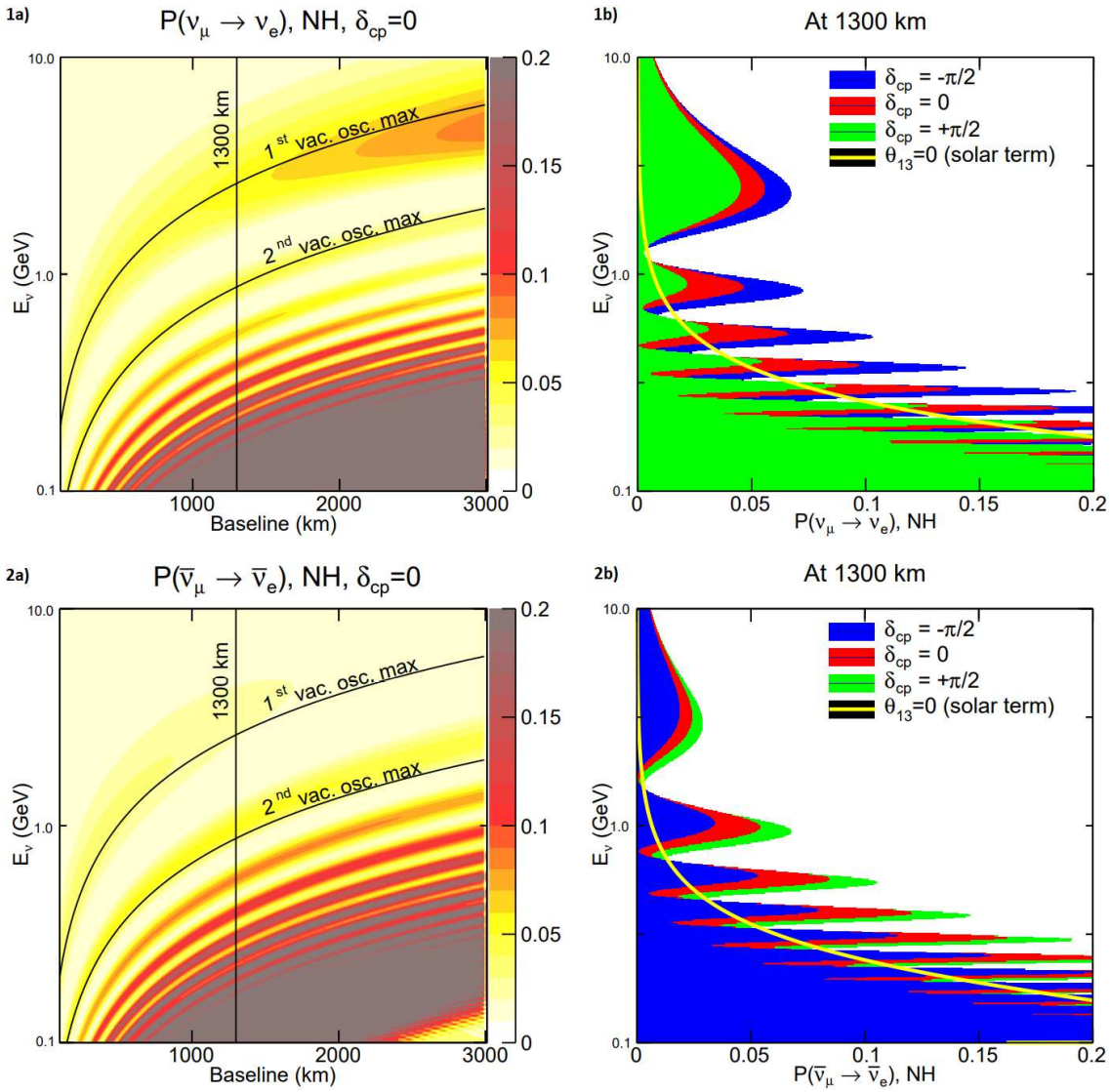

Figure 1.5: From [11]: neutrino oscillation probabilities as a function of beam energy and baseline, for different values of δ_{CP}, in the normal hierarchy scenario.

Both the figures report the $\nu_\mu \to \nu_\mathrm{e}$ oscillation probabilities as functions of E and L with $\delta_{\mathrm{CP}} = 0$ (1a for neutrinos, 2a for antineutrinos) and its projection on the neutrino energy axis at L = 1300 km (1b for neutrinos, 2b for antineutrinos). The probabilities reported in the plots 1b) and 2b) refer to $\delta_{\mathrm{CP}} = 0$ (red), $\delta_{\mathrm{CP}} = \frac{\pi}{2}$ (green), and $\delta_{\mathrm{CP}} = -\frac{\pi}{2}$ (blue), respectively, while the yellow curve is the ν_e appearance due to the mixing of the ν_1 and ν_2 mass eigenstates.

The black line in figure 1.4 c) on the previous subsection represents the same oscillation probability reported in figure 1.5 1a), but as a 1D function of L/E.

The influence of CP violation and MSW effect on the oscillation probabilities of neutrinos and antineutrinos have, in general, the following properties:

- $P(\nu_\mu \to \nu_\mathrm{e})$ is enhanced and $P(\bar{\nu}_\mu \to \bar{\nu}_\mathrm{e})$ is suppressed in the normal hierarchy case, this effect

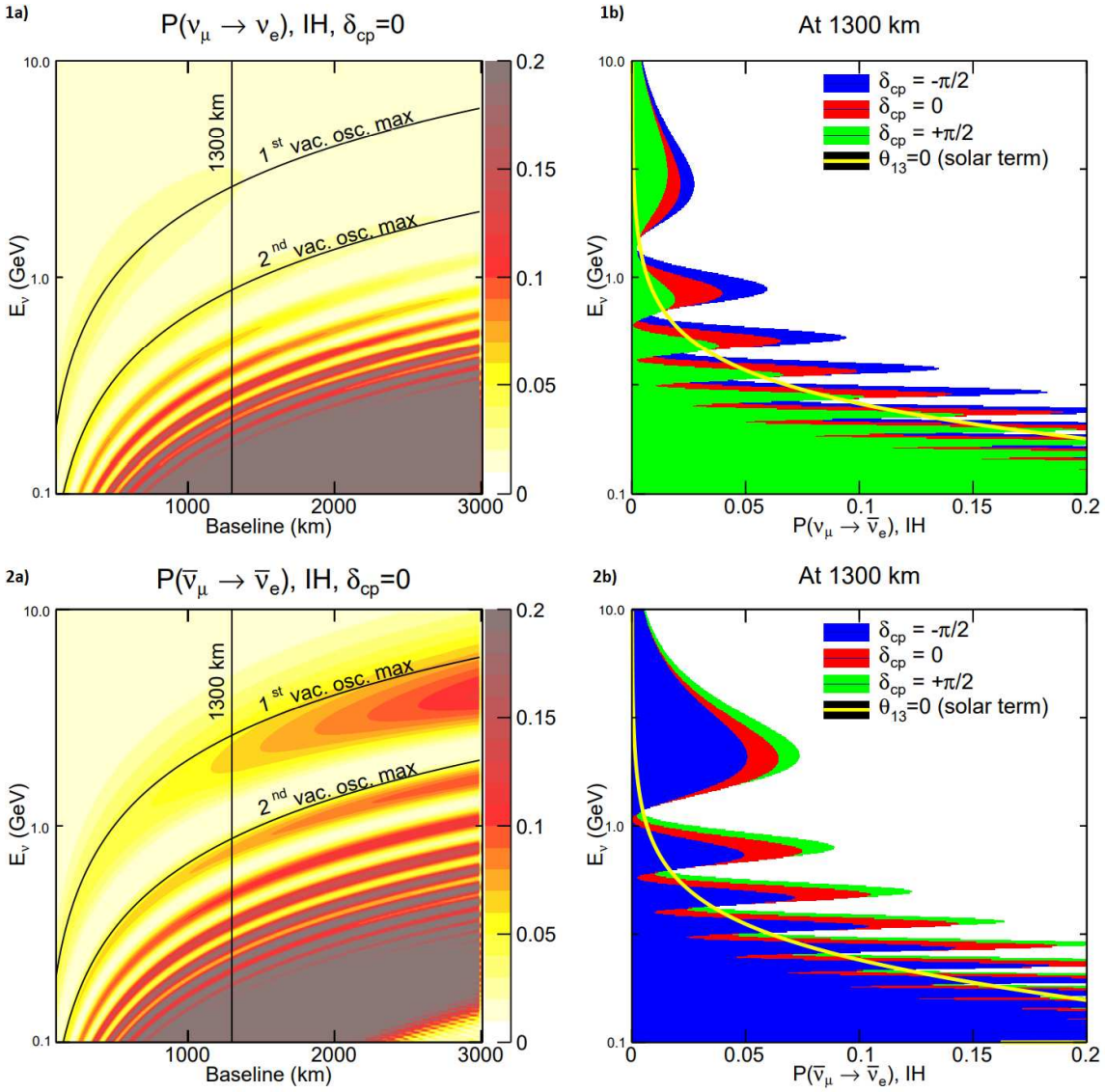

Figure 1.6: From [11]: neutrino oscillation probabilities as a function of beam energy and baseline, for different values of δ_{CP}, in the inverted hierarchy scenario.

increases with the baseline at a fixed L/E ratio;

- $P(\bar{\nu}_\mu \to \bar{\nu}_e)$ is enhanced and $P(\nu_\mu \to \nu_e)$ is suppressed in the inverted hierarchy case, this effect increases with the baseline at a fixed L/E ratio;
- the matter effect on the probability amplitude is dominant at the first oscillation maximum;
- the matter effect introduces a phase shift in the oscillation pattern, shifting it to a lower energy[4] when switching the hierarchy from normal to inverted.

The total asymmetry in the neutrino flavour oscillations can be expressed as a sum of a CP-violating term and a MSW term:

[4] by approximately 100 MeV for the DUNE case.

$$A = \frac{P(\nu_\mu \to \nu_e) - P(\bar{\nu}_\mu \to \bar{\nu}_e)}{P(\nu_\mu \to \nu_e) + P(\bar{\nu}_\mu \to \bar{\nu}_e)} = A_{\mathrm{CP}} + A_{\mathrm{MSW}}$$

The dependence of the asymmetries on baseline and energy, at the largest oscillation probability peak, can be approximated as $A_{\mathrm{CP}} \propto L/E$ and $A_{\mathrm{MSW}} \propto L \cdot E$. This means that with a neutrino beam of $O(1\,GeV)$, an oscillation experiment would require a baseline of at least several hundred kilometers to cancel any ambiguity on the interpretation of the results. In this case the matter asymmetry would increase enough to remove the degeneracy among possible combinations of δ_{CP} and mass ordering.

The plots in figure 1.7 illustrate the ambiguities that can arise from the interference of the MSW and CP asymmetries, and how these vanish by raising the baseline length. The curves in black and

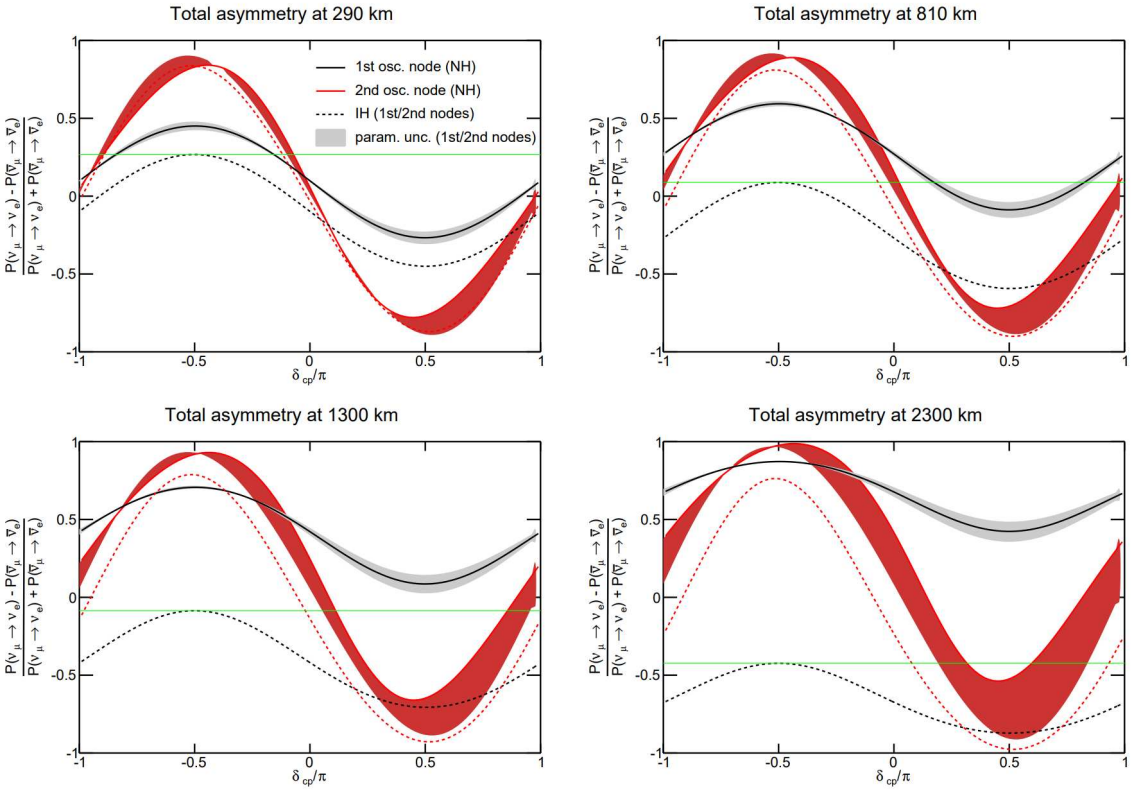

Figure 1.7: From [11], total $\nu/\bar{\nu}$ oscillation probability asymmetry as a function of δ_{CP} at four different baseline values: 290 km (top left), 810 km (top right), 2300 km (bottom left) and 1300 km (bottom right).

red illustrate the asymmetries at the first and second oscillation nodes, respectively. The solid lines represent the normal hierarchy (NH), while the dashed lines represent inverted hierarchy (IH). The green lines indicate the asymmetry at the first node for maximal CP violation ($\delta_{\mathrm{CP}} = \pi/2$) and inverted hierarchy.

The plots demonstrate that experimental measurements of the asymmetry at the first oscillation node could yield to ambiguous results for short baselines, given that both δ_{CP} and the hierarchy are unknown. For example, at a baseline of 290 km there is a degeneracy in the measured asymmetry between $\delta_{\mathrm{CP}} = \pi/2$ in IH conditions and $\delta_{\mathrm{CP}} = 0$ in NH conditions at the first node (green line in figure 1.7). On the other hand, at very long baselines there is no degeneracy since the matter asymmetry

exceeds the maximal CP asymmetry at the first oscillation node, in this case the mass hierarchy and CP asymmetries can be resolved within the same experiment. According to the current best-fit values of the neutrino oscillation parameters, the matter asymmetry exceeds the maximal possible CP asymmetry at baselines of ≥ 1200 km [11].

The aforementioned considerations suggest that a baseline above 1200 km is enough to search for CP violation and determine the mass hierarchy simultaneously, but in order to achieve quantitative predictions, a study of the sensitivities to CP violation and mass hierarchy as a function of baseline must be carried out using a realistic neutrino beamline (with a specific design optimized for each baseline individually).

In the simulations carried out by the DUNE collaboration [15], a 34 kt LArTPC was assumed as FD, due to its high ν_e-identification efficiency[5], and the beamline design was based on the NuMI (*Neutrinos at the Main Injector*) beamline utilizing a 120 GeV, 1.2 MW proton beam from the Fermilab Main Injector (MI). By varying the distance between the target and the magnetic horn in a $[280-580]$ m range, the resulting beam spectrum can be selected to cover the first oscillation node and part of the second oscillation node.

For baselines shorter than 1000 m the on-axis beams flux is too small in the energy range where oscillations occur, in these cases the simulations feature off-axis beam configurations[6]. The off-axis angle was chosen to provide covering for most of the first oscillation node.

With baselines above 1500 km the correct mass hierarchy could be determined with a probability greater than 99% for all values of δ_{CP} with a large LArTPC far detector, since the aforementioned degeneracy between the MSW and CP violating asymmetries would be more suppressed. However, for such baselines the magnitude of the MSW effect becomes too large with respect to the δ_{CP} effect to observe an explicit CP-violation asymmetry, because one of the neutrino beam polarities ($\nu/\bar{\nu}$ for inverted/normal hierarchy) undergoes a significant event rate suppression.

For these reasons, the baseline studies indicate that in realistic experimental conditions there is a range of baselines ($[1000-1300]$ km) that optimize the determination of the CP violating phase.

1.2 Aims of DUNE

This section describes the aims of the DUNE experiment and the key features of its physics reach, which is complementary to other existing and planned experiments [16, 17, 18].

The cumulative results of all the neutrino oscillation experiments performed to date permit to estimate five of the neutrino mixing parameters [19, 20]: the three mixing angles θ_{12}, θ_{23} and θ_{13}, and the two squared-mass differences Δm^2_{21} and $|\Delta m^2_{31}|$.

The neutrino mass ordering (sign of Δm^2_{31}) is currently unknown, even though recent results show a weak preference for the normal ordering scenario [21, 22, 23]. The value of δ_{CP} is also not defined, but recent neutrino oscillation data are beginning to provide some information on its value [21, 24].

The DUNE experiment has the following primary physics goals [11]:

[5] which is flat over a large range of energies

[6] This because off-axis beams feature narrow-band, low-energy neutrino fluxes

- precise measurement of the parameters governing the $\nu_\mu \rightarrow \nu_{e,\mu}$ oscillations, in particular: the mixing angles θ_{13} and θ_{23}, the CP-violating phase δ_{CP}, the squared mass difference $|\Delta m^2_{32}|$. Determination of the sign of Δm^2_{32} (which would solve the neutrino mass hierarchy problem) and test of the three-flavour paradigm;
- improve the current limits on the search for proton decay, in particular for the partial lifetime (τ/BR) in some important candidate decay modes such as $p \rightarrow K^+\bar{\nu}$;
- precise measurement of the neutrino flux from a possible core-collapse supernova event within our galaxy, should one occur in the DUNE lifetime.

DUNE is designed to achieve these goals by pushing both the beam intensity and the detection precision beyond the current state of the art for long-baseline neutrino oscillation experiments.

The key features of the DUNE experiment are the world's most intense neutrino and antineutrino beams, a large FD located deep underground to reduce background signals and thus enhance the sensitivity, and a broad neutrino spectrum to probe the shape of the oscillation pattern over a wide range of energies, enabling extended fit over more than one oscillation peak. As mentioned before, the FD will be based on LArTPC technology, which is highly performing in particle identification and energy measurement, and the usage of the same technology within the ND complex will constrain systematic errors to world-leading precision. Furthermore, the combination of neutrino beam energy with the selected baseline will enhance the matter effect, raising its amplitude above the maximal possible CP-violating asymmetry and allowing to measure both the δ_{CP} and the mass hierarchy in a single experiment. This choice also provides enough sensitivity to the CP violating phase δ_{CP} (for a wide range of possible δ_{CP} values) to push forward the current knowledge of δ_{CP} and possibly discover its true value at the 5σ confidence level.

The performance of the DUNE FD was estimated with complete simulations using convolutional neural network (CVN) algorithms for flavor classification [25]. This procedure permits to reach efficiencies of 90% for electron neutrinos and 95% for muon neutrinos identification on CC interactions.

The results of the Monte Carlo simulations carried out by the DUNE group [15] permits to give more details about the DUNE sensitivities as functions of exposure, an example is reported in figure 1.8.

DUNE will be able to establish the neutrino mass ordering at the 5σ level for 100% of δ_{CP} values between two and three years of exposure [1]. The CP violation can be observed with 5σ significance after a 7 years exposure if $\delta_{CP} = -\pi/2$, and the range is extended to 50% of the possible δ_{CP} values after 10 years. Lastly, after 13 years of running the CP violation can be measured with 3σ significance for 75% of δ_{CP} values.

DUNE has the capabilities to make numerous high-impact, world-leading findings over several decades, for example a unambiguous determination of the neutrino mass ordering would resolve a longstanding question in neutrino physics, which has several implications for astrophysics, cosmology, and neutrino-less double beta decay experiments. A precise determination of the θ_{23} octant could point to a new symmetry, while the observation of CP violation in the lepton sector would be an important step in understanding the baryon asymmetry of the universe through the leptogenesis theory.

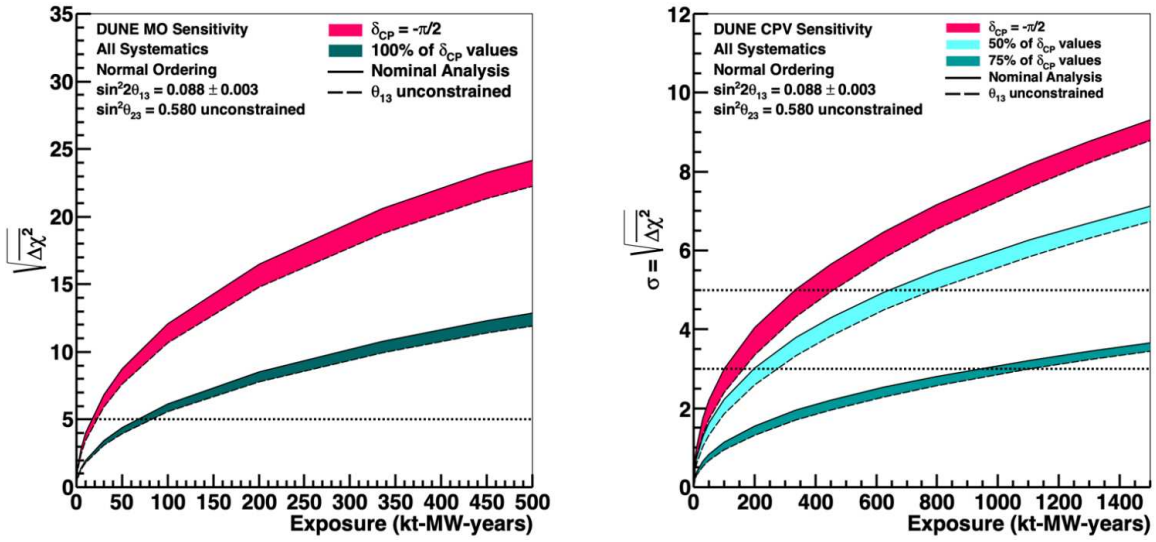

Figure 1.8: From [1]: sensitivity to the neutrino mass ordering (left) and CP violation (right) as a function of exposure in kt-MW-years. Only the Asimov sensitivity is considered, and the curves are shown for maximal CP violation ($\delta_{\rm CP} = -\pi/2$) and for different fractions of $\delta_{\rm CP}$ values.

The current three-flavour picture of neutrinos theory will gain resolution due to the DUNE high precision measurements of mixing parameters, but it will also be tested in its fundamental structure with possible evidences of physics beyond the three-flavour model.

The DUNE FD will be able to detect a large sample of neutrinos from a possible supernova burst within the Milky Way, together with a wide range of astrophysics measurements, featuring unique sensitivity to the electron neutrino component. Furthermore, the DUNE experiment will be uniquely sensitive to a broad range of physics *beyond the Standard Model* (BSM), including also nucleon decays.

The secondary objectives of the DUNE physics program, possibly enabled by the facility designed to achieve the primary ones, include [11]:

- additional accelerator-based, neutrino oscillation measurements such as nonstandard BSM interactions;
- measurements of neutrino oscillation phenomena using atmospheric neutrinos;
- measurement of other astrophysical phenomena using medium-energy neutrinos.

The DUNE capabilities for sensing BSM phenomenology permits to improve the existing constraints on sterile neutrino mixing, non-standard neutrino interactions, CPT violation, nucleon decay and new physics enhancing neutrino trident production. This high sensitivity could also bring DUNE to the discovery level for a vast range of phenomenology beyond the Standard Model, for example finding evidences of dark matter created in the high-power proton beam interactions or from cosmic sources, searches for sterile neutrino mixing, non-standard neutrino interactions, new physics related to neutrino trident production, CPT violation and baryon number violating processes.

The DUNE scientific scope includes also some additional secondary objectives, which may require additional upgrades to the far site facility[7]:

- detection and measurement of the diffuse supernova-neutrino flux;
- measurement of solar neutrino oscillations and test the *Standard Solar Model* (SSM);
- measurements of astrophysical and geophysical low-energy neutrinos.

The full physics program of DUNE requires four FD modules, a proton beam intensity of 2.4 MW and a highly capable ND system. The initial configuration for this experiment (Phase I) will include two FD modules, a limited ND complex and a 1.2 MW proton beam, but it will be sufficient to achieve DUNE's early physics goals and demonstrate the potential of the final design (Phase II).

1.3 The DUNE design

The DUNE design is the product of a worldwide collaboration of scientists and engineers from over 200 institutions in more than 30 countries, an international effort to measure neutrino oscillation as a function of energy in a broadband beam with unique precision, to resolve degeneracy among the oscillation parameters.

The DUNE collaboration will achieve high control on systematic uncertainties by employing the LArTPC technology, which permits advanced imaging techniques with unprecedented performances, in both the FD and (a component of the) ND.

The 40 kt (fiducial) FD is designed in a modular structure of four 10 kt (fiducial) components, each featuring a different LArTPC technology, and its deep underground location facilitates the possible observation of nucleon decay and other rare processes including low-energy neutrino detection.

The general physics requirements for the DUNE design are:

- Long baseline: as mentioned in section 1.1, with a baseline greater than 1000 km the asymmetry due to the MSW effect is much larger than that arising from CP violation phenomena, regardless of the value of δ_{CP}. This removes the experimental degeneracy between the neutrino mass ordering and the determination of δ_{CP}, giving DUNE the unique capability to measure both using the same data set unambiguously.
- Large far detector mass in combination with high-power beam: the number of neutrino interactions occurring at the far site depends almost linearly on the fiducial mass of the FD and on the intensity of the proton beam.
- Wide-band neutrino beam: in order to attain a definitive CP violation estimation, to precisely test the three-neutrino mixing paradigm and to resolve ambiguities between the oscillation parameters, DUNE needs to measure the neutrino fluxes as a function of E over more than one full oscillation period.

[7] Such as additional detector mass or other detector technologies.

- Precise reconstruction of neutrino flavour and energy: the flavour reconstruction requires excellent discrimination between muons and electrons and is critical to accurately distinguish ν_μ and ν_e charged-current (CC) interactions in the FD. To enable an accurate measurement of neutrino oscillations as a function of energy, the FD must have the ability to reconstruct the energy of each neutrino event with high precision.

- Precise constraints on systematic uncertainties: a reliable estimation of δ_{CP} requires a precise measurement of muon-to-electron oscillations as a function of neutrino energy. The related systematic uncertainties (due to the neutrino flux prediction, interaction cross sections and detector response) must be constrained at a lower level with respect to the statistical error.

- Deep underground location for the FD: the deep underground location is critical to absorb part of the high rate of activity from cosmic particles on the surface, in order to search for rare non-beam related signals. These signals include baryon number violating processes and low-energy neutrinos from supernova bursts, both requiring a nearly zero background in order to be detected (which also greatly simplifies the reconstruction of accelerator neutrinos).

In order to meet these requirements, the DUNE collaboration made a number of choices for the detector design, and the motivations for these choices are reported in the following:

- LArTPC technology for FD: given the baseline of DUNE, the first oscillation maximum occurs at a neutrino energy of 2.5 GeV, this energy region includes many neutrino interaction processes, some of which featuring multiple final-state mesons. The LArTPC technology combines both tracking and calorimetry capabilities, allowing to distinguish ν_μ and ν_e CC interactions, as well as good resolution for both the leptonic and hadronic energies. The imaging capability of the FD also plays an important role for the DUNE research in the BSM flied, and the Ar target provides unique sensitivity to electron neutrinos from supernova bursts.

- ND complex including LArTPC: the role of the ND is to measure the neutrino beam prior to the oscillation phenomena and to minimize the systematic uncertainties in the FD long-baseline oscillation measurements. The neutrino energy spectrum depends on the convolution of beam flux, cross sections and detector response, and all these three factors have large *a priori* uncertainties. The ND complex features, among other technologies, a small-scale version of the FD, called *ND-LAr*, as will be described more in detail in section 1.3.2. By having a LArTPC detector on both the near and the far sites it is possible to be sensitive to all three of these classes of uncertainty simultaneously[8].

- Calibration: to achieve the systematic uncertainty level required for the DUNE physics goals, the energy and position of charge deposits in the FD must be precisely calibrated at the few percent level, for this reason it is important to have as many independent calibration procedures as possible. The DUNE calibration strategy features test beam measurements, analysis of calibration data from physics samples, detector instrumentation and cumulative results of the various simulations.

[8] Supposing that the ND has the a kinematic acceptance at least as good as the FD.

- Photon detection (PD): the PD system is used to observe prompt scintillation light induced by charged particles interacting with the Argon nuclei in the LArTPC, thus providing the timing information for non-beam physics events. The scintillation signal is used in combination with the TPC information to localize the event in the drift direction, but enables also a more precise energy reconstruction.

- Data acquisition (DAQ) system: the trigger and DAQ system is responsible for the data receiving, processing and recording, and for providing synchronization to the electronics and calibration systems. The main requirements for the DAQ design include wide up-time window[9], data rate and throughput optimization, these requirements stem mostly from the goal of detecting supernova neutrino bursts (abbreviated SNB).

As mentioned in the previous section, the DUNE scientific program is divided in two main Phases. In Phase I the collaboration will start collecting physics data with only two FD modules and a first-stage ND design, with a 1.2 MW proton beam. This phase will serve to demonstrate the potential of DUNE, as the collected data will enable unambiguous determination of the neutrino mass ordering, the δ_{CP} value with 3σ significance if $\delta_{\mathrm{CP}} = -\pi/2$ and the other oscillation parameters (including the $\Delta {m_{32}}^2$ with world-leading precision). This early stage design permits also to detect neutrinos from possible core-collapse supernovae and to search for BSM physics.

The full scope of the DUNE program will be reached during the Phase II, this will permit to upgrade to 5σ the CP violation discovery potential, to perform independent measurement of $sin^2 2\theta_{13}$ with precision comparable to that of reactor neutrino experiments and to achieve significant sensitivity to the θ_{23} octant. The DUNE experiment guarantees also unique sensitivity to neutrino astrophysics phenomena, BSM physics and evidences of additional neutrinos beyond the three-flavour paradigm.

The three main upgrades related to the passage from Phase I to Phase II are all necessary to achieve the aforementioned physics goals (as well as the sensitivities reported in the previous section), and are reported in the following list:

- expansion of the FD with two additional modules, reaching a total fiducial mass of 40 kt;

- perform a series of upgrades on the proton injector to double the beam power, from 1.2 MW to 2.4 MW;

- upgrade the ND complex towards a more sophisticated setup.

The Long Baseline Neutrino Facility (LBNF) has received extensive investment to provide detector facilities and neutrino beam with the required properties: the excavation of more than 800 kt of rock in the caverns at SURF is currently underway, the final beamline complex and ND complex designs have been completed.

The Fermilab's proton accelerator will require some improvements to raise the neutrino beam intensity to the DUNE requirements, these are grouped in the so-called *Proton Improvement Plan-II* (PIP-II), which is well underway and expected to be ready by 2029.

[9] to increase the chances of being already collecting data when one of these rare transient events occurs

In the next subsections there will be a brief description of the current design for the neutrino beamline (1.3.1), the ND (1.3.2) and the FD (1.3.3), with a particular attention on the FD since it is related to the main topic of this thesis[10].

1.3.1 Neutrino beam

As mentioned in the previous sections, the DUNE neutrino beamline involves a conventional horn-focused neutrino beam produced from pion decay-in-flight [11]. This technique relies on focusing the pions before their decay in order to achieve a focused neutrino or antineutrino beam. The horn-focused neutrino beamline relies on the NuMI[11] design [11], this design was already employed in the MINOS, MINERνA and NOνA experiments, and for DUNE the focusing parameters will be optimized to maximize sensitivity to CP violation.

The primary beam is composed of 60 GeV to 120 GeV protons from the Main Injector accelerator, the related neutrino beam operates at 1.2 MW (supporting a possible upgrade to 2,4 MW) and can be produced in forward (reverse) horn current mode, resulting in a predominately $\nu_\mu(\bar{\nu}_\mu)$ flux. This flux is peaked at ≈ 2.5 GeV, near the first oscillation maximum for the DUNE baseline, and the whole energy spectrum ($[0.5-5.0]$ GeV) covers more than one oscillation period.

The primary beam of protons will be extracted from the MI-10 straight section of the Main Injector using single-turn extraction. The beam will then enter a transport section, designed for very low losses, which brings the protons to an engineered earthen embankment (hill), the latter is depicted in figure 1.9.

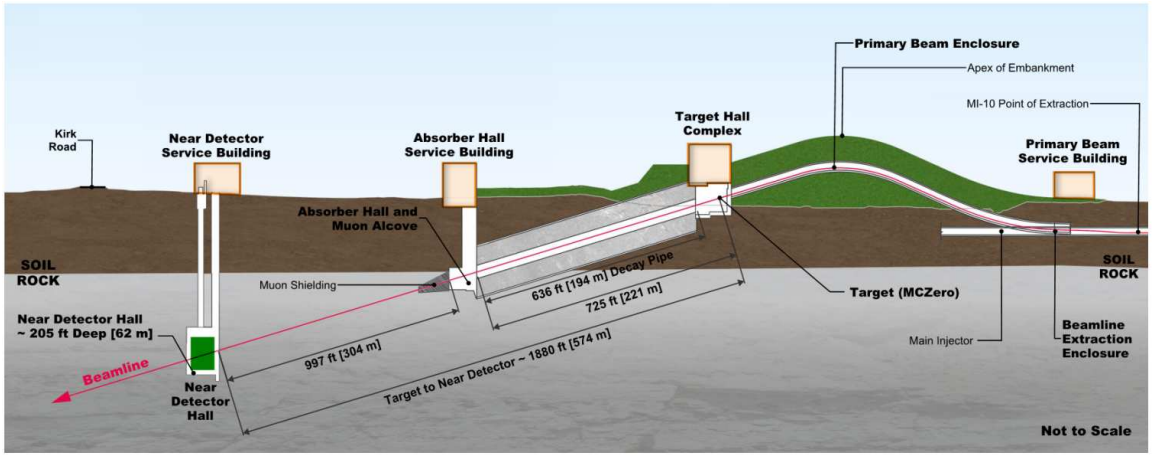

Figure 1.9: From [26], longitudinal section of the DUNE beamline facility at Fermilab. The proton beam enters from the right, after being collected from the MI-10 extraction point of the Main Injector.

The beam undergoes a net 5.8° downward vertical bend from a system of dipole magnets, and is then buried by soil shielding. A fast single-turn extraction (in the 120 GeV regime) can deliver 4.9×10^{13} protons to the graphite target[12], in a 10 μs pulse operation. The PIP-II accelerator upgrade will in-

[10] Which is the description of the experimental setups and procedures adopted to characterize, select and test the SiPM sensors for DUNE-FD1 and ProtoDUNE2-SP (chapter 4 and 5).

[11] The name NuMI stems from the homonym neutrino beam production facility.

[12] which consists in 47 segments of 2 cm long POCO graphite ZXF-5Q.

crease the protons per cycle to 7.5×10^{13} and reduce the cycle time from 1.33 s to 1.2 s, with a resulting initial beam power of 1.2 MW (starting from the 700 kW of the current design).

This beamline is designed to support additional upgrades beyond PIP-II, as already mentioned in section 1.2, in order to increase the beam power up to 2.4 MW and accomplish the full DUNE scientific program.

In the 1.2 MW regime, the accelerator complex is expected to deliver 11×10^{20} protons per year to the target, a portion of these protons (approximately 85%) interact with the target producing, among other particles, kaons and pions, which are then focused by a set of magnetic horns into a decay pipe. These products decay into muons and muon neutrinos inside the decay pipe, and the horn polarity permits to switch among high purity (> 90% in the oscillation region) neutrino and antineutrino beams. The beam contamination stems from the presence of $\bar{\nu}_\mu(\nu_\mu)$ particles in the $\bar{\nu}_\mu(\nu_\mu)$ beam (currently at the 10% level, but will be upgraded to 5% in the NuMI design), and also from the presence of electron neutrinos (less than 1%).

The decay volume design is optimized to produce neutrinos in the energy range of interest, in compliance with the Fermilab site boundaries. The current plan foresees a 250 m He-filled pipe with a circular cross-section of $6\,m^2$, which ends with an absorber[13] used to remove residual hadrons from the neutrino beam. The absorber is instrumented to measure the transverse distribution of the hadronic showers on a pulse-by-pulse basis, and it is followed by an array of muon detectors to measure tertiary-beam muons, in order to provide (indirect) information on the neutrino beam direction, profile and flux.

1.3.2 DUNE ND

At 574 m downstream of the neutrino production target there is a key component of the DUNE design: a high-resolution near detector (ND), which is going to be an integrated system of multiple components. The ND complex will enable the achievements of DUNE's primary scientific goals, such as discovery-level sensitivity to the CP-violating phase δ_{CP} and high precision measurements of other neutrino oscillation parameters, but it will also use the high-intensity neutrino beam as a probe of BSM physics.

The ND statistics alone will permit to engage a rich physics program, due to the 240000 (85000) ν_μ ($\bar{\nu}_\mu$) charged current and 90000 (35000) neutral current interactions per ton per 1×10^{20} protons-on-target (at 120 GeV) in the $\nu(\bar{\nu})$ beam. These numbers correspond to 10^7 neutrino interactions per year for the beamline/ND configurations evaluated for the DUNE design.

The reconstructed energy spectrum at the ND is a convolution of interaction cross section, flux of the unoscillated neutrino beam and energy response of the detector. The ND must independently constrain uncertainties on each of those components, considering that both the acceptance and the flux for this detector are much different from the FD case. The ND will measure $\nu_\mu - \mathrm{Ar}$ interactions with high precision using both gaseous and liquid argon targets, this choice will further reduce the systematic uncertainties associated with the modeling of these interactions [27].

The main energy range relevant for the oscillation analyses in DUNE corresponds to $0.5 < E <$

[13] a water-cooled structure of Al and steel

10 GeV, but the measurement of fluxes, cross sections and particle production must cover an extended energy range (up to 50 GeV) to reach the DUNE-ND full physics scope.

The sensitivity to different values of δ_{CP} increases at $E < 5$ GeV, but the higher energy region is important for normalization purposes and to search for effects beyond PMNS oscillations. The neutrino interactions are particularly challenging to study in this energy range, since they receive significant contributions from different processes: $\sim$ 25% quasi-elastic (QE), 42% resonances (RES), and 33% deep inelastic scattering (DIS) [27]. As a result, the DUNE-ND data analysis relies on understanding all the QE, RES, and DIS processes on Argon nuclei. More in particular, the most critical region being related to the resonance productions and to the transition region to DIS, which is rather complex to model properly due to the interplay of various effects.

The ND design must outperform the FD in various aspects [27], for the following reasons. The ND must have the ability to measure events in a similar way to the FD, as discussed above, while operating in an environment with much higher event rates. The design should rely on multiple methods for measuring neutrino fluxes, each featuring a different (or negligible) dependence from the cross-section uncertainties. With the necessity of relying on complicated and not fully refined models, the ND needs to measure neutrino interactions with much better detail than the FD. This includes having a higher detection efficiency across the kinematically-allowed phase space, a more reliable charged and neutral particles identification and better energy reconstruction.

To achieve the required performances, the ND complex will need to measure the unoscillated neutrino flux spectrum to a few percent precision, and for all the neutrino species in the beam (ν_μ, $\bar{\nu}_\mu$, ν_e, $\bar{\nu}_e$). This requires a low-density detector with an adequate physical radiation length, in order to distinguish e^+ from e^-.

The connection between the observations in the ND and the FD is made using a simulation that includes models for the neutrino flux, neutrino interactions, nuclear effects, and detector response. An important issue is the presence of backgrounds, for example, the intrinsic ν_e content of the beam is a background for the ν_e appearance oscillation signal at the FD. An additional background for this signal stems from the NC events with a π^0 that leads to electromagnetic showers from converted photons, since they can appear as ν_e CC interactions.

In the case of maximal CP violation (e.g. $\delta_{CP} = -\pi/2$), the number of signal events can differ by $\sim$ 40% relative to the expected population at $\delta_{CP} = 0$. However, this deviation in the total number of selected $\nu_e/\bar{\nu}_e$ events is reduced to $\sim$ 15% once backgrounds are accounted for [27]. In order to obtain $3(5)\sigma$ significance to $\delta_{CP} \neq 0$ in these conditions, the total uncertainties must to be constrained to 5%(3%) or better, with target systematic uncertainties better than 3%(2%)[14]. These constraints must consider not only the background (already mentioned misidentified events, intrinsic ν_e and "wrong sign" ν_μ content in the beam) but also an accurate modeling of the expected oscillation signal, in order to extract the related parameters from the number and spectrum of these events.

A level of $3(5)\sigma$ significance to maximum CP violation is expected after 3(7) years in the standard LBNF/DUNE beam and detector staging scenario. The graph reported in figure 1.10 illustrates the impact of systematic uncertainties on the observed ν_e signal for the CP violation sensitivity [27]. This plot shows that a change in the relative uncertainties from 1% to 3% can substantially increase the

[14] To prevent systematic uncertainties from being the dominating contribution to the total uncertainty

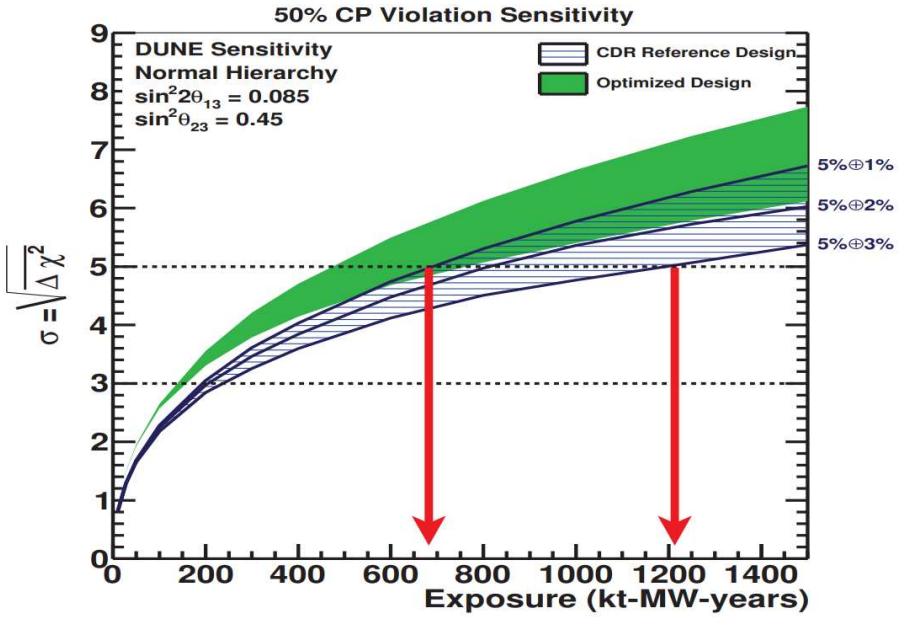

Figure 1.10: From [27]: impact of systematic uncertainties on the sensitivity to the CP violation search in the FD, reported as a function of the exposure. In this plot are reported both the ND design as it is defined in the CDR (dark blue) and as it results from simulations to search the optimized design (green).

total exposure needed to achieve the discovery level (5σ) on the determination of δ_{CP}. This gives a simplified example of cost and benefits related to the reduction of systematic uncertainties.

Since the ND data will feature a high-precision reconstruction and a large population of events, it can be used for nucleon structure and electroweak physics studies, as well as for searches for BSM physics in unexplored regions such as heavy sterile neutrinos or light Dark Matter particles.

The current ND design, developed to achieve the aforementioned requirements, is a suite of three complementary detectors, these are reported in the following list.

- the ND-LAr detector: a modular LArTPC (300 tons) called *ArgonCube* which is also optically segmented;
- the ND-GAr detector: a magnetized high-pressure gaseous argon TPC (HPgTPC) surrounded by an *electromagnetic calorimeter* (ECAL) in a 0.5 T magnetic field;
- the *System for on-Axis Neutrino Detection* (SAND): a magnetized beam monitor consisting of an electromagnetic calorimeter, an inner target/tracker system and an active LAr target.

SAND is placed permanently on the neutrino beam, while the ND-LAr + ND-GAr detectors can move to take data in positions up to 33 m off the beam axis: this feature is known as DUNE-PRISM and is sketched in figure 1.11.

As the detectors move off-axis, the mean energy of the incident neutrino flux decreases and the spectrum becomes more monochromatic. The neutrino interaction rate drops off-axis, but the beam intensity, combined with the size of the LArTPC, yield enough statistics also in this configurations.

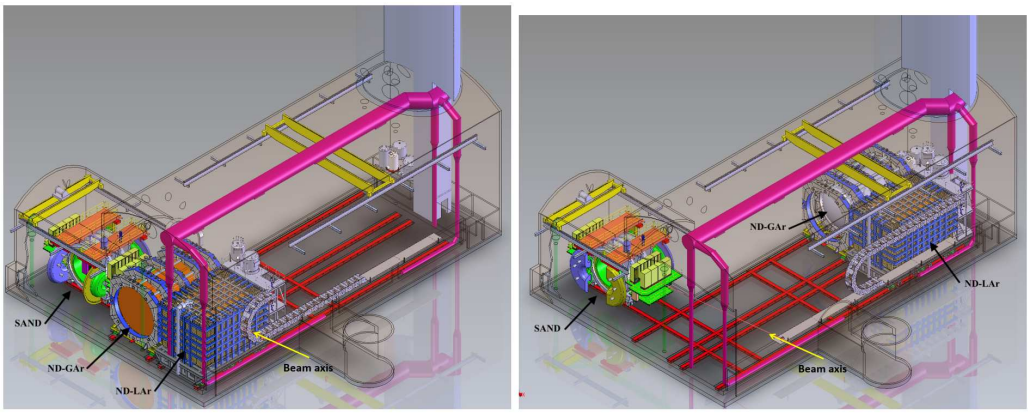

Figure 1.11: From [27]: schematic of the DUNE ND hall, shown with component detectors all in the on-axis configuration (left) and with the ND-LAr + ND-GAr in an off-axis configuration (right). The SAND detector is in position on the beam axis, which is directed as the yellow arrow.

The DUNE concept is based on reconstructing the energy-dependent neutrino spectrum and comparing the FD and ND data, and the ability to modify the ND energy spectrum by measuring off-axis flux will allow disentangling degenerate effects in the energy reconstruction procedures.

The three detector components have individual and overlapping functions, and are described in detail in the following subsections.

ND-LAr

As discussed above, having a ND component which is similar to the FD design is of crucial importance to reduce as much as possible systematic uncertanties on the neutrino beam parameters. The details of the LArTPC working principle and main properties are discussed in details in section 2.1, by now it is worth mentioning that it is a detector capable of measuring charge and scintillation light produced by the $\nu-$Ar interactions inside the TPC.

With the intense neutrino flux and high event rate at the ND, traditional, monolithic, LArTPCs with charge and light readout would be stretched beyond their performance limits [27]. To overcome this issue, the proposed DUNE ND-LAr design is a matrix of small and optically isolated TPCs, which are individually instrumented in a pixelized read out system, this technology is called *ArgonCube*. The subdivision of the volume into many smaller TPCs allows for shorter drift distances and times which in turns, combined with the optical isolation, reduces the overlapping interactions inside the same TPC module. The detector modularization also improves drift field stability, while reducing the high voltage (HV) and LAr purity requirements, while pixelized charge readout provides unambiguous 3D imaging of particle interactions. The pixelization of the readout allows for full 3D reconstruction of tracks, and each of the TPC modules is equipped with its own optical readout, in order to provide the timing information to associate tracks and events across the whole TPC matrix.

The ND-LArTPC volume is designed for being sufficiently large to provide an expected population of $1 \times 10^8 \nu_\mu$ (on axis) charged current events per year, featuring good hadron containment. The tracking and energy resolution of LArTPC technology, combined with the ArgonCube mass, will allow measurement of the beam flux using several techniques, including the rare $\nu - e^-$ scattering process.

This detector begins to lose acceptance for muons with a measured momentum above $\approx 0.7\,\text{GeV/c}$, because these particles are no longer contained in the LArTPC volume, in the Phase I the solution will rely on a magnetic spectrometer (TMS) placed downstream of the LArTPC to measure the charge sign and momentum of escaping muons, but in the full DUNE ND design concept this function is left to the ND-GAr detector. Beyond the ND-GAr, the SAND component of the ND will serve as on-axis beam monitor. The 5 m (along beam) $\times$7 m(horizontal, transverse to beam) $\times$3 m (height) dimensions and the 67 t fiducial mass of ND-LAr are optimized primarily for hadronic containment, under the assumption that ND-GAr will measure the sign and momentum of downstream exiting muons.

ND-GAr

ND-GAr consists of a high-pressure gaseous argon TPC (HPgTPC) surrounded by an electromagnetic calorimeter (ECAL), both immersed in a 0.5 T magnetic field, plus an external muon system [27]. A schematic of ND-GAr detector is reported in figure 1.12.

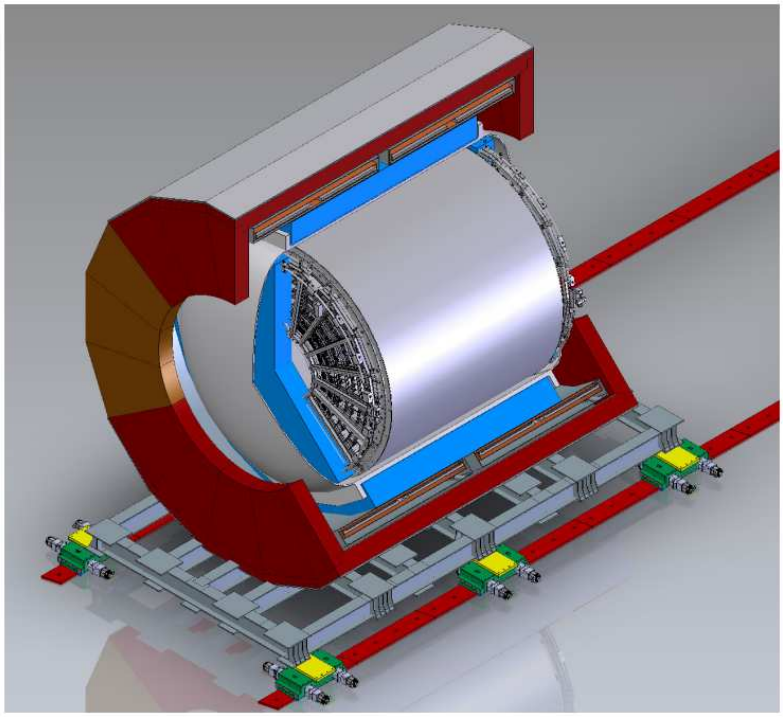

Figure 1.12: From [27]: schematic of ND-GAr showing the HPgTPC, its pressure vessel, the ECAL, the magnet and the return iron. The detectors for the muon-tagging system are not shown in this picture.

The HPgTPC provides a low density medium with excellent tracking resolution for muons, furthermore, the ν – Ar events in gaseous TPC can be studied with a very low charged-particle tracking threshold and a superior resolution with respect to the liquid phase TPC. For neutrino interactions taking place in the HPgTPC, it will reduce the energy threshold for detecting charged particle to lower values w.r.t the far or near LArTPCs and will also greatly extends the particle identification (PID) performances, particularly for $p-\pi$ separation.

The high pressure ensures a population of 2×10^6 ν_μ-CC events per year, these events can be studied to detect the charged particle activity near the interaction vertex, and the HPgTPC can better

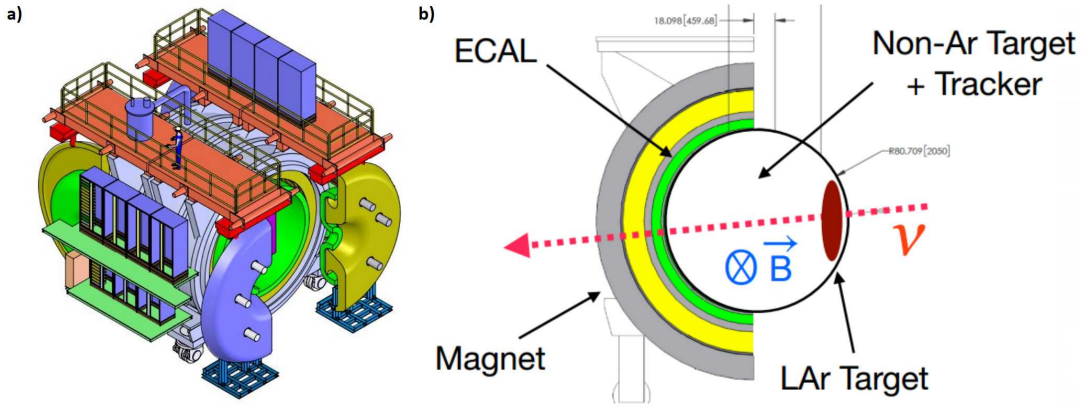

Figure 1.13: From [28]: drawings of the current SAND design, in particular the SAND engineering model (a) and a sketch of the SAND vertical cross-section (b).

identify charged pions with respect to the LAr detector (and thus access lower momenta protons).

The HPgTPC shares the same target with the FD, this similarity reduces sensitivity to detector-driven systematic uncertainties in the FD measurements, while the gaseous phase is required by the expected high intensity of the neutrino beam at the ND.

The basic geometry of the HPgTPC is a gas-filled cylinder with a high voltage (HV) electrode at its mid-plane, which provides the drift field for ionization electrons. It is oriented inside the magnet such that the magnetic and electric fields are parallel, reducing transverse diffusion to achieve higher resolution. The gas is an Ar-CH_4 mixture, in a 90% – 10% molar fraction proportions, at 10 bar. The primary ionization electrons drift toward the end plates of the cylinder, which are instrumented with multi-wire proportional chambers (MWPCs) to initiate avalanches at the anode wires, enhancing the charge signal with high gain factor. These avalanches induce signals on cathode pads placed behind the wires, and the induced pad signals provides the hit coordinates in two dimensions, while the drift time provides the third coordinate of the hit.

The ECAL adds neutral particle detection capabilities which otherwise would be lacking in the ND-GAr, while the external muon-tagging system is designed to separate muons from charged pions.

SAND

The final component of the DUNE ND concept is the on-axis beam monitor (SAND), placed downstream of ND-GAr and ND-LAr in an alcove of the ND hall. SAND consists of an inner tracker surrounded by an ECAL, inside a large solenoidal magnet [27]. Both the ECAL and the superconducting coil are repurposed from the *KLOE* experiment, that was designed to collect data at the INFN-LNF (Frascati, Italy) for studying the ϕ-meson decays with high precision, while for the inner target/tracker system a new design has been developed.The structure includes also a small LAr active target (called GRAIN) placed in the upstream region of the internal magnetized volume, as visible in figure 1.13.

The primary goal of SAND is to monitor the stability of both the beam spectrum and profile over time, and this task is fulfilled mostly by the upstream part of the calorimeter, combined with the inner

tracker. SAND is also capable of performing independent $\nu_\mu/\bar{\nu}_\mu$ flux and flavour content measurements, representing an important cross-check for the other components of the ND complex, especially during the off-axis campaign [28]. The inner tracker and the LAr target provide a large sample of ν interactions on different nuclear targets (Ar, CH_2, C) which can be used to study interaction models and constrain nuclear effects. Moreover, the inner tracker design was developed to be able to incorporate neutrons in the event reconstruction, in order to improve the energy resolution and probe new phase space regions w.r.t previous experiments for the neutrino interactions.

The solenoidal magnet is a composite of a Rutherford Nb-Ti cable, co-extruded with high purity aluminium and wrapped with two half-lapped layers of insulator (glass tape). The coil contains two layers of conductor, separated by a high purity Al sheet, and it is located inside a cryostat. The magnet is cooled via liquid and gaseous He, and the whole structure is surrounded by an iron yoke.

The electromagnetic calorimeter (ECAL) is a lead/scintillating-fiber sampling calorimeter, originally developed for the KLOE experiment [29]. It is divided in a cylindrical barrel section, made of 24 trapezoidal modules and two end-caps, each with 32 C-shaped modules of different sizes. A sketch of the vertical cross-section of this calorimeter is reported in figure 1.14.

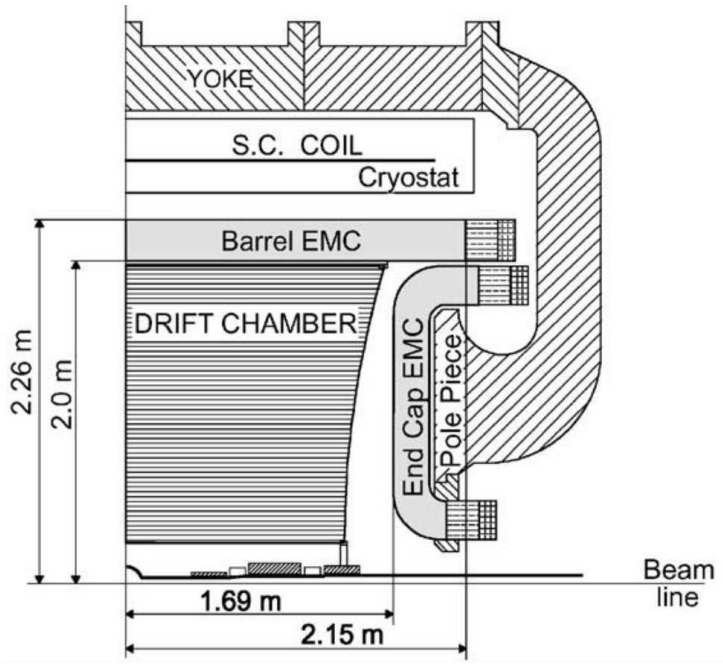

Figure 1.14: From [29]: vertical cross-section of the KLOE detector (EMC stands for electromagnetic calorimeter).

Once closed, the large overlap of barrel and end-caps modules leaves no inactive gap, covering the whole 4π solid angle. All ECAL modules are made with approximately 400 alternating layers of scintillating fibers and grooved lead foils, glued together with a fiber-compatible epoxy. The resulting density of these fine-structured modules is $5\,g/cm^3$ and the radiation length is $\approx 1.5\,cm$. The fibers are grouped in cells and connected through light guides to both the sides of the module, where a system of photomultipliers (PMTs) is used to measure the scintillation signal. The position of the hit along the module is determined by the difference in the arrival times at the two ends of the module, while

the cell readout granularity defines the other two coordinates.

A ≈ 1 ton LAr active target will be placed upstream in the magnetized volume of SAND, this component is called *GRanular Argon for Interaction of Neutrinos* (GRAIN). It will provide an on-axis Ar target reference for cross-calibration with the other detectors, and also inclusive Ar interactions for the nuclear effect studies. The cryostat is under optimization and it is based on a C-composite material reinforced with an internal Al foil. GRAIN will be instrumented with VUV scintillation light detectors to localize and reconstruct the events in combination with the ECAL/tracker system.

The inner tracker technology currently relies on straw-tubes design[15], this component is referred to as *straw-tubes tracker* or STT [28]. The STT design is based on a modular structure of orthogonal planes made of straw tubes with thin target foils dispersed between them. The default STT module includes a target layer, a radiator layer and four straw layers glued together in a XXYY disposition order. The current design assumes 78 default modules with CH_2 targets, 7 modules with graphite targets and 5 "tracking-only" modules, it also permits the installation of additional nuclear targets.

The particle momenta can be reconstructed using transverse plane kinematics with high resolution ($< 3\%$), and the presence of radiator layers enhances the particle ID capabilities via transition radiation, allowing good $e-\pi$ separation. The STT design will also allow to extract ν-H samples by performing a model independent subtraction between CH_2 and C data with a kinematic analysis.

1.3.3 DUNE FD

To achieve the full DUNE physics program, the FD must combine a many-kt fiducial mass with a high granularity detection system, in order to search for rare events and track them with spatial resolution below 1 cm [30]. To give a more quantitative estimation, the DUNE collaboration has set the goal of achieving a least exposure of $120\,\text{kt}\cdot\text{MW}\cdot\text{year}$ by the 2035 time frame with a 1.2 MW beam power, in order to reach the required number of neutrino interaction events over a period of about ten years[16].

The LArTPC technology (if massive and instrumented enough) permits to achieve these goals, since it provides a sub-cm resolution on the liquid argon ionization tracks resulting from the MeV-scale interactions with solar and supernovae neutrinos up to the GeV-scale interactions with neutrinos from the beam [11]. The lower limit on the on the neutrino energies (5 MeV) stems from the intrinsic detection energy thresholds for the $\nu-$Ar CC interactions[17]. This technology allows high-precision identification of ν flavours, offers excellent sensitivity to proton decay modes with kaons in the final state and provides unique ν_e sensitivity to core-collapse supernova events. These characteristics allow the LArTPC to reconstruct single events with high efficiency, and the underground location permits to reject low-threshold background signals. The combination of FD size and location will enable DUNE to reach its primary scientific goals, such as probing a large range of possible δ_{CP} values or refining the lifetime limits for the proton decay.

[15] Another proposed alternative was the a combination of plastic scintillator cubes with TPCs (3DST+TPC option), but the STT is the current choice for the final design.

[16] The number of interactions is the product of the neutrino beam intensity, neutrino oscillation probabilities, interaction cross section and detector mass.

[17] The energy threshold is based not only on the ability to pick up low-energy electrons, but also on the light collection efficiency of the photon-triggering system as well as background suppression.

The simulation and analysis carried on by the DUNE group enabled the definition of the experimental requirements needed for the measurement of the δ_{CP} value. Some of these general requirements, like the energy resolution of reconstructed events or the particle identification capabilities, are reported in the following. The charged lepton and hadronic shower energies are reconstructed separately in the analysis, and the relative contributions are summed *a posteriori*. In ν_e CC events, the leptonic energy resolution (averaged over the spectrum) is 8%, the hadronic energy resolution is 49%, while the neutrino energy resolution is 13% [5]. The energy smearing for these measurements stems mainly from the physics of $\nu - Ar$ scattering and hadronic shower production, and the performance of the detector have much less impact on the final neutrino energy resolution. Particle identification is critical for the estimation of δ_{CP}, since the analysis of the oscillation signal relies on neutrino flavor identification. The particle type can be identified by the related energy deposition (dE/dx function) and track pattern[18]. For ν_e appearance in particular, one must be able to identify the presence of a high-energy electron while avoiding misclassification of high energy photons as electrons [5]. This requires the ability to separate electromagnetic activity induced by CC ν_e interactions from similar activity arising from photons generated in π^0 decay. The flight path before the first interaction from the vertex is a useful information to distinguish photons from electrons, since photon showers are typically preceded by a gap prior the conversion. Furthermore, the initial part of a photon shower, where an electron-positron pair is produced, has a related energy deposition which is twice the dE/dx value of an electron-induced shower. The DUNE-FD LArTPC design features a spatial resolution that is much smaller than the radiation length (14 cm), to make visible the gaps between the vertex and any photon conversions in the reconstructed events. In addition to that, the charge resolution provides enough dE/dx separation for electrons and photons in pre-EM-shower depositions, as demonstrated with DUNE simulations [5] and in the ArgoNeuT experiment[31].

For what concerns the detection of SNB events, a core-collapse supernova at 10 kiloparsecs (or kpc) from the Earth will provide an estimated amount of 1000 neutrino interactions in the FD over the course of ~ 10 seconds with typical energies between 5 and 30 MeV. Much of the desired astrophysical information comes from the time-dependent energy spectrum of ν_e neutrinos, and given the dominance of ν_e CC events in the SNB sample of interactions, the particle identification is not a critical for these measurements. However, high particle ID capabilities could enable more advanced studies on SNB events by identifying separately the contributions of NC and elastic scattering interactions. Timing, on the other hand, is important for reconstructing SNB events. During the first 50 ms of a 10-kpc-distant supernova, the mean interval between successive neutrino interactions is $0.5 - 1.7$ ms[19]. Nearly half of galactic supernova candidates are closer than 10 kpc from the Earth, so the rate could be ten or hundred times higher than the estimation made above. As will be discussed in chapter 2, the LArTPC technology relies on collection of both charge and scintillation signal from LAr. The prompt scintillation light provides the starting time for the reconstructed event[20]. The TPC alone can provide a time resolution of 0.6 ms, commensurate with the fundamental statistical limitations at 10 kpc distance, but the prompt scintillation signal permits to reach a time resolution better

[18] such as decays of stopping particles

[19] depending on the model

[20] i.e. the time at which the ionization electrons begin to drift under the applied electric field

than 10 μs. This ensures that the measurements of neutrino burst time profile are always limited by the event rate and not by the resolution of the detector. To give a synthetic view on the DAQ requirements for these measurements, the full reconstruction of possible SNB events requires an estimated data-rate of 2 TB/s for 30 s to 100 s, including a $\sim$ 4 s pre-trigger window.

The assumed measured low-energy neutrino spectrum do suffer some degradation from the neutrino interaction process itself, for example energy lost to neutrons. The DUNE collaboration developed a model, called *Model of Argon Reaction Low Energy Yields* (MARLEY) event generator [5], to simulate tens-of-MeV neutrino-nucleus interactions in liquid argon taking into account the aforementioned limitations. Detailed simulation studies involving the usage of both TPC and photon information for the energy reconstruction of the events are currently underway. The simulations show that combining the measurements of ionization charge (TPC signal) and scintillation light can improve the determination of the energy deposition, as visible in figure 1.15. The figure reports the

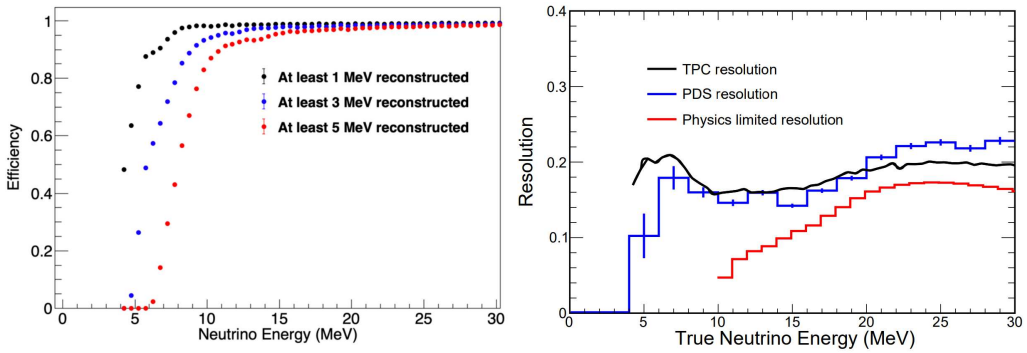

Figure 1.15: From [5]. Left: reconstruction efficiency as a function of neutrino energy for MARLEY events, for different minimum required reconstructed energy. Right: fractional energy resolution as a function of neutrino energy for TPC tracks (black) and photon detector calorimetry (blue). The red "physics-limited resolution" assumes all energy deposited by final-state particles is reconstructed; the finite resolution represents loss of energy from escaping particles.

impact of this solution, referred to as *photon detector calorimetry*, on the neutrino energy threshold and resolution.

In order to search for nucleon decay, where the primary channel of interest is $p \rightarrow K + \nu$, the identification of short kaon tracks (few centimeters) is of critical importance. Another important requirement is the accurate fiducialization of these nucleon-decay events to suppress the cosmic muon-induced background contribution. As for the SNB events, the detection of scintillation photons is important for determining the time of the nucleon-decay event with enough precision.

The DUNE full-scope FD design is a modular LArTPC of 40 kt fiducial mass, located around 1.5 km under sea level in the Sanford Underground Research Facility (SURF), and divided in four identically sized modules [5]. Each of the four cryostats will hold 17.5 kt (10 kt fiducial) of LAr each, for a total of 70 kt, although some of the proposed designs feature higher usable fractions of the total LAr volume. The four FD modules will be arranged in two separated lines (each line containing two detectors that share the same angle w.r.t. the neutrino beam) as visible in figure 1.16, this approach has several benefits:

- each cryostat can be filled and commissioned while the other remains available for liquid storage;
- allows possible repairs to be made in one of the two vessels after the start of commissioning;
- allows deployment of different LArTPC designs.

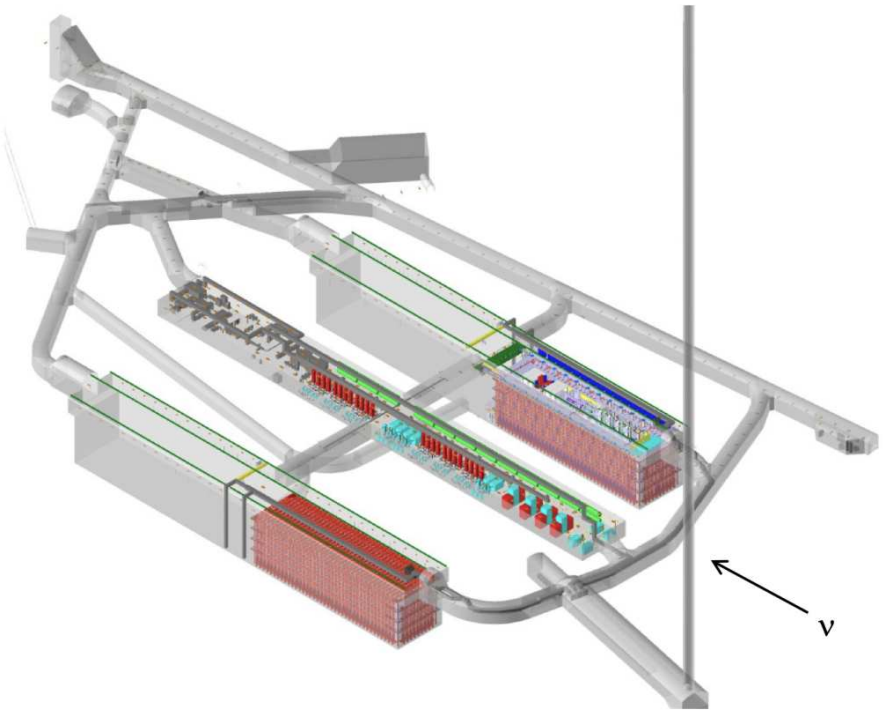

Figure 1.16: From [26]: underground caverns for the DUNE FD at SURF. The picture shows the cryostats (red) for the first two FD modules, each cryostat is 65.8 m long, 18.9 m wide and 17.8 m tall.

The Phase I FD will make use of two modules as depicted in figure 1.16. The cryogenics will employ two 85 kW liquid nitrogen (LN_2) liquefaction plants, a LAr receiving station, and other three components related to LAr circulation, purification and re-condensation, respectively [30]. This large-scale design is similar to the ones employed for industrial applications.

DUNE initially planned to develop two LArTPC technologies: a single-phase (SP), in which all the detector elements inside the cryostat are immersed in liquid argon, and dual-phase (DP), in which some components operate in a layer of gaseous argon above the liquid. After a prototyping campaign at CERN, the first run of the so-called *ProtoDUNE* experiment, the DP technology was abandoned to make room for a different LArTPC technology, as will be discussed in the subsection 2.1.4.

The current plan foresees two SP modules for the DUNE far detector, one featuring a horizontal drift (HD) design and the other a vertical drift (VD) design, leaving undefined the design of the remaining two modules which may use more advanced technologies.

The presented work falls in the context of the *photon detection system* (or PDS) of the first FD module (briefly DUNE-FD1) which, according to the current construction plan, will be a single-phase horizontal-drift TPC. For this reason, the VD design will not be included in the following description.

Chapter 2

Silicon Photomultipliers for the DUNE experiment

This chapter is focused on the first module of the DUNE Far Detector (DUNE-FD1), it begins with a brief description of the working principle and main features of the LArTPC technology in the section 2.1, and continues with the requirements and baseline specifications for the DUNE-FD1 design. The subsection 2.1.3 describes the photon detection system, or PDS, which is of particular interest for the scope of this thesis. The section 2.1.4 outlines the prototypes developed by the DUNE group to test and validate this technology in the FD context, while the section 2.1.5 reports the plan outlined to select and test the best choices for the fundamental photon detection units for both ProtoDUNE2-HD and DUNE-FD1.

2.1 DUNE-FD1

The operating principle of a SP LArTPC has been previously demonstrated by ICARUS [32], ArgoNeuT [31], MicroBooNE [33] and LArIAT [34], and it is sketched in figure 2.1.

The LArTPC is a chamber filled with liquid argon (LAr) and instrumented to detect both electrons and photons that are produced by the interactions on neutrinos with the argon nuclei. A strong electric field is applied to accelerate the electrons generated by the ionization of argon atoms inside the detector, producing a drift toward the anode wall where these electrons are then collected. The anode is a multi-layered grid of active wires, the relative voltage between the layers is chosen to let the first layers produce bipolar induction signals as the electrons pass through them, while the final layer collects these drifting electrons and generate a mono-polar signal.

Besides providing a charge signal, LAr is also an excellent scintillator, emitting a prompt scintillation light at a wavelength of 128 nm. This signal is shifted into the visible region and collected by photon detectors, providing the starting time t_0 of the event, this is the time at which the ionization electrons begin to drift.

The electron arrival time at the anode, relative to t_0, allows reconstruction of the event topology along the drift direction, while the pattern of signals observed on the anode grid wires provides the two coordinates perpendicular to the drift direction. The spatial resolution can be upgraded by re-

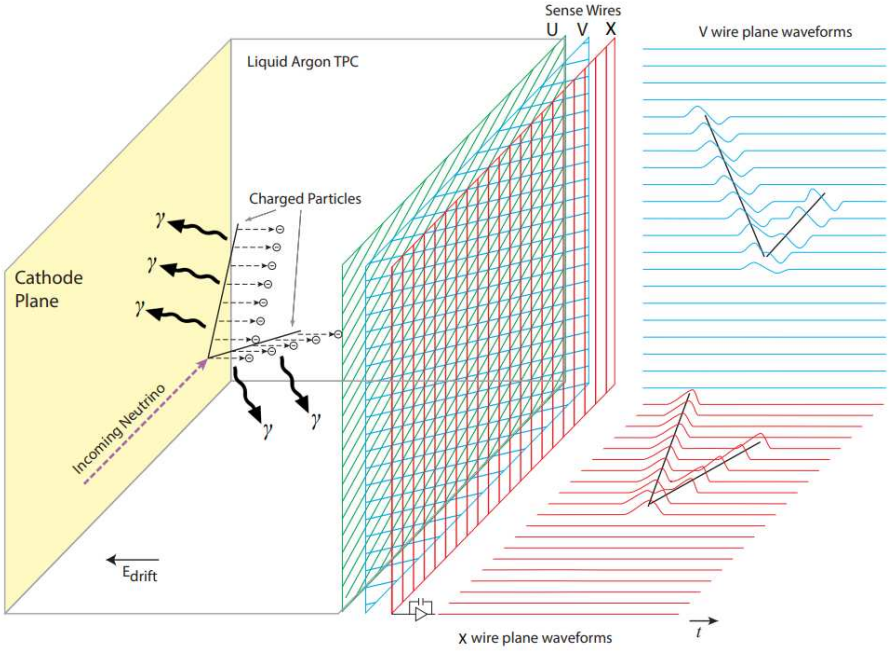

Figure 2.1: From [30]: sketch of the general operating principle of the SP LArTPC detector.

ducing the space between the wires, but there is a trade-off since it also worsens the *signal-to-noise* (SNR) conditions, because the collected charge is divided over more channels. The spatial resolution on the localization of the event along the drift direction is related to the resolution on the measurement of t_0, so it relies on the performance of the photon detection system, as will be discussed in section 2.1.1.

The light signal is also useful to reconstruct the energy of single events, since the number of scintillation photons generated in the LArTPC is proportional to the energy deposited in the argon by the passing particle.

2.1.1 General requirements

It is possible to identify several high-level design specification that together characterize the requirements for the DUNE SP LArTPC module. The main parameters, together with their specification (and goal) values, are reported in table 2.1.

parameter	Specification	Goal
Drift field	> 250 V/cm	500 V/cm
Electron lifetime	> 3 ms	10 ms
Electronics system noise	< 1000 enc	-
Light yield (at cathode)	> 0.5 photons/MeV	> 5 photons/MeV
Time resolution	> 1 μs	100 ns

Table 2.1: From [5]: high-level DUNE-FD SP design parameters and specifications.

The specification values in table 2.1 are upper or lower limits for the related parameters, while the *goal* column reports the target values that would offer some benefits (if cost effective). While in some

cases the goal value offers potential physics benefit directly, the rest of the cases are more for a risk mitigation purpose.

The drift field, electron lifetime and TPC system noise together determine the ability to distinguish the ionization signals of physics events from the noise. On the other hand, the light yield and the timing resolution both pertain to the ability of collecting scintillation photons. The light yield represents the fraction of energy loss by a charged particle as scintillation light, which is collected by the PDS. More precisely, the light yield is the amount of scintillation photons generated (and successfully collected) per unit of deposited energy.

As mentioned above, the basic operating principle of the TPC involves the transport of ionization electrons to the detection plane. A strong drift field correspond to a faster electron transport and thus a minor electron loss due to LAr impurities, it reduces the ion-electron recombination probability and electron diffusion, it increases the induction signals due to increased electron momentum. The design goal of 500 V/cm electric field inside the DUNE-FD1 detector implies (considering its geometry) an electron drift velocity of 1.6 mm/μs and a maximum drift time of 2.2 ms. By comparing this drift time with the electron lifetime τ_e, which is dictated by the liquid argon purity, it is possible to estimate the signal attenuation inside the LAr volume. As an example, at $\tau_e = 3$ ms, signals originating near the cathode will be attenuated to 48% of their original strength with an applied field of 500 V/cm. For the minimum field of 250 V/cm, this transmission drops to 14% after taking into account all the effects deriving from a lower drift field. On the other hand, this signal attenuation is still acceptable as long as the charge readout maintains good SNR and resolution.

As mentioned above, electro-negative impurities (e.g., H_2O, O_2) within the liquid argon must be kept at low levels to prevent capture of ionization electrons. The electron lifetime τ_e is inversely proportional to the density of these impurities. The values of 3 ms and 10 ms in table 2.1 correspond to contamination levels of of 100 ppt and 30 ppt O2-equivalent, respectively [5].

The system noise, in particular the noise level in the front-end electronics, can worsen the charge detection performances. The specification in table 2.1 is given in units of *e - equivalent noise charge* (enc), which is the noise level in terms of input charge signal, expressed in units of elementary charge.

The PDS provides an event time based on the LAr scintillation light which, in conjunction with the TPC ionization signal, allows the localization of the event along the drift direction. The specifications in table 2.1 are given for the worst-case event location within the fiducial volume, which means near the cathode and far from the PDS (integrated in the anode planes). Given the electron drift velocity of $\sim$ 1.6 mm at 500 V/cm, a photon-based time resolution of 1 μs for the measurement of the starting time t_0 corresponds to an effective spatial granularity in the drift direction which is similar to the wire pitch [5].

The fiducial volume must be defined at the 1% level for both accelerator-based neutrino oscillation measurements and SNB events. The precise event time, and thus location, allows to mitigate backgrounds for non-accelerator measurements, and also enables corrections for electron attenuation. The minimum TPC performance considered above (with $E = 250$ V/cm and $\tau_e = 3$ ms) would correspond to an energy smearing of 22% due to electron loss, but this effect is negligible at 1 μs time resolution.

2.1.2 DUNE-FD1 design

The DUNE-FD1 TPC design consists of three vertical rows of *anode plane assemblies* (APAs) interspersed with two *cathode plane assemblies* (CPAs) rows, which divide the chamber in four regions as visible in figure 2.2.

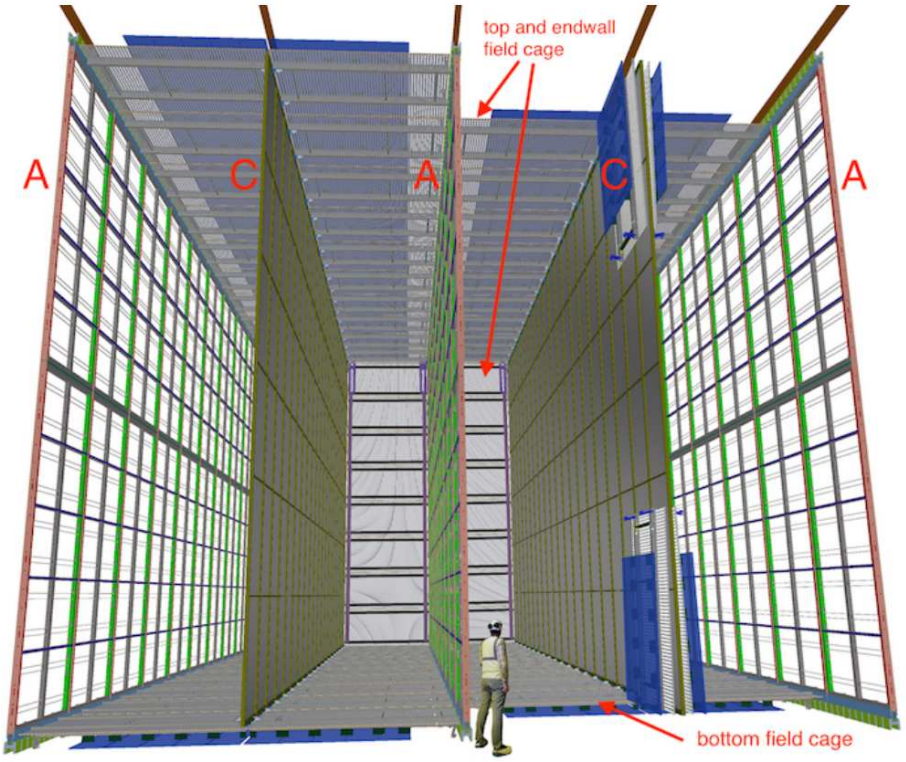

Figure 2.2: From [26]: sketch of the 10 kt DUNE FD SP module design, showing the alternating anode (A) and cathode (C) planes, as well as the field cage (FC) that surrounds the drift regions between the anode and cathode planes.

The CPA and APA rows are designed in a modular fashion, these will be placed at a 3.5 m distance from each other and the CPA modules will operate at 180 kV. This configuration corresponds to a drift field of 500 V/cm and a corresponding maximum drift length of 3.5 m [30]. The front-end readout electronics is mounted directly on the APA frames and the whole structure is covered by a field cage (FC) for shaping the internal electric field, the FC ensures an electric field uniformity better than 1% across all the active volume.

The APA/CPA single module dimensions are chosen for ease of transportation and installation in the cryostat. Each cathode wall is an array of 150 CPA modules (3-modules height and 50-modules length), and each APA wall contains 50 modules (2-modules height and 25-modules length), for a total of 150 APAs and 300 CPAs inside the cryostat.

The single APA frame design contains three sense wire planes with wire spacing around 5 mm mounted on each side, used to sense ionization signals originating within the TPC cell on either side, plus a shielding layer, also called the grid layer (or G-layer). The wire spacing is chosen to optimize the spatial resolution, SNR and cost. The wires are two induction planes (called V-layer and U-layer)

and a collection plane (called X-layer), they are oriented vertically (X, G) and at ±35.7° to the vertical (V, U)[1] [30].

The compact APA (and CPA) design permits to maximize the LAr active volume, and its modular configuration allows the readout electronics to be placed at the top and bottom of each APA row, thus minimizing the uninstrumented region in the gaps between the two adjacent APA modules. The low-noise CMOS preamplifiers and ADC ASICs have been developed for being mounted directly on the APA frames, ensuring good SNR performance, and also offering the possibility of digital signal processing[2], while also relaxing the requirements on the performances of the downstream DAQ systems outside the cryostat.

A Global Positioning System (GPS) one-pulse-per-second (1PPS) signal is used as reference for event timing, allowing to match the beam window, while a local 62.5 MHz master clock keeps all detector components within the single 10 kt module synchronized.

2.1.3 Photon detection system

The LAr offers good scintillation properties, featuring orders of 10^4 photons per MeV of energy deposition at 128 nm, in DUNE-FD1 these photons will be collected by the so-called *X-Arapuca* modules [30], which are light traps mounted in the APA frames as shown in figure 2.3.

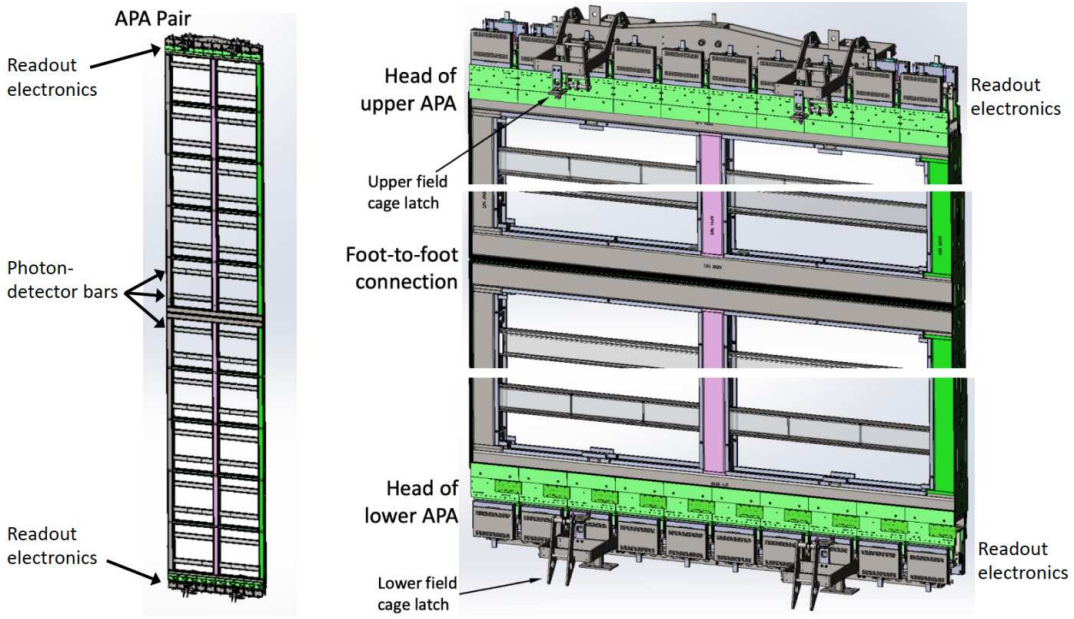

Figure 2.3: From [30]. Left: two APA modules linked together to form one APA wall unit. The PD bars are installed across the width of the single APA module. Right: a zoom into the top and bottom ends of the APA stack showing the readout electronics, and at the foot-to-foot connection of the stack center.

The arrival times at the APA frames of ionization electrons and scintillation photons run on different time scales, more precisely the milliseconds and nanoseconds, respectively. The comparison of the arrival time of these two signals enables the reconstruction in the electron drift direction. As

[1] The order of these layer from inside the TPC to outside is G, U, V, X.

[2] multiplexing, zero suppression and other procedures

mentioned in the requirements of section 2.1.1, the timing resolution of the PDS have a huge impact on the LArTPC detection capabilities for low-energy physics, backgrounds identification and non-beam events. For example, a 1 μs timing resolution enables $\sim$ 1 mm position resolution for 10 MeV SNB events[3].

The DUNE-FD1 PDS design consists in ten X-Arapuca PD bars mounted directly on each APA module, each bar running the full width of the APA, as visible in figure 2.3. These photon collectors cannot be placed outside of the FC since it is opaque to the scintillation light. Their implementation in the APA frames, on the other hand, should not compromise the compactness of APA modules (i.e. should not influence the active LAr volume). These requirements pose a series of geometrical constraints which led to the aforementioned PD bar design.

The X-Arapuca is a layered structure of a dichroic filter, coated with p-Terphenyl (PTP), and a wavelength-shifter-doped polystyrene light guide[4] (WLS bar) that shifts the VUV scintillation light into the visible region, traps these shifted photons and transports them to the *silicon photomultiplier* (SiPM) devices, which are placed on the lateral sides of the structure [35]. SiPMs are the fundamental photon detection unit of the DUNE-FD1 design [30], and they will be described in detail in chapter 3. The signals from these sensors are sent to the cryostat roof and then to the DAQ system where the data streams of light and charge signals are merged.

The PD bars, shown in figure 2.4, are mounted in each APA between the wire layers. Each APA

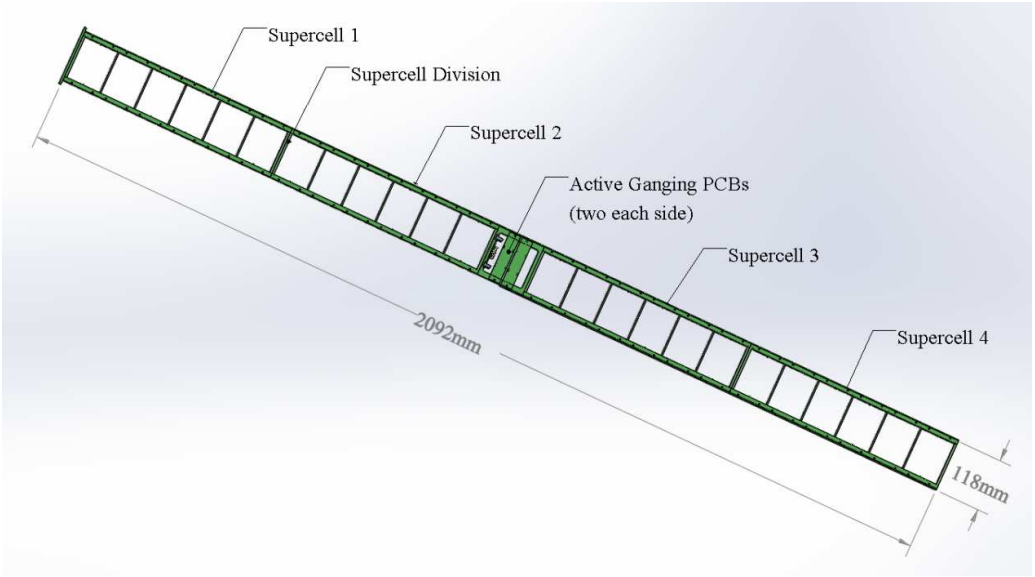

Figure 2.4: From [30]: X-ARAPUCA module overview. A single module includes 24 X-ARAPUCA cells, grouped into a set of four supercells of six cells each. In the center there are active ganging PCBs which collect the signals from the SCs.

module contains 10 PD bars, each bar is divided in four X-Arapuca *supercells* (SCs) and each SC is composed of 8 cells, as visible in figures 2.4 and 2.5.

The figure 2.5 shows a single X-Arapuca cell. The outer layers is a dichroic filter coated with PTP, which shifts the scintillation photons from 128 nm to 350 nm [35]. The filter is transparent to 350 nm

[3] considering the other standard design parameters of table 2.1
[4] Eljen EJ-286 blue wavelength shifting plate

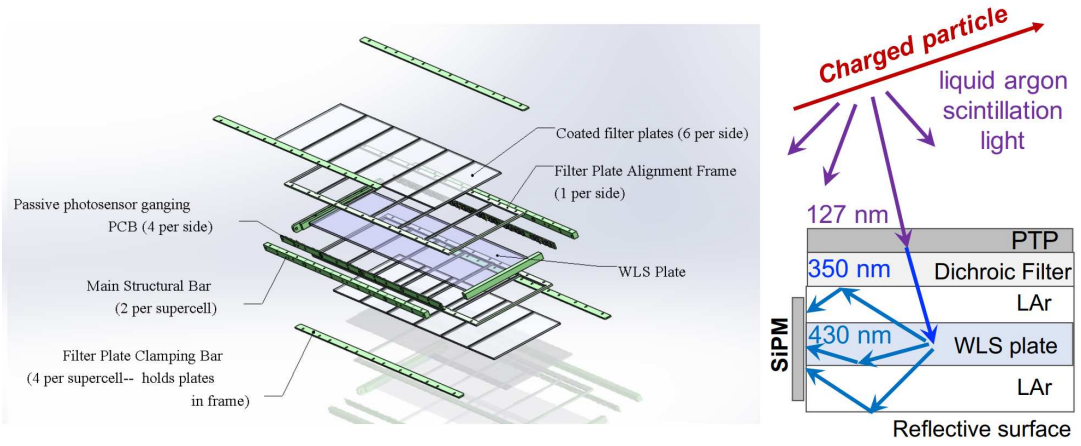

Figure 2.5: From [30]. Left: detailed exploded view of X-ARAPUCA supercell Right: Schematic representation of a single-sided readout X-ARAPUCA operating principle, assuming a filter cutoff of 400 nm.

light, and the underneath WLS plate converts these photons to the visible spectrum (430 nm). The visible photons emitted at an angle greater than the critical value remain inside the WLS plate and eventually reach the SiPMs in the internal lateral sides, while visible photons that escape the WLS plates are still collected, since they are reflected by the dichroic filters back into the WLS plates. The LAr gaps between the WLS plate and the surfaces of the cavity ensure a discontinuity of the refractive index ($n_{\text{plate}} = 1.58$ and $n_{\text{LAr}} = 1.24$) that contributes to the photon trapping. The current design foresees a single WLS plate which runs over the full length of each SC, and an alternative X-Arapuca design with two dichroic filters is also available to detect photons from both sides of the PD bar. The optical window(s) of each SC consists of dichroic filters with a cut-off at 400 nm, and each SC mounts 48 SiPMs.

The SiPMs are mounted in PCBs called *photosensor mounting boards* (or strips), these are placed on the long sides of the SC, and each strip mounts 6 SiPMs which are electrically connected in parallel (passive ganging). The eight passively ganged signals from a single SC are actively ganged into one output channel by a PCB placed at the center of the PD bar.

The chosen design for the front-end electronics permits to achieve the 1 μs timing resolution requirement for the DUNE-FD1 PD system [30] (as reported in table 2.1).

The baseline DUNE-FD1 PDS design includes 192 SiPMs per PD module, with groups of 48 sensors per channel, for a total of 288,000 SiPMs for the whole LArTPC. The usage of traditional large area *photomultiplier tubes* (PMTs) is forbidden by the structure of the APA, and the choice of a solid-state alternative also permits to maximize the active volume of LAr by placing the PD bars in the inactive areas of the APA modules.

2.1.4 ProtoDUNE(s)

The DUNE collaboration has constructed and tested two large prototypes of a FD LArTPC module at CERN, this is known as the ProtoDUNE experiment. The to prototypes, *ProtoDUNE-SP* and *ProtoDUNE-DP*, were located in an extension to the EHN1 hall (Experimental Hall North 1 — EHN1)

in CERN's North Area, where a new charged-particle test beamline was constructed as part of the CERN NP program. Each of the two detectors has approximately a 20 times smaller size w.r.t the planned FD modules, but it features identical size components (including the PDS) [36]. A picture of the two cryostats is reported in figure 2.6.

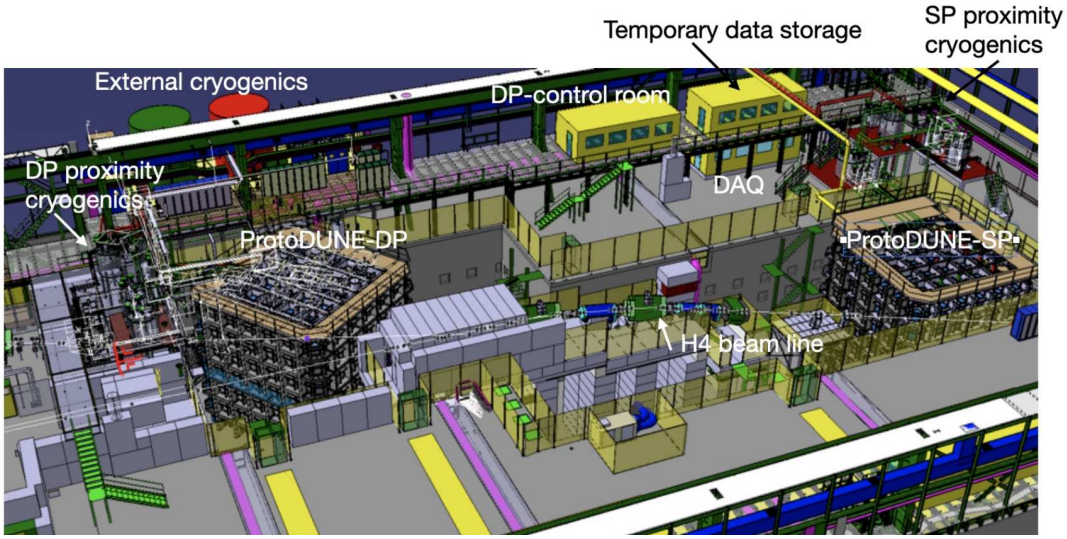

Figure 2.6: From [36]: layout of the EHN1 experimental area, the DP cryostat is on the left, while the SP cryostat is on the right. The rotation angle of the cryostats have been defined to maximise the path of the particle beams in the drift volume.

This massive prototyping program was undertaken to validate the components production (stress tests for the production and quality assurance tests of detector components), to validate the installation procedures, and to probe the operation of the detector with cosmic rays and test beam.

A thorough inspection of the results of the first run (ProtoDUNE1) led to the decision of abandoning the DP technology in favor of a second SP LArTPC, which features a vertical drift design. For this reason, the second run of the experiment (ProtoDUNE2) will involve an upgraded version of the "standard" *ProtoDUNE-SP* module, which is now called *ProtoDUNE-HD*, and will replace the DP module with a vertical-drift SP LArTPC, referred to as *ProtoDUNE-VD*.

In the ProtoDUNE-HD detector the ionization electrons, generated by the neutrino interactions with the LAr, drift horizontally toward a readout system of vertical anode planes (APA modules). The detector dimensions are 7 m along the beam direction, 7.2 m wide in the drift direction, and 6.1 m high. Six APA modules are arranged into the two APA planes, each consisting of three contiguous APAs, as visible in figure 2.7.

Between these planes, a central cathode plane (composed of 18 CPA modules) splits the TPC volume into two drift regions. A field cage surrounds the four open sides of these two drift regions to remove the influence of the cryostat walls and other nearby conductive structures on the electric field uniformity.

With a total LAr mass of 0.77 kt, ProtoDUNE-HD represents the largest monolithic SP LArTPC detector built to date, and a significant experiment in its own right. Construction and installation of ProtoDUNE-HD was completed in early July 2018, and LAr filling took place the next month. The first

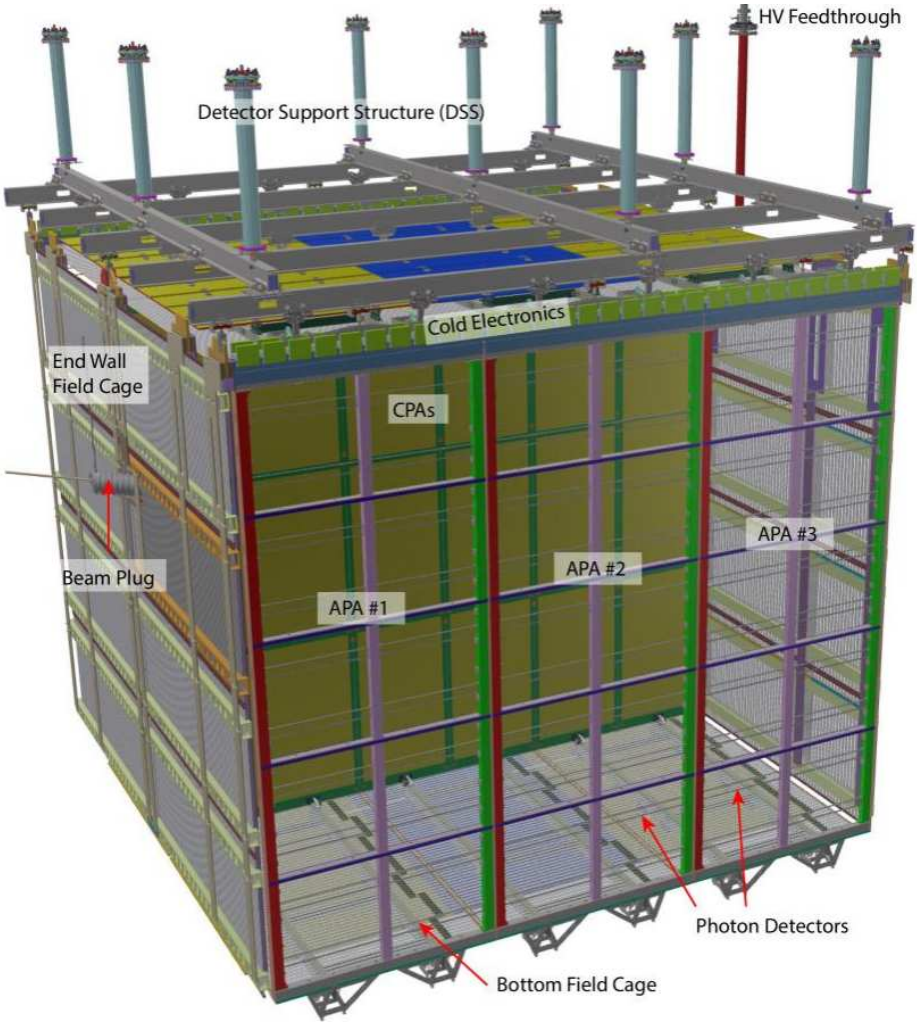

Figure 2.7: From [36]: sketch of the ProtoDUNE-HD internal components.

test beam was delivered to EHN1 on August 29, 2018 and the run was completed on November 11 of the same year. The detector continued to operate through July 19, 2020 collecting (only) cosmic ray data [36].

The data taken with ProtoDUNE-HD demonstrated the SP LArTPC performances and provided valuable information on the design, simulation and calibration of the DUNE-FD1.

2.1.5 SiPM for ProtoDUNE2-HD and DUNE-FD1

The first run of ProtoDUNE-HD (ProtoDUNE1-SP) involved around a thousand of SiPMs of different models, mounted in early versions of the X-Arapuca devices (called S-Arapucas or simply Arapucas), and validated these technologies for the next run (ProtoDUNE2-HD), which is currently at the commissioning phase [36].

The baseline devices selected as fundamental PD units are 6 mm ×6 mm SiPMs by *Hamamatsu Photonics K. K.* (Japan) and by *Fondazione Bruno Kessler* (FBK) (Italy) [37], the latter being developed for operation in LAr in the context of the *DarkSide* experiment [38]. The HPK models are S13360 prototypes tailored to full-fill the DUNE requirements improving the performance with respect to

commercially available products. The FBK models are based on the NUV-HD-SF technology, these are one of the first technologies tested for the new X-Arapuca design due to their good performance at cryogenic temperatures and ideal matching with the emission spectrum of the WLS bars [35]. Cryo-reliability is a key issue in the DUNE PDS design, for this reason these baseline devices were both designed to reduce the effects of thermal gradients stress the SiPMs at the level of detector, bonding and packaging.

As mentioned above, the SiPM inside the X-Arapuca modules are operated in ganging mode. More precisely, the signals of 48 SiPMs are summed and amplified in the SC in low temperature conditions. During the X-Arapuca R&D phase, several SiPM technologies have been tested in view of the installation in ProtoDUNE2-HD [36]. A 2-window SC has been tested in Milano Bicocca [35] to estimate the light collection efficiency of X-Arapuca modules, resulting in a *photon detection efficiency* (PDE) larger than 3% on the basis on analytical calculations, Monte Carlo simulations and experimental tests. The PDE reported above is defined as the ratio of detected photons to the total number of photons impinging to the X-Arapuca window, both the tests and the simulations were carried out using SiPMs of the baseline models mentioned above.

The DUNE PDS consortium is the group in charge of selecting and testing SiPMs for both the ProtoDUNE2-HD and DUNE-FD1 detectors, starting from the most performing SiPM models among the ones selected for ProtoDUNE1-SP. The strategy adopted to achieve this task relies on a 3-phases plan:

- The first phase involved the full characterization of single SiPM devices, in order to estimate the main parameters and the working point of each SiPM model, this phase will be described in chapter 4. In this phase I contributed to the campaign performing part of the characterization measurements and developing custom algorithms for offline data analysis.

- The second phase was divided in a number of passive ganging tests on SiPM strips, in order to down-select the best choices the ProtoDUNE and DUNE-FD detectors, this is briefly described in chapters 3 and 4. The single characterizations involved the same setup and procedures used in the first phase (for what concerns the Ferrara division of the PDS Consortium). Furthermore, the Ferrara group did not took part on the actual ganging tests, for this reason the results will be described only qualitatively.

- The third phase consists in a quality assurance test of a large number of SiPMs: the entire ProtoDUNE2-HD and DUNE-FD1 SiPMs productions, counting 6000 and 288000 sensors respectively. As will be described in chapter 5, the Ferrara group of the PDS Consortium developed a custom experimental setup, named CACTUS, to perform these quality assurance tests. As a member of the Ferrara division, I took active participation on the development and calibration of the CACTUS setup, as well as on its usage for the characterization of part of the ProtoDUNE2-HD SiPM production.

Chapter 3

SiPM properties and applications

This chapter begins with a brief description of the *Silicon Photo-Multipliers* (SiPMs) working principles, then continues explaining the circuital model that is often used to simulate their behaviour and the main properties of their output signal. In the section 3.2 there will be defined some parameters to quantify the SiPM performances and briefly describe the experimental procedures to measure these parameters in section 3.3, focusing on noise characterization at cryogenic temperature in subsection. The last section describes the plan developed by the DUNE Photon Detection System (PDS) Consortium for the selection, production and characterization of SiPMs for ProtoDUNE2-HD and DUNE-FD1.

3.1 SiPM working principles

This section describes the physical mechanisms underlying the SiPMs, which are solid state optical devices capable to detect single photons in the visible range.

The first SiPM appears in the late 90' thanks to the work of V. Golovin [39] and Z. Sadygov [40], although it was the product of a slow process of technical upgrades made on its predecessors since the 60' (as will be mentioned in section 3.2.6). This technology was extensively investigated over the following years, undergoing various optimizations along with the development of advanced semiconductor fabrication techniques and front-end architectures. These numerous upgrades permitted also to extent the SiPM applications to multiple fields.

The analytical models developed through years permit to perform a quantitative estimation of the core physical properties of these sensors [41, 42, 43, 44], which can be functionally represented by an equivalent circuit independently of the particular fabrication technology, as will be described in subsection 3.1.1.

The SiPM is a large matrix of independent single-photon avalanche diodes (SPADs) which all contribute to a single output signal, since they are connected to a common readout in parallel configuration [45]. The single SPADs are also called the *pixels* or *cells* of the SiPM, they are all biased at the same voltage V_{bias} and are all connected to the same readout channel inside the SiPM matrix[1], as in

[1] The common cathode and the common anode are at a voltage difference of V_{bias}; more precisely, the cathode is at $\pm V_{\text{bias}}$ (the sign depends on the SiPM type) and the anode is connected to ground through the front-end electronics, which

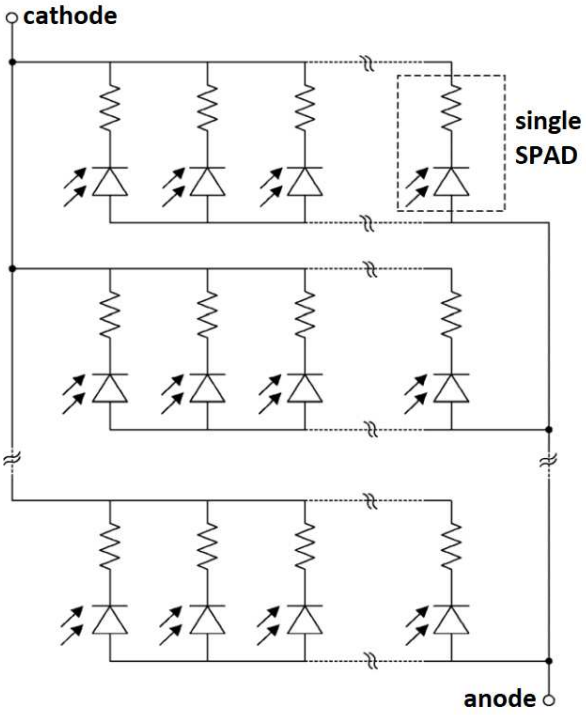

Figure 3.1: From [45], schematic circuital representation of a SiPM as a parallel connection of single SPADs.

figure 3.1.

The SPAD is an *Avalanche PhotoDiode* (APD) operating in the Geiger-Müller regime: it is essentially a highly depleted p-n junction in strong reverse polarization, in which the avalanche multiplication (or Geiger discharge) process serves as internal gain mechanism [43] to achieve single photon resolution.

If a visible photon with enough energy (above the energy gap of the Silicon, $h\nu > E_{\text{gap}}$) is absorbed in the depletion region, it can generate a free e-h pair which can be separated by the internal electric field contributing to the diode leakage current, as reported in figure 3.2. This mechanism is proper of photodiodes, in which the generated current variation is proportional to the light intensity but there is no signal amplification.

If the bias voltage V_{bias} is raised above the V_{APD} threshold, the high internal electric field at the junction can give to the electrons enough energy to generate an avalanche of secondary charge carriers via impact ionization [44]. In the APD regime the device still maintains the proportionality of the inverse current to the incident light intensity, but it acquires an internal gain (typically below 10^3) due to the avalanche multiplication process, even if single photon detection is still out of range.

Only electrons have enough energy to create additional e-h pairs because they have a lower effective mass in Silicon with respect to the holes, for this reason the generated avalanche flows in only one direction and it is eventually self-quenched after the secondary charge carriers are collected.

In order to reach the SPAD regime, the voltage V_{bias} must be higher than the so-called *breakdown*

acquires the related signals.

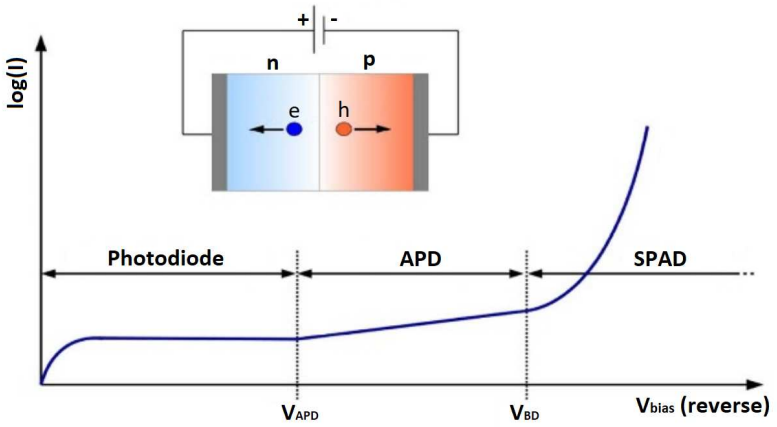

Figure 3.2: Above: sketch of a p-n junction in reverse polarization. Below: IV curve representation with different ranges of operation for the SPAD sensor.

voltage V_{BD}, this is the threshold at which the multiplication process of primary generated carriers via impact ionization becomes divergent and the avalanche process becomes self-sustained. More precisely, V_{BD} is the bias at which the multiplication factor M diverges, where M is defined as the total number of secondary charge carriers produced by each primary one. Under these conditions the electric field is of the order of 10^5 V/cm at the junction and both the electrons and the holes can generate avalanches. In this condition the gain increases by orders of magnitude (order 10^6 [46, 47]) and permits to reach the single photon resolution. The avalanche process is self sustained because the minority charge carriers generated by impact ionization can be accelerated by the high electric field toward the depleted region and re-iterate an avalanche process from there. For this reason, each SPAD inside a SiPM is connected in series to an internal quenching element as visible in figure 3.3, this is called the *quenching resistance* R_Q which is typically in the range $[1-20]\,M\Omega$.

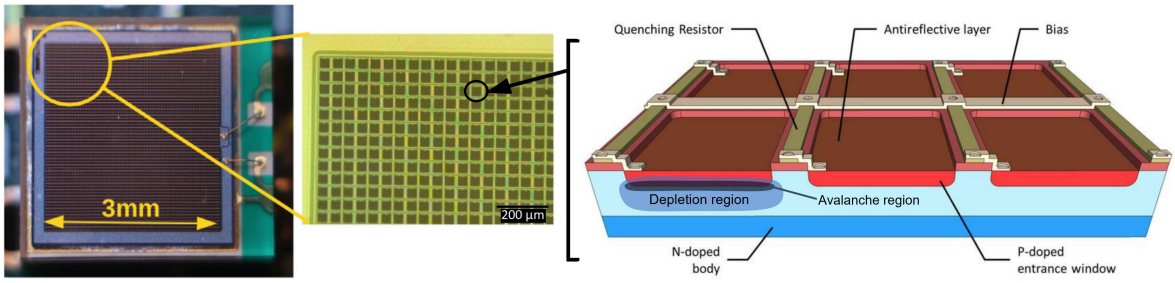

Figure 3.3: Starting from the left: front picture of a SiPM, zoom on a portion of the SiPM surface and schematized structural profile of the single cells. The first two pictures are from [44] while the last is from the *Ketek* website (modified).

The mechanism underlying the multiplication process (*avalanche build-up*) has been reproduced using Monte Carlo simulations [48], finding different initial current growth from event to event. These differences are due to the first steps of the multiplication, which involve only few carriers and can develop in various ways depending on many factors. According to the simulations, the avalanche builds up as a narrow line of high carrier density before starting to spread due to lateral diffusion, eventually covering all the high-field region of the junction if no quenching mechanism is applied. If instead

the avalanche is quenched, the lateral spread is reduced to few micrometers around the starting point [49]. The lateral diffusion may also be assisted by photons: the emission and re-absorption of photons in different locations of the high-field region can generate secondary avalanches which contribute to the lateral spread.

The avalanche is quenched because as the current flowing through the SPAD raises, the voltage drop across R_Q becomes larger, decreasing the effective voltage across the SPAD below the breakdown level. After the quenching, the bias is restored with a time constant τ_{reset} that depends on the structure of sensor, in particular on R_Q and on the capacitance of the SPAD C_d, as will be mentioned in the subsection 3.1.1. After absorbing a photon, the SPAD is no longer sensitive to the incident light until the avalanche is quenched and the bias restored above V_{BD}, resulting in a dead time equal to τ_{reset}.

In some new devices an active *quenching circuit* is used instead of a passive element [50], but the general quenching mechanism remains the same. These are the CMOS SPADs and the *digital* SiPMs (dSiPM) models, where in some cases the quenching resistance is replaced by a quenching circuit with a transistor used to force the bias, either quenching or resetting the SPAD, these new technologies will be described in section 3.2.6. Thanks to the active elements, this solution permits to have a fine control on the τ_{reset} value and so on the dead time of the sensor, which instead would be a fixed parameter for analog SiPMs.

The SPAD is inactive during an avalanche, so the relative current signal have a fixed amplitude which is independent on the number of absorbed photons, for this reason these sensors are sometimes called *Geiger-Mode* APDs (GM-APDs). Besides that, the thousands of SPADs connected in parallel inside the SiPM do act as a single detector, giving an output signal which is proportional to the number of photons absorbed in the whole matrix. Supposing that a portion N_f of the total cells N_{cells} was triggered (or fired), which means that each one has absorbed a photon and is producing an avalanche simultaneously[2] with the others, the output signal of the SiPM would be the sum of N_f signals with the same amplitude.

The general structure of a SPAD is a thin layer of highly doped p^{++} Si right under the entrance window, under this layer there is an abrupt junction with a n^+ layer which is called avalanche region, then follows the depletion region of low doped n^- epitaxial layer where the internal electric field is almost constant and finally a thick (hundreds of μm) n-substrate that connects the sensor to the anode, as visible in figure 3.4. The schematics defined above is called *p-on-n* structure, but SPADs can be also made inverting the doping profile (i.e. replacing all the n-layers with p-layers and vice versa) to obtain a *n-on-p* structure.

One can define the *avalanche breakdown triggering probability* P_t (or simply triggering probability) as the probability for a primary charge carrier to generate a divergent Geiger discharge. P_t is related to the separate triggering probabilities of electrons $P_{t,e}$ and holes $P_{t,h}$, these depend on the position at which the free charge carrier is created and both increase with the electric field [51].

$$P_t(x) = P_{t,e}(x) + P_{t,h}(x) - P_{t,e}(x)P_{t,h}(x)$$

$P_{t,h}$ is high in the n-side of the sensor, since from there the holes can be accelerated by the electric field towards the junction with the p-side and generate an avalanche, while for $P_{t,e}$ shows the oppo-

[2] here the definition of simultaneous events is related to the maximum bandwidth of the front-end readout electronics

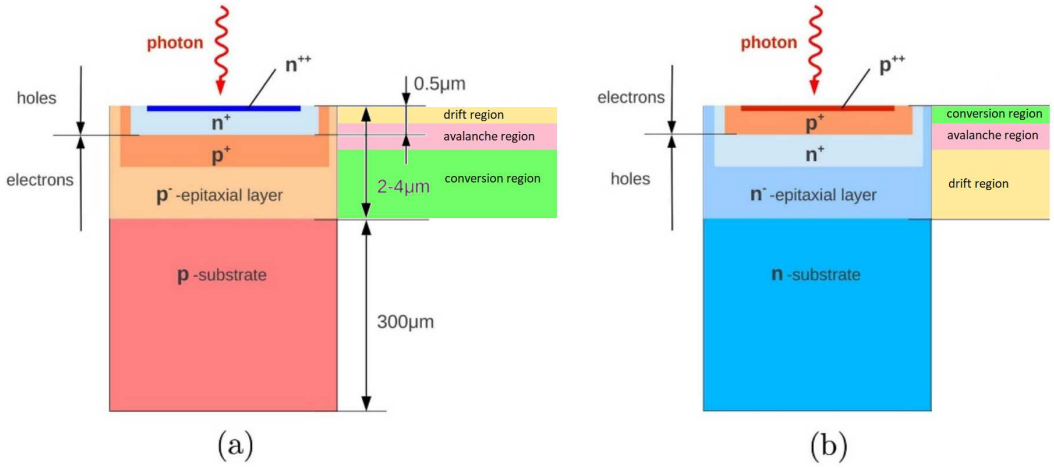

Figure 3.4: Modified from [42]. Schematic structure the SPAD doping profile for the n-on-p (a) and p-on-n (b) structures. The convention used for the nomenclature of the different regions (drift and conversion) is referred to the electrons.

site behaviour. The more space a free carrier have at disposal to travel under the acceleration of the electric, the more probable will be for it to have enough energy to generate a Geiger discharge, with the maximum located in the region where the carriers can cross the whole high-field zone. In case of the n-on-p junction this is the depleted layer below the junction (figure 3.4), while in case of the p-on-n it is adjacent to the junction within the p^+ layer, as visible in figure 3.5.

As mentioned above, the electrons are more efficient in triggering avalanches with respect to the holes, and in the high-field region we have that $P_{\mathrm{t,e}} \sim 2P_{\mathrm{t,h}}$, this makes the two SPAD structures sensible to different regions of the impinging photon frequency spectrum. Photons at different wavelengths have a different penetration in Silicon, for this reason the p-on-n structure is more responsive to light in the blue region (penetration $\sim 0.6\,\mu$m) while the n-on-p structure is more sensible red photons (penetration $\sim 2.9\,\mu$m).

The drift region in figure 3.4 marks the region in which the optically generated electrons are drifted by the electric field without triggering any divergent multiplication, while the conversion region is defined as the part of the sensor in which an optically generated electron have the maximum probability to trigger Geiger discharge.

As will be described in section 3.2, the technical design of a SPAD should take into account additional factors like the exact doping profile, the individual possible drift paths, the electric field distribution around the junction and also the depth of the junction itself to estimate the final detection efficiency [43].

3.1.1 Circuital model

The behaviour of a single SPAD can be represented by the circuit in figure 3.6 a), where C_{d} is the capacitance of the inner depletion layer, which can be the sum of the SPAD area capacitance and any kind of perimeter capacitance, and R_{d} is the resistance of the internal space-charge region [44].

The simulations used to estimate the C_{d} of a SPAD must take into account possible parasitic ca-

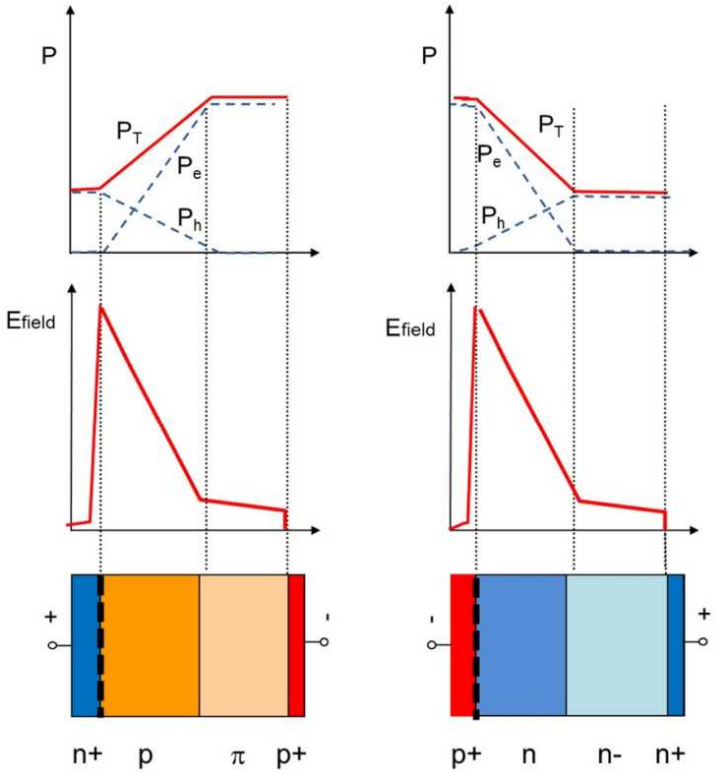

Figure 3.5: From [42], avalanche triggering probability (top), internal electric field (center) and doping (bottom) profiles as a function of the position inside the SPAD, for both the n-on-p (left) and p-on-n (right) cases.

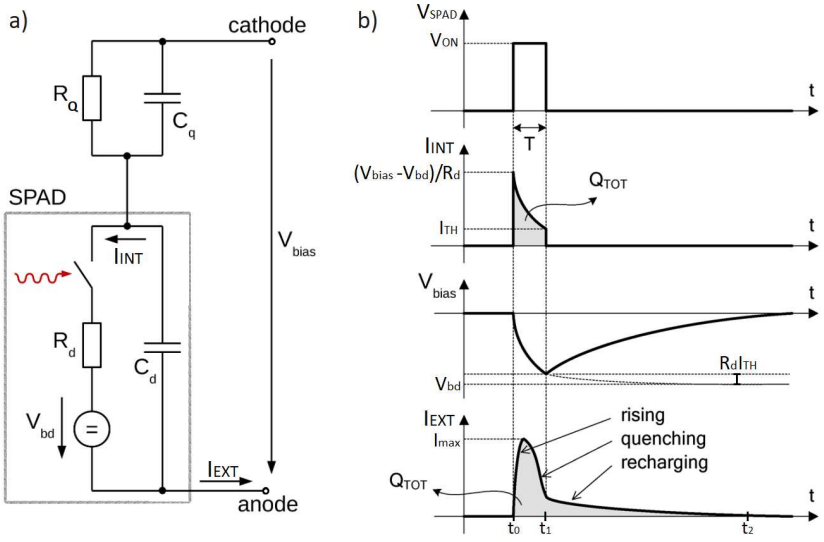

Figure 3.6: From [44]. a) circuital scheme of a SPAD: closing the switch mimics the absorption of a photon. b) plots of the internal (I_{INT}, I_{EXT}) and external currents and voltage differences (V_{bias}, V_{SPAD}) versus time.

pacitances, but most importantly the C_{d} dependence on the depletion layer depth and geometry, which in turn depends on bulk parameters, doping profile and internal electric field [43].

The quenching circuit is represented by a parallel of a quenching resistance R_Q and a parasitic capacitance C_Q, while both the SPAD internal current signal I_{INT} and the SPAD + quenching circuit current signal I_{EXT} involved in the photon absorption process are reported in figure 3.6 b).

The avalanche starts at t_0, the quenching of the current starts while the current is raising, reducing both I_{INT} and I_{EXT} concurrently, and stops at the time t_1, while at t_2 the cell is fully recharged and ready to detect another photon.

The difference between V_{bias} and V_{BD} is often called the overvoltage $V_{OV} = V_{bias} - V_{BD}$, this is an important quantity since the sensor is considered active only if $V_{OV} > 0$V, and most of the SiPM parameters are functions of V_{OV}.

As soon as the photon is absorbed by the SPAD, or more generally a Geiger discharge is triggered inside the sensor, the switch in figure 3.6 a) is closed and the capacitor C_d, initially charged at V_{bias}, starts its discharge. On the other hand, C_Q starts charging via R_d as soon as C_d begins the discharge process, resulting in an overall rise time constant $\tau_{rise} \sim R_d(C_d + C_q)$, neglecting the contribution of R_Q since it is higher than R_d by various orders of magnitude. Even if the multiplication factor M diverges above the breakdown level (as mentioned before), the quenching resistance counters the rise of the output current as the avalanche builds up, and the current reach a finite maximum before starting to decrease. Even without any quenching element the internal resistance R_d alone would prevent the current from diverging, and at some point there would be a current saturation to an asymptotic value.

The current I_{INT} quickly raises to its maximum V_{OV}/R_d due to the divergent multiplication of the Geiger discharge, then it starts decreasing under the quenching effect. The $C_d(C_Q)$ discharge(recharge) stops when I_{INT} reaches a certain threshold $I_{TH} = V_{OV}/(R_Q + R_d) \sim V_{OV}/R_Q$, which is close to the minimum current that would generate a self-sustained avalanche. The quenching process stops at the same point, as visible in figure 3.6 b), and then the SPAD starts the recharging process. The total charge provided by the SPAD is $Q_{TOT} = V_{OV}/(C_q + C_d)$ and the gain of the sensor can be calculated dividing this quantity by the electron charge.

$$G = \frac{V_{OV}}{(C_Q + C_d)e}$$

The gain for a SPAD is an adimensional quantity which defines the average amount of free charge carriers collected during a Geiger discharge, its value ranges from 10^6 to 10^8 depending on the model [46]. This range is roughly an order of magnitude lower for recent models, which are optimized in other parameters [44].

The avalanche triggering probability P_t and the quenching probability P_Q together govern the state of the switch, as the first is the probability to close the switch and the second is the probability to open it. As mentioned before, P_t is the probability for a primary charge carrier to generate Geiger discharge, this quantity will be discussed more in detail later in the definition of the Photon Detection Efficiency (PDE). P_Q is the probability that the number of free carriers crossing the avalanche region, which depends on the current intensity through the junction and is affected by statistical fluctuations, goes temporarily to zero. This is the condition that permits to extinguish the discharge, so $P_q(t)$ is the probability to quench the avalanche at the time t. P_Q can be estimated as the mean duration $\Delta t = t_1 - t_0$ of the switch "on" state [52], which for a current lower than $20\,\mu A$ is on average under the ns [45]. This value sets a minimum for P_Q, since for higher current amplitudes it grows significantly,

increasing also in terms of fluctuations. As mentioned before, the passive quenching element R_Q described above can be replaced by an active circuit to provide a higher degree of freedom on the recharge time after a Geiger discharge.

The circuital model described so far represents a single SPAD, without considering the surrounding SiPM structure and the effects of the front-end electronics, but most importantly it does not consider the influence of the other cells. In general for a SiPM with N_{tot} cells there can be N_f firing SPADs at the same time and $N_{tot} - N_f$ sensors at rest, the latter acting as passive elements. A more reliable representation must also take into account the parasitic capacitance C_g due to the metal grid connecting all the cathodes, which spans over all the SiPM surface and affects the pixel terminals. A more realistic SPAD circuit is reported in figure 3.7 a), while figure 3.7 b) shows the SiPM circuital scheme with additional passive components like the grid capacitance mentioned before, the parasitic resistance of the SiPM bonding (and trace) R_{par} and its inductance L_{par}.

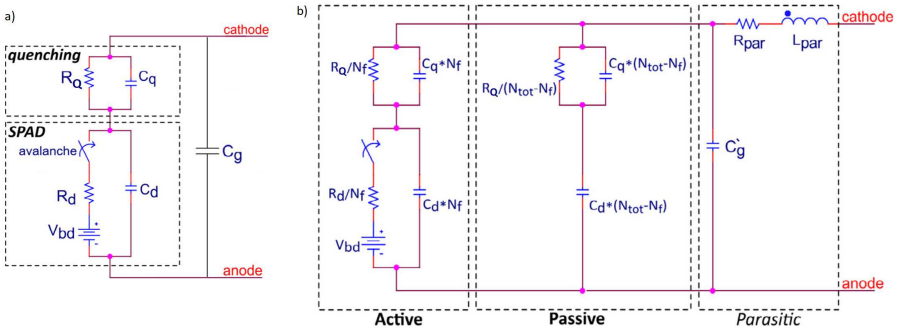

Figure 3.7: a) modified from [45], equivalent electrical circuit of a SPAD as in figure 3.6 but with the introduction of a parasitic capacitance across the terminals. b) modified from [43], equivalent electrical circuit of a SiPM with N_{tot} micro-cells, with a portion N_f of firing pixels.

For a more detailed model, the C_g value could include a further fringe capacitance due to the geometry of the cathode bonding pad structure over the detector surface [45]. The fringe capacitance is a passive element of each pixel in the SiPM, and its value is independent on the pixel state (firing or at rest), so the parallel SPAD fringe capacitances can be incorporated in C_g ($C'_g = N_{tot} C_g$).

The values of some of the parameters involved in the SiPM equivalent circuit can be estimated by studying the frequency domain of its output [53], using for the SiPM model the following impedance:

$$|Z(\omega)| = |j\omega L_{par} + R_{par} + (j\omega C_g + N_{tot} Y_{SPAD})|$$
$$Y_{SPAD} = (\frac{1}{j\omega C_d} + \frac{1}{R_Q{}^{-1} + j\omega C_Q})^{-1}$$

where Y_{SPAD} is the admittance of the single cell or pixel, in this equation all the pixels are considered at rest. The number of firing cells N_f impacts not only the amplitude of the SiPM output (being N_f times the amplitude of a single SPAD), but also its shape, since the changes in N_f in the equivalent circuit result in different load and current partitioning. As mentioned before, the C_d value depends on the depletion region depth and so, among other parameters, on the V_{OV} value.

The complex transmittance $Y(\omega) = \frac{1}{Z(\omega)}$ can be written, neglecting some parasitic effects (L_{par}, R_{par} and R_d), as

$$Y(\omega) = G_{\mathrm{SiPM}}(\omega) + j\omega C_{\mathrm{SiPM}}(\omega) = [(\frac{R_{\mathrm{Q}}}{N_{\mathrm{tot}}} \| \frac{1}{j\omega N_{\mathrm{tot}} C_{\mathrm{Q}}} + \frac{1}{j\omega N_{\mathrm{tot}} C_{\mathrm{d}}}) \| \frac{1}{j\omega C_{\mathrm{g}}}]^{-1}$$

where the parallel vertical lines denote the parallel connection of the two equivalent components. By inverting this equation we can obtain the C_{d} and C_{g} values from the SiPM parallel conductance $G_{\mathrm{SiPM}}(\omega)$ and capacitance $C_{\mathrm{SiPM}}(\omega)$, respectively.

$$C_{\mathrm{d}} = \sqrt{\frac{1 + \omega^2 (C_{\mathrm{d}} + C_{\mathrm{Q}}) {R_{\mathrm{Q}}}^2}{\omega^2 N_{\mathrm{tot}} R_{\mathrm{Q}}} G_{\mathrm{SiPM}}(\omega)}$$

$$C_{\mathrm{g}} = C_{\mathrm{SiPM}}(\omega) - N_{\mathrm{tot}} C_{\mathrm{d}} + \frac{\omega^2 {C_{\mathrm{d}}}^2 {R_{\mathrm{Q}}}^2 N_{\mathrm{tot}} (C_{\mathrm{d}} + C_{\mathrm{Q}})}{1 + \omega^2 {R_{\mathrm{Q}}}^2 (C_{\mathrm{d}} + C_{\mathrm{Q}})^2}$$

The quenching resistor value R_{Q} can be obtained from the IV curve in forward region as will be mentioned in the next subsection, while $G_{\mathrm{SiPM}}(\omega)$ and $C_{\mathrm{SiPM}}(\omega)$ can be estimated acquiring the spectrum of the SiPM signal or directly measured with specific instruments like a precision LCR meter [43]. Even if the single C_{d} and C_{g} values are the unknown parameters, their sum can be estimated by measuring the gain of the detector $(C_{\mathrm{q}} + C_{\mathrm{d}}) = \frac{V_{\mathrm{OV}}}{G \cdot e}$. The standard procedures adopted to measure the gain of the SiPM detectors, and also to measure the other parameters introduced so far, will be discussed in section 3.3.

The presented calculations, combined with measurements, permit to estimate almost all the parameters involved in the SiPM equivalent electrical model, the only exception is R_{d}, which is considered as a parasitic parameter since it is smaller by orders of magnitude with respect to R_{Q}. The value of R_{d} can be measured from the rise time of the SPAD signal, although is requires advanced instrumentation with high bandwidth and very low parasitic inductance to be measured. A standard approximation of $R_{\mathrm{d}} \sim 1\,k\Omega$ can be assumed without introducing significant errors on the simulation results [54].

3.1.2 SiPM output signal

As mentioned in the previous subsection and visible in figure 3.6 b), the SiPM output signal can be divided in three distinct temporal ranges: the *rising* region in the rising part of the $[t_0 - t_1]$ range, the *quenching* region on the falling part of the $[t_0 - t_1]$ range and lastly the *recharging* region from t_1 to t_2. Is worth noticing that the avalanche discharge and its quenching process both start at the same time t_0, as the switch is closed, and both persist until the switch is re-opened (t_1) [45]. The nomenclature of the regions stems from the fact that the exponential rise is dominant in the rising region, while the exponential drop due to the quenching effect is dominant in the quenching region.

This subsection describes the estimation of the SiPM output signal parameters such as the peak current and the time constants involved in the different regions, deriving these quantities from the properties of the SiPM representative circuit discussed in the previous subsection.

The small-signal equivalent of the circuit in figure 3.7 b) is reported in figure 3.8 a). Here V_{bias} is grounded and the voltage supply inside the SPAD is set to V_{OV} instead of V_{BD}, since it is the difference of the two voltage drops across two sources with opposite polarization. This approximation is true as long as the switch is closed, and a different circuital model will be used for the time constants involved in the recharge region. The parasitic effects of L_{par} and R_{par} are neglected, the output signal I_{EXT} is the current flowing through the load resistor R_{L} and all the parasitic capacitances are grouped in C_{eq}.

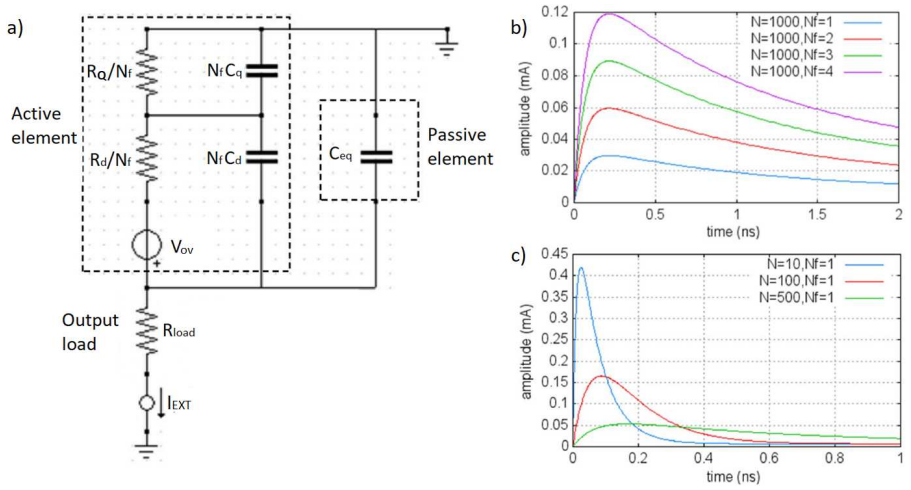

Figure 3.8: Modified from [45]. a) Small-signal equivalent circuit used for the estimation of the τ_{rise} and τ_{fall} time constants, b-c) plot of the output current amplitude as a function of time from the simulated circuit represented in a), varying the number of firing pixels N_{f} with fixed total number of cells $N_{\text{tot}} = N = 1000$ (b) and for a single firing pixel varying the number of total cells in the SiPM $N_{\text{tot}} = N$ (c). The time scale is set with the zero corresponding to the avalanche start t_0.

$$C_{\text{eq}} = (N_{\text{tot}} - N_{\text{f}}) \frac{C_{\text{d}} C_{\text{Q}}}{C_{\text{d}} + C_{\text{Q}}}$$

The R_{d} and R_{Q} of the passive pixels are not considered since they do not contribute to the total capacitance of the circuit C_{eq}, and in general their contribution to the overall impedance is negligible assuming that if R_{L} is much lower than $R_{\text{Q}}/(N_{\text{tot}} - N_{\text{f}})$, which is a fair approximation since R_{L} is usually 50 Ω. The signals associated to the described equivalent circuit are reported in figure 3.8 b) and c). The values of the parameters used for this simulation are reported in table 3.1.

parameter	value
R_{Q}	300 kΩ
R_{d}	300 Ω
R_{L}	50 Ω
C_{d}	200 fF
C_{Q}	20 fF
C_{m}	5 fF

Table 3.1: Typical values of the parameters involved in the equivalent circuital model of a standard SiPM. The functional dependencies reported in figures 3.8 b), 3.8 c) and 3.9 were produced using these parameters in the simulations.

We can define the exponential rise time constant τ_{rise} and exponential drop time constant τ_{fall} for the signal in the rising and quenching ranges respectively. These time constants are roughly independent on the number of firing cells, as visible in figure 3.8 b), but for a single firing SPAD they are both strongly influenced by N_{tot}, as reported in figure 3.8 c).

From this model is possible to evaluate τ_{rise} and τ_{fall} by further assuming that $R_{\text{Q}} \gg N_{\text{f}} R_{\text{L}}$, $R_{\text{Q}} \gg R_{\text{d}}$ and $N_{\text{tot}} \gg N_{\text{f}}$ and neglecting the contribution of C_{g}' [45]. To a first-order approximation, the resulting time constants are:

$$\tau_{rise} \approx \frac{N_{\text{tot}} R_{\text{d}} R_{\text{L}} C_{\text{d}} C_{\text{Q}}}{R_{\text{d}}(C_{\text{d}} + C_{\text{Q}}) + N_{\text{tot}} R_{\text{L}}(C_{\text{d}} \| C_{\text{Q}})}$$

$$\tau_{\text{fall}} \approx R_{\text{d}}(C_{\text{d}} + C_{\text{Q}}) + N_{\text{tot}} R_{\text{L}}(C_{\text{d}} \| C_{\text{Q}})$$

For a large number of total cells N_{tot}, the rising time constant reduces to $\tau_{\text{rise}} \sim R_{\text{d}}(C_{\text{d}} + C_{\text{q}})$, which is the factor mentioned in the previous section.

The peak current amplitude I_{max} can be calculated by further assuming that $\tau_{\text{rise}} \ll \tau_{\text{fall}}$:

$$I_{\text{max}} \approx \frac{N_{\text{f}} V_{\text{OV}} C_{\text{Q}}}{R_{\text{d}}(C_{\text{d}} + C_{\text{Q}}) + N_{\text{tot}} R_{\text{L}}(C_{\text{d}} \| C_{\text{Q}})}$$

Besides the expected linear dependence on N_{f}, the peak amplitude decreases with the total number of pixels N_{tot} and the influence of the front-end electronics (R_{L}) becomes larger as N_{tot} increases.

From the derived formulas for τ_{rise}, τ_{fall} and I_{max} it is clear that the contribution of the passive cells is the same of a low-pass filter, because by increasing N_{tot} the peak amplitude is reduced and the time constants are dilated. These effects are also visible in figure 3.8 c), where the area underlying the current signal remains the same for different N_{tot} values due to the charge conservation principle.

The third and last phase of the SiPM output signal starts as the switch is opened (t_1) and continues until the diode voltage recovers to the initial bias [45]. This region is distinguished by two distinct time constants, that can be estimated with a simplified circuit similar to the one in figure 3.8 a). In the new equivalent circuit the V_{OV} branch is absent since now the switch is open, and the capacitances firstly act as voltage sources. Adopting a similar the approach used for τ_{rise} and τ_{fall} on this circuit, one can estimate two time constants $\tau_{\text{rech},1}$ and $\tau_{\text{rech},2}$ which govern the signal drop during the recharge time.

$$\tau_{\text{rech},1} \approx \frac{N_{\text{tot}} R_{\text{Q}} R_{\text{L}} C_{\text{d}} C_{\text{Q}}}{R_{\text{d}}(C_{\text{d}} + C_{\text{Q}}) + N_{\text{tot}} R_{\text{L}}(C_{\text{d}} \| C_{\text{Q}})}$$

$$\tau_{\text{rech},2} \approx R_{\text{Q}}(C_{\text{d}} + C_{\text{Q}}) + N_{\text{tot}} R_{\text{L}}(C_{\text{d}} \| C_{\text{Q}})$$

where the dominant term is $R_{\text{Q}}(C_{\text{d}} + C_{\text{q}})$, for standard R_{Q} values. An example of complete output signal considering all the ranges mentioned above is reported in figure 3.9, where the parameters used for the simulations are the ones listed in table 3.1, with $V_{\text{OV}} = 2\,\text{V}$ and $I_{\text{TH}} = 100\,\mu\text{A}$.

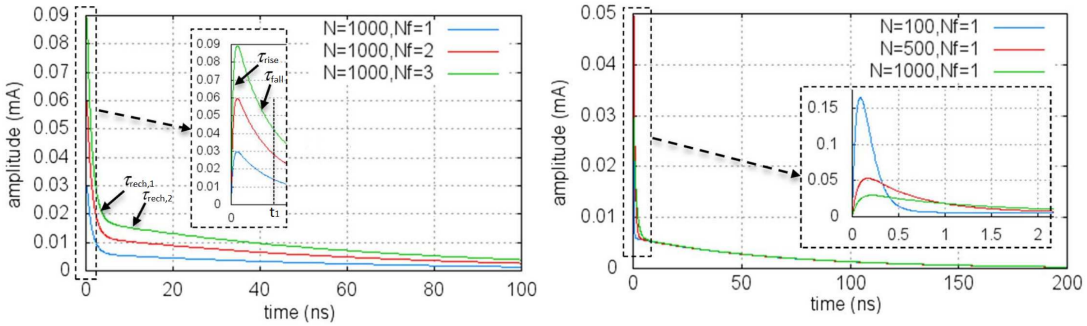

Figure 3.9: Modified from [45]. Left: simulated response of the SiPM for $N_{\text{f}} = 1,2,3$ firing pixels and with $N_{\text{tot}} = 1000$ in extended range, the four time constants τ_{rise}, τ_{fall}, $\tau_{\text{rech},1}$ and $\tau_{\text{rech},2}$ are marked in the plot and its zoom in the $[t_0, t_1]$ range. Right: simulated response of the SiPM for a single firing pixel and with increasing N_{tot} values in extended range.

The time constant $\tau_{\text{rech},2}$ is one of the most significant parameters for modeling the SiPM response since, being clearly dominant with respect to all the other time constants described so far, it defines the recovery time of the SPADs. As a rule of thumb, we can consider that any other photon arriving prior to $\sim 5\tau_{\text{rech},2}$ from the first detected one has a lower avalanche triggering probability in the same SPAD.

3.2 SiPM Properties and applications

This section covers the most important parameters involved in the SiPM characterization and their relation with the SiPM structural parameters, together with their dependence on the applied overvoltage $V_{\text{OV}} = V_{\text{bias}} - V_{\text{BD}}$. The subsection 3.2.6 describes the general history of the SiPM technology and the subsection 3.2.7 covers its range of applications, which increased with time along with and the fabrication techniques.

3.2.1 Breakdown Voltage

As mentioned above, the breakdown voltage is the bias at which the multiplication factor M diverges, this means that a Geiger discharge is triggered only if enough secondary carriers are generated by impact ionization per unit distance, more precisely when the so-called *ionization integral* is equal to 1:

$$\int_0^W \alpha_{\text{n}} \cdot e^{\int_0^x (\alpha_{\text{p}} - \alpha_{\text{n}})\, dx'}\, dx = 1$$

where α_{n} and α_{p} are the impact ionization rates per unit distance of the electrons and holes respectively and W is the width of the depletion region.

Different models has been developed to solve the ionization integral equation [55], showing in general an exponential dependence of the ionization coefficients on the SPAD internal electric field, and finding that:

- The collision probability raises with W, since there is more space in the depletion region, and this effect reduces the critical electric field for the breakdown condition and ultimately the breakdown voltage V_{BD}.
- The V_{BD} value is the integral of the internal electric field over the whole depletion region width, so wider depletion regions lead to higher V_{BD} values.
- The net effect of the previous points is that V_{BD} increases with W.

These models simplify the depletion region geometry to one dimension and do not take into account, among other factors, the W dependence on V_{bias}, but the resulting conclusions reported in the list are confirmed by more recent simulations done with Technology Computer-Aided Design (TCAD) [56]. These new simulations employ sophisticated models representing more realistic structures, and inspect all the possible trajectories of the free charge carriers during the Geiger discharge.

The difference of the V_{BD} values from SPAD to SPAD inside the SiPM also increases with W, this means that the exact value of V_{BD} is more reproducible using cells with thinner depletion regions. The

low-W condition can be easily met in blue/UV SiPM technologies, but for the red/IR technologies the V_{BD} uniformity could be an issue in some applications.

The importance of the V_{BD} uniformity stems from the fact that many parameters, for example the gain, are strongly influenced by V_{OV}, which in turns depends only on V_{BD} since V_{bias} is equal for all the parallel pixels. In the following description we will distinguish the cases in where the overvoltage V_{OV} is constant, which means that the bias voltage is always V_{OV} Volts above V_{BD}, from the cases there V_{bias} is constant, which means that the actual overvoltage may change due to the V_{BD} variations. The former is an ideal situation since it is not possible to control the bias of a single SPAD inside the SiPM, while the latter is a more realistic one.

As mentioned before, the recent models used for the V_{BD} estimation take into account the 3D shape and geometry of the depletion region, or at least its 2D lateral section (i.e. the view in figure 3.4). The one-dimensional models can be considered as approximations of the general case which is valid at the centre of the p-n junction, but do not take into account the so-called *edge effects*. At the edges of the p-n junction the multiplication factor is higher due to the higher electric field, so the Geiger discharge has more probability to occur. Due to the non uniformity of the electric field within the depletion region, the breakdown level is different for different carrier paths, and M is in general higher for paths that pass through the edges, so the center of the SPAD area is in general less responsive than the perimeter [43]. For this reason the p-n junction is surrounded by a *guard-ring* or virtual guard-ring to avoid the edge effects, as reported in figure 3.10 a) and b), respectively. These

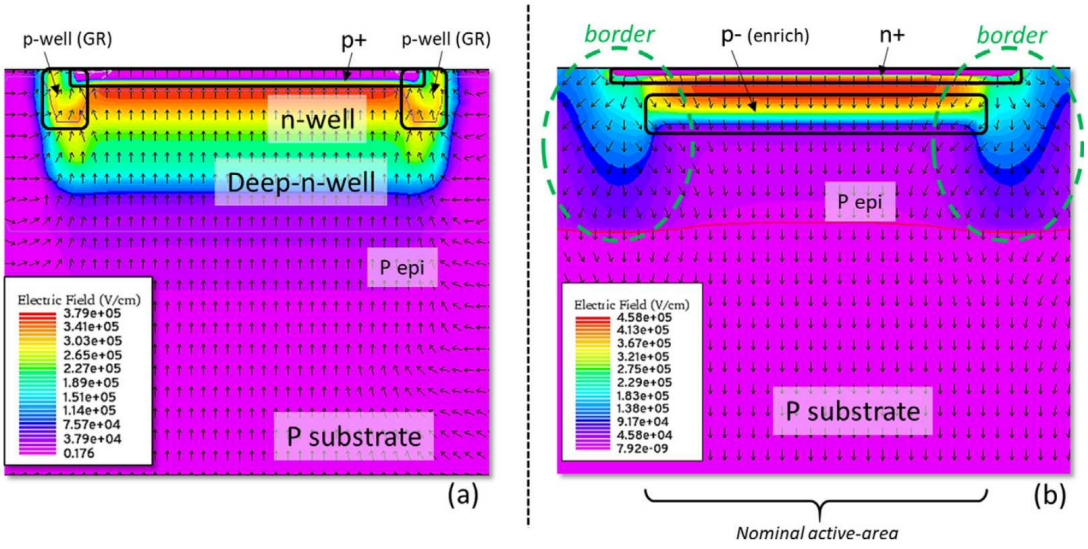

Figure 3.10: From [43], 2D lateral profile of the electric field inside the SPAD from a TCAD simulation for a) a p-well guard ring exploited on a p-on-n structure and b) a p-enrichment guard ring on a n-on-p structure. The common purpose of the two solutions is to reduce the edge effects, at expenses of the SPAD active area.

solutions reduce significantly the edge effects but also reducing the pixel active area, which is the portion of the SPAD surface sensible to incident photons.

3.2.2 Gain

As mentioned before, the gain can be defined as $V_{OV}(C_d + C_q)/e$ and it is typically of the order of $10^5 - 10^7$, so generally the single photon signal is well above the electronic noise level for standard front-end electronics. The gain dependence on V_{OV} is in general not linear, because the depletion layer thickness W increases with V_{bias}, leading to a reduction in the SPAD capacitance C_d. A more general definition is $Q_{TOT}/(N_f e)$ since in a SiPM there can be more than one firing cell at the same time, and in this case the total charge is the sum of the single charges of each SPAD.

Is worth specifying that even if the multiplication factor M of the Geiger discharge diverges, the gain does not diverge since the quenching process stops the Geiger discharge prior to a finite time, if no quenching is applied the gain diverges, since the avalanche is self-sustained and the cell is never recharging. In fact, by lowering the R_Q value in standard conditions the single SPAD recharge time increases.

At the single pixel level, by increasing the dimension (or pitch) of the cell the gain value of the SiPM increases accordingly, but in general the charge amplitude Q_{TOT} of the output signal has a complex dependence on the SPAD internal structure. The Q_{TOT} value can change for different events in the same cell, because it depends on the multiplication factor M of the avalanche process, which variations are related to the position of the primary e-h pair generation inside the pixel. For this reason the width of the gain distribution of the single SPAD events, which differs from the Q_{TOT} distribution only by a constant factor e, will depend on the cell internal structure.

Considering the whole SiPM there can be additional variations of Q_{TOT}, this time between signals of different pixels, due to the V_{BD} spread among the SPAD population. This also affects the width of the gain distribution because the V_{bias} value is equal for all the cells in the matrix, while the single cell bias V_{OV} is different from pixel to pixel due to the changes in the V_{BD} value.

3.2.3 Photon Detection Efficiency

Another important parameter to mention is the *Photon Detection Efficiency* (PDE) which quantifies the ability of the SiPM to detect incident photons, more precisely it is defined as the ratio of the number of detected photons $N_{detected}$ to the number of photons impinging on the total exposed area of the sensor $N_{photons}$.

$$PDE = \frac{N_{detected}}{N_{photons}}$$

The number of detected photons $N_{detected}$ represents the number of photons which are absorbed inside the SPAD creating a primary e-h pair, which successfully triggers an avalanche inside the sensor.

The general formula used to estimate the PDE of a SiPM contains both the overvoltage value V_{OV} and the wavelength λ of the incident photons [44]:

$$PDE(V_{OV}, \lambda) = QE(\lambda) \cdot P_t(V_{OV}, \lambda) \cdot FF(V_{OV}, \lambda)$$

where P_t is the already mentioned triggering probability, which depends on the internal electric field of the SPAD, so it ultimately depends on V_{OV}. P_t is also a function of λ since different wavelengths have different penetrations in the sensor, this dependence comes from the $P_t(x)$ relation with the

depletion region depth at which the primary charge carriers are generated $x(\lambda)$. As mentioned before the $P_t(\lambda)$ dependence, more precisely its electronic component $P_{\mathrm{t,e}}(\lambda)$, is the reason why the p-on-n(n-on-p) structure has a higher PDE in the blue/UV(red/IR) spectral region.

The *Fill-Factor FF*, also called geometric factor, is defined as the ratio of the (total) active area of the SPAD matrix to the total area of the SiPM surface. The FF value is always < 1 since the active area is the total SiPM area minus the the metal grid (and cathode pads) area, this active area is furthermore reduced due to the inactive portion around the depletion region of each cell, which stems from additive structures such as the guard rings or optical trenches. The former was mentioned before and serves to achieve a higher electric field uniformity at the p-n junction, while the latter are used to isolate the single cells and will be described more in details in subsection 3.2.5. The FF factor also depends on the overvoltage because the response of the SPAD, as a function of the position inside the depletion region, depends on the V_{OV} value. The spatial SPAD response also depends on λ, since different penetrations correspond in general to different transversal active areas. In some modern SiPM technologies the metal grid area is reduced using a transparent metal film as quenching resistor (MFQR) [44], but considering a similar fabrication procedure the metal grid influence is in general constant for the different SiPM models. For this reason a higher cell pitch will increase the fill-factor, for example for a $50x50\,\mu\mathrm{m}^2$ SPAD total area the fill factor can reach 80% while for cell sizes of $10x10\,\mu\mathrm{m}^2$ it is around 30%.

The QE factor is the *quantum efficiency*, which quantifies the probability for an incident photon to enter the detector and reach the active region of the SPAD before being absorbed. Since these active regions are different for electrons and holes, the QE factor can be divided in two separated contributions: QE_{e} and QE_{h}. A more general distinction involves QE_{top} and QE_{bottom}, which are referred to the active regions above and below the p-n junction, using the following arguments. Since we are distinguishing the electron and the hole contributions separately, we split the triggering probability contributions in $P_{\mathrm{t,e}}$ and $P_{\mathrm{t,h}}$, and also the total PDE can be divided in the same manner. In the following equations the $P_{\mathrm{t,e}}$ and $P_{\mathrm{t,h}}$ factors will be replaced by $P_{\mathrm{t,top}}$ and $P_{\mathrm{t,bottom}}$ considering the upper and lower part of the depletion region with respect to the p-n junction. This generalization can be done because the electrons have more probability to trigger an avalanche in the p regions, while $P_{\mathrm{t,h}}$ is higher in the n regions. This is done to have a general formula which represents both the n-on-p structure, where $P_{\mathrm{t,top}} \sim P_{\mathrm{t,h}}$ and $P_{\mathrm{t,bottom}} \sim P_{\mathrm{t,e}}$, and the p-on-n structure, where $P_{\mathrm{t,top}} \sim P_{\mathrm{t,e}}$ and $P_{\mathrm{t,bottom}} \sim P_{\mathrm{t,h}}$.

$$PDE = T_{\mathrm{ARC}} \cdot FF \cdot e^{-\frac{x_{\mathrm{i}}}{l(\lambda)}} (QE_{\mathrm{top}} P_{\mathrm{t,top}} + QE_{\mathrm{bottom}} P_{\mathrm{t,bottom}})$$

$$QE_{\mathrm{top}} = 1 - e^{-\frac{x_{\mathrm{d}}}{l(\lambda)}}$$
$$QE_{\mathrm{bottom}} = 1 - QE_{\mathrm{top}}$$

$T_{\mathrm{ARC}}(\lambda) = 1 - R_{\mathrm{ARC}}(\lambda)$ is the transmission coefficient of the anti-reflective coating (ARC) layer, FF is the aforementioned fill-factor.

Starting from the top of the sensor, right below the ARC layer, there is a region of thickness x_{i} where the carriers generally recombine before reaching the depletion region, then another region x_{d} where the generated charge carriers are able to trigger an avalanche. The factor $e^{-x_{\mathrm{i}}/l(\lambda)}$, common to both

holes and electrons, is the probability for the photon to be transmitted through the topmost x_i region below the ARC layer, and QE_{top} represents the probability of being absorbed in the successive x_d region. The p-n junction is situated at $x_i + x_d$ from the ARC layer, and the width of the depletion region under the junction is generally larger than the maximum penetration of light for visible wavelengths, for this reason QE_{bottom} can be written as $1 - QE_{top}$.

Today, the main vendors such as *Hamamatsu Photonics* (HPK), *Fondazione Bruno Kessler* (FBK) Ketek and SensL (now part of ON-semiconductors) can produce SiPMs with PDE values up to 60% [43], as summarized in figure 3.11.

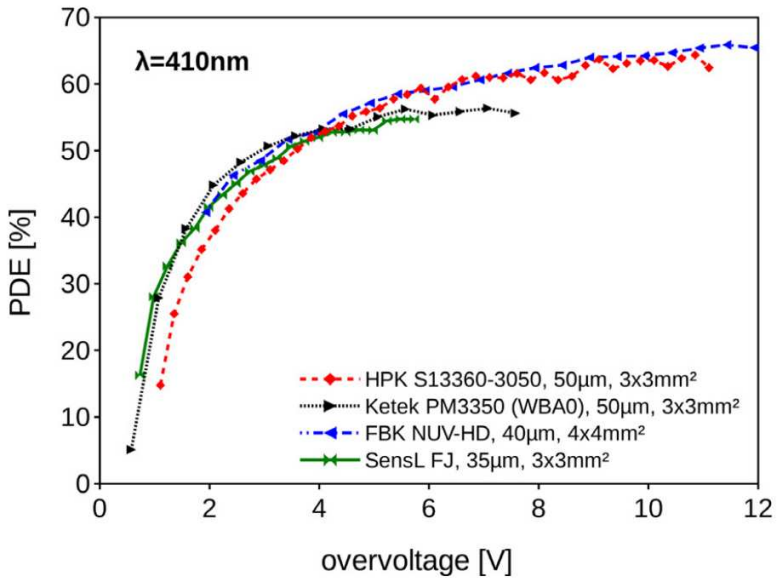

Figure 3.11: From [43], state-of-the-art PDE values as functions of V_{OV} measured for p-on-n SiPMs of different vendors with $\lambda = 410\,nm$.

3.2.4 Linearity and dynamic range

As mentioned before, the output signal of the SiPM is the sum of the signals from all the N_f firing cells, and sometimes the SiPM signals is represented in photo-electron (p.e.) units. Using the p.e. units means representing the signal with the associated N_f value, since the gain is almost the same for all cells apart from the previously mentioned fluctuations around the average value. At first approximation, the signal amplitude is proportional to $N_{photons}$ since the average N_f value is $PDE \cdot N_{photons}$, but the linearity holds only as long as $N_{photons}$ is small compared to the total number of cells N_{tot}, because each cell becomes inactive after detecting a photon. A more realistic equation to represent the number of firing cells, based on statistical processes under uniform illumination, is [57]:

$$N_f = N_{tot}[1 - exp(-\frac{N_{photon} PDE}{N_{tot}})]$$

At this point all the parameters involved in most important the state-of-the-art SiPM models are all covered, except for the *Single Photon Time Resolution* deriving from the time-domain analysis of the SiPM signal, which is out of the scope of this thesis. The remaining factor to discuss is the noise associated to the SiPM, which will be described in subsection 3.2.5.

3.2.5 Primary and correlated Noise

The noise related to the SPAD matrix within the SiPM is related to the events which are not (directly) triggered by the absorption of an incident photon, these events can be grouped in *Primary noise* and *Correlated noise*. The former represents the avalanches triggered by the primary charge carriers which are created by either tunnel effect or thermal generation, and can be quantified by the so-called *Dark Count Rate* (DCR). The DCR is a rate of events in general expressed in Hz, but it is common to consider its value per unit area, expressed in mHz/mm^2.

In the correlated noise group there are all the events generated as a consequence of a previous one, regardless on the mechanism that triggered the first avalanche discharge (incident photon, primary noise or even another correlated noise event). For this reason this noise type is quantified as the probability for a primary event to trigger a correlated noise event, and is often expressed as a percentage. The correlated noise can be related to either a single SPAD being triggered two consecutive times, or two SPADs firing by mutual influence, in the first case the secondary events are called *afterpulses* (AP) while in the second case we speak about *crosstalk* (CT) events.

The SiPM output signals related to DCR, CT and AP events are represented in figure 3.12, and will be described in the next subsections.

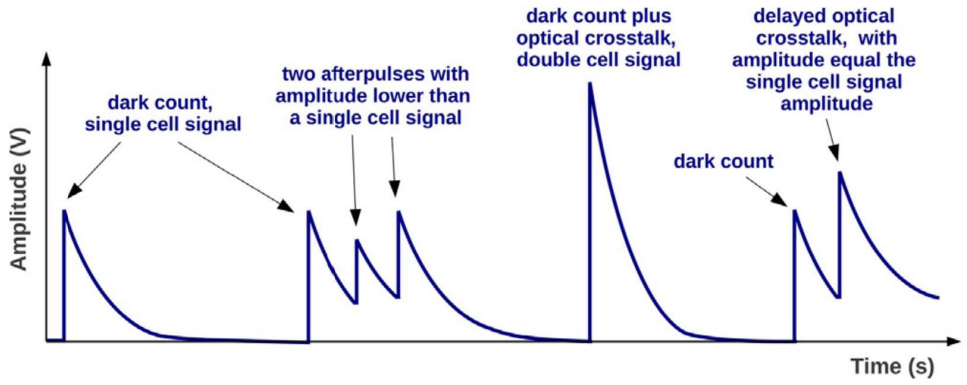

Figure 3.12: From [43] examples of SiPM output signals for DCR, AP and CT/DeCT events.

Primary noise: dark count rate

In contrast with the correlated noise events, the collection and trigger of primary dark counts are independent from each other [42]. The number of dark counts occurring within a time interval Δt is follows a Poisson distribution with an average $\lambda\Delta t$, where λ is the DCR value. The probability density function $f(t)$ for two consecutive dark events separated a time delay t follows an exponential distribution with parameter λ:

$$f(t) = \lambda e^{-\lambda t}$$

The thermal generation of primary charge carriers in depleted silicon, mediated by the states within the bandgap (impurities and crystal defects), can be studied with the Shockley-Read-Hall (SHR) model resulting in the following generation rate:

$$G_{\mathrm{SRH}} = \frac{n_{\mathrm{i}}}{\tau_{\mathrm{g}}}$$
$$\tau_{\mathrm{g}} = \frac{2}{N_{\mathrm{t}}\sigma v_{\mathrm{th}}} cosh(\frac{E_{\mathrm{F}}-E_{\mathrm{t}}}{kT})$$

where n_{i} is the intrinsic carrier concentration in silicon and τ_{g} is the so-called *generation lifetime*, which is the reciprocal of the generation rate of e-h pairs in the depleted silicon, and E_{F} is the Fermi level of the bulk material. The trap energy level E_{t} and concentration N_{t} depend on the doping profile and lattice structure of the sensor, while the capture cross section σ and the thermal velocity V_{th} depend on the carrier type but are assumed equal for holes and electrons. This mechanism for primary charge carrier generation is depicted in figure 3.13 a).

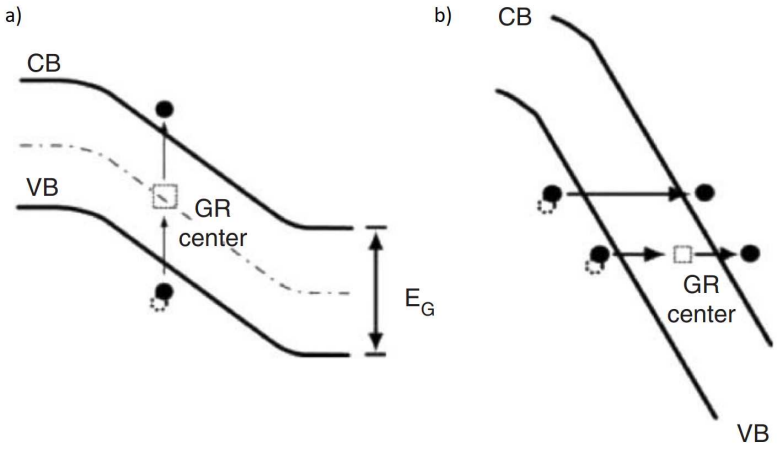

Figure 3.13: From [57], a) thermal generation of primary free carriers assisted by a mid-gap level, also called trap or generation rate (GR) center. b) direct tunneling (top) and field-assisted generation (bottom) of primary free carriers. VB and CB denote the valence and conduction bands, respectively.

The primary charge carriers can be generated also by tunnel effect inside the silicon, as visible in the sketch of figure 3.13 b), and in general the associated generation rate increases with the internal electric field intensity. This can be either direct inter-band tunnel effect or field-enhanced SRH (FH-SRH) generation, in which the charge carriers can be trapped or released by tunnel effect in addition to the thermal effects [58]. The SRH statistics can be modified introducing the Γ factor, which takes into account the generation rate dependence on the electric field due to the tunnel effect:

$$G_{\mathrm{FH-SRH}} = \frac{(1+\Gamma)n_{\mathrm{i}}}{\tau_{\mathrm{g}}}$$

Both direct tunneling (DT) and FE-SRH are present in the high-field region, but the thermal generation of charge carriers is the dominant generation process at room temperature. The drift region is characterized by standard SRH generation, while in the un-depleted regions the major DCR contribution is the diffusion of minority carriers toward the high-field region [42]. The different mechanisms for the primary e-h pair generation described so far are reported in figure 3.14, where the SPAD lateral section is divided in different regions depending on the dominant source of DCR events.

The electric field intensity is crucial for the activation of certain generation centers because in standard SRH conditions the V_{OV} dependence of the DCR value is given only by the triggering probability P_{t} of charge carriers, which saturates as P_t approaches the unity, while in the FE-SRH regime the

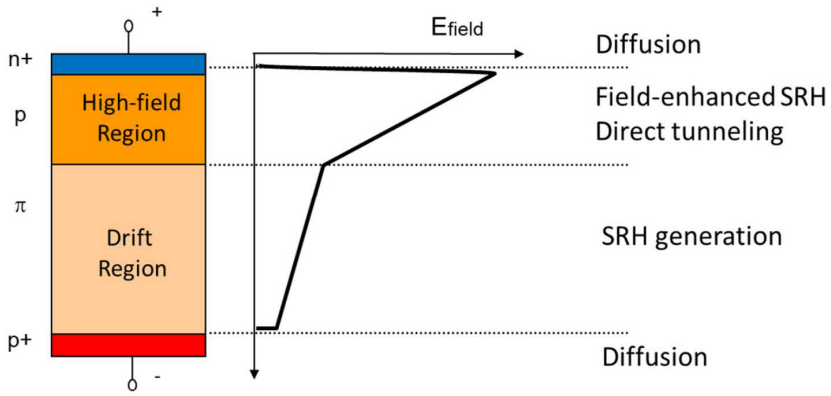

Figure 3.14: From [42], sketch of the doping profile for a n-on-p SPAD and relative plot of the electric field, the different regions of the sensor are marked with the dominant mechanisms for primary charge carrier generation.

generation rate also increases with V_{OV}. For these reasons the DCR value grows with the overvoltage even beyond the P_t saturation.

A secondary effect on the DCR dependence on V_{OV} is the depletion region width W, which increases with the overvoltage including more generation centers.

Correlated noise: Afterpulse

The numerous charge carriers generated in the avalanche region during a Geiger discharge have a non-zero probability of being captured by trapping centers and eventually being re-emitted triggering a secondary discharge in the same SPAD, as represented in figure 3.15 a), with typical time delays in the order of the μs. This phenomenon is called afterpulsing (briefly AP), and the related probability

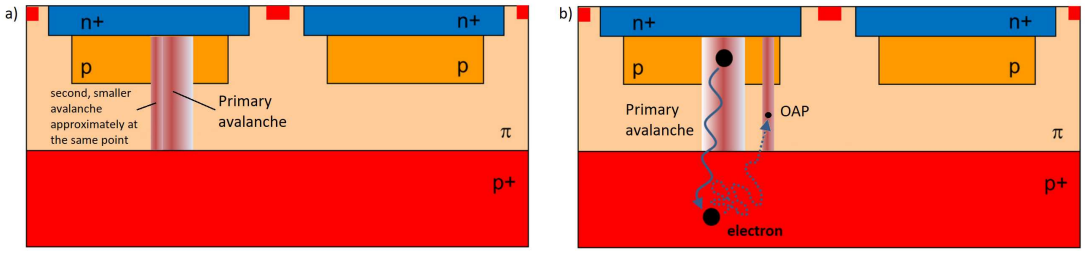

Figure 3.15: From [42] (a) and (b), two examples of afterpulsing: a standard AP (a) event and an OAP (B) event. The vertical lines represents the single avalanches.

for a single SPAD is

$$P_{AP,SPAD}(t_{release}) \sim G \cdot P_{trap,SPAD} \cdot P_t(V_{OV}) \frac{e^{-t/\tau}}{\tau}$$

where $P_{trap,SPAD}$ represents the probability that a charge carriers in the avalanche is captured, it is related to the position of the trap in the high-field region, the gain value represents the average number of carriers involved in a single avalanche. τ is similar to the generation lifetime mentioned above since it is the average trap lifetime in the high-electric field region, it depends on the trap energy level and

other factors such as the electric field intensity and the temperature. $P_t(V_{OV})$ is the triggering probability discussed above, this time concerning trapped carriers released after a time $t_{release}$, which drops significantly outside the high-field region [42]. After a first avalanche the junction is discharged and cannot trigger AP events until its bias is increased above V_{BD} during the SPAD recharge, so $P_{AP,SPAD}$ is equal to 0 in the range prior the time $t_{release} \leq t_1$ (with t_1 defined in figure 3.6) and the equation holds only if $t_{release} > t_1$. If the trapped carrier is emitted while the SPAD is recharging ($t_1 < t_{release} < t_2$), the probability of triggering after-pulses starts from a maximum value and decrease exponentially with a time constant τ. In general SPAD structures the trapping centers can have different energy levels, thus $P_{AP,SPAD}(t_{release})$ could follow a multi-exponential law with different τ values.

The afterpulsing can be also induced by photons, in this case it is called *optically-induced afterpulsing* or simply optical afterpulsing (OAP). As will be discussed in the following subsection (3.2.5), the Geiger discharge can actually generate photons in the avalanche region which travel through the sensor structure and can be re-absorbed in the substrate generating additional e-h pairs. These charge carriers can escape the un-depleted by diffusion and reach the active region, triggering a secondary avalanche in the same SPAD as in figure 3.15 b). For OAP the τ value is the carrier lifetime in the un-depleted region, so it can be reduced using a substrate with lower minority carrier lifetime. Another way to reduce OAP is the introduction of a buried junction below the active region to block the diffusion of photo-generated carriers towards the p-n junction.

For what concerns the output signal, the AP events have in general a smaller amplitude w.r.t. the DCR events since the SPAD is not completely recharged when the second avalanche is triggered, this is visible both in figure 3.12 and is also highlighted by the size of the vertical lines representing the Geiger discharges in figure 3.15.

Correlated noise: Cross-talk

During the avalanche discharge, the highly accelerated carriers inside the high-field region collide with atoms, dissipating energy by generating either lattice vibrations (phonons) or emitting optical photons, and the generated photons can reach the neighboring SPADs directly or through internal reflections on the SiPM structure. The generated photons are almost isotropic, and when they reach the depletion region of neighboring cells they can trigger secondary avalanches, as visible in figure 3.16 a).

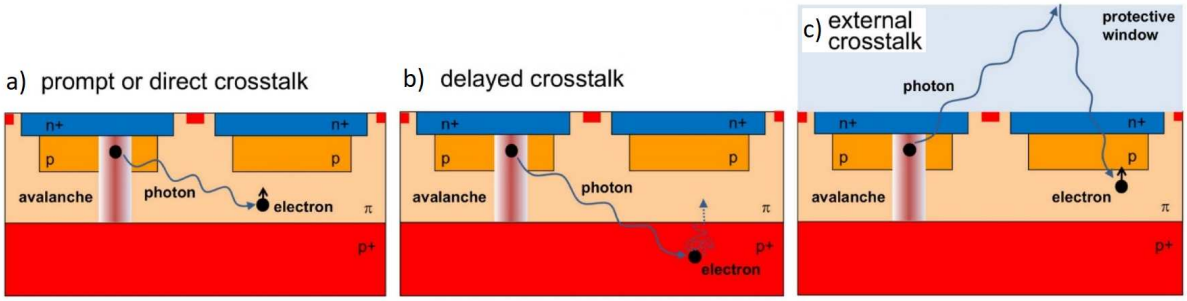

Figure 3.16: From [42], representative sketches of a prompt CT event (a), a delayed CT event (b) and an external (direct) CT event (c), respectively.

This phenomenon is called *prompt* (or direct) crosstalk (prompt CT), and the name stems from the fact that the time distance between primary and secondary avalanche is of the order of tens or at most hundreds of ps. This short time delay corresponds to a pile-up effect (for standard front-end input bandwidths), resulting in a single output signal with double amplitude.

The prompt CT is so fast because is related to the speed of light in Silicon and the distances are of the order of tens of μm. The CT events could also be induced by absorption of the photon in the substrate and subsequent diffusion of the generated charge carriers, in this case it is called *delayed* CT (DeCT). This mechanism is depicted in figure 3.16 b), it is similar to the OAP but involves two neighboring cells. Being related to the diffusion time constant on the substrate, the DeCT events have time delays similar to the OAP events, but in general different amplitudes since the avalanche comes from a fully charged SPAD, as visible in figure 3.12.

It is worth mentioning that the CT can be also *external*, in the sense that the photon is reflected outside the SPAD matrix by the SiPM window, used to protect the SiPM surface from mechanical and environmental stresses and generally made of epoxy resin or glass. These events can be either prompt, as depicted in figure 3.16 c), or delayed.

The CT dependence on the gain is almost linear, like for the AP case, because the more e-h pairs are produced per each avalanche, the more photons will be generated. The CT value also depends on the photon emission spectrum, which is difficult to measure because of the low CT-light intensity and due to its absorption inside the SiPM [42]. The mechanism of photon emission during the avalanche is also difficult to determine, and it is probable that it is the sum of different effects:

- direct/indirect inter-band transitions, corresponding e-h recombination
- direct/indirect intra-band transitions (hot-intraband luminescence) such as bremsstrahlung or light/heavy hole band transitions

A simple way to reduce the prompt CT probability is to decrease the thickness of the active region in order to reduce the height-width ratio and, consequently, the solid angle involved in CT events. Another widely adopted solution is the introduction of optical trenches between the cells, which are similar to the previously described guard rings but are made of light-absorbing (or either light-reflecting) materials. The delayed crosstalk, on the other hand, can be minimized by reducing the thickness of the un-depleted region, by extending the aforementioned trenches to the substrate depth [42], or in general with the same solutions used to decrease the OAP probability.

3.2.6 Development of the SiPM technology

The commercialization of the first photomultiplier tube (PMT) model in 1936, roughly 20 years after the development of the first photoelectric tube by Elster and Geiter, paved the way for single-photon detection by introducing an internal cascade of dynodes for secondary emission to achieve photo-electric signal amplification. A valid competitor for the vacuum technology in single-photon detection applications was lacking for roughly 60 years later [57]. During the following years the PMT technology was upgraded and has ramified in different designs, for example the multi-anode PMT

(MaPMT) with pixelated active area or the Microchannel-Plate detector, but the main backgrounds has almost remained the same:

- they need a high voltage to be activated (order of kV)
- they are very sensitive to external magnetic fields
- their price (per piece) is high due to the complicated mechanical structure inside the vacuum container

For the last item of the list it should be noticed that they can be cheaper with respect to SiPMs in low granularity applications since in general the PMT covers a larger area, resulting in a lower price per mm^2. On the other hand, the SiPMs can also be modified to increase their entrance window at expenses of granularity and efficiency, using simple mirrors or either more complex light traps like the X-ARAPUCA technology.

The PIN photodiodes were used as an alternative to PMTs for some high-energy physics applications, more precisely for the light detection in calorimeters where strong magnetic fields are employed (CLEO, L3, BELLE, BABAR, GLAST), but these solid-state detectors lack of internal multiplication ($Gain = 1$). The single-photon detection in semiconductor based sensors started with the development of APDs, which are PIN diodes with internal gain as mentioned in the previous section, but also in this case the minimum detectable light is in general tens of photons instead of one.

After the pioneering work of McIntyre (RCA company) [59] and Haitz (Shockley research laboratory) [60] in the early 60' the Geiger-mode APDs became a fertile technology for both experimental and theoretical research. In the 70' the first models describing the G-APD behavior were developed and verified experimentally with test structures [61]. The APDs that reached the single-photon level operated in Geiger mode with a V_{OV} bias of several Volts and were not much efficient, but later improvements lead to the development of the first SPAD.

As mentioned when describing the SiPM working principle, a single SPAD has a dual state which can be either "on" or "off" depending if there is impinging light or not, so its output signal is not proportional to the number of incident photons. The next step was reducing the SPADs size and implement them in a matrix structure to extend the dynamic range of the sensor, giving birth to the first SiPM. This process was favoured by new semiconductor fabrication and doping techniques developed to refine the production of CMOS logic structures.

One of the first examples of SPAD array is the $6x14$ matrix developed by *Radiation Monitor Devices* (RMD) in the 90' for DIRC applications (*Detection of Internally Reflected Cherenkov light*), where each unit has an area of $150x150\,mm^2$ [62]. In 1987 Stapelbroek et al. developed the so-called Solid State Photo-Multiplier (SSPM) [63]: an Ar-doped APD with very high donor concentration and wide PDE spectral range $[0.4-28]\,\mu m$, this detector that was later modified to restrict the PDE range in the visible region, changing its name to Visible Light Photon Counter (VLPC). These sensors operated at temperatures of few Kelvins, due to the small band gap which brings high thermal noise.

At the beginning of the 90' the *Metal-Resistor-Semiconductor* (MRS) APD was invented [57]: a very thin metal layer ($\sim 10\mu m$) upon a layer of SiC (or Si_xO_x) which acts as quenching resistor ($R_Q = [30-80]\,M\Omega$). The next step was subdivide the MRS structure into many cells and connect them all

in parallel via an individual limiting resistor, leading to the first SiPM structure, officially patented by V. Golovin [39] and Z. Sadygov [40].

Nowadays the photomultiplier tube technologies remain currently the best choice for some applications, but the solid-state technologies are replacing the PMTs also in those fields where it is not strictly necessary, as will be discussed in the next subsection (3.2.7). The reason is the fact that the commercially available SiPMs outperformed the PMTs in terms of intrinsic timing performances and overall PDE around 2010, and their are still upgrading now.

3.2.7 Applications of SiPMs

With respect to other photo-detectors, SiPMs are characterised by high sensitivity and dynamic range, as described above, good compactness and mechanical robustness, relatively low operating voltage and magnetic field immunity. In addition to that, the reduced cost and size of SiPMs allow to fill large surfaces with high granularity of channels, and they are fast enough to obtain a very precise arrival time for the detected photons. These properties permit the SiPM technology applications to span in a very wide range of fields, from particle physics and astronomy to industrial and medical sectors, and the different requirements of each field pushed the SiPM improvements toward various directions, from timing performances to noise level [44].

Typical low photon count applications of SiPMs are the *light detection and ranging* (LIDAR) technologies for the industrial field (automotive and life science) [64], or time correlated single photon counting and fluorescent light detection for other fields such as physics, biology and medicine [65]. The SiPM applications can be found also in recent fields such as quantum optics [66] and quantum information [67], or in general in High Energy Physics (HEP) for scintillation light (PANDA TOF and LHCb SciFi tracker) and/or Cherenkov light detection (RICH and DIRC detectors for particle physics, FACT and CTA in astroparticle physics). Due to their high granularity and their insensitivity to magnetic fields, SiPMs are preferred to PMTs in applications such as nuclear medical imaging, gamma ray spectroscopy and time-tagging of high energetic particles [44]. SiPMs also found massive applications in the medical field in *time of flight positron emission tomography* (TOF-PET), due to their high PDE and good timing performances [68], and also in other alternative PET designs such as the Axial PET (AXPET) or combined with magnetic resonance devices (SPECT/MR, PET/MR). Is worth mentioning that the CALICE Analog Hadron Calorimeter (AHCAL) used a large matrix of SiPM units for the photon detection system, and the SiPM technology was already applied in neutrino oscillation studies in the T2K experiment (around 60k SiPMs in ND280 and INGRID) [69].

Some effects of the many SiPM applications on their fabrication designs are reported in the following list [44]:

- some new applications such as the dark matter or double beta decay research pushed the developments of the PDE towards the vacuum ultraviolet (VUV) and deep ultraviolet (UV);

- the LIDAR technologies, in contrast with the previous point, drag the PDE upgrades towards the NIR spectrum, with particular interest in the automotive sector R&D due to their applications in autonomous driving technologies;

- new challenges in TOF-PET, high energy physics (HEP), time resolved x-ray detection and spectroscopy push developments of the SiPM single photon time resolution (SPTRs) towards the ps domain.

3.3 SiPM characterization

This section covers the standard procedures involved in the SiPM characterization, which are used to measure the main parameters described in the previous sections. Many of these parameters are measurable in different ways, some more complex than others, for example the quenching resistance R_Q can be extrapolated either from the IV characteristic curve of the sensor or from the shape of its output signal. Some practical examples of these measurements will be given in section 4.2.

Other parameters such as PDE, SPTR, excess charge and excess noise factor will not be discussed, since they are outside the scopes of this thesis[3], so as for the average capacitance C_d and resistance R_d values of the SPADs in the SiPM. The PDE values of tested sensors where furnished by the vendors and measured by other groups within the DUNE PDS Consortium (see chapter 4), the SPTR value is not a critic parameter for the DUNE application of SiPMs, the excess noise factor generally quantifies the amplitude dispersion of the single p.e. signal due to cumulative effect of gain spread and correlated noise

3.3.1 Quenching resistance

In the DC regime, the SiPM behaves as a standard avalanche diode, since it is essentially a matrix of parallel and highly depleted p-n junctions, but the underlying physics is different. From the IV characteristic curve in the forward region it is possible to estimate the R_Q value by interpolating the linear part of the curve as visible in figure 4.6 (left), because the internal resistance of the SPADs in forward polarization is negligible w.r.t. R_Q. It should be noticed that the inverse of the IV curve slope is the parallel resistance of all the SPAD, so it must be divided by N_{tot} to get the R_Q value of the single cell[4]. Another way to extrapolate the R_Q value is by fitting the exponential decay(s) of the I_{EXT} signal, retrieving the correlated time constants. This method is more complex since it relies on the temporal analysis of the output signal and on the knowledge of other SiPM parameters, in order to invert the equations defining the recharging time constants $\tau_{rech,1}, \tau_{rech,2}$ defined in subsection 3.1.2. The method selected by the DUNE PDS Consortium to estimate the R_Q value of the tested SiPMs relies on the IV curve characterization, since it is less complex in terms of both experimental procedure and data analysis, it does not imply the knowledge of other parameters and it is easier to automatize[5].

[3] The PDE values of tested sensors where furnished by the vendors and measured by other groups within the Consortium (see chapter 4), the SPTR value is not a critic parameter for the DUNE application of SiPMs and the excess noise factor generally quantifies the amplitude dispersion of the single p.e. signal due to cumulative effect of gain spread and correlated noise, which are both measured separately.

[4] in figure 4.6 the R_Q values are referred to all the SiPM, so they are equal to $N_{tot} R_Q$

[5] This last feature refers to the experimental setup described chapter 5, this setup was developed to perform automatic SiPM characterizations for a large number of sensors.

3.3.2 Breakdown voltage

There are different techniques that can be used to measure the breakdown voltage V_{BD} of a SiPM, for example it can be extrapolated from the gain measurement, as reported in the following. For low V_{OV} values, the gain value increases linearly with the overvoltage V_{OV}, as visible in figure 3.17 6), and its value is zero below V_{BD}. With a linear interpolation of the $G(V_{bias})$ function, the V_{BD} value can be

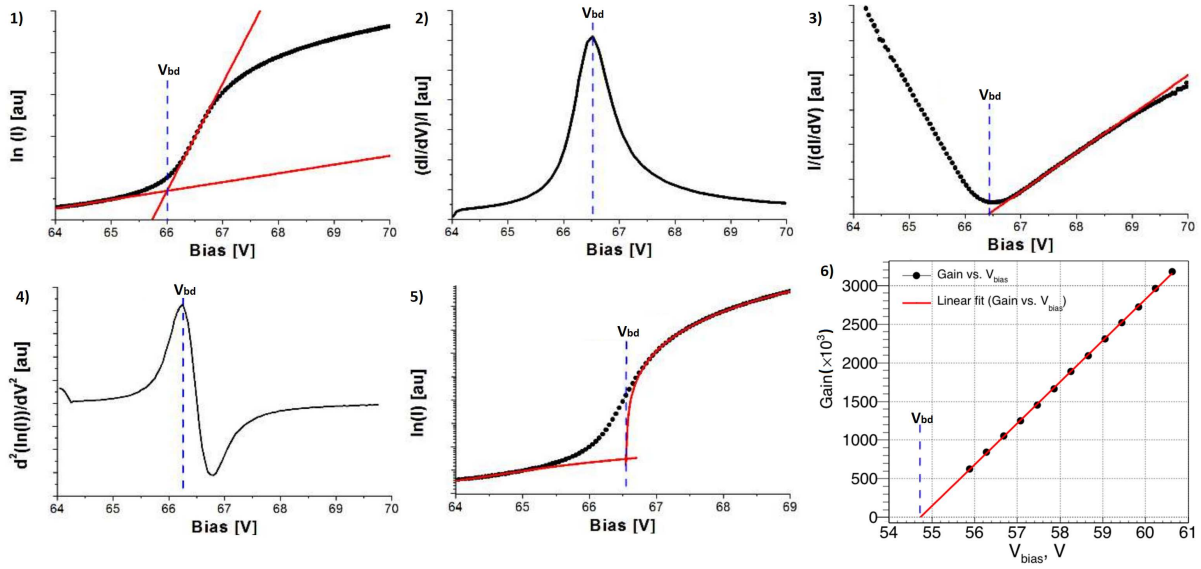

Figure 3.17: 1)-5): from [70], 5 different methods to extrapolate the V_{BD} value from the $ln(I) - V$ plot, the red lines marks the fit/tangent functions. 6): from [71], gain dependence on the bias voltage (for a different device w.r.t. the other cases), the red line show the linear fit from which V_{BD} is calculated. The vertical blue dotted lines represent the resulting V_{BD} value

found as the zero-crossing voltage $G(V_{BD}) = 0$.

Another way to measure the V_{BD} value relies on the IV curve characterization in reverse polarization, where I is given by the effective DC current of the SiPM output pulses. In contrast with a standard avalanche diode, the SiPM illumination is another parameter to take care of during the reverse IV curve measurement, because for low photon rates the reverse DC current is due only to the dark counts and the avalanche current could may be too small compared to the readout noise level, while an intense illumination could damage the device at high overvoltages. As visible in figure 4.6 (right), the logarithm of the current $ln(I)$ presents a sharp rise in correspondence of the breakdown voltage and the V_{BD} value can be defined in different ways starting from the $ln(I) - V$ curve, as depicted in figure 3.17 1)-5) and reported in the following list [70]:

1. the *tangent* method: intersection point between the linear fit on the signal baseline and the tangent on the rising part of the plot;
2. the *relative derivative* method: position of the maximum of the derivative function $\frac{d(ln(I))}{dV} = I^{-1}\frac{dI}{dV}$;
3. the *inverse relative derivative* method: taking the inverse of the derivative $[\frac{d(ln(I))}{dV}]^{-1}$ and finding the intersection of the tangent to the linear raise with the x-axis;

4. the *second derivative* method: position of the maximum of $\frac{d^2}{dV^2}(ln(I))$;
5. the *parabolic fitting* method: intersection point between the linear fit on the signal baseline and the parabolic fit of the raising part.

The DC measurement approach is in general less complex than the indirect estimation from the gain measurement, but the reverse IV curve requires typically a source and measurement unit (SMU) with high dynamic range to detect the current variations from the leakage to the breakdown levels.

The procedure used by the DUNE PDS Consortium to measure the V_{BD} value of the tested SiPMs relies on IV curve characterization. As for the case of R_Q estimation, this procedure was chosen for its reduced complexity and ease of implementation in an automatized setup. Time management of the single measurements was also a key factor for the choice of this method. The Gain vs V_{bias} interpolation is in general more precise than DC measurements since the results are not influenced by variations in the SiPM illumination [72], but it relies on AC measurements of single events. The method chosen for the definition of V_{BD} is the relative derivative method, because it involves searching a maximum instead of performing fits and finding intersections. The second derivative method also relies on the search of a maximum, but the related function features a lower SNR with respect to the relative derivative[6].

3.3.3 Gain

The gain measurement is based on the acquisition of the single SiPM events, so it is different from the parameters discussed until now, that are measurable by means of DC current measurements. A typical front-end electronics scheme comprehends a stabilized voltage supply to bias the SiPM and a standard oscilloscope to acquire the single events. The sample is typically illuminated by a faint pulsed light source and the signal acquisition triggered by the rising edge of the light pulse amplitude. The precise timing of each signal is not important, because the analysis is done on the amplitude distribution of the current peaks, more precisely on their charge Q_{tot} distribution. As mentioned before, the resulting distribution is featured (in standard conditions) by distinct peaks which are referred to $N = 1,2,3...$ p.e. amplitudes, and the gain value can be calculated for each peak as $\frac{Q_N}{N \cdot e}$, where Q_N is the amplitude of the $N-th$ peak and e is the electron charge. Furthermore, an estimation of the signal-to-noise ration (SNR) can be done by measuring the single p.e. amplitude and dividing this value by the FWHM of the peaks.

3.3.4 Primary and correlated noise

The front-end electronics used for both the noise characterization of SiPMs is generally similar to the experimental setup used for the gain measurements, without the faint light pulses generator and with low input impedance to reduce the filtering effect of the grid capacitance and of parasitic components. The SiPM must be in complete darkness, to prevent signals related to incident photons, and this time particular attention must be taken to the time resolution of the readout system, specially

[6] Because the derivative operation in general increases the distortions of a signal.

if the aim is a precise estimation of AP and DeCT probabilities. For the gain measurements the signal is a superposition of many SPADs firing at once and its amplitude does not usually need amplification, while the SiPM noise measurement requires all 1 p. e. events to be measured in a defined time window, so the SiPM signal is typically magnified by a trans-impedance amplifier, sometimes followed also by a second amplification stage.

As mentioned before, both the primary and correlated noise can be extrapolated by studying the amplitude versus the inter-time distribution of the SiPM events, where the inter-time is the time delay from the previous event. The definition of the different clusters is related to constraints on both the x and y axis of this plot, as visible in figure 3.18. The Primary DCR events have 1 *p.e* amplitude and time

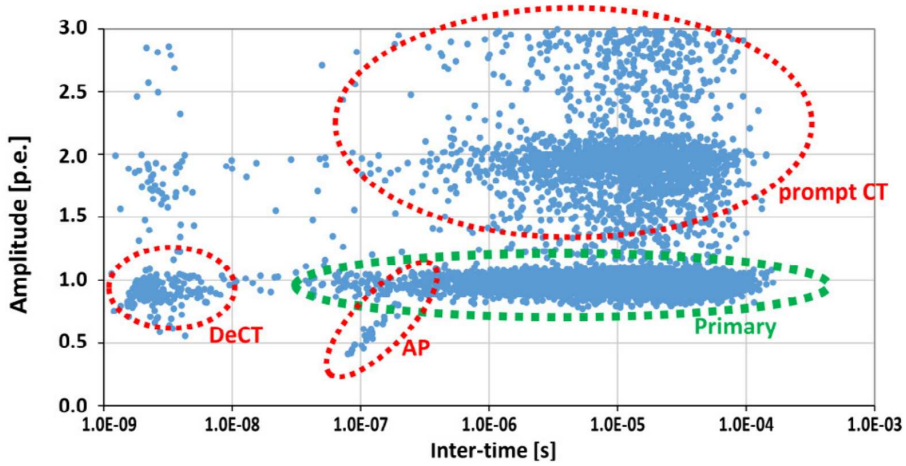

Figure 3.18: From [43], example of amplitude (in p.e.) vs. inter-time distribution of the SiPM events. The single clusters of DeCT, AP, Primary (DCR) and Prompt CT events are marked by dotted lines (green for primary noise and red for correlated noise).

delays of the order of the ns (at room temperature), and the AP events are sometimes difficult to disentangle from this cluster since they have similar inter-time values, but in general the AP amplitude is below the 1 p. e level and it decreases with the inter-time value. The prompt CT events are the ones with amplitude is above 1 *p.e*, and the number of *p.e.* defines the number of cells involved in the CT effect, while the DeCT events are in general faster than APs and with amplitudes of ~ 1 p. e.

As will be described in the next subsection (3.3.5), the DCR value drops significantly at cryogenic temperatures, so in this case the primary/correlated noise distinction is easier due to their different inter-time signatures.

3.3.5 SiPM characterization at cryogenic temperature

As mentioned before, the the DUNE-FD will work at liquid Argon temperature (~ 87 K), so the functional characterization of its photon detection system must be done at cryogenic temperatures. As will be mentioned in chapter 3 the SiPM models chosen for DUNE and ProtoDUNE are characterized at liquid nitrogen (LN_2) temperature (~ 77 K), in order to reproduce as far as possible the FD working conditions while containing the overall price. The ProtoDUNE-HD tests on the other hand, that employ a small-scale twin of the DUNE-FD1 TPC, are performed with liquid Argon.

As will be described in this subsection, some SiPM parameters show a more pronounced T dependence than others, but in general the behaviour of the sensor is strongly influenced by its temperature. The breakdown voltage generally decreases with the temperature, since the mean free path of charge carriers increases at low T, requiring a lower electric field to start an avalanche, and the temperature dependence of V_{BD} increases with the depletion region thickness W. The breakdown voltage is the integral of electric field over the SPAD structure, but avalanche effect is related only to the charge carriers in the depletion region, so a wider W would increment the V_{BD} variations with temperature.

For what concerns the dark noise, the three main DCR contributions derive from diffusion, generation of charge carriers (SRH, FE-SRH) and direct tunneling (DT) effect, as mentioned in the subsection 3.3.4. The general dependence of the related generation rates can be written as [42]

$$G(T) \sim e^{\frac{E_a}{kT}}$$

with E_a being the activation energy of the generation process, which is equal to the silicon bandgap E_g (= 1.21 eV) for diffusion processes, for pure SRH processes $E_{a,SRH} \sim \frac{E_g}{2}$ and generally $E_{a,FE-SRH} < E_{a,SRH}$. The diffusion process has typically the higher temperature dependence, SRH processes show in general less pronounced variations with T, while the DT carrier generation remains almost constant[7], as depicted in figure 3.19. The net result is that the DCR generally halves every times the

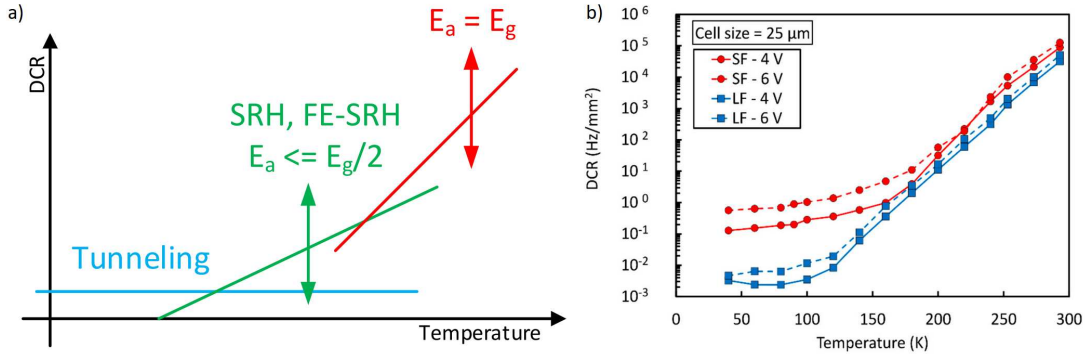

Figure 3.19: a) From [43], temperature dependence of the different DCR contributions. b) from [73], DCR as a function of temperature for the NUV-HD (SF) and NUV-HD-LF (LF) technologies from FBK at two values of V_{OV}.

temperature is diminished by 10 degrees.

The AP events are generally more frequent at lower temperatures, probably because a higher amount of charge carriers is released after the "dead time" of the pixel, described in the subsection 3.2.5, due to the longer average lifetime τ of the trapping centers [73]. The gain of the SiPM increases by lowering the temperature due to the shift on V_{BD}, but if the V_{bias} value is adjusted to maintain the same overvoltage the gain shows negligible changes. Other parameters show a similar behaviour, for example the SPTR, PDE and CT probability are almost insensitive to temperature variations as long as V_{OV} is constant. The quenching resistor on the other hand can display different low-T behaviours

[7] the variations in the DT generation rate are an indirect effect of the $E_g(T)$ dependence

depending on the material of which it is made, in general the R_Q value of poly-silicon resistors is more influenced by the temperature with respect to metal ones.

3.3.6 SiPMs in ProtoDUNE and DUNE

The DUNE PDS and SiPMs high-level requirements are reported in the following list:

- the PDE of SiPMs in the WLS bar emission spectrum should be at least as good as commercial devices (example for Hamamatsu S13360 > 35% at 430 nm)
- the SiPM dimensions should be compatible with the geometry of the X-ARAPUCA design described in chapter 2
- the signal amplitude (and associated uncertainty) from a single channel with an active SiPM area equivalent to a single SC (i.e. 48 SiPMs of the baseline model) should allow for adequate PDE in low-energy neutrino interactions
- the performance of SiPM and associated front-end electronics should allow to reach the 1 μs time resolution requirement mentioned in chapter 1
- the dark count rate (DCR) of the SiPM at the given threshold should not dominate that from radiological decays in LAr
- the SiPMs should be reliable to remain within specifications after > 10 years of operation in a LAr environment
- the sensors must be able to withstand multiple room-to-LAr temperature cycles without compromising their electrical or mechanical characteristics.

As mentioned above, the SiPM inside the X-Arapuca modules are operated in ganging mode. More precisely, the signals from 48 SiPMs are summed and amplified in the SC in low temperature conditions. For this reason, another important parameter is the breakdown voltage uniformity: the V_{BD} values within the same SC module cannot spread over a certain threshold, because the SiPMs should all operate at the same over-voltage.

The DUNE collaboration designed a Consortium of research groups from different countries to select the best choice among the available the SiPM models to be mounted in the DUNE-FD1 and ProtoDUNE2-HD photon detection systems (PDS) and engage a massive SiPM characterization for the samples of the selected model(s) [37]. The DUNE specifications for the LArTPC photosensors are reported in the following list:

In 2018-2019 the Single Phase Photon Detection System (SP-PDS) Consortium selected two SiPM technologies from two vendors respectively, *Hamamatsu Photonics K.K.* (HPK) and *Fondazione Bruno Kessler* (FBK), in order to start the pre-production phase of the 288000 sensors for the first DUNE module. The initial guesses for SiPM technologies where chosen for their low DCR and correlated

parameter	range
Breakdown voltage (V_{BD})	< 50 V (not critical)
Dark count rate (DCR)	< 200 mHz/mm^2
Cross talk (CT) probability	$< 35\%$
After pulse (AP) probability	$< 5\%$
Raise time (t_{raise})	< 100 ns
Recovery time ($t_{recharge}$)	$< \mu$s
Gain (G)	$> 2 \cdot 10^6$
V_{BD} spread (supercell)	< 0.1 V
Photon detection efficiency (PDE)	$> 35\%$ (at 430 nm)
V_{BD} spread	< 200 mV per PDS module (240 SiPMs)
Maximum V_{BD} spread	< 2 V for the entire PDS (global spread)

Table 3.2: List of upper and lower thresholds dictated by the DUNE specifications for SiPM operation ar 77 K (and a 0.5 p. e. trigger). Another general specification is that the sample must withstand at least 20 thermal cycles between room temperature and liquid nitrogen temperature without significant changes in the SiPM performances. The V_{BD} spread value refers to the spread of the breakdown voltage values for the SiPMs inside the same super-cell.

noise, together with high gain and reliability for low temperature operation and their main specifications are reported in the following list:

- The Hole Wire Bond (HWB) technology from HPK, implemented in the S13360 chip with Silicon resin package (series S13360-PE). This technology permits to raise the fill-factor because the cathode is connected by a hole in the middle of the sensor, reducing the dead space due to the connector area. HWB technology is also characterized by low cost and good performances at cryogenic temperature, while the 13360 series features low C_d and low correlated noise. After a series of thermo-mechanical tests, the vendor opted for a 150 μm silicon resin window for a higher mechanical robustness.

- The NUV-HD-SF technology from FBK, implemented in SMD epoxy resin package with lateral bond connections. The acronyms in the model name stand for near-ultraviolet, high density and standard-field, respectively [47]. These SiPM are tuned for near UV photons and they feature a high density of micro-cells. The last acronym is used to distinguish this model from the low-field (LF) model, which relies on a weaker internal electric field w.r.t. standard models. The microcells are separated by deep trenches, filled with silicon dioxide, to provide electrical isolation. A variation of this technology can features the so-called *triple-trenches* (TT), which are a trench structures with a triple-layer stack $SiO_2/Poly-Si/SiO_2$ [73].

Both the models are fabricated with a n-on-p structure, to maximize PDE in the UV region (around 430 nm), and in surface mount type packaging (called *Surface Mount Technology* or SMT) with a $6x6$ mm surface. As will be described in the following chapters, the Consortium also defined a general procedure to test the reliability of these sensors in operating at cryogenic temperatures for long time.

The initial guess technologies were employed by the vendors to create a first batch of sensors for the pre-production phase, more precisely 2 models for FBK and 4 models for HPK, divided in 6 groups of 25 sensors for each SiPM model. This pre-production phase served to fully characterize each SiPM

model and was followed (in 2020) by a series of ganging mode tests on 6-unit arrays (measuring the output of 250 sensors at board level). These procedures permitted to down-select one model per vendor according to the combination of measured parameters and performance in active ganging mode [37].

After the down-selection procedure, a sample of one SiPM per vendor was randomly selected for tests of long-term stability at cryogenic temperature. These measurements will be discussed briefly since they were not performed by the Ferrara group of the Consortium[8]. The SiPMs operated at LN_2 temperature for 2 months without interruptions, with a continuous monitoring of the DCR value. The test was performed in a dark room with the SiPMs wrapped in Teflon tape, black insulating tape and finally aluminum foil for electromagnetic shielding. The DCR value (after burst removal) was found to be stable during all the time window, varying within a 3.15 mHz/mm^2 range from the initial DCR value.

This initial phase was followed by the production of 6000 SiPMs of the selected models (3000 per vendor), then the test campaign proceeded with the development of a custom apparatus (CACTUS) to characterize all the 6000 sensors of the production phase for ProtoDUNE2-HD, and the same apparatus is currently operating for the characterization of the DUNE-FD1 SiPMs (288000).

[8]The Milano Bicocca group performed these tests.

Chapter 4

Characterization of single SiPM sensors

This chapter covers the first part of the DUNE pre-production phase, where the Consortium performed a full characterization on the 6 splits of sensors produced by the two vendors, precisely four splits from Hamamatsu photonics K.K. (HPK) and two from Fondazione Bruno Kessler (FBK). Each split contains 25 sensors of the same model, the specification of each model are reported in table 4.1, where the last column reports the actual number of samples received by the Ferrara group.

vendor	model	window	pitch	N_{cells}	Ferrara
HPK	**6050HS-LRQ**	**silicon resin**	**50 μm**	**14331**	**2**
HPK	**6075HS-LRQ**	**silicon resin**	**75 μm**	**6364**	**7**
HPK	6050HS-HRQ	silicon resin	50 μm	14331	0
HPK	6075HS-HRQ	silicon resin	75 μm	6364	0
FBK	**Standard**	**epoxy resin**	**30 μm**	**37300**	**6**
FBK	**Triple Trench**	**epoxy resin**	**50 μm**	**11188**	**6**

Table 4.1: Characteristics of the 6 different SiPM models belonging to the 6 splits received by the Consortium. The number of samples received for each model at the Ferrara site are reported in the last column. The rows with the models tested by the Ferrara group are highlighted in bold.

This chapter will describe the characterizations performed by the Ferrara group of the Consortium, which received a total of 21 SiPMs from different splits. The procedure concerns the IV curve measurement, the dark noise characterization and the photo-electron response tests and it is described in detail in section 4.2, while the results will be discussed in section 4.3. The purpose of these tests was the validation of the information of the vendors for the specifications at room temperature, the estimation of the main parameters describing the SiPM performances at LN_2 temperature and the evaluation of the best working conditions for the selected sensors. The parameters measured with this characterization are also important to set the boundaries for the ProtoDUNE and DUNE FD1 simulations.

During the dark noise characterization at liquid nitrogen (LN_2) temperature the team encountered an unexpected behaviour of the sensors, which consist in fast series of correlated events happening in absolute darkness [74]. The team called this phenomena *bursts* of events and started a campaign of tests to study this behaviour, in parallel with the other measurements. A detailed de-

scription of the *bursts* phenomenon is reported in section 4.4, together with the discussion of the performed tests.

4.1 Experimental apparatus

The sketches of the two different setups used for the IV curve measurement and for the dark noise characterization are reported in figures 4.1 a) and 4.1 b) respectively, and two pictures of the apparatus are visible in figures 4.2 and 4.3.

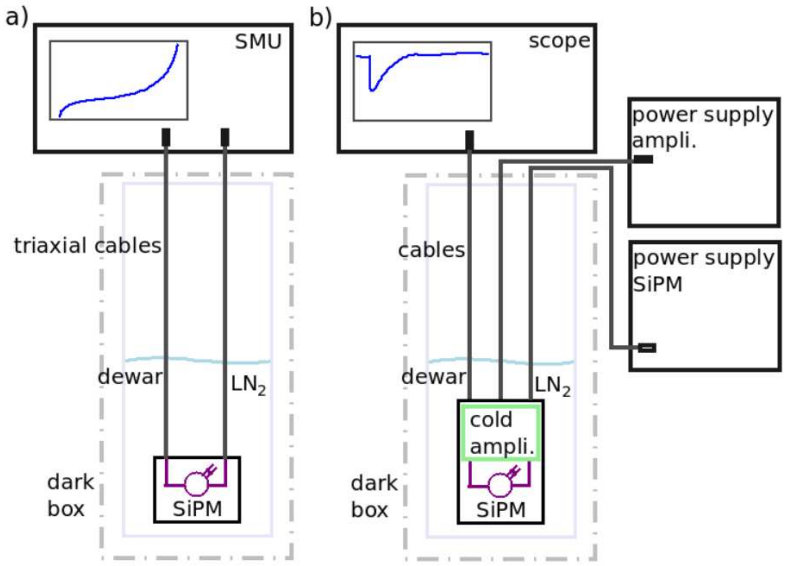

Figure 4.1: From [74], a) shows a Sketch of the set-up used for IV-curve measurements, while b) shows a sketch of the set-up used for dark count rate measurements.

The SiPM is hosted in a metallic box, which is placed inside a 20 dm^3 large-aperture dewar filled with LN_2 as visible in figure 4.2. The box contains also a Pt100 temperature sensors close to the sensor and also the amplification stage for the dark noise characterization setup.

The dewar is enclosed in a custom dark box made of a metallic support with a cover of polyurethane-coated black fabric to shield the SiPMs from external light. The cover is adjusted to get the best working conditions during the IV curve measurements, while for the dark noise characterization the light shielding is enhanced with two additional black fabric layers around the dewar.

The IV curve measurement is performed by a source meter unit (*Keithley Sourcemeter 2450*), which is connected to the SiPM through triaxial cables to reduce the electronic noise. The source meter unit (SMU) provides the stabilized bias for the SiPM and measures the output current, then it automatically repeats this process for each point of the IV curve.

The dark noise characterization requires a more complex apparatus, as it employs the SMU to bias the SiPM with a stabilized voltage and an oscilloscope (*Tektronix MSO 6 series - C014318*) to acquire the signals. The SiPM anode is connected to a custom cryogenic AC charge amplifier, which was designed by the INFN Bologna group. The amplifier has a (nominal) Bandwidth of 300 MHz and a (measured) Gain of (19 ± 2) mV/fC and is coupled to the oscilloscope with a 50 Ω input load. One

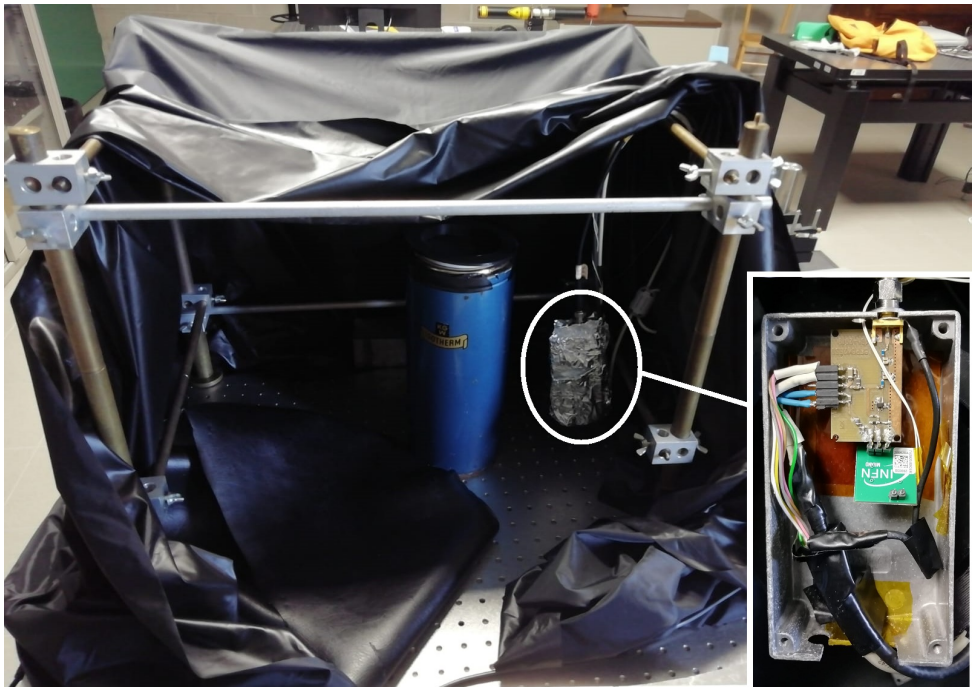

Figure 4.2: Picture of the dark box with the dewar and the metallic box. On the bottom-right part there is a picture of the box with a SiPM mounted on it. The box has a removable cover and contains some holes to enhance the leakage of liquid nitrogen inside.

of the transistors in the amplifier has been replaced after developing some failures due to fast cool downs, resulting in a different Gain value ((15 ± 2) mV/fC).

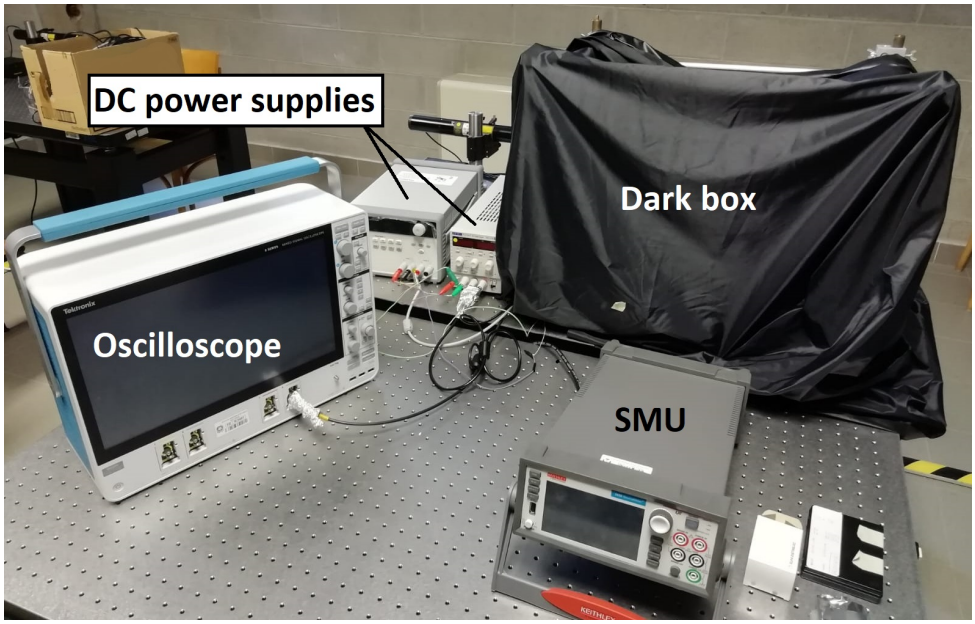

Figure 4.3: Picture of the experimental setup used for all the measurements described above. The two stabilized DC power supplies (*Keysight E3648A dual power supply* on the left and *TTI EX354T DC power supply* on the right) are used to bias the cold amplifier and the LED controller respectively.

The p. e. response measurement is performed similarly to the dark noise characterization, but

employing a faint LED light to populate high amplitude events.

4.2 Characterization procedure

The parameters involved in the characterization of SiPMs ProtoDUNE and DUNE application were discussed in section 3.3.6, while this section covers the procedures adopted by the Ferrara team to measure these parameters. These procedures where designed following the general requirements discussed within the Consortium [75], in compliance with the characteristics of the available instrumentation at each laboratory. The following list reports for each parameter discussed in the section 3.3.6, the experimental procedures followed by the group for the relative measurements.

- IV curve at room temperature.

  The first test is the measurement of the IV characteristic curve at room temperature, this is performed to validate the information provided by the vendors. The source meter is configured to perform automatically a voltage ramp to scan the bias voltage of the SiPMs in a user defined range, which is divided in N steps, and it measures the relative SiPM output DC current for each step. The first measurements were used to calibrate the parameters involved in the IV curve characterization, such as the range of the measurement, the full-scale range of the instrument, the number of acquisition to average for the single step measurement and the number of steps N. The bias voltage range for the forward polarization was initially set to $[0,4]\,\mathrm{V}$ but then was reduced to $[0,2]\,\mathrm{V}$ to avoid high current amplitudes that could damage the sensors. The range in reverse polarization is $[V_{\mathrm{BD}}-2\,\mathrm{V}, V_{\mathrm{BD}}+2\,\mathrm{V}]$ and differs for each model, it is approximately estimated with a fast scan around the expected value before the actual measurement. Once the acquisition is finished, the voltage and current data points are stored in a csv file by the source meter and then analyzed offline with a custom algorithm to estimate the R_{Q} and V_{BD} values. A detailed description of the offline data analysis is reported in the subsection 4.3.1. These measurements are performed, as far as possible, in controlled light conditions: the SiPM is hosted in a closed metallic box which is covered by a polyurethane-coated black fabric and the cover is adjusted to reach the desired illumination conditions. Each measurement is repeated five times with the same sensor to get a more precise estimation of the parameters by averaging the five results.

- IV curve at liquid nitrogen (LN_2) temperature.

  The following test is the measurement of the IV characteristic curve at LN_2 temperature, this is performed to extrapolate the quenching resistance R_{Q} and the breakdown voltage V_{BD} with the same analysis performed in the room temperature case. The immersion procedure is crucial because excessive thermal gradients could damage the sensors, which are not required to withstand fast thermal stresses for the ProtoDUNE and DUNE applications. A sensors undergoing a fast cooling could develop some failures and eventually change its characteristic parameters, misleading to the wrong conclusion that the SiPM is out of thermal specifications, for this reason the cool down procedure goes as follows. The immersion in LN_2 is performed manually

and it is divided in three step: a first thermalization with the LN_2 gas phase for around 5 minutes, a slow immersion in the liquid phase for around 10 minutes and a final thermalization with the liquid phase for another 30 minutes. The IV curve measurements start after the sensor has a reached a stable temperature, with variations under the 0.1 K level. The first measurements were used to calibrate the parameters involved in the IV curve characterization, which differ from the room temperature ones. This measurement is also performed in controlled light conditions, similarly to the room temperature case, adjusting the lid of the dewar which hosts the sensor to reach the desired illumination conditions. The data is saved and analyzed as described in the previous item of this list, and the detailed description of the analysis is reported in the subsection 4.3.1. Similarly to the room temperature case, each measurement is repeated five times with the same sensor, to get a more precise estimation of the parameters by averaging the five results.

- Primary Dark Count Rate (DCR) and correlated noise.

  After the IV curve characterization at LN_2 temperature the lid of the dewar is fully closed and the dewar covered with two polyurethane-coated black fabric shelters to enhance as possible the light shielding, then the DCR measurement take place. For the DCR measurement the SiPM is biased at $V_{\text{bias}} = V_{\text{BD}} + V_{\text{OV}}$ and the output signal of the AC amplifier is read by the oscilloscope, which acquires and stores all the events above the 0.5 p. e. amplitude threshold. The trigger level corresponding to 0.5 p. e. amplitude on the negative slope of the signal was measured during the calibration of the setup and takes a different value for each of the four SiPM models. The oscilloscope acquisition is set to the *fast frame* mode, which consists of saving the recorded waveforms at each trigger and store them in a temporary buffer. Once the selected number of waveforms (or *(*frames)) N_{frames} is reached, the data is transferred from the buffer to the hard disk. This technique enables relatively long data acquisitions with dead times below the 1 μs scale, which is a negligible since the expected DCR is around 1 Hz. The instrument permits only certain combinations of the number of frames N_{frames}, the resolution of the instrument, the sampling frequency f_{s} and the time duration of a single frame t_{frame}, due to the limited space of the temporary buffer. All these parameters must be maximized: a long t_{frame} permits to enclose the main DCR event and possible after pulses in the same waveform, reducing the possibility to miss after pulse events due to the acquisition dead time, the final event population is N_{frames} so this quantity must be maximized to reach enough statistics for the analysis and lastly, the amplitude and temporal resolutions must be maximized to get a better reconstruction of the single waveform. A typical set of parameters is reported in table 4.2, these were chosen to maximize the performances in compliance with the limitations of the instrument as explained in the previous paragraph, and correspond to about one hour of data acquisition. The analog input bandwidth was selected following a different trade-off since it must cut the noise without introducing appreciable distortions on the SiPM signal, it has been estimated during the calibration measurements similarly to the trigger level at 0.5 p. e.. The acquired data is stored in the internal hard disk in two comma-separated values (csv) files, one containing the single frames and the other containing for each frame the relative time of the

N_{frames}	f_s	t_{frame}	resolution	input bandwidth
$[2000-5000]$	$[1.25-6.25]$ Gs/s	$[1-10]\,\mu$s	12 bit	20 MHz

Table 4.2: Parameters used for the oscilloscope acquisition in the DCR measurements. In some case there is a range instead of a single parameter indicating that more than one value was used for the measurements. Not all combinations are possible, for example setting $N_{\text{frames}} = 5000$, $t_{\text{frame}} = 5\,\mu$s or $N_{\text{frames}} = 2500$, $t_{\text{frame}} = 10\,\mu$s the only allowed sampling frequency is 1.25 Gs/s. With these parameters a single measurement can take up to one hour.

trigger with respect to the previous one, these files are then analysed offline by custom python scripts. A detailed description of the offline analysis is reported in the subsection 4.3.2. The DCR measurement is performed three times at three different values of over-voltage V_{OV}, the three values where chosen because they correspond to 40%, 45% and 50% PDE, as stated by the vendors and are reported in table 4.3 for each SiPM model.

vendor	model	V_{OV} @ 40% PDE	V_{OV} @ 45% PDE	V_{OV} @ 50% PDE
HPK	6050HS-LRQ	3 V	4 V	5 V
HPK	6075HS-LRQ	2 V	3 V	4 V
FBK	Standard	4 V	5 V	6 V
FBK	Triple Trench	2.5 V	3 V	4 V

Table 4.3: values of the over-voltages relative to 40%, 45% and 50% PDE percentages for the tested SiPM models. These are the values used for both the DCR and the Photo-electron response measurements.

The tests are repeated at different PDE percentages in order to find the best working conditions for ProtoDUNE and DUNE in terms of SiPM bias voltage, since both the Gain and the DCR should increase with the V_{OV} value. A higher Gain (and PDE) leads to a higher efficiency and to higher amplitude output signals, which are easier to detect, but the raise in the DCR value enhances also the background noise.

- Photo-electron (p. e.) response.

  The photo-electron response measurement is similar to the DCR measurement, but in this case the sensor is illuminated by a LED source. The LED is coupled with the detector through optical fibers and emits light pulses at 1 kHz repetition rate, with $\lambda \sim 450$ nm and 10 ns pulse duration. The acquisition of the oscilloscope is set with the same parameters of the DCR measurement, apart from the trigger which is set to the rising edge of the LED pulse and the t_{frame} which is always $1\,\mu$s since the after pulse probability is not calculated. The LED illumination is calibrated to acquire signals with amplitudes up to 8 p. e. with enough statistics. This measurement permits to calculate the Gain and the signal-to-noise ratio (SNR) of the SiPM, but also to test the linearity of its response. A detailed description of the analysis is reported in the subsection 4.3.3. The tests are repeated at the V_{OV} values reported in table 4.3.

- Thermal cycles.

Each SiPM undergoes a total of 20 thermal cycles, where a thermal cycle is defined by the immersion of the sample in LN_2 and the following extraction. The immersion time is the one discussed in the second item of this list, without the 10 minutes thermalization in the liquid phase and with an extraction time of about 5 minutes. An example of 8 consecutive thermal cycles is reported in figure 4.4. All the measurements (except for the ones at room temperature)

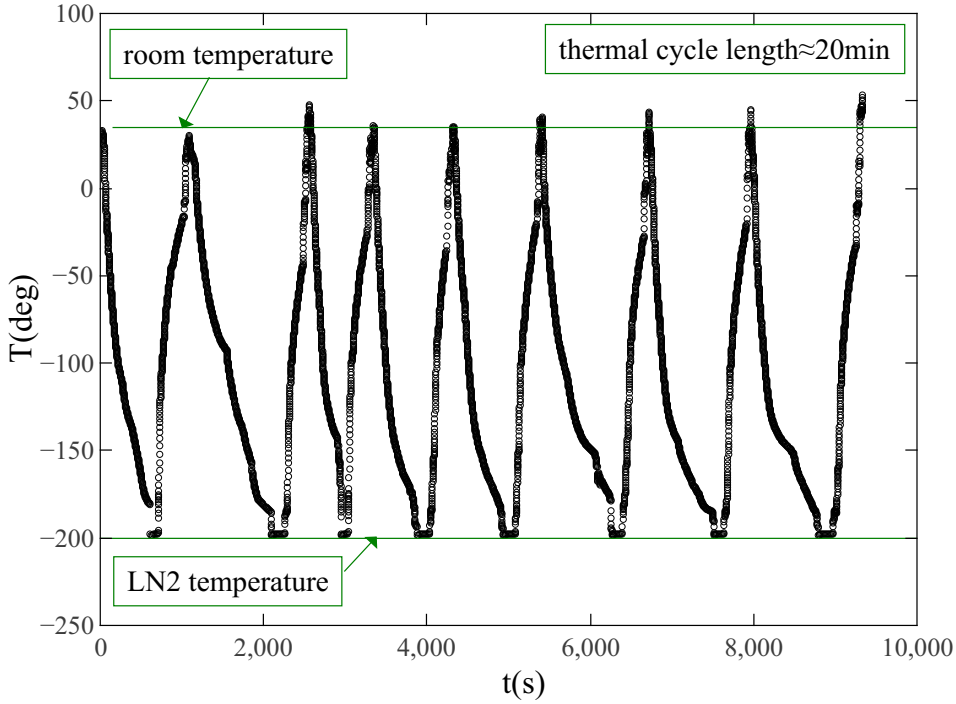

Figure 4.4: Example of the temperature versus time plot for 8 consecutive thermal cycles. Both the immersion and the extraction of the samples are performed manually, so the time duration of each cycle is not exactly 20 minutes.

are performed at the first immersion and then repeated after the 20^{th} immersion to check the resilience of the sensors to long cryogenic operations. The IV curve in reverse polarization and the amplitude of the single p. e. signal at fixed over-voltage must remain unaltered to consider the test passed. The team also tried to perform cycles with faster immersions of around 150 s for a subset of samples, in order to raise the thermal stress level. An example of three fast cycles is reported in figure 4.5.

As will be discussed in the conclusions in section 4.5, no appreciable differences were found in the parameters after the 20 thermal cycles, for both the fast-cycled and the slow-cycled SiPMs.

4.3 Data analysis and Results

This section contains a detailed review of the data analysis carried out for each measurement, discussing the results and their implications. The subsection 4.3.1 describes the IV curve analysis, the subsection 4.3.2 concerns the dark noise characterization and the subsection 4.3.3 refers to the p. e. response tests.

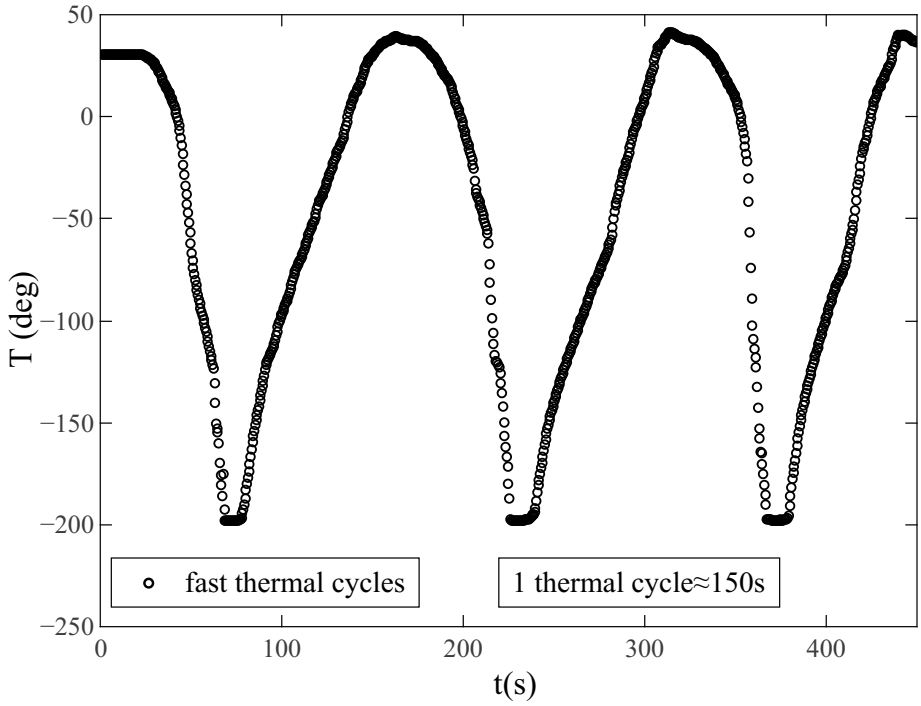

Figure 4.5: Example of the temperature versus time plot for the fast thermal cycles. In this case the time duration of single cycles is less than 3 minutes, instead of 20 minutes for the standard thermal cycles.

4.3.1 IV curve analysis

As mentioned in the section 4.2 the IV curve data is analyzed offline with a Python script. Two examples of the plots generated by the algorithm are shown in figures 4.6 and 4.7.

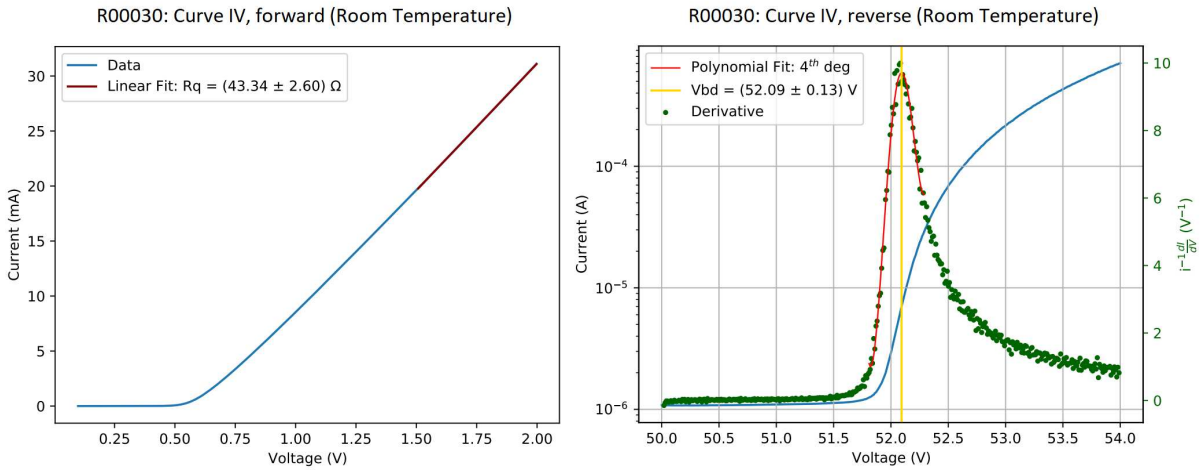

Figure 4.6: Example of IV curve plot produced by the Python script in forward and reverse polarization for the room temperature measurements. The data refers to one of the SiPMs from HPK (model 6075HS-LRQ). The red line represent the polynomial fit of degree 1 in the forward case and degree 4 in reverse case, while the breakdown voltage is highlighted by a vertical yellow line.

The IV curve analysis for the forward region is a linear fit which starts at 1.5 V and ends at the end

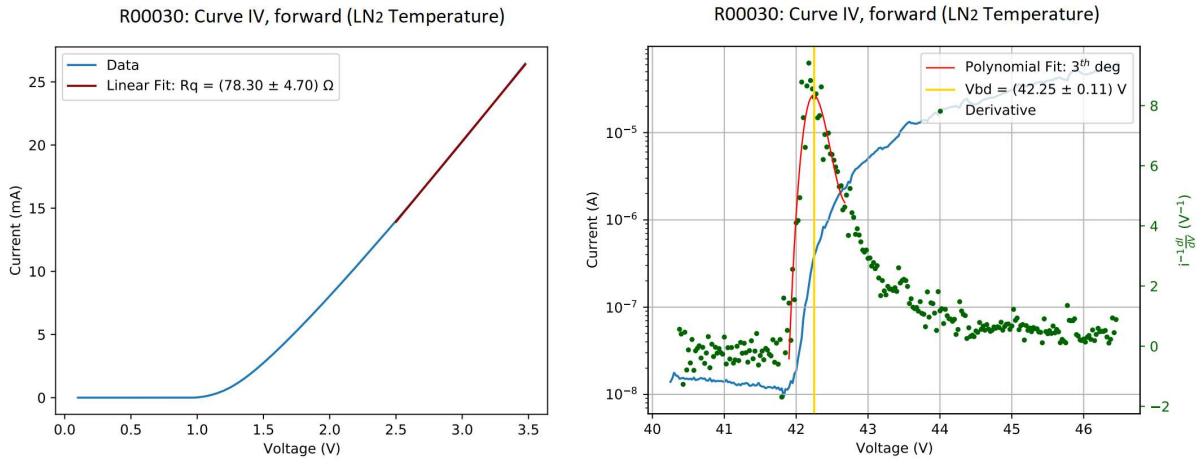

Figure 4.7: Example of IV curve plot produced by the Python script, regarding a SiPM of the 6075HS-LRQ model from HPK (the same as in figure 4.6). This plot reports the IV curve in forward and reverse polarization for the LN_2 temperature measurements. The red line represent the polynomial fit of degree 1 in the forward case and degree 3 in reverse case, while the breakdown voltage is highlighted by a vertical yellow line.

of the curve, this range is equal for all the SiPM models. In the reverse region case, the algorithm numerically calculates the function $I^{-1}(dI/dV)$, which has a maximum at the breakdown voltage. The function is interpolated with a polynomial fit of degree 3 to 5 around the maximum

The measurements at LN_2 temperature are subject to higher relative fluctuations, and the numerical derivative calculation enhances these fluctuations, so the data is often filtered with a moving average before the calculation. The initial number of points in the IV curve at LN_2 temperature is higher than the room temperature case, in this way the averages can be performed without appreciable distortions on the curve shape.

The results of the analysis for the five measurements of each forward(reverse) IV curve are averaged to get the final estimation of $R_Q(V_{BD})$, which are reported in table 4.4.

The relative errors of the values shown in the table are 6% for the R_Q values and 0.25% for the V_{BD} values, the former derives from the tests done in the calibration phase while the second is a conservative estimation, as explained in the following. The calibration phase involved also the measurement of the resistance of the electrical path from the SMU to the SiPM R_{path}. This measurement was performed several times (more than 20) unplugging and re-plugging the connectors between each test, finding a spread of few Ω among due to the different electrical interface created each time the connectors are plugged. The standard deviation calculated for the R_{path} distribution is equal, apart from differences up to 0.2 Ω, to the standard deviation of R_Q, this implies that the error on repeated measurements of R_Q is dominated by the variations in R_{path} among independent measurements. This contribution is cancelled if the measurements are repeated without unplugging the connectors. For the V_{BD} case, the conservative value of 0.25% is chosen since it is above the standard deviation of repeated measurements for all the SiPM models, given that the light conditions for the measurements

model	name	room Temperature		first LN_2 immersion		20^{th} LN_2 immersion	
		$R_Q\,(\Omega)$	$V_{BD}\,(V)$	$R_Q\,(\Omega)$	$V_{BD}\,(V)$	$R_Q\,(\Omega)$	$V_{BD}\,(V)$
6050HS-LRQ	R00020	24.8	52.72	48.0	42.30	48.7	42.43
6050HS-LRQ	R00021	24.6	52.87	47.7	42.40	48.5	42.67
6075HS-LRQ	R00024	36.7	52.05	69.8	41.68	70.4	41.68
6075HS-LRQ	R00029	39.8	52.06	74.9	41.95	other lab	
6075HS-LRQ	R00030	40.1	52.04	76.8	41.98	76.8	41.90
6075HS-LRQ	R00031	36.9	52.05	75.4	41.69	70.9	41.58
6075HS-LRQ	R00032	40.6	51.78	78.9	41.28	85.0	41.67
6075HS-LRQ	R00033	37.8	51.73	68.6	41.64	69.2	41.68
6075HS-LRQ	R00034	39.9	52.28	76.0	41.85	77.0	41.91
Standard	FBK11	36.9	33.12	other lab		90.8	27.11
Standard	FBK13	26.4	33.20	other lab		83.6	27.09
Standard	FBK16	35.3	33.12	97.4	27.11	108	27.11
Standard	FBK17	33.5	33.11	93.0	27.12	97.2	27.14
Standard	FBK18	32.3	33.21	89.2	27.16	95.7	27.16
Triple Trench	FBKTT15	90.3	33.01	313	27.08	314	27.07
Triple Trench	FBKTT16	89.5	33.27	293	27.10	295	27.10
Triple Trench	FBKTT17	82.6	33.12	294	27.11	301	27.09
Triple Trench	FBKTT18	87.1	33.04	352	27.09	321	27.11
Triple Trench	FBKTT19	88.4	33.25	293	27.08	299	27.09
Triple Trench	FBKTT20	78.2	33.07	327	27.09	322	27.08

Table 4.4: Results of the IV curve characterizations at room temperature and at LN_2 temperature for all the received SiPMs. The results at LN_2 temperature are reported for both the first and the 20^{th} immersion, showing no appreciable differences in the parameters after the thermal cycles. The relative errors are 6% for the R_Q values and 0.25% for the V_{BD} values, the former derives from the tests done in the calibration phase while the second is a conservative estimation. The results marked as *other lab* are missing since were performed by other groups of the Consortium.

are similar[1], while the error associated to the fit procedure and the uncertainty related to the step division of the IV curve are negligible compared to this value.

The FBK12 SiPM is not present because the noise level for this sensor was too high to conduct a proper analysis, this could derive from the various failures in the resin surface of the SiPM, which were found after a detailed inspection with an optic microscope. Two of the results for the FBK batch, marked as *other lab* in the table, are missing since the two samples were firstly measured by the Bologna group of the consortium and then sent to the Ferrara team after the third thermal cycle. The sensor R00029 has also missing results for the last thermal cycle, because it was sent to the Bologna group after the third cycle in exchange of the FBK sensors to cross-check the results from the two laboratories, which finally result in agreement with each other.

4.3.2 Dark noise analysis

The analysis of the dark noise characterization is performed offline with two Python scripts called *waveform_analyzer* and *peak_analyzer*, which are related to the search of dark count events and to

[1] For each measurement the black covers are removed and then placed again. This is done manually, so it introduces a human error on reproducing the same light conditions.

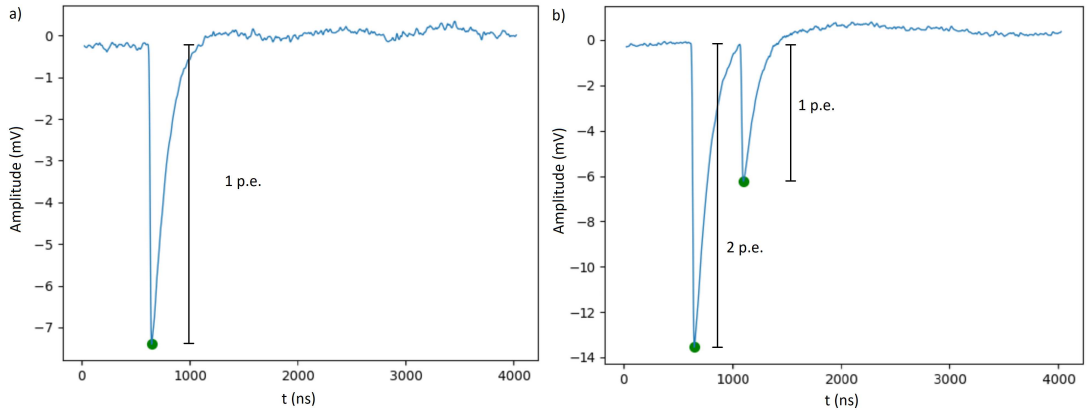

Figure 4.8: From [74], two examples of waveforms recorded by the oscilloscope and analyzed by the algorithm. The data refers to one of the SiPMs from HPK (model 6075HS-LRQ). The plot on the left (a) shows a single dark count signal, while on the right (b) two events are clearly visible. The first is a cross talk between two different SPADs, visible as a peak with double amplitude, while the second is an after pulse event happening during the recharging of one cell, resulting in a smaller delayed peak.

the analysis of the peak distribution, respectively.

As mentioned in section 4.2, the oscilloscope stores two csv files in the internal memory: one with the single waveforms, or frames, and the other with the relative times of the trigger for each waveform with respect to the previous one. The *waveform_analyzer* script analyze the two files to retrieve the single events, rejecting the events related to false triggers. The script evaluates the amplitude and the time relative to the beginning of the measurement for each event, and stores these values in a csv file, which is then used by the other algorithm to evaluate the dark count rate, the cross talk (CT) probability and the after pulse (AP) probability.

For each event, the algorithm produces an amplitude vs time plot and stores it in a folder which is selected by the user, an example of these plots is shown in figure 4.8. The false triggers could be generated by electronic noise in the power line, switching noise or either mechanical vibration of the apparatus. The discrimination of the dark noise events from the others is performed by the user by inspecting all the event plots generated by the algorithm and removing the false trigger events from the list. This procedure was adopted for the first measurement while the script was developing, but was soon dropped to reduce the long time duration of the analysis and to avoid the human errors.

The last version of the algorithm extrapolates the baseline amplitude by averaging the last 300 points of the pre-trigger region, these are the last points before the peak since the trigger is set to falling edge. In order to be categorized as a valid dark count and be stored in the final csv file, a single event must satisfy several conditions. The amplitude of the peak with respect to the baseline must be higher than a threshold (defined by the user) which depends on the SiPM model. Furthermore, this amplitude threshold must be followed by a fast fall in the signal, in a range below the 30 points (the range is almost the same for all the tested SiPMs). The final csv file contains the amplitudes and times of the peaks recognized as dark events, in particular these are the coordinates of the minima of the peak signals in the amplitude vs time plots generated by the script, which are marked with green points in figure 4.8.

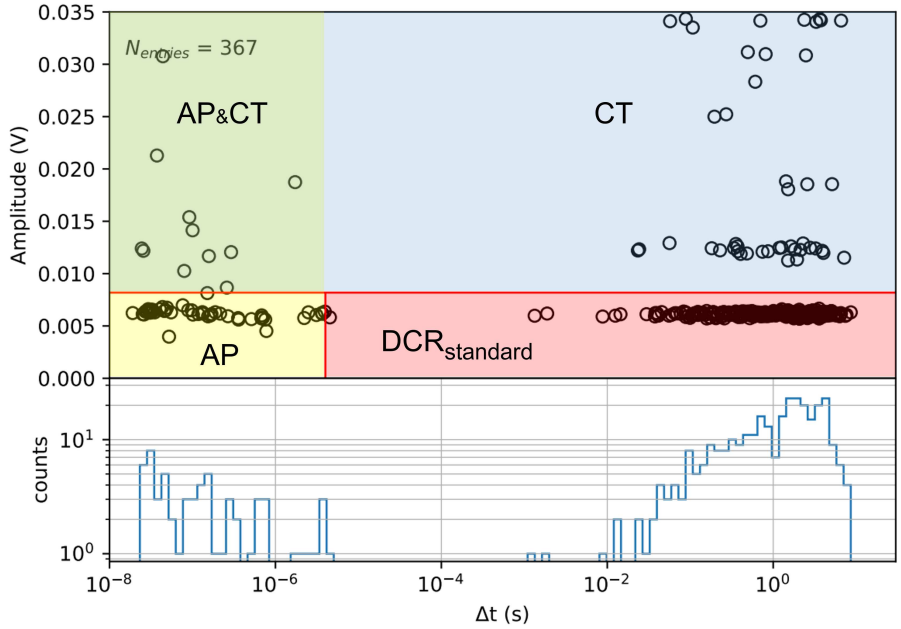

Figure 4.9: Example of an amplitude vs time-delay plot (above) and an event distribution (below) for one of the tested SiPMs. This data set was filtered to remove the burst events, as will be described in the subsection 4.4.

The second script is used to analyze this file and study the amplitude and time distributions of the events to estimate the DCR of the sample, together with the AP and CT probabilities. The algorithm performs a Gaussian fit on the first peak of the amplitude distribution of events to get the amplitude of the single photo-electron peak. The algorithm then generates a plot with the distribution of the event amplitude with respect to the time delay Δt relative to the previous event, as shown in figure 4.9.

All the events contribute to the total DCR of the sample, which is calculated as the total number of counts divided by the total duration of the measurement. The CT events are recognized as the peaks with amplitude above the 1.5 p. e. threshold, while the AP events as the peaks with Δt values below the 5 μs threshold. The results of the DCR, AP percentage and CT percentage measurements for all the tested SiPM model are visible in figures 4.10, 4.11 and 4.12 respectively.

All the SiPMs resulted to be within the DUNE specifications, showing DCR values[2] below the 100 mHz/mm^2, and AP(CT) probabilities below the 5%(15%) threshold. The exceptions are some CT values of the (standard) FBK models and some AP/CT values for the 6075HS-LRQ models from HPK.

During these measurements, the sensors revealed an unexpected behaviour involving fast series of correlated events with amplitude of 1 p. e., called *bursts* of events. The team engaged a series of tests aimed to study this phenomenon, as discussed in the section 4.4.

4.3.3 Photo-electron response analysis

The measurement procedure for the p. e. response analysis is similar to the one for the dark noise characterization, but it requires also a pulsed LED source at 1 kHz. In these measurements, the os-

[2] after burst removal, as will be explained in section 4.4

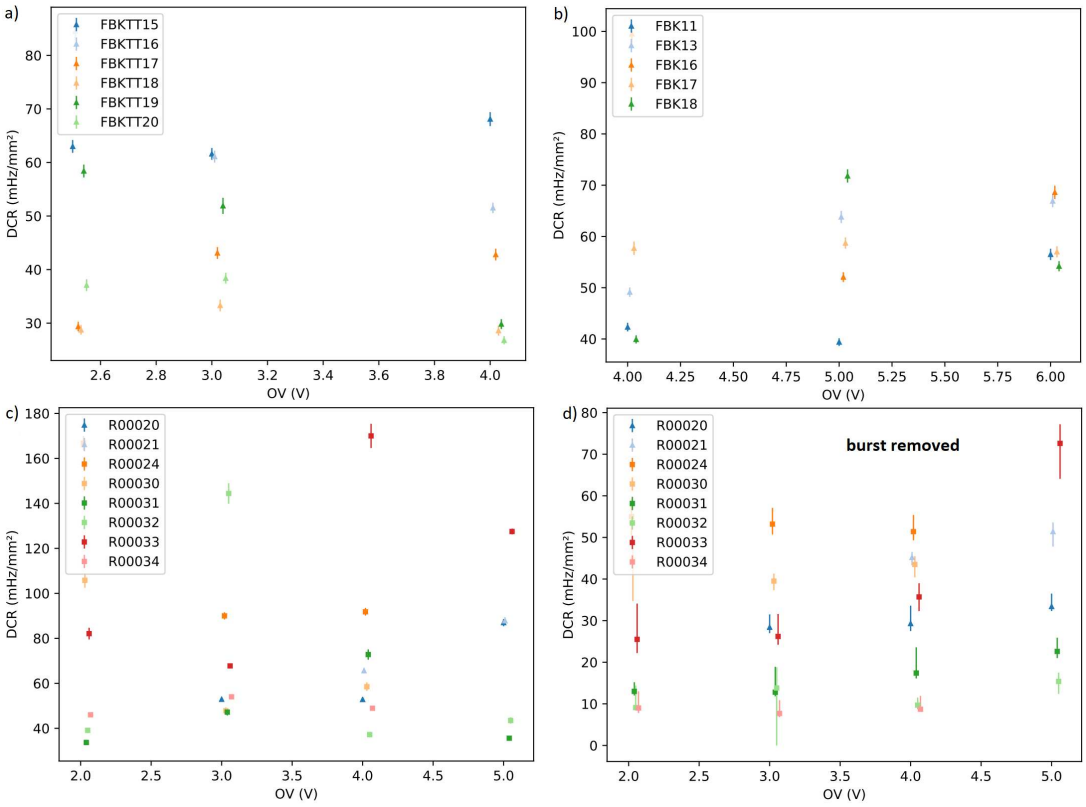

Figure 4.10: Measured DCR values for all the SiPMs tested by the Ferrara DUNE group, the last plot represents the DCR values for the HPK samples without the burst contribution, as will be explained in section 4.4. Here the single SiPMs are identified by their name, the corresponding model can be found in table 4.4.

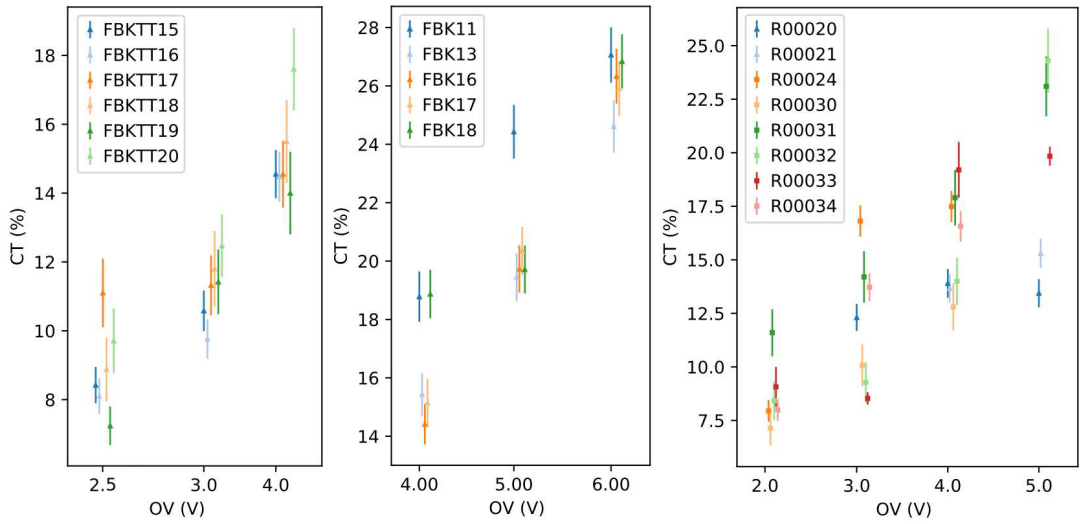

Figure 4.11: Measured CT values for all the SiPMs tested by the Ferrara DUNE group. As will be explained in section 4.4, the CT value drops with the DCR after the burst removal operation. Here the single SiPMs are identified by their name, the corresponding model can be found in table 4.4.

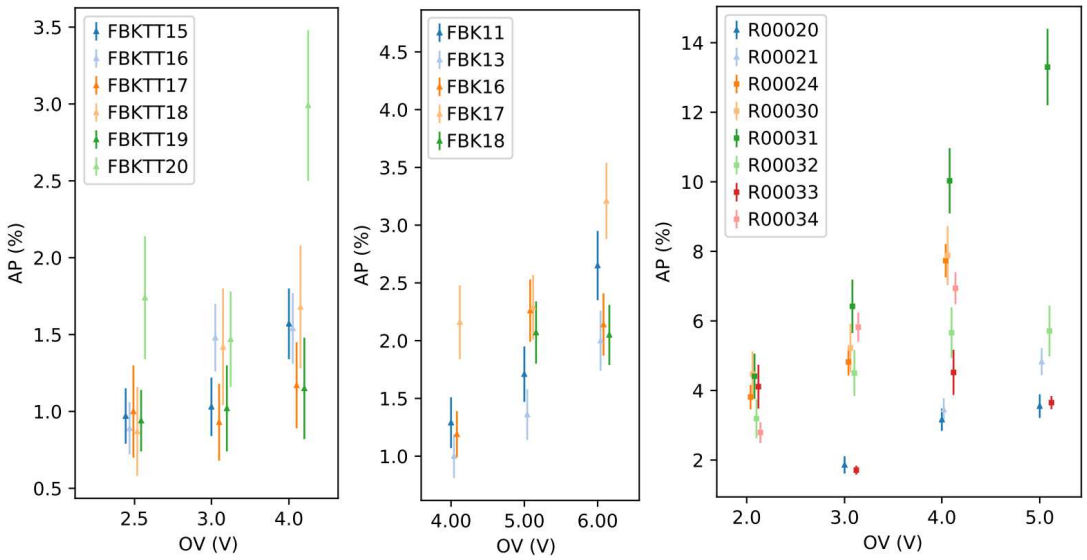

Figure 4.12: Measured AP values for all the SiPMs tested by the Ferrara DUNE group. Here the single SiPMs are identified by their name, the corresponding model can be found in table 4.4.

cilloscope trigger is set to the rising edge of the pulse as described in section 4.2. An example of the oscilloscope signals for a p. e. response measurement is visible in figure 4.13, in this case there is a larger population of events with amplitude higher than 1 p. e. with respect to the dark noise characterization case.

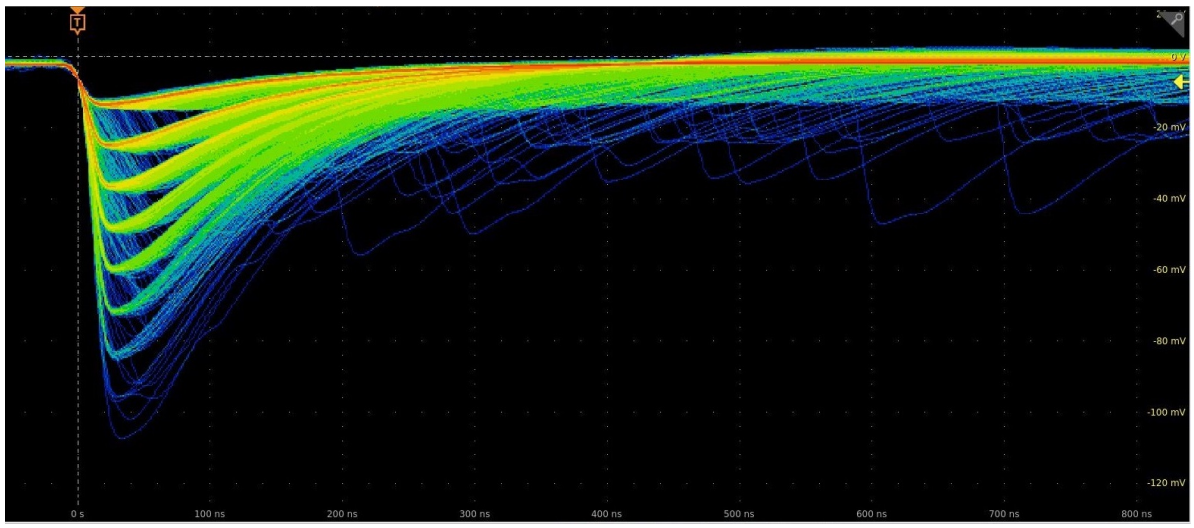

Figure 4.13: Screenshot of the oscilloscope view in *infinite permanence* mode.

The analysis of the p. e. response is performed by the same algorithm of the dark noise characterization (*waveform_analyzer*) for what concerns the extrapolation of the waveforms.

All the event amplitudes and times are stored in a csv data file like for the dark noise characterization case, but the second algorithm is a different version of the *peak_analyzer*, since it does not calculate the DCR nor the CT/AP probabilities. This second script analyzes the amplitude distribution of the events, using the procedure discussed in the subsection 4.3.2 to retrieve the single p. e.

peak amplitude and extending it to the higher amplitude peaks, as shown in figure 4.14.

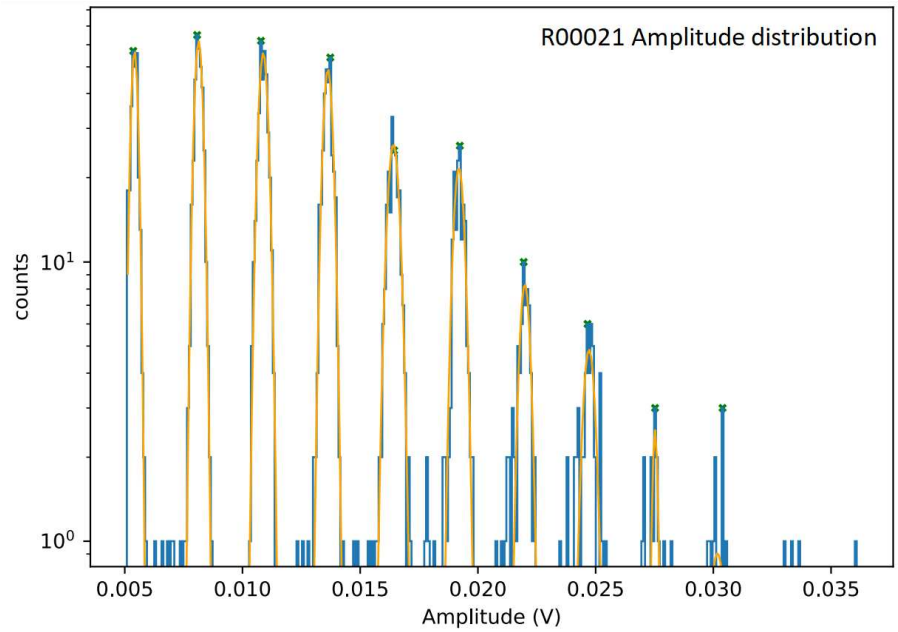

Figure 4.14: Example of an amplitude distribution plot produced by the *peak_analyzer* script for one of the tested SiPMs (HPK 13360-6050LRQ). The yellow lines represents the Gaussian fits on the peaks and the green crosses mark the maxima found with the fit procedure.

The algorithm uses a recursive function to recognize the peaks in the amplitude distribution, then performs a Gaussian fit in a small range around each peak. The script then selects the best peaks according to the combination of peak population and sum of squared residuals of the fit. To ensure the validity of this procedure, the resulting fit parameters are cross-checked by the user after inspecting the amplitude distributions. The Gaussian fit is performed also for the baseline peak, referred to as the 0 p. e. peak, which is the distribution of the baseline amplitudes. This peak is centered in the origin because the trans-impedance amplifier produces an AC output signal.

The Gain is estimated by averaging the amplitudes V_N of the first N peaks, excluding the baseline peak. V_N is the output voltage of the trans-impedance amplifier, this quantity is divided by N to get the amplitude relative to a single avalanche $V_{avalanche}$. To get the adimensional Gain of the SiPM G_{SiPM}, which is the average number of carriers generated in a single avalanche, this value must be divided by the amplifier Gain $G_{amplifier}$ and by the charge of a single electron $e \approx 1.602 \cdot 10^{-19}$ C.

$$G_{SiPM} = \frac{Q_{tot}}{e} = \frac{V_{avalanche}}{G_{amplifier} \cdot e}$$

The amplification stage Gain was measured during the calibration of the system using a reference capacitance and a calibrated source of electrical square pulses, giving the result of $G_{amplifier} = (0.019 \pm 0.002)$ mV/fC.

The figure 4.15 shows an example of Gain estimation for a single SiPM, the results are reported as function of the over-voltage since the measurements are repeated at different V_{OV} values.

The overall results of the Gain estimation are reported in figure 4.16.

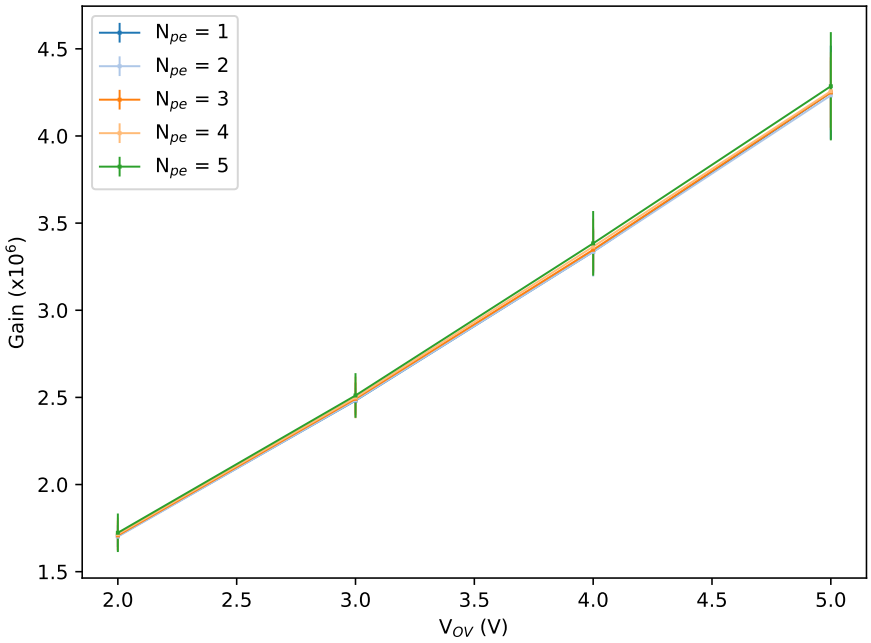

Figure 4.15: Example of Gain versus over-voltage dependence of the first five peaks for one of the tested SiPMs (HPK, model 6075HS-LRQ). This plot shows the linear relation between the adimensional Gain and the over-voltage.

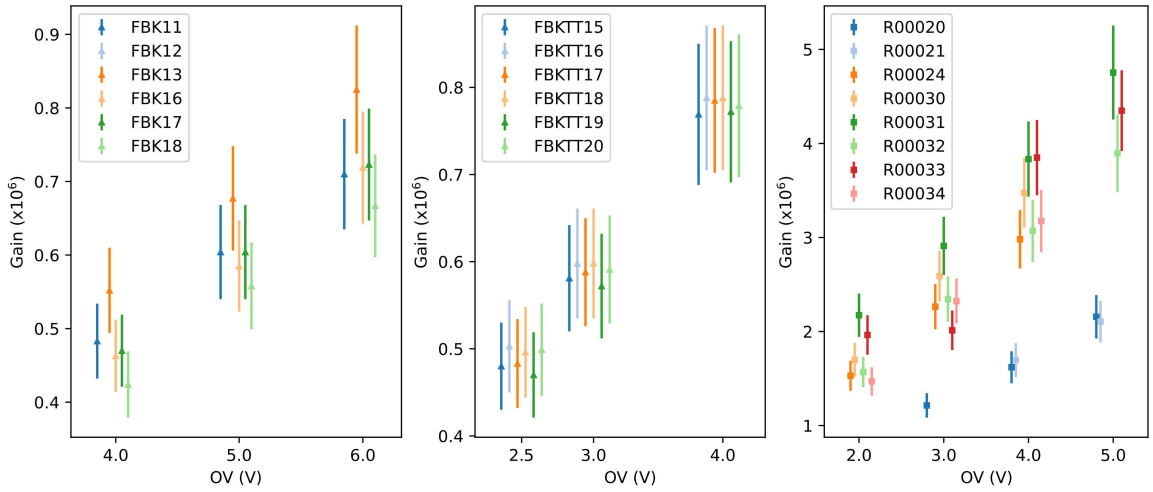

Figure 4.16: Measured Gain values for all the SiPMs tested by the Ferrara DUNE group. Here the single SiPMs are identified by their name, the corresponding model can be found in table 4.4.

As visible in these plots, the measured Gain value increases linearly with the over-voltage for all the tested SiPMs.

The Gain results revealed to be all within the DUNE and ProtoDUNE specifications, for all the over-voltages and all the tested SiPMs.

The SNR value is estimated involving the distance-to-width ratio of the amplitude distribution peaks, as reported in the following equation:

$$SNR = \frac{V_{\text{avalanche}}}{\sqrt{{\sigma_{0\,\text{p.e.}}}^2 + \sigma^2_{1\,\text{p.e.}}}}$$

where $V_{\text{avalanche}}$ is the distance between the 1 p. e. peak and the baseline peak, this corresponds to the amplitude of the 1 p. e. peak since the 0 p. e peak is centered in zero. $\sigma_{0\,\text{p.e.}}$ and $\sigma_{1\,\text{p.e.}}$ are the standard deviations of the 0 p. e. peak and of the 1 p. e. peak, respectively.

The figure 4.17 shows the results of the SNR estimation at different over-voltages.

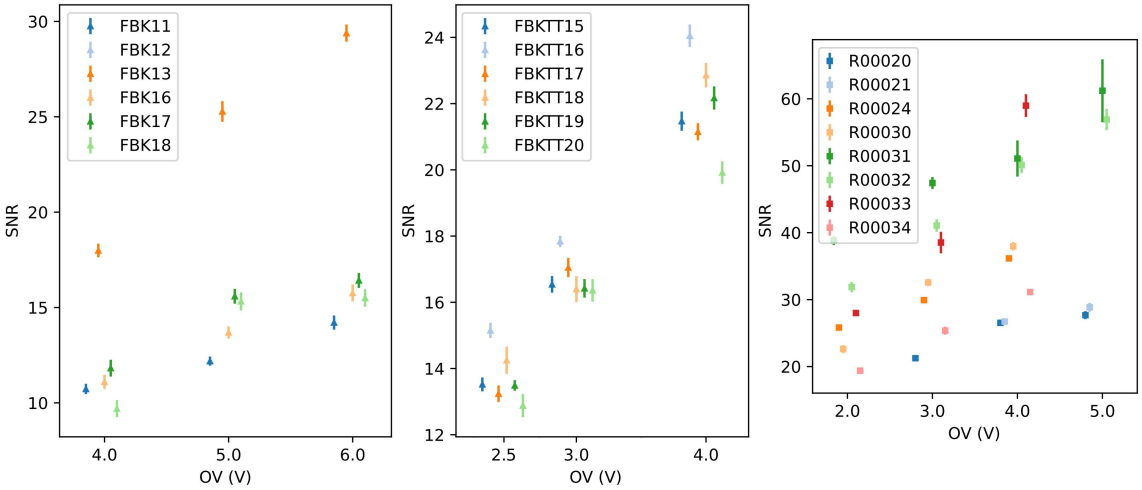

Figure 4.17: Measured SNR values for all the SiPMs tested by the Ferrara DUNE group. Here the single SiPMs are identified by their name, the corresponding model can be found in table 4.4.

4.4 Burst phenomenon

Even in all the SiPMs characterized with the procedure described in previous sections are within the DUNE and ProtoDUNE specifications, an unexpected behaviour was found in all the sensors during the dark noise characterization: the samples show quick trains of correlated events, the origin of which is yet to be understood. This phenomenon was not reported in literature at the time, so the Ferrara team published an article about it [74], choosing the name *bursts* for these set of correlated events.

Tests and studies of the burst phenomenon went on involving also the participation of other groups of the PDS Consortium and of the two vendors, but neither the cause nor the underlying physical mechanism are known so far. This section covers the burst phenomenon, describing the tests carried out by the Ferrara team to study this behaviour.

4.4.1 Burst definition

The figure 4.9 shown in the previous section to explain the data analysis is not a real example of the Amplitude vs time delay distribution found during the dark noise characterization. More precisely, it is the distribution of a filtered data set, in which the burst events are removed with a custom algorithm, as will be explained in subsection 4.4.2. The standard dark noise characterization foreseen

by the test protocol was outlined expecting distributions like the one in figure 4.9, with a DCR peak in the range $[1-10]$ Hz. A real example of Amplitude vs time delay distribution is visible in figure 4.18, here the whole set of events is used without any filter. The sensors present additional events outside

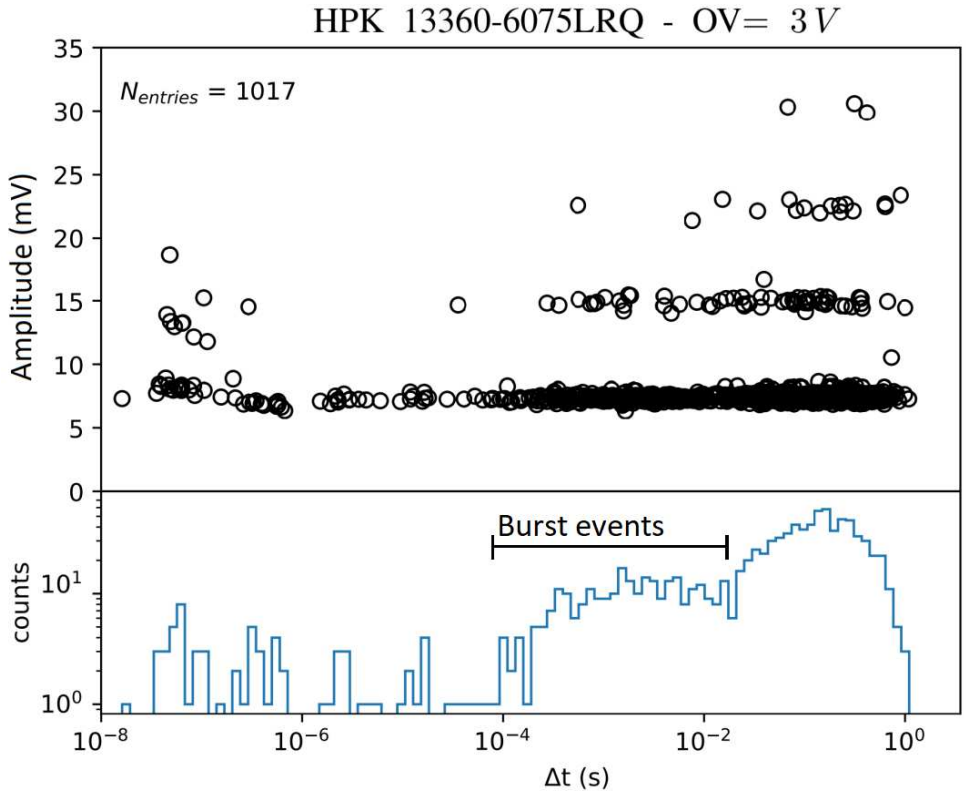

Figure 4.18: From [74], example of an amplitude vs time-delay plot (above) and an event distribution (below) for one of the tested SiPMs, these are produced using all the (unfiltered) data.

the $[1-10]$ Hz range of frequencies which are too fast for being primary dark counts and too slow to be after pulses. Another distribution is visible in addition to the CT, AP and primary (or standard) DCR events: a set of correlated events with 1 p. e. amplitude and time delays in the $[0.1-1]$ ms range is distinguishable from the other clusters. The 2 p. e. amplitudes are also populated in this range because the CT probability is the same as for the DCR events, so as the AP probability, as merges by the event by event analysis carried out by the team.

The presence of such bursts is visible also from figure 4.19, which shows the time delay Δt relation with the event ID N_{ev}, where Δt is the time elapsed from the last event. The Δt value drops in correspondence of one burst occurring, growing back to the expected time scale as the burst ends.

The following subsection describes the analysis carried out by the Ferrara team to isolate and study the burst events.

4.4.2 Burst analysis

The team developed a custom algorithm, starting from the *peak_analyzer* script, to distinguish chains of events with short Δt from the primary dark count events, separating the burst cluster from the primary DCR one. The conditions to meet for burst recognition are highlighted in the sketch in

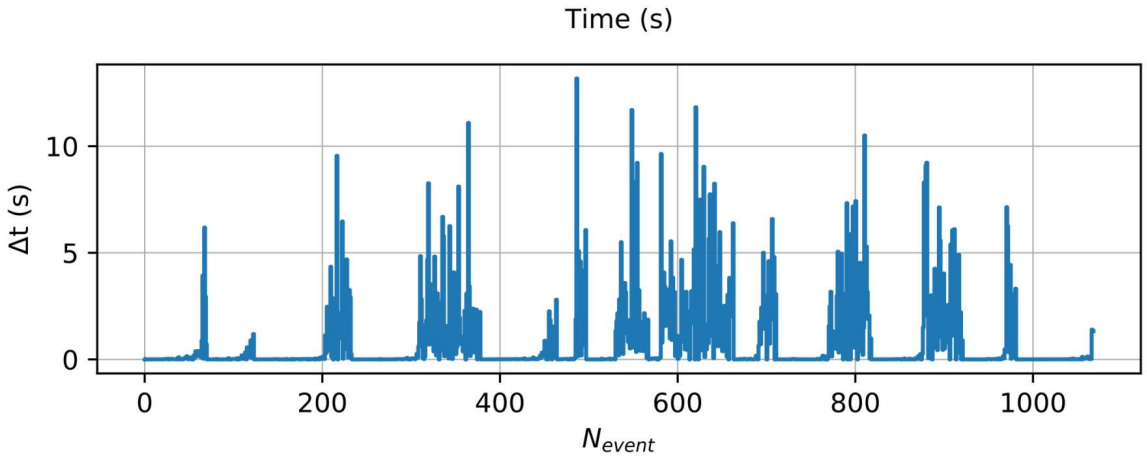

Figure 4.19: From [74], plot of the time delay Δt between events versus the event number N_{ev}, for the same sensor used as example in figure 4.18. The bursts are visible as valleys where the time delays Δt drop below the 0.1 s threshold for many consecutive events.

figure 4.20. The set of events must have a time delay below a certain threshold $\Delta t_{max} = 0.1\,s$ to avoid

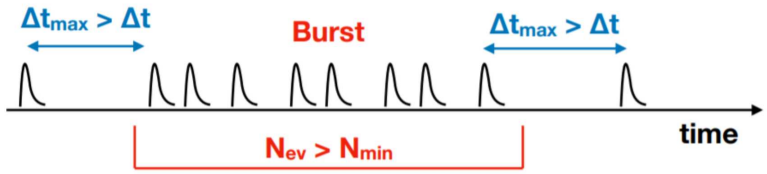

Figure 4.20: Sketch representing a single burst, the Δt value is the time delay between consecutive events while the N_{ev} value is the number of events in the burst.

the inclusion of primary DCR events, and a number of elements N_{ev} above $N_{min} = 5$ to avoid DCR + AP events. This allows to remove offline the burst cluster from the distribution of the events, as visible in figure 4.9.

The algorithm was also used to find some common features by studying the isolated burst distribution:

- the first event of the burst tend to have an amplitude above 4 p. e., as visible in the distribution reported in figure ;
- the time delay between consecutive events in a burst lies in the [0.1 − 10] ms range, and it returns to the ∼ 1 s level with an approximately exponential growth as the burst ends;
- the average number of events within a burst is ∼ 100, as visible in figure 4.21;
- a single burst of events lasts generally few tenths of a second.
- all the peaks in the train of events are distributed around the 1 p. e. level, except for the starting event as discussed in the first point of this list. The exception stands also for the CT and AP events, which are still present.

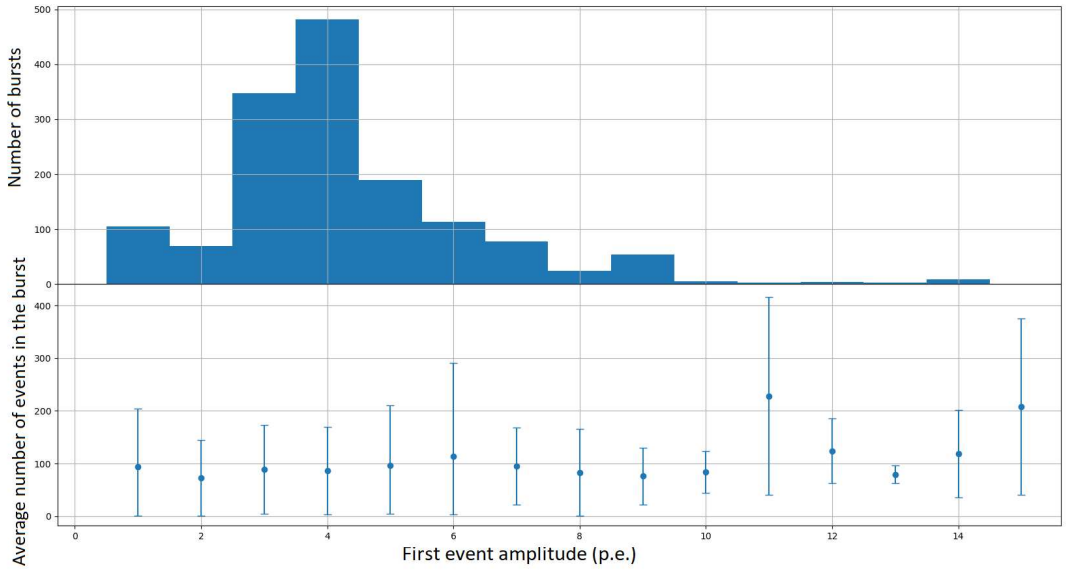

Figure 4.21: From [74], histogram of the number of bursts (top) and distribution of the number of event in the bursts (bottom), versus the amplitude of the first event in the burst.

- none of these parameters show evidences of being correlated to the IV characteristic parameters (R_Q and V_{BD}).

4.4.3 Additional tests

One of the first tests performed to study the burst phenomenon (and not included in the starting DUNE characterization protocol) was a coincidence test, and it was induced by the suspect that the bursts may have a cosmic rays genesis. The experimental setup is similar to the one for the dark noise characterization but the metallic box hosts two SiPM, facing each other as visible in figure 4.22, and the trigger of the oscilloscope is set on the falling edge of one of the two sensors. Initially the

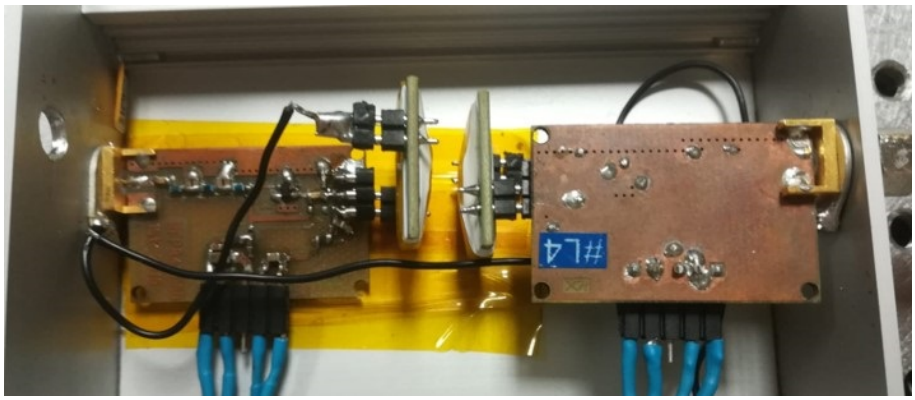

Figure 4.22: Setup for the measurement of the coincidence events. The two SiPMs are at a distance of ~ 0.5 cm facing each other, each one is covered with six layers of Teflon tape and one layer of Kapton tape.

team tried a measurement without shielding the two SiPMs, with the result of a 5% to 8% of optical CT probability between the two samples. Then each sensor was optically shielded with six layers of Teflon tape and one layer of Kapton tape, reducing the aforementioned reciprocal CT to a negligible percentage. The tests were performed for two SiPM models, one per each vendor, in two configurations: with the faces of the sensors parallel to the ground (horizontal arrangement) and with the faces perpendicular to the ground (vertical arrangement). The results are an average frequency of coincidences of $f_{\text{horizontal}} \sim 3.3\,\text{mHz}$ for the horizontal arrangement and $f_{\text{vertical}} \sim \frac{f_{\text{horizontal}}}{4}$ for the arrangement arrangement for both the SiPM models. Although these measurements could give some hints of cosmic ray influence on the SiPM dark counts it does not prove them as the cause of the burst phenomenon, more tests are needed before drawing conclusions.

The team expanded the pool of tested SiPM models to check if also these additional samples show the burst phenomenon. The additional SiPMs belong to five commercial HPK models, and one FBK model of the same type used for the *DarkSide* experiment. The measurements where the standard DCR measurements (with and without the offline burst removal) used for the standard DUNE split and the results are reported in the table 4.5, together with the main characteristics of each of the tested SiPM model.

model	pitch	N_{cells}	Package	units	bursts
HPK 13360-6050LRQ*	50 μm	14331	surface mount type	14	yes
HPK 13360-6075LRQ*	75 μm	6364	surface mount type	20	yes
HPK 13360-6025CS	25 μm	57600	ceramic	2	no
HPK 13360-6055CS	50 μm	14331	ceramic	3	no
HPK 13360-6075CS	75 μm	6400	ceramic	2	no
HPK 13360-6050VE	75 μm	14331	surface mount type	2	yes
HPK 14160-6050HS	50 μm	14331	surface mount type	2	yes
FBK NUV-HD-STD*	30 μm	37300	chip on board	11	yes
FBK NUV-HD-TT*	50 μm	11188	chip on board	12	yes
FBK NUV-HD-DS**	30 μm	106000	chip on board	2	no

Table 4.5: Characteristics of the different SiPM models have been tested by the Ferrara team. * = DUNE split, ** = DarkSide split. The 5^{th} column reports the number of tested sensors, while the last column reports if the SiPM generates bursts of events. All sensors have the same area of $36\,\text{mm}^2$ except for the FBK NUV-HD-DS whose area is $96\,\text{mm}^2$. The NUV-HD-DS sensors were tested at $V_{\text{OV}} = 5\,\text{V}$, the HPK 13360-6075CS and FBK NUV-HD-STD at $V_{\text{OV}} = 4\,\text{V}$ and the others at $V_{\text{OV}} = 3\,\text{V}$.

The pitch of the single SPADs do not influence the presence of bursts for the tested SiPMs, which is absent in the sensors with ceramic package.

The last test to mention are the underground measurements, which involved a subgroup of two researchers, one from the Ferrara team and one from the Bologna team. To study more in detail the possible cosmic nature of the burst phenomenon, the two researchers was sent to perform a 2-days test campaign at the *Laboratori Nazionali del Gran Sasso* (LNGS) underground research facility. Due to their particular location under the Gran Sasso mountain, the LNGS laboratories dispose of a natural cosmic ray shield made of almost homogeneous rock (height of the shield: 1.4 km, H_2O equivalent:

3.8 km). The two experimental setups used for these measurements are the ones used for the previous dark noise characterizations, respectively in the Ferrara and Bologna laboratories, so they share the same general setup configurations but make use of different components.

Each researcher brought one HPK and one FBK sensor from the DUNE split, for a total of four sensors, and performed acquisitions also with a radioactive Thorium source ^{232}Th. During the test campaign, each SiPM was measured many times at different V_{OV} values and with various acquisition time windows, from around 10 minutes to 2 hours (chosen by adjusting the number of frames in the oscilloscope). For the tests with radioactive source, the SiPMs were placed at ~ 10 cm from the ^{232}Th sample, the acquisition time windows are all equal to 20 minutes and the V_{OV} value is always the same. This choice stems from the time restrictions, which limited the total number of tests, and the general guideline was to maximize the population on few type of measurements instead of performing many tests with low statistics.

The data taken during the tests at the LNGS laboratories was later analyzed offline, giving the following results:

- the burst contribution is present also underground;
- the rate of the bursts, that is the inverse of the average time between the starting events of two consecutive bursts, is reduced roughly by a factor 4, similar to the difference between the number of coincidences in the horizontal and vertical arrangement tests described before;
- the DCR value (either with or without the burst contribution) is reduced approximately by a factor 3.5, as visible in the amplitude versus time delay distribution reported in figure 4.23;
- the percentage of events which fall within a burst is almost the same as at the surface, so as the average frequency ($[0.1-10]$kHz) and number of events inside the single bursts (~ 100);
- the DCR value (either with or without the burst contribution) grows by a factor ~ 3.5 when the sample is close to a radioactive source, while the rate of the bursts raises by a factor ~ 4 and a single burst contains 100 to 1000 events.

These are preliminary results and have not enough statistical significance to claim reliable interpretations, but they point to the possibility for burst to be a product of natural radioactivity. Further investigations on the burst phenomenon are currently going on, while these preliminary results were presented in various scientific conferences with specific talks and posters (in addition to the aforementioned article [74]).

4.5 Conclusions

The characterizations performed in the pre-production phase revealed that all the tested SiPMs are within the DUNE and ProtoDUNE specifications, in terms of breakdown voltage, Gain, DCR, AP and CT percentages.

The unexpected burst phenomenon, encountered during the dark noise characterizations at LN_2 temperature, was studied by means of *ad hoc* analyses and tests, engaging also the collaboration of

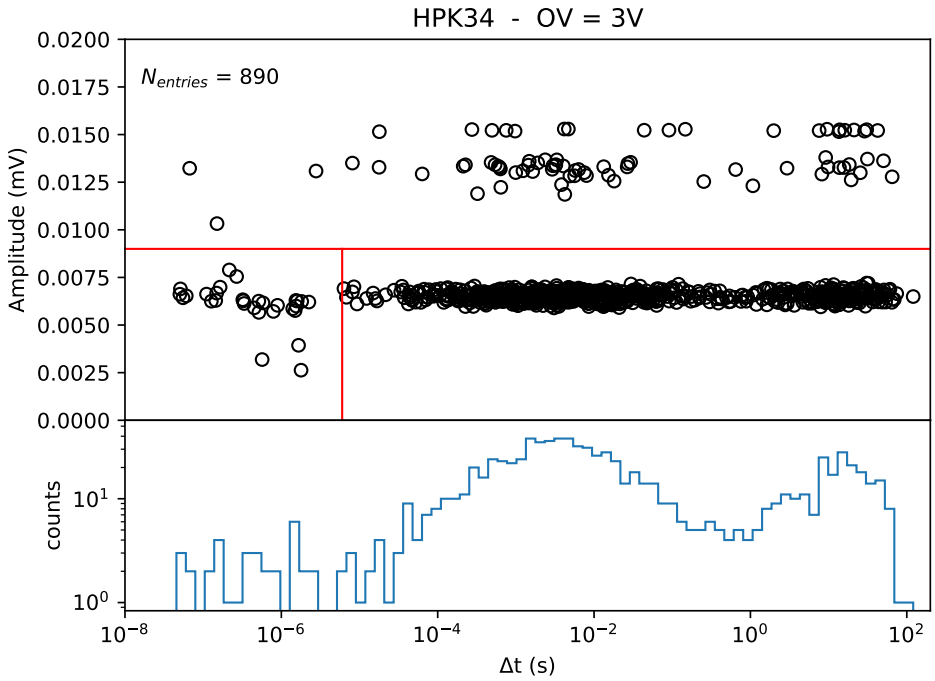

Figure 4.23: Example of an amplitude vs time-delay plot (above) and an event distribution (below) for one of the dark noise characterization measurements at the LNGS laboratories. The red lines divide the DCR, cross-talk and after pulse regions. As visible by the proportions of the peaks in the event distribution, the burst cluster is more populated with respect to the measurements taken at the university laboratories.

other members of the Consortium and of the two vendors. Neither the cause nor the mechanism of this behaviour are currently understood, but the SiPMs are within the DCR specifications even with the presence of these fast trains of events, further investigations are currently going on to better understand this phenomenon.

Most of the measured parameters are similar for the two FBK models, as reported in section 4.3. The triple trench technology features a lower CT probability and a higher SNR value with respect to the standard FBK SiPMs, but the second value depends on the noise conditions of the single measurements[3]. For the HPK case, the results reported in section 4.3 show that the high pitch model (6075HS-LRQ) features a higher Gain with respect to the low pitch model (6050HS-LRQ), as well as a higher signal-to-noise ratio. The high pitch model presents also a higher AP probability, but this parameter is of secondary importance with respect to the Gain.

As described in chapter 2 and 3, this initial phase of characterization of single SiPM was followed by a set of tests performed in active ganging mode on 8 strips of 6 sensors each. In these tests the signals from the 48 SiPMs were all collected by a cold amplifier into a single channel. The results of these measurements left two SiPM models (one per vendor), which shown best performance in active ganging mode, as final choice for the DUNE-FD1 and ProtoDUNE-SP2 photon detection systems. For

[3]The FBKTT SiPMs were tested with the same experimental apparatus w.r.t. the standard FBK case, but with different environmental noise conditions

the HPK vendor, the chosen SiPM model is the one with 75 μm pitch and high R_Q value (6075HS-HRQ), while for the FBK vendor, the chosen model is the triple trench (FBKTT) [37]. The Consortium down-selected also the working point of each SiPM model in terms of V_{OV} (= 4 V for the FBK model, = 3 V for HPK).

Chapter 5

Massive SiPM characterization

As mentioned in chapter 3, after the single unit characterization phase (and ganging mode tests), the SP-PDS consortium has selected the best choice for the ProtoDUNE and DUNE SiPM models in terms of dark (and correlated) noise, SNR, Gain and PDE at LN_2 temperature. The down-selection ended leaving one model for each vendor, then the pre-production phase continued for both the vendors involving only these models[1]. The selected SiPM models are reported in table 5.1.

vendor	model	V_{OV}
Hamamatsu photonics K.K.	6075HS-HRQ	3 V
Fondazione Bruno Kessler	Triple Trench	4 V

Table 5.1: The two SiPM models selected by the DUNE PDS Consortium, we refer to table 4.1 for a detailed description of each model. The last columns reports the selected operating over voltage V_{OV} for each model, which corresponds to a PDE of 50%.

This phase involved the production of the remaining part of the 8000 SiPMs (4000 per vendor), that must be mounted in 30 X-ARAPUCA modules in ProtoDUNE-SP Run II. This phase ended in September 2022 and was followed by the mass test campaign phase, which concerns the SiPMs for the first DUNE-FD module (abbreviation *FD1-HD*) and counts a total of 288000 sensors.

The consortium engaged a massive SiPM test campaign to validate the expected behavior of all the detectors for both the ProtoDUNE and the DUNE productions, the ProtoDUNE SiPM characterization campaign ended in September 2022 while the DUNEFD1-HD SiPM characterization campaign is still ongoing. The procedure involves a quicker characterization w.r.t. the single unit tests mentioned in chapter 3, still covering the most important parameters for LArTPC applications (i.e. DCR and V_{BD}). The DCR is important to check that the background signals during normal operation are within the expected range, while the V_{BD} sets the working point of the sensor. It is important to know the exact V_{BD} value of each SiPMs since they will be placed in arrays of 6 units inside X-ARAPUCA modules, and all the sensors inside a single module are ganged together at the same voltage bias. Selecting the single arrays according to their V_{BD} values permits to reduce the spread inside a single module and provide almost the same V_{OV} to all the SiPMs.

[1] The 6075HS-HRQ was not present in the SiPM split tested in Ferrara.

The choice of the aforementioned characterization procedure stems from a time optimization, since the validation has to be performed on a high number of samples. The GAIN and SNR measurements are not performed and the whole tests are not repeated at different overvoltages. The dark noise measurement is not based on a single event analysis and it is not possible to distinguish after pulse or cross talk contributions. On the other hand, a complex experimental setup was developed to automatize this procedure, making possible to test up to 120 SiPMs in parallel in one measurement session. This apparatus was developed by the the Ferrara members of the consortium in collaboration with the Bologna ones. After the ProtoDUNE production validation with the Ferrara and Bologna setups, also the Milano Bicocca, Granada and Prague Universities joined the mass-test group, building their own replicas of the apparatus. In this way, a total of five mass-test setups will be involved in the validation of the DUNE production.

This chapter contains a detailed description of each component of the aforementioned experimental apparatus developed for massive SiPM characterization, i.e. the CACTUS (*Cryogenic Apparatus for Control Tests Upon SiPMs*) apparatus.

5.1 The CACTUS apparatus

CACTUS is a complex apparatus for automatic SiPM characterization at both room temperature and liquid nitrogen temperature. The main components, as visible in figure 5.1, are reported in the following list:

- a dewar filled with liquid nitrogen and a mechanical stage for controlled immersions
- two custom electronic chains for low-noise measurements of IV and DCR respectively
- PC station to control the tests and visualize the results
- dark box for DCR measurement and LED controlled illumination system for IV, which surrounds all the electronics.

The SiPMs are arranged in PCBs containing six units, in a common cathode configuration as visible in figure 5.2. These PCBs are $12 \times 0.8\,\mathrm{cm}^2$ boards in which the sensors are mounted at 1.4 cm distance from each other. Each PCB hosts the SiPMs on the front and a QR code or data matrix that encodes an ID on the back, together with 8 pins: one for the common cathode, one for the common ground and another six for the anodes. These PCBs are mounted in groups of five units in the *cold boards*, which are custom ASICs designed to work at LN_2 temperature. Each cold board contains a connection with a stabilized DC power supply to bias the SiPMs and a Pt100 temperature sensor, as visible in figure 5.3.

These boards are bound to the lid of the dewar and to the *warm boards*, the whole structure is anchored to the mechanical stage and slides with it during immersions and thermal cycles. The stabilized DC power supply mentioned above is a source meter (Keysight B2962A 6.5 Digit Low Noise Power Source) and it will be referred to as the SMU (*Source Meter Unit*).

The warm boards are placed above the lid and they work at room temperature. Each warm board is connected to a cold board by a set of micro-coaxial cables and it hosts the amplification stages, an

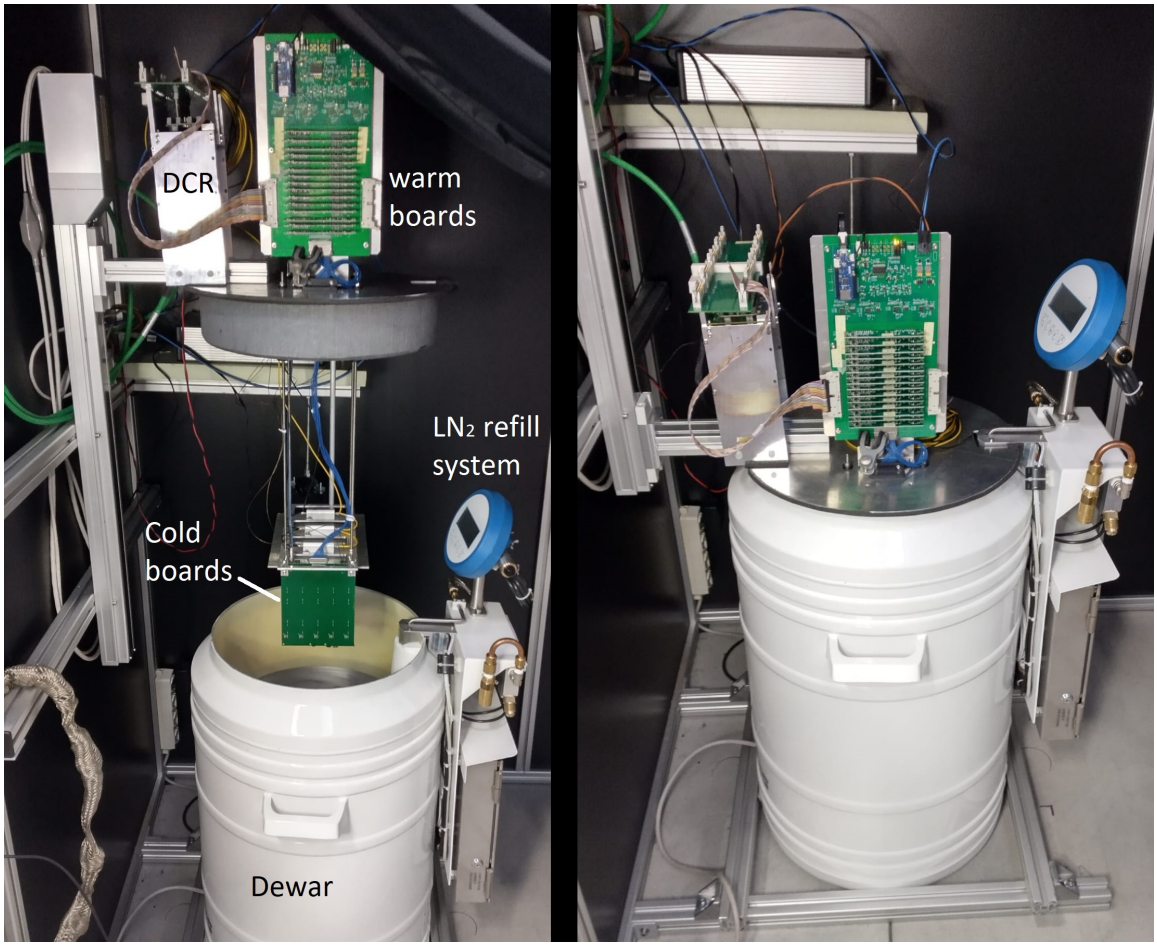

Figure 5.1: Two pictures of the dark box of the CACTUS apparatus, on the left the slider of the mechanical stage is at its highest position, while on the right the slider is at the lowest position. At the lowest slider position, all the SiPMs are immersed in LN_2 and the dewar is closed. The single components are labelled in the left picture. The PC station, the power supplies and the controllers of both the DCR system and the mechanical stage are not visible in this picture, since they are placed outside the dark box.

Figure 5.2: Picture of the front of one PCB used in the CACTUS apparatus. The *G1* pin is the common ground, the *K* pin is the common anode and the pins *A1*-*A6* are the six anodes of the sensors. The labels *S1*-*S6* mark the six sensors in ascending order.

offset compensation section and an ADC. Inside the warm board, the signal from each SiPM passes through a trans-impedance amplification stage and then it is split in two channels. One of the two channels is connected directly to the DCR system, while the other is amplified and digitized before being redirected to a Raspberry board for the IV curve measurement.

The Raspberry communicates via TCP protocol through LAN connection with the SMU, to set the voltage for each point of the IV curve. It also retrieves and process the data from the warm boards in order to generate the IV plot and calculate the results for each measurement on each SiPM. The

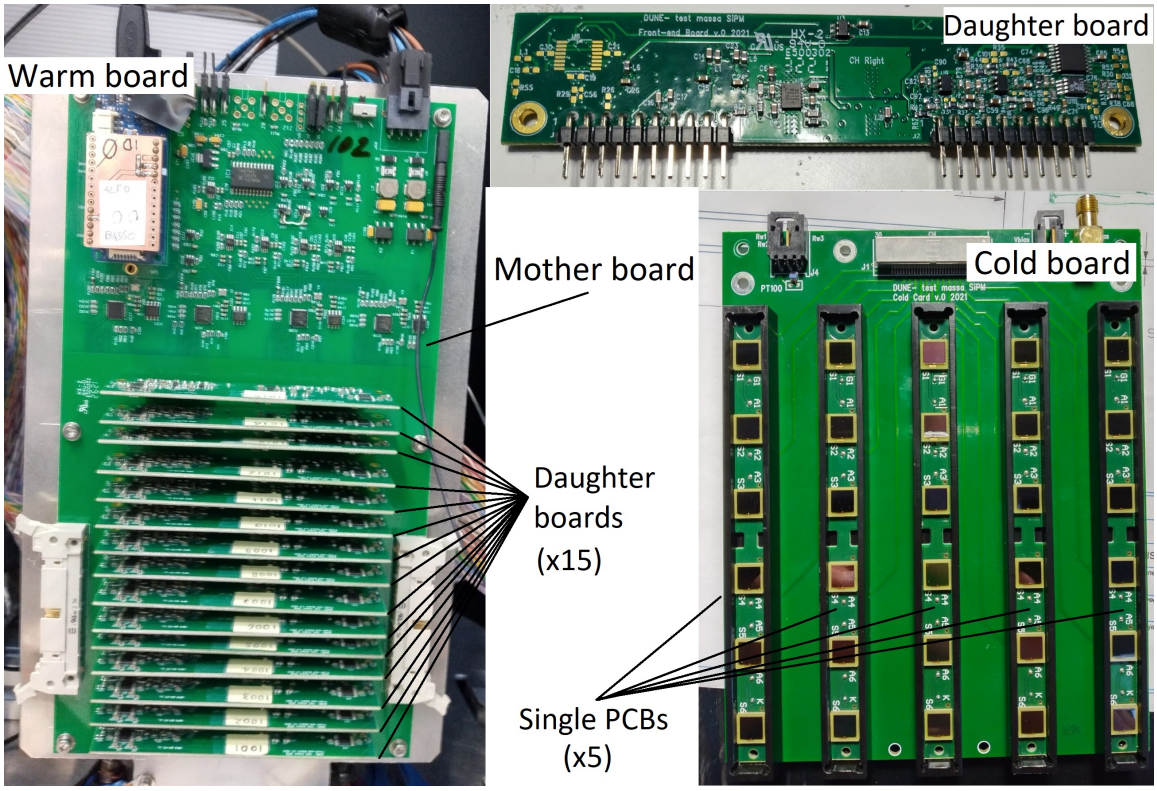

Figure 5.3: Pictures of a warm board (left), a single daughter board (top) and a cold board (bottom). The warm board is divided in a mother board and 15 daughter boards and is controlled by an Arduino controller, while the cold board hosts the SiPMs, arranged in 5 PCBs of 6 units each.

Raspberry also communicates via UDP protocol to the PC station, in order to receive instructions before starting the IV measurement and send back the results once the analysis is done.

For the DCR measurement the electronic chain is less complex, since the analog signals are simply sent to the DCR sub-systems through flat cables. The DCR sub-systems is a FPGA-based counter with charge discriminator which is used to count the events of each SiPM in a fixed time window. This system is connected to the PC via LAN connection and they communicates via TCP/IP protocol. The communication, the retrieval of the results and the data storage are all handled by a python script running in the PC.

The PC station runs a LabVIEW VI (*Virtual Instrument*), which controls the mechanical stage, the Raspberry operation, the DCR system and the interactions with the user. The user can have full control on the tests in manual mode or either very shallow interactions with the interface in automatic mode. The LabVIEW VI also handles all the side tasks like temperature monitoring, parameter setting, data parsing and storage, result visualization, control of led luminosity and so on.

5.1.1 Cold boards

The cold boards represent the cold stage part of the CACTUS electronics. Each of these four boards can host up to five PCBs, for a total of 30 SiPMs, and connects them to the warm electronics (i.e. the warm boards), as visible in figure 5.1.

The connection is based of micro-coaxial cables (*Samtec FCF8-30-01-L-30.00-S*), the choice of these cables stems from the fact that they have a high density and they are suited for both low-noise and cryogenic applications.

The cold boards are connected in a daisy chain configuration to the SiPM bias line, so there is a small voltage drop between two consecutive boards. These drops are taken into account with a correction factor introduced in the Python script running in the Raspberry, which handles the measurement and analysis of the IV curve. This correction factor will be discussed more in detail in the sub-section 5.2.1.

The bias line within each board is connected in a daisy chain configuration to the five PCBs in common cathode configuration, so the voltage drops by small amounts by passing from the first to the last PCB. These drops turned out to be negligible for the R_Q and V_{BD} estimations and do not introduce any correction factor in the script.

Lastly, each cold board contains a Pt100 sensor to monitor its temperature.

5.1.2 Warm boards

Each of the four warm boards of the CACTUS system is a PCB controlled by a micro-controller (ARDUINO MKR Zero) and it hosts the warm amplification stage together with a zero-calibration section. The choice of the ARDUINO MKR Zero stems from its low cost compared to the performances: the 48 MHz clock speed processor of the micro-controller (SAMD21 Cortex®-M0+ 32bit low power ARM MCU) permits to perform multiplexed tasks introducing a negligible delay for the time scale of the single IV point measurements.

A single warm board is composed of 15 removable *Daughter boards* connected to a *Mother board*, as visible in figure 5.3, and each daughter board contains the amplification stages for two SiPMs. This modular structure permits to replace the least amount of hardware if a single channel develops some failures in the amplification stage, or to use custom daughter boards to get different Gain values.

The working principle of a warm board is quite simple and is reported in the following. The current signal coming from each micro-coaxial cable is amplified and converted to a voltage signal by a trans-impedance amplifier (feedback resistor $R_f = 50\,\Omega$) and then it is split in two lines: one for the IV characterization and the other for the DCR measurement. Here we will focus on the IV line, since the DCR analog signal is simply redirected as output through flat cables and sent directly to the DCR subsystem, which is described in details in the sub-section 5.1.4. The current signal of each SiPM is firstly amplified by a factor G_1 and then split in two channels, one of which passing through another amplification stage of Gain G_2. These are the so-called *high Gain channel* and the *low Gain channel*, the names stem from the different Gains (G_1 for the low Gain channel and $G_1 \cdot G_2$ for the high Gain channel) of the operational amplifiers. This choice was made to enhance the dynamic range of the apparatus, because the signal in the low current region of the reverse IV curve is usually 2 to 3 orders of magnitude smaller than the signal in the avalanche region. The high Gain channel gives a better measurement in the low current region, but it saturates quickly at high currents, while the low Gain channel is less precise in the low current region but it can measure higher currents. The current measurement of every point of the IV curve is obtained combining these two signals where is possible,

and using the low Gain signal only when the other is saturated. In forward polarization the difference between high and low signal magnitudes is more prominent, but the usage of both channel serves only for a better curve plot reconstruction, as the region of interest (the linear part of the IV curve) can be measured with the low Gain channel with no lack of accuracy.

Another important feature to mention is the possibility to switch from forward to reverse measurement: this operation do not only enables signal inversion, but also changes in the amplification stages. Since the IV curve in reverse region has a different current scale w.r.t. the forward region (order of mA in the linear part of the forward region, order of μA in the reverse region), the system is designed to switch to higher Gains when set in reverse mode. The amplified signals are returned from the daughter boards to the mother board and digitized by four ADC modules and the Arduino sends these signals to a Raspberry SBC via serial communication.

Each Arduino controls its own warm board following the instruction received by the Raspberry in the form of string commands. The four Arduino boards all run the same firmware coded in C language, that is designed to perform different tasks depending on the received string:

- assign an ID to the hosting Arduino
- initialization of the Arduino
- enable or disable the zero calibration mode
- switch between forward and reverse mode
- acquire 100 measurement for each channel at 1 kHz sampling frequency, then it performs the average and the rms of the acquired data
- send the average and rms of each channel to the Raspberry
- send the Arduino ID to the Raspberry
- reset to default setup

5.1.3 Raspberry

The Raspberry unit is a Raspberry Pi 4 (*model B, 2018*) that runs a Python script which handles the measurement of each IV curve, as it controls the Arduino boards in coordination with the SMU. It is connected to an ASIC board together with the four reading circuits of the Pt100 sensors, as visible in figure 5.4.

The ASIC board simply connects all the devices to an AC/DC converter, which is plugged on the general power line of the lab, and connects each Pt100 reader to the Raspberry via serial communication.

As mentioned in the previous subsection, the script controls the four Arduino units by sending command strings and it receives the digitized data of all the channels after each acquisition (i.e. each point on the IV curve). The raw data is stored and processed in order to generate the IV plots before sending the results of the IV curve analysis to the main PC station. The Raspberry is connected with

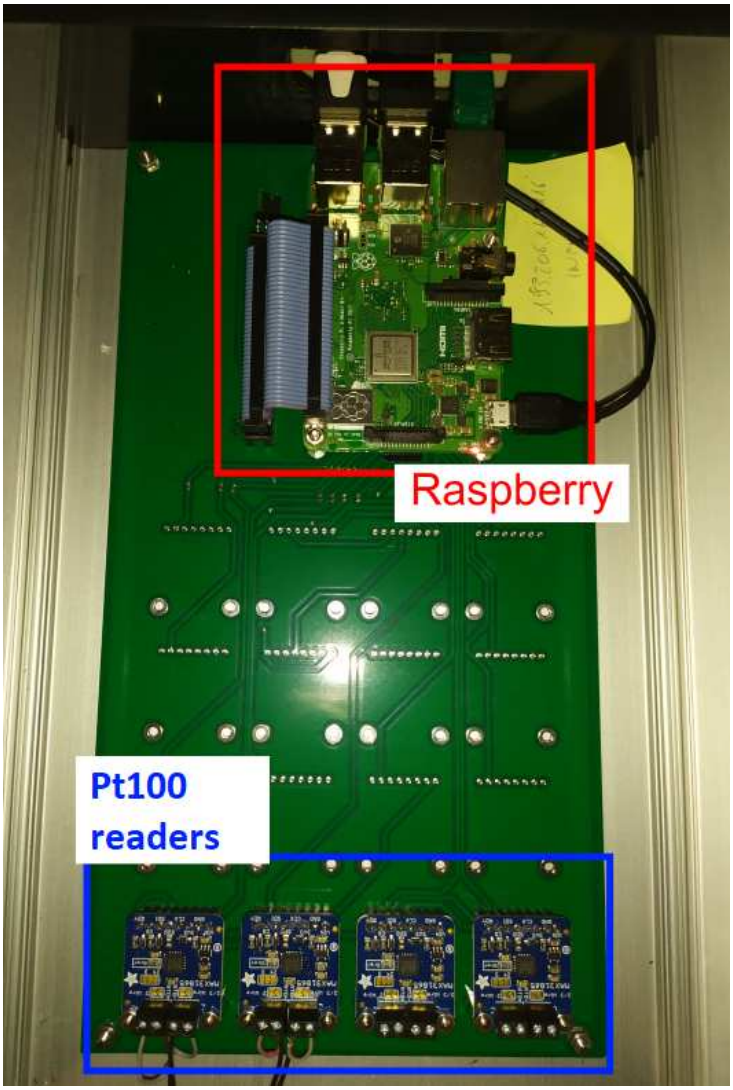

Figure 5.4: Picture of the ASIC hosting the Raspberry unit and the four Pt100 reading circuits. The ASIC board provides the bias power for all the devices and connects the four readers to the Raspberry.

the SMU and the PC station in a LAN network, and all communicates through string-based messages. All the commands are custom strings, except for the SMU commands which follow the SCPI standard.

Besides the IV curve daemon script, which will be described more in details in the following, the Raspberry also handles the Pt100 temperature measurements, by running a second Python daemon that reports the temperatures of all the cold-boards to the main PC station every 5 seconds.

The IV curve script is structured in parallel threads, in order to remain in standby waiting for commands from the PC station, execute the requested command when received and then return in a standby state again, the threads are:

- *IV control*, which is the main thread
- *sender UDP*, which handles the outgoing UDP messages
- *listen UDP*, which handles the incoming UDP messages

- *SMU controller*, which controls the source meter unit
- *check serial ports*, which constantly checks the Arduino boards serial connections
- *Arduino controller* (x4), which controls a single Arduino
- *storage controller* (x4), which stores the data acquired by a single Arduino

Values and parameters are passed among threads through custom data queues. With this modular structure it is possible to pilot a single device, like one of the Arduino boards or the SMU, directly from the PC station, using specific keywords before the command string. This feature can be used for single-point measurements and it was important in the debug phase of this project.

The threads designed for the communications are *sender UDP*, *listen UDP* and *check serial ports*. As suggested by their names, *sender UDP* and *listen UDP* are related to the UDP communication with the main PC station. The first constantly checks all string output data queues from the (verbose) active threads and send the strings to the PC. *listen UDP* is similar to *sender UDP* but it works in the opposite way, it reads the string command coming from the PC and redirect it to the main thread queue. In standard automatic operation, all messages coming from the PC are sent to the main thread, but there are some keywords that the user can put before the string command in order to communicate with a single device only. These can be "ARDU N " with N being an integer in the $[1-4]$ range, to control the N-th Arduino board, or "SMU " to pilot the SMU. When the string contains one of these two keywords, the *listen UDP* thread redirects the command to the Arduino queue or the SMU queue respectively. The last communication thread is the *check serial ports*, that monitor the four USB ports of the Raspberry to check is a new Arduino is connected or if a previously connected Arduino is currently disconnected.

The *SMU controller* thread is the one responsible of controlling the SMU resource. The constructor creates and initializes a *sourcemeter* object, among the other internal thread parameters. The sourcemeter object represents the SMU resource and receives simple string-based commands:

- *on* to turn on the device
- *off* to turn off the device
- *cfg* to configure the measurement, the involved parameters are $V_{\text{max}}, I_{\text{max}}, t_{\text{delay}}, \Delta V$ and must follow the "cfg" command all separated by a space character. V_{max} and I_{max} are the full-scale voltage and current values, t_{delay} is the time delay between setting a bias voltage and performing the readback measurement and ΔV is the threshold difference between the set and the readback voltage values to consider the measurement valid (if $|V_{\text{set}} - V_{\text{measured}}| > \Delta V$ the codes returns an error).
- *set* to set a voltage bias V_{set} and measure the readback voltage and current. The V_{set} value (in Volts) must follow the "set " command.

The *Arduino controller* thread handles a single Arduino resource and the data queue shared with the related storage control thread. There are an *Arduino controller* active thread and a storage con-

troller active thread for each of the four warm board during normal operation of the apparatus. This thread receives string commands from the *IV control* thread, the commands can be:

- *CFG*, in this case the thread will automatically send a set of messages to the Arduino resource via serial communication. These configuration messages are "reset" to reset the device to default parameters, "zcaloff" to turn off the zero-calibration mode, "fwd" or "rev" to set the board in forward or reverse configuration respectively and then "initmeas" to initialize the measurement session.

- any other string message, in this case the string will be redirected to the Arduino device. The thread then automatically reads the response and stores it into the storage controller queue if it is a data string. The particular string "ARDUINO ID N OK" is the correct response after and ID check from the N-th Arduino device, so in this case the thread refreshes its Arduino ID parameter with the N value. If it is any other verbose string the thread redirects it to the PC, then if a error or an unexpected message occurred, the thread sets an alarm flag.

The *storage controller* thread is related to the Arduino controller thread as mentioned in the previous paragraph. The storage queue, which is constantly checked by the thread, can contain verbose strings or data strings. The main thread (the IV control thread) only sends verbose strings, which can be "NEW ARDU ID" to refresh the ID of the associated Arduino device, or "IV FINISHED" to retrieve the stored data and reinitialize the internal parameters. If the string is a data string, the thread recognizes it comes from the Arduino controller thread. The data string contains one measurement for all the channels of the associated warm board, for a total of 30 values (each with associated error). As the storage controller receives a single data point measurements, it parses the channels and stores the values in a data frame, according to some conditions. For each channel, the values are stored only if more than 2/3 of the 100 acquisitions are successful and if the measured signal is in the $(0, 2300)$ mV range. A zero is considered in saturation because is the expected behaviour of the ADC, while the 2300 mV value stems from the saturation level of the trans-impedance amplifier which is 2.3 V, the saturation level of the ADC modules is designed to be the same of the amplifier but the tolerances of these values sometimes gives as a result measured values slightly above 2300 mV. At the end of the IV measurement, the thread returns a pandas data frame to the IV control thread via data queue. The data frame contains, for each point of the IV curve and for all the 30 SiPMs of the associated cold board:

- the voltage and current values measured by the SMU

- the low Gain value with associated error (if not discarded)

- the high Gain value with associated error (if not discarded)

- the SiPM number

- the ARDUINO ID

- the step number within the IV curve

IV control is the main thread of the program, as it handles the entire IV acquisition by coordinating the other threads and communicating with them through queues. This thread recognizes only two messages from the PC: "SET IV" e "RUN IV". The first one is used to set the IV parameters such as the connected Arduino devices, the path where to save the test data and results, the t_{delay} and ΔV parameters discussed above in the *SMU controller* paragraph. These parameters must be included in the command string after "SET IV " all separated by space characters. The "RUN IV" command defines the start of the IV curve, it also need some parameters to be included in the string and separated by space characters. These parameters are the temperature at which the measurement is done and the polarization of the IV curve (to change the normalization Gain values accordingly), the V_{max} and I_{max} parameters discussed above, the IV curve voltage start V_{start} and end V_{stop}, the number of steps to perform N_{step} and the voltage starting point of the fit $V_{\text{start}_{\text{fit}}}$. When the IV measurement begins, the IV control thread configures the SMU and all the Arduino resources, with the parameters received from the main PC station and then checks the Arduino IDs. The bias voltage is firstly set to 0 V and a data point is acquired, this will be used as an offset compensation in the analysis, then the SMU voltage is set at the IV curve starting point. If the curve is in reverse polarization the SMU voltage is increased gradually in ten steps from 0 V to the starting point. For each point of the IV curve, the thread sets the SMU voltage and store the current and voltage read-back in the storage queue, then it coordinates the acquisition of all the arduino devices and lastly it checks the measured point by comparing the read-back and the set values of the SMU.

After the IV curve measurement the thread turns off the SMU, checks if the Arduino IDs are changed, and saves the raw data returned by the storage controller threads, merged in a single data frame. The general data frame is then passed to a custom function to be analyzed, together with the parameters useful for the analysis. The structure of this function is described in the *run-time data analysis* sub-section. The *analyze* function returns the results for each SiPM and stores the all IV curve plots in a pdf file. The numerical results are sent to the LabVIEW VI of the PC station and printed on the Raspberry shell. After the analysis is finished, the thread re-initializes the internal parameters and returns in standby status, ready for the next IV curve.

5.1.4 FPGA-based counter

The FPGA-based counter, controlled by the main PC station with a custom Python script, is the component related to the DCR measurement. We will also refer to it as the *DCR system*. The output signal from each SiPM passes through a current integrator and a charge threshold stage, and the charge threshold can be set as hard coded parameter. If the amplitude of an event is above the charge threshold, the FPGA automatically increases a counter associated to the SiPM that generated that event. The python script firstly configures the counters according to the selected threshold, then it initializes the counters to 0 and waits for the specified time window before retrieving the results of the counting measurements. The results are then stored and printed in the shell. This script can run alone or automatically launched by the LabVIEW VI, and the results are converted in frequency values: the count for each channel is divided by the time window and by the active area of the SiPM, to get the resulting DCR in mHz/mm^2.

A second version of the script was developed in order to calibrate the device, this script is similar to the previous one but it handle only one SiPM and it repeats the measurement several times, scanning the charge threshold over a user defined range. With this device is possible to measure the DCR in an automatic way, but since we are not analyzing the single events, it is not possible to determine the AP and the CT probabilities.

5.1.5 Mechanical stage

The lid of the dewar is attached to the slider of a mechanical stage, this allows to perform the thermal cycles on the whole system of 120 sensors. The mechanical stage is divided in two components, the electric actuator driven by a step DC motor and the step motor controller (*SMC JXC91/Controller*), which is connected to the PC station through serial communication. The serial protocol is used only for debugging or to work with the mechanical stage without using the LabVIEW main interface. The controller is also connected to the LAN network, communicating with the PC station using EtherNet/IP protocol during normal operation of the apparatus.

Some specs of the mechanical stage are reported in the following table:

parameter	range	error
communication speed	[10, 100]1,Mbps	-
slider positioning precision	[0, 600] mm	0.01 mm
slider speed precision	[8, 30] mm/s	0.01 mm/s
acceleration precision	[8, 30] mm/s^2	1 mm/s^2

The controller can be controlled by the PC station via USB connection with the *ACT controller* software, which is furnished by the vendor. This software permits to store a maximum number of 60 steps in the controller memory, each step being a complete set of parameters involved in a single movement. Some important parameters are the target position, the maximum speed and acceleration, the maximum pushing force and the positioning tolerance. The software permits also to select a single point operation or perform loops with any number of points.

The LabVIEW VI communicates with the controller using 288 channels, divided in sets of 18 words, each with a length of 16 bit. The VI handles only 8 bit words, so the words are split or joined when needed in order to communicate in compliance with the standards. The first of the 18 words permits to select a step and define the state of the device. With this word is possible to turn ON or OFF the servomotor, switch to a standby state, reset the alarms or make the slider return to the origin for a re-calibration. The second word is used to enable or disable the data reading of each of the step parameters, this can be used to make the device insensitive to variation in certain channels. The third word sets the operation mode switching between two cases, the *recorded step* mode and the *define step* mode. In *recorded step* mode the controller performs the step selected in the first word, if it is stored in memory otherwise it sets up an alarm. In *define step* mode the controller performs the step defined by the following words, which together encode the full set of parameters described above in the previous paragraph. In the first case these words are ignored, since the parameters are stored in the controller memory.

The interaction between the controller and the LabVIEW VI in the CACTUS apparatus is based on the *define step* mode. This choice stems from the usage of the memory of the PC instead of the controller, which makes possible to store far more than 60 steps. The step storage structure can also be more complex, as it will be described in the subsection 5.1.7.

5.1.6 Other components

The other components of the CACTUS apparatus are listed in the following:

- The dark box containing the dewar, the electric actuator with warm boards, cold boards and DCR system, the Raspberry board, a 100 L LN_2 stock for refilling and the board for the Pt100 measurements. The controller of the actuator is placed outside the dark box since its switching noise would compromise the DCR measurements.

- the four Pt100 sensors attached to the cold boards are connected to a temperature reading module, which is connected to the Raspberry. A Python daemon script parses the data received from the module and sends the resulting temperatures to the LabVIEW VI once every 5 seconds.

- The dewar (*ARPEGE 55 liquid*) has a capacity of 55 L and is equipped with a LN_2 level controller, which deploys a sonar sensor to regulate the LN_2 refilling system, maintaining the selected LN_2 level with 0.5 cm (nominal) precision. Some specs of the dewar are: 378 mm internal diameter, 675 internal height with up to 425 cm of liquid phase

- Few centimeters above the dewar aperture there is a LED illumination system, which is used to control illumination inside the dark box during the IV curves. The system is placed close to the aperture in order to get the desired illumination also in LN2, by leaving a small gap above the dewar after immersion. Two strips of LED are placed at the opposite sides of the dewar and are controlled by an Arduino MKR zero, which runs a custom C firmware and is connected to the PC station. The illumination is automatically controlled by the LabVIEW VI during measurements, by launching a simple Python script that interact with the Arduino via serial communication.

- As mentioned in the general description of the CACTUS apparatus, the SiPM PCB IDs are encoded in QR-codes (sometimes data matrices) that are printed on the back of the PCB. These codes can be read by an infrared laser scanner connected to the PC station. The scanner is connected to the PC as a USB device and acts as an external keyboard.

- The power supplies all share the same ground together with the SMU, except for the LED system which has its own electric chain because its connections are distant from the boards and do not influence the measurements. The warm boards need a both positive and negative Voltage supplies, respectively $V_+ = 7\,\mathrm{V}$, $V_- = -5.5\,\mathrm{V}$. In the CACTUS apparatus, there are two DC power supplies (*IPS3303S* and *RS-D3305P*) and each one is connected to two warm boards in parallel. The DCR system controller is simply plugged to the power line of the laboratory like the Raspberry or the PC, while the FPGA-based counter is connected to a DC power supply (EX354D, set at $V_{\mathrm{biasFPGA}} = 7.6V$)

5.1.7 PC station and LabVIEW interface

The PC station is the central component of the apparatus, as it controls all the other components. In a similar way, the LabVIEW VI running on the PC station is the master process w.r.t. all the chain of slave processes in the other devices. All the other codes are either sub-codes that are launched by the interface in autonomous way or daemons interacting with the interface. The former are the Python scripts used for DCR measurement and LED control. The latter are the two Python scripts in the Raspberry board: one to manage the IV curve measurements and the other used to monitor the temperatures of the cold boards. The final validation of results is performed by the LabVIEW algorithm, but all the data analysis is done by the Raspberry daemon, and the DCR results are directly returned by the related Python script.

The main interface is a finite-state machine that perform some automatic tasks as it starts running, before entering in the main *exec test* state that actually performs the measurements. The single tasks or measurements are labelled as *tests* and each test has its own graphical interface in a subpanel, these tests are also structured in a finite-state machine that is nested inside the exec test state. The finite-state machine fashion is not only coherent with the general structure of the interface, it also has a correlation with the actual measurements, as visible in figure 5.5.

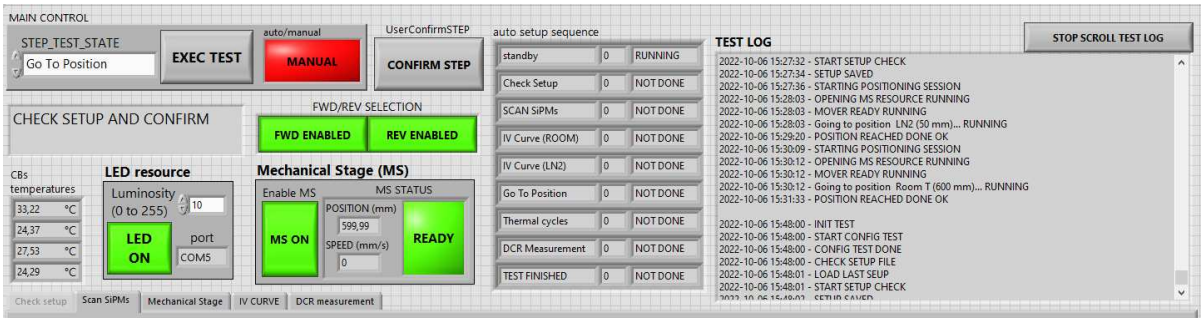

Figure 5.5: Screenshot of the upper part of the main LabVIEW interface. The *MAIN CONTROL* section permits to choose the test to perform, the *FWD/REV SELECTION* cluster permits to select the polarization of the IV curves. The *CBs temperatures* cluster shows the temperatures of the four cold boards, the *LED resource* section controls the LED luminosity while the *Mechanical Stage (MS)* cluster is related to the mechanical stage. The interface also shows the test sequence chosen by the user (or the default one if none are chosen) and the log of the previous tests. On the bottom of the screenshot is visible the upper part of a tab control, and the pages are related to the single test types.

As the algorithm starts running, it checks the connections with the peripheral devices and configures the parameters using JSON files to load the last configuration used, if there was any saved, otherwise it skips to the next part with default parameters. The interface is structured in order to save the current state of the machine every time a test is finished, saving the list of performed tests with related results (where it makes sense) and re-starting from the first unfinished one. The multiple JSON files generated for this purpose are divided in groups and saved in related folders, the *TEST LOG* in the front panel is also saved and loaded in the same manner.

After the initial automatic configuration there is a second configuration phase in which the user can chose the tests that wants to perform, the parameters involved in each test and set parameters to identify the measured SiPMs. The latter include the load number, which refers to the group of 120

SiPMs tested in a single measurement session, and the SiPM type. A *CHECK SETUP AND CONFIRM* page is opened by the interface automatically, showing the parameters used the last time the interface was launched (if there are any, otherwise it will show default parameters) as in figure5.6.

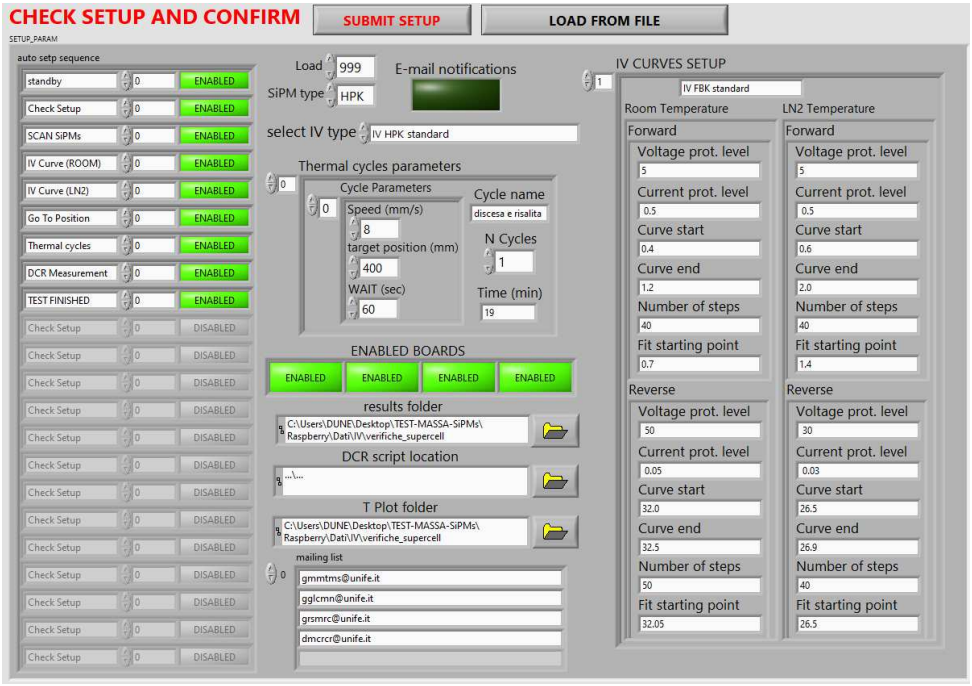

Figure 5.6: Screenshot of the *CHECK SETUP AND CONFIRM* page, which is automatically opened by the LabVIEW VI after the first automatic setup configuration. Here the parameters involved in the measurements can be manually set or load from a text file before being submitted. After the setup submission, these parameters are automatically stored in a JSON file in order to fill the page in the next run.

The list of selected tests is used only in *AUTO* mode, as it sets which tests to automatically perform and in which order, while for the *MANUAL* mode each test is selected at run time before it is performed. For the IV curve parameters, it is possible to create a custom number of IV curves, defining for each of them the name and the parameters involved in the measurement. These parameters are V_{max}, I_{max}, V_{start}, V_{stop}, N_{step} and V_{startfit} and were discussed before in the *IV control* paragraph of sub-section 5.1.3, they must be defined for forward and reverse polarization, both at room temperature and LN2, for a total of four sets of parameters for each IV curve. The thermal cycles follow the same principle: the user can define any number of thermal cycles by specifying a name, a movement speed value, a 2D array with target position Y and time delay t for each displacement and a number of cycles N_{cycles}. For each point in the array, the slider will go to position Y (mm from the bottom) and then wait t seconds, and after finishing the steps the apparatus will repeat the sequence of displacements N_{cycles} times. All the mentioned parameters can also be uploaded from a txt file. It is also possible to select the number of enabled boards, in order to perform measurements with less than 120 SiPMs. In the setup interface is possible to select only one thermal cycle and one IV curve, since it is designed to perform one test per each test type in manual mode, while for the auto mode there is a numeric value for each test which define the type of IV curve for the *IV curve (ROOM)* and *IV curve*

(LN2) tests and the type of thermal cycle for the *Thermal cycles* test.

The complete set of test is listed in the following, ordered as in a typical measurement session (except for repetition of measurements).

- *Check setup* test is another check on the connections with the Raspberry and with the controller of the mechanical stage. This task is already performed automatically by the algorithm as it starts running but (that is why it is grayed out in figure 5.5, to highlight the fact that at the beginning of the measurement session this test was already performed once), but it is possible to perform it again both in MANUAL mode and AUTO mode.

- *Scan SiPMs* is the test related to the reading and storage of the SiPM IDs. As mentioned in the beginning of this section, the SiPMs are arranged in arrays of 6 units on custom PCBs, each PCB is marked with a QR code or a data matrix (sometimes both) that identifies its ID. This test has a visual representation which resembles a cold board (in order to be more intuitive for the user) as shown in figure 5.7. As the test starts the PC cursor is automatically pointed to the first array of the first (enabled) cold board, indexed in the top left of the figure. From here, the user can start scanning the PCBs as it mounts them in the cold boards (in ascending order), the algorithm automatically fills the array ID indicator and passes to the next one in ascending order. The interface is filled dynamically as the user scans the PCBs, it is possible to navigate manually among arrays and cold boards by selecting them with the cursor, and when the scanning process is done the user is asked to check the resulting IDs.

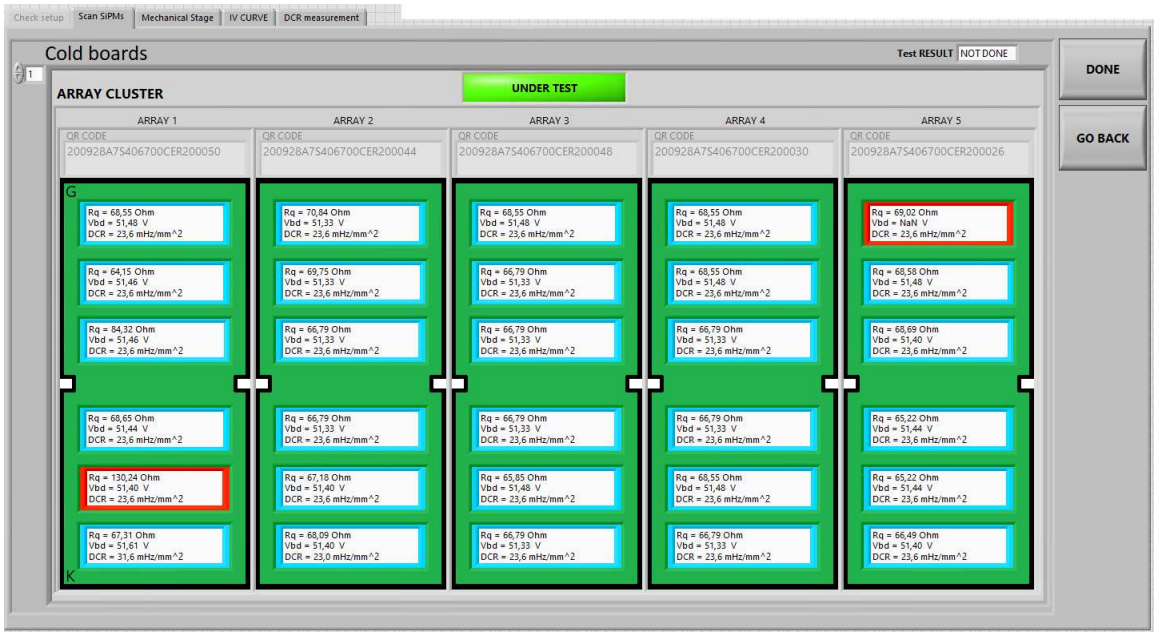

Figure 5.7: Screenshot of the *Scan SiPMs* panel related to the homonym test. Each strip reports its ID on the top and contains the results of the measurements for the SiPMs mounted on it. The single SiPM boxes turns red if the results are out of specs and light blue if the results are in specs, here the boxes are filled with dummy values to show both the possible outcomes, but the tested SiPMs which are out of threshold were less than 0.1%.

Below the boxes with the array IDs there are 6 white boxes in the green arrays that correspond

to physical SiPMs in the PCB, these boxes will be filled with the results of the measurements as soon as they are available to the interface (i.e. after the first IV curve or DCR measurement). Furthermore, the black corners of each box will turn blue if all the result are in specs, red if any result (R_Q, V_{BD} or DCR) is out of specs.

- The *Go to position* test permits to perform single displacement of the slider. This test is related to the *Mechanical Stage* page in the sub-panel of the interface, which is reported in figure 5.8.

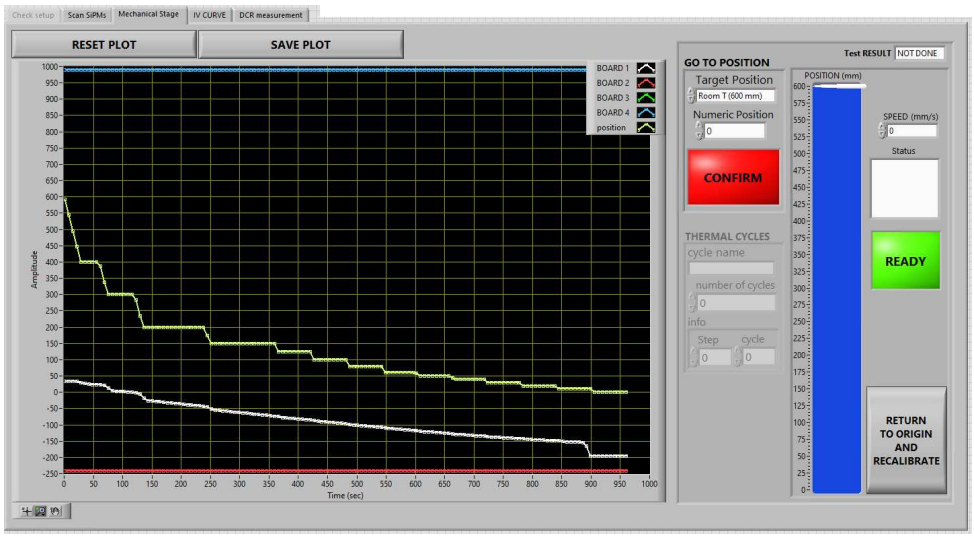

Figure 5.8: Screenshot of the *Mechanical Stage* panel related to the *Go to position* and *Thermal cycles* test. This panel contains a plot which shows the position of the slider and the temperatures of the four Pt100 sensors versus the elapsed time in seconds (w.r.t. the beginning of the first measurement). The plot is updated run time during the tests and can be reset or saved in any moment. The panel contains also a cluster of controls and indicators to drive and monitor the slider.

The sub-panel contains a plot which shows the position of the slider and the temperatures of the SiPMs for each cold board as functions of the time elapsed from the beginning of the test. The plot has a single y axis scale that is intended in mm for the slider and in °C for the temperature, a multi-scale plot would solve the issue but it would also make the zooming procedures less intuitive. Near the Plot there is a cluster of controls and indicators which are used to pilot the mechanical stage in MANUAL mode and monitor its state during displacements. It is possible to set some predefined positions or to go to the desired position expressed in mm, a virtual slider on the right will show the current position and the speed is set to 8 mm/s which is the minimum specified by the vendor.

- The *Thermal cycles* test is used to perform controlled immersions in LN2, each followed by extraction and heating phase. The whole process is called thermal cycle and it is used to validate the resilience of the sensors under thermal stresses, normally performing multiple thermal cycles to the same sample. As discussed before, the user can define any number of thermal cycles, each one with a finite number of displacement at constant speed (8 mm/s) separated by some time delays. The test starts, the apparatus performs the cycle previously selected in the setup page and then repeats it for N_{cycles} times. This test is related to the same panel of *Go to position*

test, as reported in figure 5.8.

The monitor cluster is the one described in the previous point. (figure 5.8), but this time the *thermal cycles* sub-cluster is enabled and the *go to position* sub-cluster is disabled. In the *thermal cycles* sub-cluster there is the target position, the time delay to wait before performing the displacement, the step number and the cycle number.

- *IV curve (ROOM)* and *IV curve (LN2)* are the test related to the IV curve measurements and are associated with the same page in the sub-panel, like in the case of the mechanical stage. A single IV curve in the setup contains parameters for both the IV curve at room temperature and the IV curve at liquid nitrogen temperature. These parameters are not divided in two separated curve setups because in a typical measurement session they are both present, separated by the immersion, so the interface is designed to reduce the chances of launching an IV curve with the wrong temperature setup.

  The IV curves is divided in two test logs, one related to the IV curve measurement that the apparatus is currently performing and the other for the previous IV curve, as visible in figure 5.9. These logs show in both cases the messages from the Raspberry script and are used to check if any error is occurred in the IV measurement.

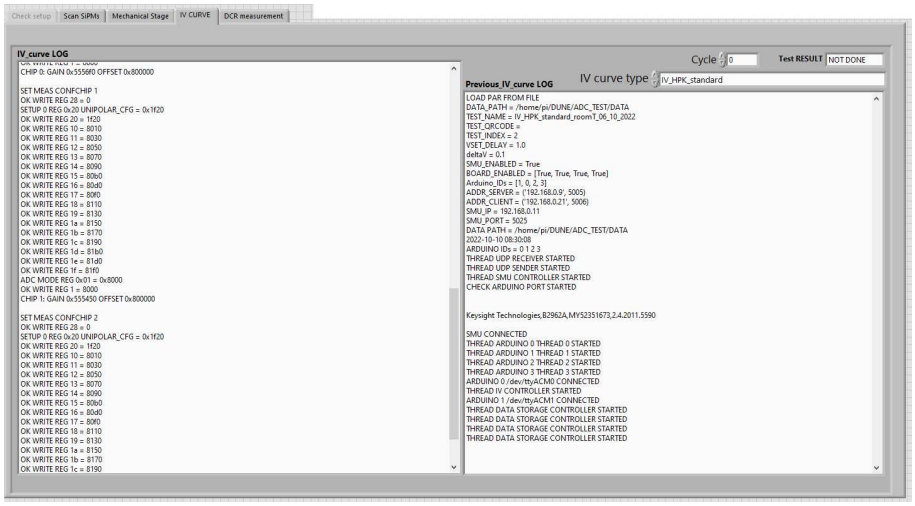

Figure 5.9: Screenshot of the *IV CURVE* page related to the *IV curve (ROOM)* and *IV curve (LN2)* test. This panel contains the two logs of the current and the previous IV curve, these logs are the output of the Raspberry script which performs the measurement and returns the results.

After the IV curve is finished, the results are sent to the main interface by the Raspberry and they appear in the text log. The LabVIEW algorithm extract these results and compare the values with a threshold (that can be set in the setup phase) in order to validate them, before storing these values in a text file. The results then appear in the white boxes of the Scan SiPM page divided per position, array and cold board as mentioned above in the discussion of the *Scan SiPMs* test.

- The *DCR measurement* test is the one related to FPGA-based counter system. The LabVIEW algorithm initially sets off the servo motor of the mechanical stage to eliminate the related

switching noise, and then sets the SMU voltage bias $V_{smu} =< V_{BD} > + V_{OV}$ where $< V_{BD} >$ is the average breakdown voltage measured in the IV curve at LN_2 temperature and V_{OV} is the over-voltage selected by the user. The LabVIEW VI launches automatically the DCR script passing as arguments the ID of the SiPM arrays, ordered from left to right inside the single cold boards and from the cold board 1 to the cold board 4. The script returns the DCR values for each SiPM of each array to the main interface and also stores these results in a txt file. The log of the DCR measurements is visible in the related page on the main interface panel, as visible in figure 5.10.

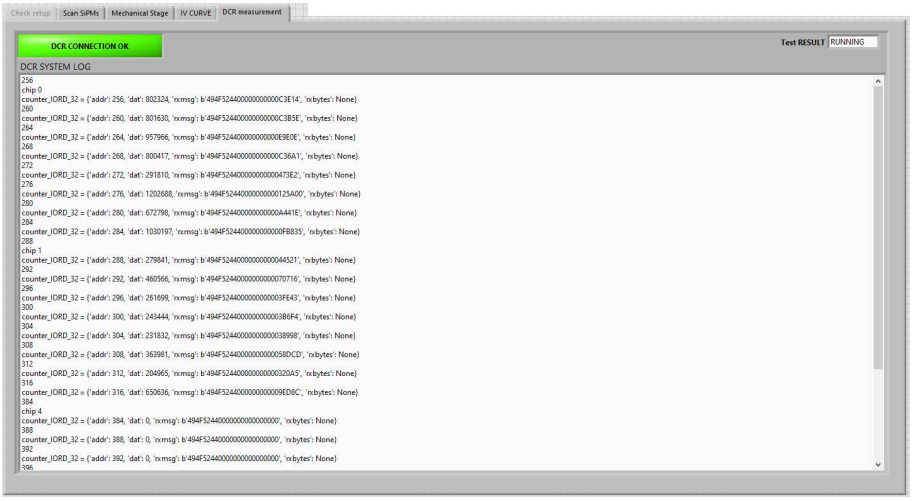

Figure 5.10: Screenshot of the *DCR measurement* page related to the homonym test. This panel contains the log of the DCR measurement performed by the related Python script, which is automatically launched by the LabVIEW VI.

- other tests are *standby* and *TEST FINISHED*. The former is the standby state of the interface, which can be used to let the interface wait for a user input while in AUTO mode (in MANUAL mode the interface goes to standby automatically after any test). The latter is used to save the test results and the state of the machine before closing the interface, it is only used to repeat the saving procedure to ensure that the algorithm has stored the data.

5.2 Run-time data analysis

This section covers the analysis of the data measured by the CACTUS apparatus. The analysis is performed at run time for both the IV curve and the DCR measurement, by the Python scripts running on the Raspberry and the PC, respectively.

5.2.1 IV curve

The IV curve analysis is encapsulated in a class method used by the Raspberry Python script. The function takes as arguments the four data frames related to the four cold boards as discussed in the previous section. One data frame contains the voltage V_{smu} and the current I_{smu} measured by the SMU, the voltage measured by the ADC channel of the warm board V_{ADC} and its error ΔV_{ADC} for all

the SiPMs in the related cold board, and for all the points of the IV curve. Starting from the raw data, the function is able to extrapolate the R_Q and V_{BD} values by fitting the plots and returns the results to the main thread.

The first operation is to subtract a correction factor to all the V_{smu}, this factor stems from the voltage drop ΔV_{bias} across the electric path from the SMU to the first warm board, which has as a resistance R_{bias}.

$$V_{smu\,corrected} = V_{smu} - \Delta V_{bias} = V_{smu} - R_{bias} I_{smu}$$

The bias line has a different effect depending on how many boards are connected, and the value of R_{bias} is changed to take account of this effect. The values of R_{bias} measured during the calibration of the apparatus in the cases of 1, 2 ,3 and 4 Boards connected are respectively 0.359 Ω, 0.553 Ω, 0.573 Ω and 0.503 Ω. After this correction, the first point of each IV curve is used as an offset compensation for the others: before starting the measurement, the Raspberry daemon sets the SMU voltage source to 0 V and launches a measurement of the Arduino boards to be stored as first IV curve point, so the first point represents the measurement without bias. For each SiPM, the voltage measured by the ADC channel in the first point $V_{ADC\,offset}$ is subtracted to the values V_{ADC} measured in all the other points, then the first point is removed from the array of values. These voltages are then converted to current values I_{iPM} by dividing for the channel Gains[2].

$$I_{SiPM\,low} = \frac{V_{ADC} - V_{ADC\,offset}}{G_{low}}, \quad I_{SiPM\,high} = \frac{V_{ADC} - V_{ADC\,offset}}{G_{high}}$$

The Gain values are reported in the table 5.2.

polarization	low Gain value	high Gain value
forward	$(50\,\Omega)\cdot 10\cdot 1.2 = 600\,\Omega$	$G_{low}\cdot 6 = 3600\,\Omega$
reverse	$(50\,\Omega)\cdot 10\cdot 101 = 50500\,\Omega$	$G_{low}\cdot 11 = 555500\,\Omega$

Table 5.2: Gain values for the high and low Gain channels in forward and reverse polarization. In these Gains also the feedback resistor of the trans-impedance amplifier is included, for this reason they are expressed in ohms instead of being adimensional. The Arduino board returns the measured signals in mV, so this conversion gives the related currents in mA

The algorithm discards the invalid measurements, and takes the average between the high Gain and low Gain values if they are both available. The IV point would not have been existed in memory if both the measurements were invalid, since the storage control thread stores only IV points with at least one valid measurement, so this case is not foreseen by the algorithm.

$$I_{SiPM} = \begin{cases} I_{SiPM\,low}, & \text{if } I_{SiPM\,high} = 0 \\ I_{SiPM\,high}, & \text{if } I_{SiPM\,low} = 0 \\ \frac{I_{SiPM\,low} + I_{SiPM\,high}}{2}, & \text{otherwise} \end{cases}$$

If the valid measurement is the low Gain value, its simply means that the high Gain value is saturated

[2] as mentioned in the previous section, each SiPM has a high Gain and a low Gain channel associated to it

as expected at some point of the IV curve, but if the only valid measurement is the high Gain value then the the algorithm sends an alarm to the main interface. This because the signal of the high Gain channel is the same of the low Gain channel for the same SiPM, it only passes through another amplification stage, so if the low Gain measurement is invalid (while the high Gain channel works properly) there must have been a problem with the acquisition of the signal.

Finally, a third correction is applied to all the SMU voltage values $V_{\text{smu corrected}}$ in order to take into account the voltage drops between consecutive cold boards ΔV_{cold} and the voltage drop in the connection between the SiPM anode and the related ADC channel of the warm board $\Delta V_{\text{channel}}$. The ΔV_{cold} voltage value depends on which couple is considered, since the cold boards are connected in a daisy chain configuration to the SMU, as depicted in the circuital scheme of figure 5.11.

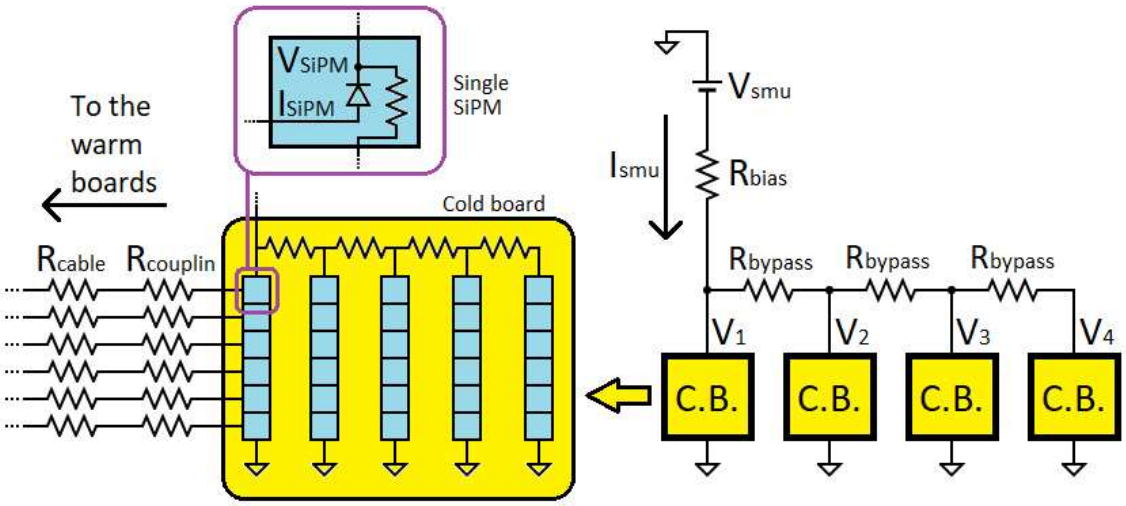

Figure 5.11: Circuital scheme of the electrical connections of the cold boards. The source meter furnishes a bias V_{smu} and measures the current I_{smu}, which passes through the resistor R_{bias}. The yellow boxes are the four cold boards connected in a daisy chain configuration, the intrinsic resistance of the inner connections are labelled as R_{bypass} and the boards are biased at the voltages V_1, V_2, V_3 and V_4 respectively. Inside e a single board, the SiPM slots are depicted as blue boxes and are connected in a daisy chain configuration to the power line in arrays of 6 units. The bypass resistors between the SiPM arrays and between the SiPMs in a single array are unknown, so they are not named in the scheme. The voltage drop on the output line from the SiPM to the warm board ADC channel $\Delta V_{\text{channel}}$ is evaluated starting from the current I_{SiPM} that enters the trans-impedance amplifier. These currents passes through the coupling resistor R_{coupling} and through the micro-coaxial cables that connects the cold boards to the warm boards, which have a measured resistance R_{cable}.

Since also the SiPMs inside the cold board are connected in a daisy chain to the bias line, we can define a parameter ΔV_{SiPM}, similar to ΔV_{cold}, that represents the voltage drop between consecutive SiPMs inside the single cold board. The ΔV_{SiPM} values are lower than the precision of the instrument used in the calibration phase, so they introduce a negligible error on the final results and will not be taken into account in the following calculations.

The three bypass cables shown in figure 5.11 have approximately all the same resistance $R_{\text{bypass}} = 0.095\,\Omega$, that was measured during the calibration phase of the apparatus. A precise evaluation ΔV_{cold} is not possible, since the calculations would include the resistance of the SiPMs which is the quantity

to measure, but ΔV_{cold} can be estimated with negligible error after making an approximation. The current I_{smu} is considered to be divided in equal currents $\frac{I_{\text{smu}}}{4}$ across the four cold boards branches, this approximation is valid since R_{bypass} is negligible with respect to the resistances of the cold boards. Under this approximation, the current passing through the first bypass cable is $\frac{3}{4} I_{\text{smu}}$, while $\frac{1}{2} I_{\text{smu}}$ passes through the second cable and $\frac{1}{4} I_{\text{smu}}$ through the third cable. As shown in figure 5.7, the i-th cold board is biased at the voltage

$$V_{\text{i}} = V_{\text{smu corrected}} - \frac{I_{\text{smu}} R_{\text{bypass}}}{4} \sum_{\text{j}=0}^{i-2} (3-j)$$

$$V_{\text{i}} = V_{\text{smu}} - I_{\text{smu}} R_{\text{bias}} - \frac{I_{\text{smu}} R_{\text{bypass}}}{4} [\sum_{\text{j}=0}^{i-2} (3-j)].$$

where $i \in [1,4]$ and the sum is considered equal to zero if $i = 1$.

The analysis function uses a more general expression for V_{i} that takes into account also the actual number of connected cold boards N_{B} which can be less than 4:

$$V_{\text{N}_\text{B},\text{i}} = V_{\text{smu}} - I_{\text{smu}} R_{\text{bias}} - I_{\text{smu}} R_{\text{bypass}} \{[\sum_{\text{j}=0}^{i-1} (1 - \frac{j}{N_{\text{B}}})]\}$$

where $i \in [1, N_{\text{B}}]$. The boards must be always connected starting from the first free slot and following in ascending order, otherwise the correction factor would be underestimated.

The voltage drop $\Delta V_{\text{channel}}$ between the SiPM anode and the related ADC channel of the warm board can take a different value for each sample and it can be estimated from the current that enters the trans-impedance amplifier, which corresponds to the I_{SiPM} value mentioned above. These electrical connections can be schematized with a coupling impedance $R_{\text{coupling}} = 50\,\Omega$ (nominal) in series with the resistance $R_{\text{cable}} = 2.05\,\Omega$ (measured) of the micro-coaxial cable that connects the cold board channel to the warm board channel. The resulting voltage drop is

$$\Delta V_{\text{channel}} = I_{\text{SiPM}} (R_{\text{coupling}} + R_{\text{cable}})$$

From now on we will refer to the current passing through the n-th SiPM of the i-th cold board as $I_{\text{i,n}}$. Putting all the corrections together we can estimate the bias voltage for the n-th SiPM of the i-th cold board in a system of N_{B} total cold boards as

$$V_{\text{N}_\text{B},\text{i,n}} = V_{\text{smu}} - I_{\text{smu}} R_{\text{bias}} - I_{\text{smu}} R_{\text{bypass}} [\sum_{\text{j}=0}^{i-1} (1 - \frac{j}{N_{\text{B}}})] - I_{\text{i,n}} (R_{\text{coupling}} + R_{\text{cable}})$$

where $i \in [1, N_{\text{B}}]$ and $n \in [1,30]$. Using the definitions of voltage drops made above in this sub-section, the equation can be written as

$$V_{\text{N}_\text{B},\text{i,n}} = V_{\text{smu}} - \Delta V_{\text{bias}} - \Delta V_{\text{cold}_{\text{N}_\text{B},\text{i}}} - \Delta V_{\text{channel}_{\text{N}_\text{B},\text{i,n}}}$$

The factors subtracted to V_{smu} are the same used above, but now the dependence on the board number i, the SiPM number n and the total number of boards N_{B} is explicit. The first term ΔV_{bias} is a general term which is the same for all the SiPMs, the second term $\Delta V_{\text{cold}_{\text{N}_\text{B},\text{i}}}$ is the same for all the SiPMs inside the same cold board as it not depends on n, while the third $\Delta V_{\text{channel}_{\text{N}_\text{B},\text{i,n}}}$ term can take a different value for each SiPM. These corrections are set to zero at LN_2 temperature because the resistance of the cables and interfaces drop significantly at cryogenic temperatures and the corrections

become irrelevant. The N_B, i and n indexes will be dropped from now on, since the analysis is performed on the same way on the corrected parameters of each SiPM of each cold board and the total number of cold boards does not influence the analysis.

For each SiPM, the resulting parameters of the IV curve are the voltage, current and the error on the current, for each valid point. The single steps of the forward IV curve analysis are listed in the following, in order of execution:

- the function firstly draws an error bar plot of the IV curve, an example is visible in figure 5.12(a),(c).

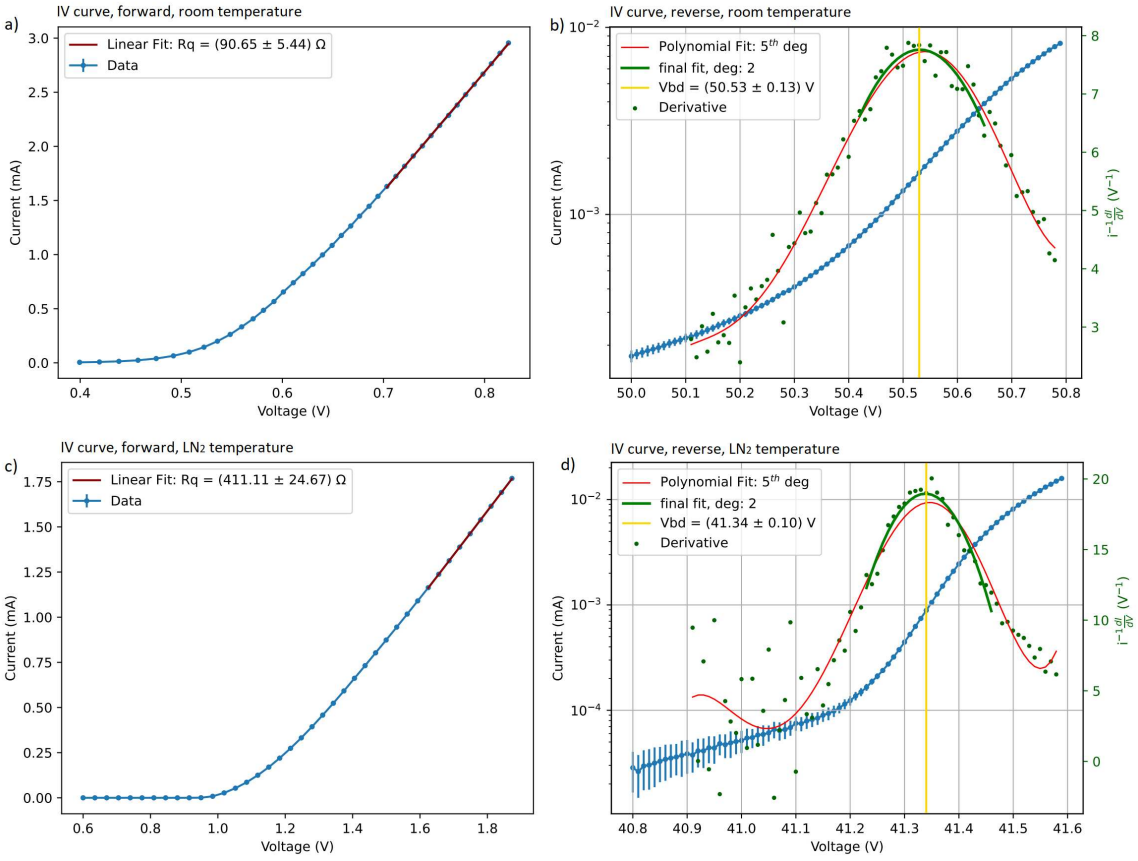

Figure 5.12: Example of four plots produced by the CACTUS apparatus after the IV curve analysis. The plots show the I(V) function in forward polarization and reverse polarization, both at room temperature (a, b) and at LN_2 temperature (c, d). The red line in the forward polarization plots defines the linear fit. In the reverse polarization plots, the blue line is the I(V) function, the green dots represents the $f(V) = I^{-1}\frac{dI}{dV}$ function, while the green line is the 5^{th} degree polynomial fit and the red line is the final 2^{nd} degree polynomial fit around the initial V_{BD} guess. The vertical yellow line marks the final V_{BD} estimation.

- the IV points outside the fit range selected by the user are removed from the arrays containing the voltage and the current values
- the function performs a linear fit on the data using a first degree polynomial function of the numpy library

- finally, the function takes the reciprocal of the fit slope to get the R_Q value of the SiPM.

The related error associated to the final result is 6%, this value stems from tests performed in the calibration phase which showed that by disconnecting and reconnecting the bias line cables, the resistance of the resulting electrical interface on the connectors can differ from the previous one by few Ohms. The uncertainty associated to the error propagation on the fit procedure is negligible with respect to these differences, for this reason error is set to 6% as an empirical value to avoid underestimations.

As for the forward case, the following list describes in detail the single steps of the reverse IV curve analysis, following the execution order.

- The function draws an error bar plot of the IV curve as in the forward case, this time in logarithmic scale. This plot is helpful for the user to check the stored IV curves *a posteriori* but it has no influence on the ongoing analysis.

- The function then numerically calculates the normalized derivative $f(V) = I^{-1}dI/dV$, which has a maximum in the break-down point V_{BD}.

- The derivative function shows some spikes in the points where the initial function $I(V)$ presents discontinuities, this can be an issue for the search of the maximum because some spikes could exceed the amplitude of the signal at V_{BD}. The discontinuities in the starting IV curve could be invalid points or in general generated by a high noise level with respect to the standard conditions. The noise could be reduced by a smoothing function, but the position of the maximum would then be subjected to an approximation error, so the algorithm simply removes from the derivative data array the points with amplitude higher than a (user defined) threshold. The amplitude of the derivative function at V_{BD} is unknown so the measurement were performed with a conservative threshold ($200\,V^{-1}$ which is the double of the highest value ever measured in the calibration phase).

- The algorithm performs a polynomial fit $p_f(V)$ of the function $f(V)$ on a fit range $[V_{start\_fit}, V_{stop}]$, then searches the maximum on this curve to get a first estimation of the breakdown voltage $max(p_f) = p_f(V_{BD})$.

- The first estimation of V_{BD} could be subjected to errors due to the noise in the initial IV curve, which could generate artifacts in the polynomial fit. Furthermore, V_{BD} is related to the quantization error of the x axis that is a discrete array of voltage values with N_{step} points which is a (user defined) parameter, this can be raised to achieve more precision but it also decreases the speed of the measurements. For these reasons, the analysis function isolates a range of $N_{range} = 24$ points around the first estimation of V_{BD} and performs a second degree polynomial fit on $f(V)$. The final estimation of V_{BD} is the maximum of this second fit function. Since the error propagation gives an underestimation of the actual uncertainty on V_{BD}, the function takes the empirical related error of 0.25%.

- The previous two points are performed again with different ranges if the resulting V_{BD} value falls at one of the fit extrema or in the low current region. If a valid V_{BD} value is not reached

after 10 iterations, then the function prints a warning and keeps the V_{BD} value from the last iteration.

An example of the IV curve plots in forward and reverse polarization is visible in figure 5.12.

The results of $V_{BD}(R_Q)$ of the reverse(forward) IV curve for each SiPM are returned from the analysis function to the main thread of the Raspberry board, which sends them to the PC interface to be displayed and stored as mentioned in the previous section.

5.2.2 DCR measurement

The DCR measurement, as already described in the previous section, is performed by a FPGA-based counter, which is controlled by a Python script. The script can either be launched alone or by the VI, in the second case the interface will automatically retrieve the DCR results from the prompt after the measurement is done. The FPGA counters are constantly counting the signals above a certain charge threshold Q_{th} as long as the bias is on, restarting from zero when the number of events N_{ev} reaches its upper bound, which is the maximum 32 bit unsigned integer. The script firstly assign to Q_{th} the value defined by the user, which is hard coded in the script, and then resets N_{ev} to 0. After a time window $t_{acquisition}$ (which is defined by the user) the script retrieves N_{ev} for each channel and calculates the DCR value for each SiPM

$$DCR = \frac{1000 \times N_{ev}}{t_{acquisition} A_{SiPM}}$$

where A_{SiPM} is the active area of the SiPM in mm^2, $t_{acquisition}$ is expressed in s and the DCR in mHz/mm^2.

The script takes as arguments the ID codes of the SiPM arrays and returns the DCR results specifying the SiPM number for each array ID. The SiPM index goes from 1 to 6 and represents the location of the SiPM inside the array, from top to bottom.

5.3 Test procedure

This section contains a detailed description of the procedure adopted to perform the tests. The first subsection is related to the calibration phase that was performed before starting the first measurement, this procedure is meant to be repeated only if the apparatus is modified. The second subsection describes a standard measurement procedure, discussing the single tests in the order in which are performed.

The apparatus was used to characterize (mainly) two types of SiPMs, i.e. the FBK and HPK models selected after the first single-unit characterization phase, and some tests involve a different set of parameters depending on the measured model. In the aforementioned cases there will be a separated description for each model.

5.3.1 Calibration

The following list contains a detailed description of each step performed in the calibration procedure.

- The first calibration on the CACTUS apparatus was performed along with the implementation of the electronics. The first tests was performed with a single warm-cold board system, for a total of 30 SiPMs. The amplification stages were calibrated for each channel of the warm board before mounting it in the apparatus, this procedure was performed separately for each of the 15 amplification cards discussed in the first section of this chapter. After mounting the first warm board and checking the correct operation of each channel, the procedure involved the Arduino board calibration, in order to set the working parameters for single point measurements. The optimal parameters found in terms of precision and speed are $N = 100$ acquisitions with the sampling frequency $f_s = 400\,\text{Hz}$. With these parameters, the Arduino board is capable to perform a multiplexed acquisition of the four ADC modules in a time $t_{\text{acquisition}} = 1\,\text{s}$. The time $t_{\text{acquisition}}$ is the duration of a single current acquisition in the IV curve measurements also in the four warm board case, since in the CACTUS apparatus the Arduino boards work all in parallel.

- Once the single point acquisition was calibrated, the second step was the calibration of the whole IV curve measurement both at room temperature and at LN_2 temperature. To complete the calibration of the single IV point, the first step was setting the parameters related to the SMU. Before beginning the first IV curve tests, a set of preliminary values for the t_{delay} and ΔV parameters was tried, and these parameters were then adjusted as the test were going, resulting in the final values $t_{\text{delay}} = 1\,\text{s}$ and $\Delta V = 0.1\,\text{V}$. With these parameters we get a total duration for the single IV curve point measurement of $t_{\text{measure}} = t_{\text{delay}} + t_{\text{acquisition}} = 2\,\text{s}$.

  The same approach was used for the IV curve measurement parameters V_{max}, I_{max}, V_{start}, V_{stop}, N_{step} for both the SiPM models in forward and reverse polarization, obtaining the final values listed in the tables 5.3.

parameter	HPK model		FBK model	
	forward	reverse	forward	reverse
V_{max}	5 V	60 V	5 V	50 V
I_{max}	700 mA	50 mA	500 mA	50 mA
V_{start}	0.4 V	50.4 V	0.4 V	32.0 V
V_{stop}	1.2 V	51 V	1.2 V	32.6 V
N_{step}	40	60	40	60
$V_{\text{start\_fit}}$	0.7 V	50.5 V	0.7 V	32.05 V

Table 5.3: values of the parameters for the IV curve measurement at room temperature for the HPK and the FBK models. These are indicative values as some of them were slightly changed during the characterization campaign, due to unexpected fluctuations of the V_{BD} values for SiPMs of the same model.

The table 5.4 is similar to the previous one but it contains the parameters used at LN_2 temperature.

Most of the parameters are different for the HPK and FBK models, and some loads of the same

parameter	HPK model		FBK model	
	forward	reverse	forward	reverse
V_{max}	5 V	50 V	5 V	30 V
I_{max}	500 mA	30 mA	500 mA	30 mA
V_{start}	0.6 V	40.8 V	0.6 V	26.4 V
V_{stop}	2 V	51.6 V	2 V	27.2 V
N_{step}	40	80	40	80
V_{start_fit}	0.6 V	40.9 V	1.4 V	26.5 V

Table 5.4: values of the parameters for the IV curve measurement at liquid nitrogen temperature for the HPK and the FBK models. These are indicative values as some of them were slightly changed during the characterization campaign, due to unexpected fluctuations of the V_{BD} values for SiPMs of the same model.

model showed a small deviation on the V_{BD} value, which means that they must be characterized using a different set of parameters, at least in reverse polarization. For these reasons the LabVIEW VI was designed to store a custom number of IV curve setups, even if almost all the tested SiPMs were in specs and the changes in the parameters were smaller than 2%.

The IV curve tests were performed for the same SiPMs with both the CACTUS apparatus and an external source meter, which was used as a reference device to validate the results. These tests initially showed some discrepancies in the results for the two devices, so a series of additional measurements was carried on to refine the calibration parameters mentioned in the previous section. The resulting values of these calibration parameters are listed in the table 5.5.

parameter	value
R_{bypass}	0.095 Ω
R_{cable}	2.05 Ω
R_{bias}	[0.359, 0.553, 0.573, 0.503] Ω

Table 5.5: values of the correction parameters found during the calibration of the apparatus and mentioned in the description of the IV curve analysis of the previous section. The R_{bias} parameter depends on the number of connected cold boards, so it is represented as an array of four values related respectively to 1, 2, 3 and 4 connected boards.

The last calibration to mention for the IV curve measurements is related to the illumination of the samples. The SiPM current signal in reverse polarization is strongly dependent on the illumination of the samples. In low illumination conditions the amplitude of the SiPM current becomes too small to estimate the V_{BD} value. If, on the other hand, the illumination is too high the channel saturates before reaching the breakdown region and the results are compromised. Furthermore, the measurement could fail if the V_{BD} value of the related sensor is close to the extrema of the fit range, because the fit has not enough points around the maximum to retrieve a valid result.

The LED system described in the previous section allows to get a fine control on the illumina-

tion on the samples. The dark box is kept always closed when performing the measurements, and the LED luminosity is controlled by an Arduino board which is controlled from the PC station by the LabVIEW VI. The lid of the dewar is left at 5 cm from the dewar aperture during LN_2 IV curve measurement, in order to illuminate the SiPMs with the external LED strips while maintaining them in the LN_2 bath. The illumination conditions used at room temperature are different from the ones at LN_2 temperature since a smaller portion of the cold boards is exposed to the LED light when the system is in LN2.

- For what concerns the LN_2 immersions and the thermal cycles, the first calibration involved the speed of each displacement, which was set to 8 mm/s which is the minimum value furnished by the vendor. This speed is still too high to avoid thermal shocks of the samples in a single displacement, so the immersion is divided in different displacement, divided by custom time delays. Different speed profiles (i.e. 2D arrays of positions and time delays) were tried before selecting the one which minimize the immersion time without causing abrupt changes in the temperature. The speed profile used for the actual SiPM characterizations is designed to perform the whole immersion in 20 minutes, as shown in figure 5.13.

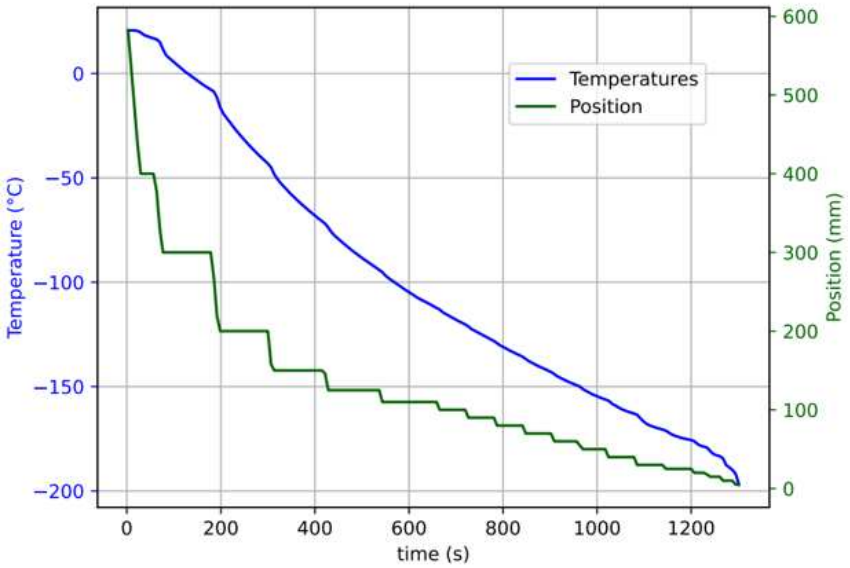

Figure 5.13: Example of a single LN_2 immersion speed profile, in which are visible the positions of the mechanical slider (green) and the temperature of one of the cold boards (blue) versus the elapsed time.

The last calibration involved the heating process on the thermal cycles. During the thermal cycles, the samples are usually left at room temperature for around 10 minutes to raise the temperature at least above 0 °C before the next immersion, but at the end of the last immersion the samples must reach the actual room temperature and be dried properly, and this thermalization would take around 2 hours in standard temperature and humidity conditions. The CACTUS apparatus contains a heating system of resistors placed above the cold boards to accelerate the thermalization process, in this way it is possible to pass from LN_2 temperature to room temperature in less than 10 minutes (without thermal shocks).

- For the DCR measurement the calibration involved searching of the 0.5 p. e. charge threshold for the analyzed SiPM models and reducing as much as possible the noise. The threshold of the charge discriminator Q_{th} can be set in the Python script related to the DCR measurement ranging from 30 ke up to 20 Me. The Q_{th} value corresponding to 0.5 p. e. was found for each SiPM model using a Python script similar to the one used for standard DCR measurement. This script performs a series of DCR measurements with a single channel, scanning the Q_{th} value in a range defined by the user, and producing the related DCR vs Q_{th} plot. In this plot the DCR value drops significantly at integer p.e. values, so the charge amplitude was set as half of the 1 p. e. value, which corresponds to the first DCR drop.

  For what concerns the noise reduction, the strategy was to keep all the switching noise sources outside the dark box. The controller of the mechanical stage is also placed outside the dark box and the servo motor is turned off before any DCR measurement. The shielding in the electrical connection between the Mother boards and the DCR sub-system is achieved with twisted pair flat cables, using a ground line and a signal line for each of the twisted pairs.

5.3.2 Measurements

The following list contains a detailed description of each step performed in a standard measurement procedure.

- Setup and measurement configuration

  Turn on the apparatus and select the parameters involved in the measurements depending on the SiPM model, activate the automatic LN_2 refill (which is off during the measurements to reduce the switching noise) and clean the SiPMs.

- ID Scan

  the first test performed with the LabVIEW VI is the ID scanner. The user scans the QR code and the data matrix (if both present) of each PCB before mounting it in the cold board, starting from the first PCB of the warm board 1 and proceeding in ascending order for the others.

- IV curve at room temperature

  The first measurement is the IV curve at room temperature, using the parameters selected in the setup phase. If some of the measurements fail, this test is repeated until all the SiPMs are correctly characterized. In some cases the SiPMs belonging to the same load show a spread on the V_{BD} values up to 1 V, in these cases the range can be extended but there is a trade-off to make. The range of the curve cannot be extended a priori, because the precision of the results would suffer if the number of points remains the same, while the time involved in the measurement would increase if the number of points increases. The limited precision of the SMU also places some restrictions, imposing a threshold N_{max} on the number of IV curve points at a fixed range: if two consecutive points are too close in terms of bias voltage, the SMU is not able to distinguish them and the resulting IV curve plot will show discontinuities that can compromise the fit. In most of the cases the measurements where performed using an extended range with

more points to preserve the precision, or repeated for two different parameter sets to achieve at least one valid measurement per SiPM. In some rare cases this trade-off has no solution, because the spread in the V_{BD} value is too high and the drain current of the amplification stages reach the limit of the DC power bias of the warm boards, introducing distortions in the signals, in these cases the PCBs with atypical V_{BD} values are marked and replaced with new ones, then the test is repeated. The SiPMs of the marked PCBs are measured *a posteriori* either with a custom set of IV curve parameters, when the number of atypical SiPM arrays is at least 3, or with an external source meter (*Keithley Sourcemeter 2450*).

- IV curve at LN_2 temperature (first)

  After the IV curve measurements at room temperature, the cold boards are immersed in LN_2 following the selected speed profile. After the immersion, the user checks the temperature of each board and launches the IV curve if all the boards are around 77 K (with 1 K tolerance). The parameters for the IV curve at LN_2 temperature are different from the ones of room temperature, as explained in the subsection 5.1.7. Like for the room temperature case, this test is repeated until all the SiPMs are correctly characterized. In the rare cases in which the V_{BD} spread (between neighbouring channels) is too high, the test is marked as failed, because it is not possible to repeat the test with an external device without extracting the SiPMs form the LN_2 bath. If the SiPMs are extracted, connected to an external device and then immersed again in LN2, the measurement would not be at the first thermal cycle anymore.

- Thermal cycles

  The schedule designed by the Consortium foresees three thermal cycles after the first IV curve measurement at liquid nitrogen temperature. The cold boards are extracted from the LN_2 bath in a 10 minutes rise to the highest position, then they are left at room temperature for 5 minutes to allow thermalization and finally immersed again in LN_2 following the speed profile described in the subsection 5.3.1, which has a time duration of 20 minutes. The whole thermal cycle described before has a total time duration of 35 minutes. Then the boards are extracted again with the same procedure and left at room temperature for 10 to 15 minutes. Meanwhile, the heating system is manually turned on when the slider reaches the highest position, the dewar is closed by a polystyrene lid and the operator dries the cold boards (with particular attention to the connectors). This last procedure is important because the next immersion is followed by the IV curve measurement and the electrical connections could develop undesired resistances if not dried properly.

- IV curve at LN_2 temperature (second)

  The second IV curve measurement is equal to the first one, with the exception that these measurements can be performed with an external device if needed. In these cases the resulting IV curves are marked to indicate that they are acquired after the fourth LN_2 immersion, and not after the third as the other measurements.

- DCR measurement

The last test is the DCR measurement, which is performed by the DCR system. The slider of the mechanical stage is lowered to the minimum position, closing the lid of the dewar, then the servomotor of the mechanical stage and the LED illumination are turned off. The operator introduces additional light shields over the dewar (two polyurethane-coated black fabric covers), this procedure is important because the dark box does not completely shield the external lights. The user launches the DCR Python script through the LabVIEW interface and checks the results after the measurements are finished.

In some cases, at the beginning of the measurement campaign when the apparatus was still under development, the noise level was too high to correctly measure the DCR with the FPGA-based counter, so the tests where repeated with an external device (*Tektronix MSO oscilloscope 6 series*).

These tests were performed on a total of 8000 SiPMs among HPK and FBK types, and the results will be discussed in section 5.4. The measurement campaign started with the apparatus still under development, so the procedure was adapted as the measurement went on, repeating some characterizations with external devices when needed as described in the previous list. All the tests were performed in manual mode in order to check the results after each measurement and also because some tasks (like heating and drying the cold boards) were still performed by the user.

5.4 Results

This section will cover the results of the analysis for the samples characterized by the Ferrara group of the SP-PDS consortium in the period from March 2022 to September 2022 of the mass-test phase, which involved more than 6800 characterizations.

The results will be discussed separately for each SiPM model and measurement type.

5.4.1 FBK model

The FBK SiPMs where characterized using the parameters and procedures described in the previous sections, and the overall results are reported in figures 5.14 and 5.15.

Both the V_{BD} and R_Q distributions at room temperature show an additional peaks, as visible in figure 5.14. These could be related to subsets of samples that present different specs with respect to the rest of the population or either due to artifacts in the histogram related to the experimental uncertainties.

The distributions of the results for the IV curve characterization at LN_2 temperature are reported in figure 5.15 and both show almost the same secondary peaks, approximately with the same related heights as in the room temperature case.

The distribution of the V_{BD} values is reported in figure 5.16, the plot also displays the V_{BD} spread within the single SiPM arrays. The V_{BD} distribution was studied only for the LN_2 case, since it simulates the DUNE and ProtoDUNE working environment. The variations on the R_Q value have less impact because the quenching resistor influences the fall time of the signal, which is a secondary parameter in order of importance.

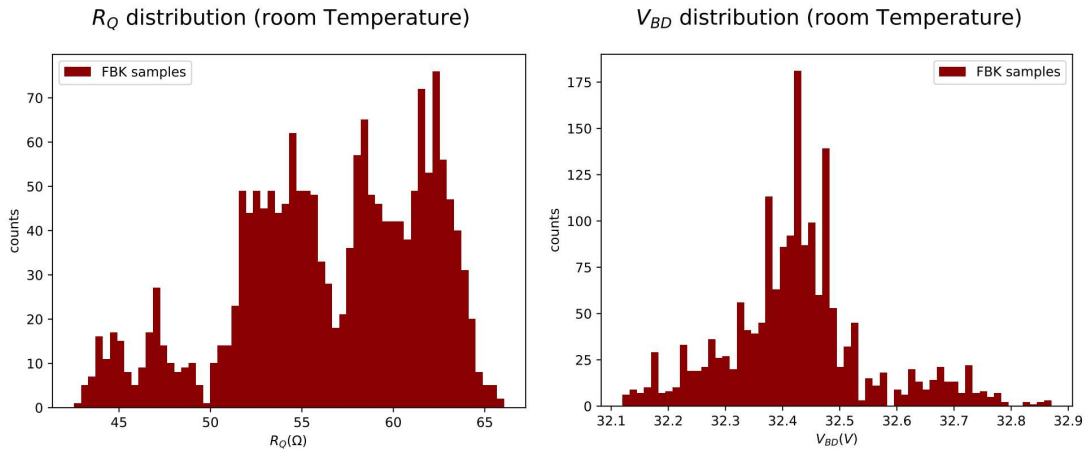

Figure 5.14: Distributions of the measured R_Q (left) and V_{BD} (right) values for the FBK SiPMs at room temperature. The R_Q distribution shows three main peaks around 63 Ω, 58 Ω and 54 Ω and two smaller peaks below 50 Ω. The V_{BD} distribution show a main peak around 32.45 V and two smaller peaks at 32.25 V and 32.70 V.

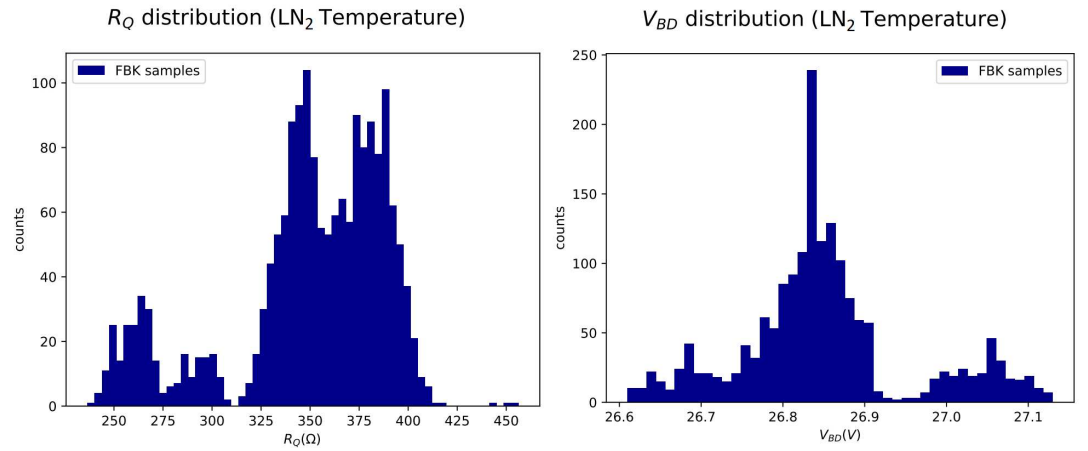

Figure 5.15: Distributions of the measured R_Q (left) and V_{BD} (right) values for the FBK SiPMs at LN_2 temperature. The R_Q distribution shows two main peaks around 385 Ω and 345 Ω and two smaller peaks below 310 Ω. The V_{BD} distribution show a main peak around 26,85 V and two smaller peaks at 26.68 V and 27.5 V, the related positions and heights are similar to the room temperature case.

As visible in the V_{BD} distribution, the V_{BD} values of SiPMs inside the same array are consistent with each other, and the arrays can be classified in four categories based on their mean V_{BD} value. These differences could stem from slightly different fabrication procedures or involved materials, but as stated before all the SiPMs fulfill the DUNE specifications on V_{BD} and R_Q.

The overall analysis of IV curve results included also the differences ΔR_Q, ΔV_{BD} between the parameters measured at the third immersion and the ones measured at the first immersion. The ΔR_Q and ΔV_{BD} distributions are reported in figure 5.17, they should both be consistent with zero since R_Q and V_{BD} were already measured before and after 20 immersions in the single unit characterization phase showing negligible variations.

Considering the conservative errors of 6% and 0.25% in the R_Q and V_{BD} measurements respec-

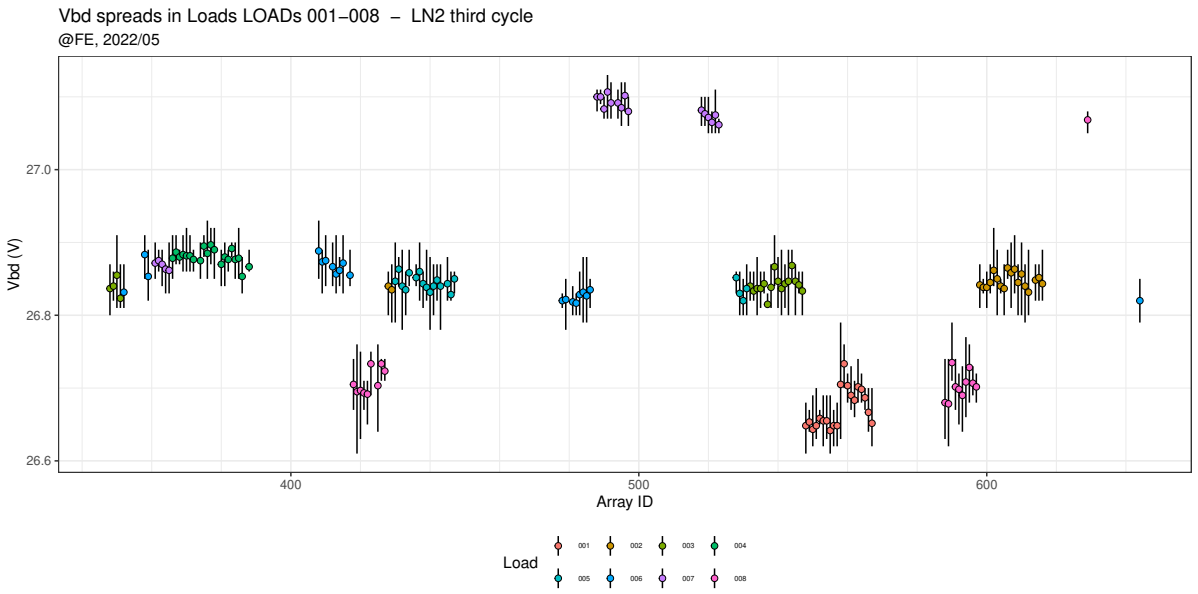

Figure 5.16: Breakdown voltage distributions within the single SiPMs strips of the FBK model, at LN_2 temperature. For each array ID the plot shows the mean value and the maximum-minimum range of the V_{BD} values. The colors are divided per load: each load contains 30 SiPM arrays and is related to a single measurement session.

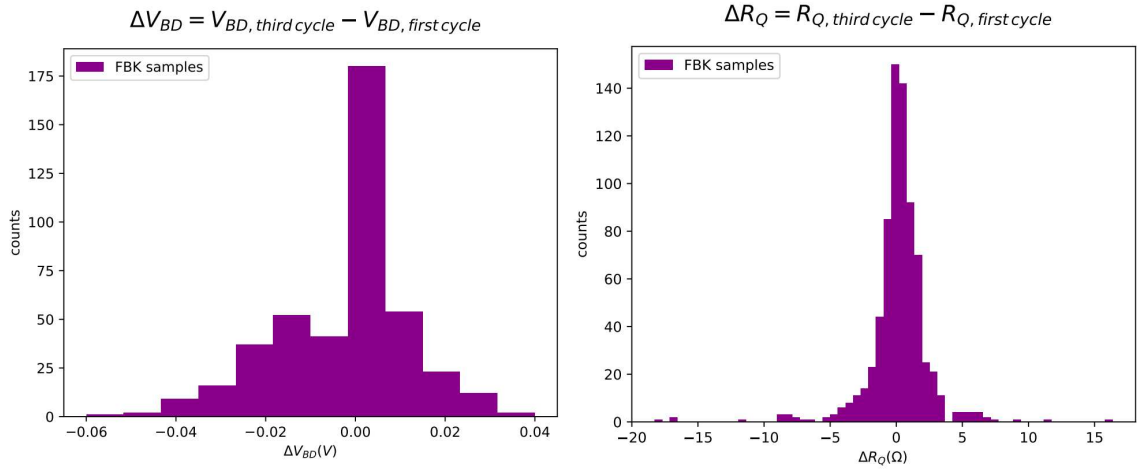

Figure 5.17: Left: distribution of the differences between the R_Q values measured at the third LN_2 immersion and at the first LN_2 immersion for the FBK model. Right: same distribution for the V_{BD} value. Both the distributions are compatible with $\Delta = 0$.

tively, both the differences ΔR_Q and ΔV_{BD} are compatible with 0 as expected.

The overall results of the DCR measurements are reported in figure 5.18. From these distributions is visible that the results are within the DUNE specifications for all the tested SiPMs.

5.4.2 HPK model

The results relative to the HPK SiPMs are reported in figures 5.19 and 5.20.

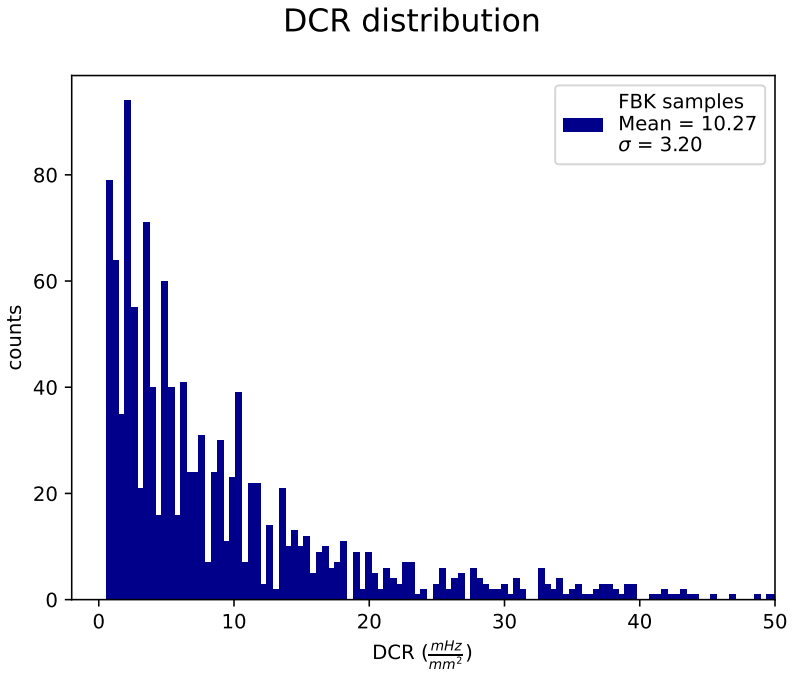

Figure 5.18: Distribution of the measured DCR values for the FBK model. This distribution has a mean value of 10.27 mHz/mm^2.

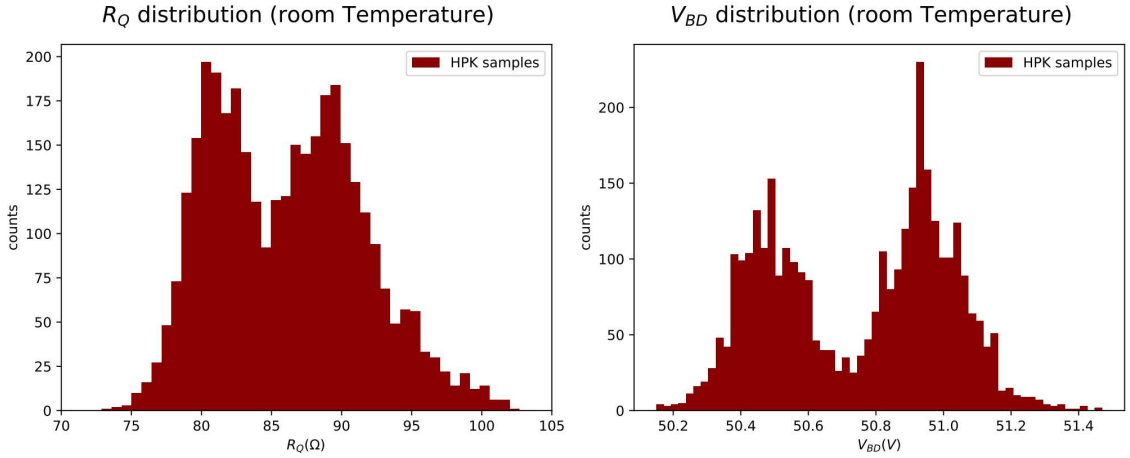

Figure 5.19: Distribution of the measured quenching resistance (left) and breakdown voltage (right) for the HPK SiPMs at room temperature. The R_Q distribution shows two peaks around 81 Ω, 89 Ω, while the V_{BD} distribution show two peaks around 50.95 V and 50.5 V.

The V_{BD} distribution at room temperature shows two peaks, as visible in figure 5.19 (right), and the R_Q distribution (figure 5.19, left) shows a similar profile. These could be related to a subgroup of SiPMs with different characteristics.

The distributions of the results for the IV curve characterization at LN_2 temperature are reported in figure 5.20 and they do not show the secondary peaks. The multiplicity vanishes at liquid nitrogen temperature in both the cases, but the V_{BD} distribution shows an asymmetry on the right part w.r.t. the center.

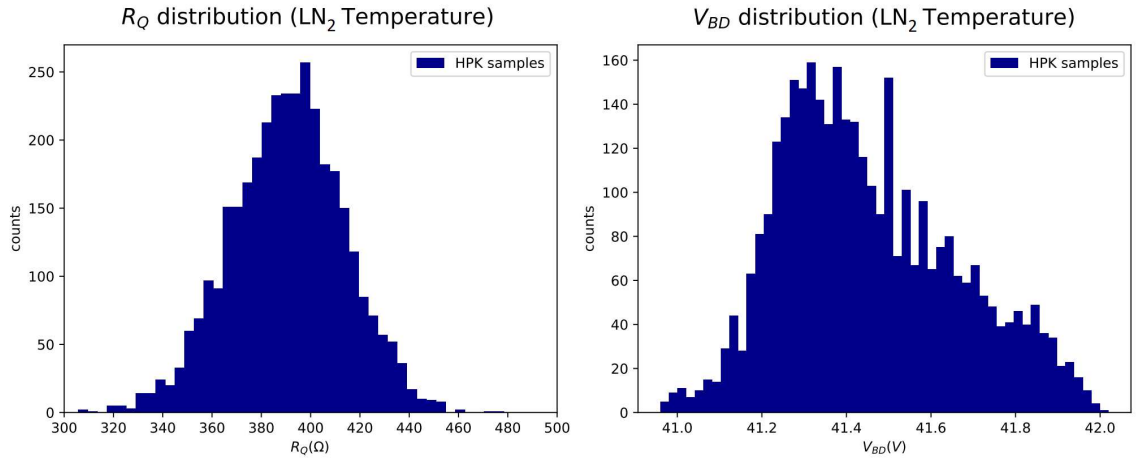

Figure 5.20: Distribution of the measured quenching resistance (left) and breakdown voltage (right) for the HPK SiPMs at LN_2 temperature. The R_Q distribution shows a single peak around 390 Ω and has a larger spread w.r.t. the room temperature case, while the V_{BD} distribution show a single peak around 41.3 V that is not symmetric with respect to the centre.

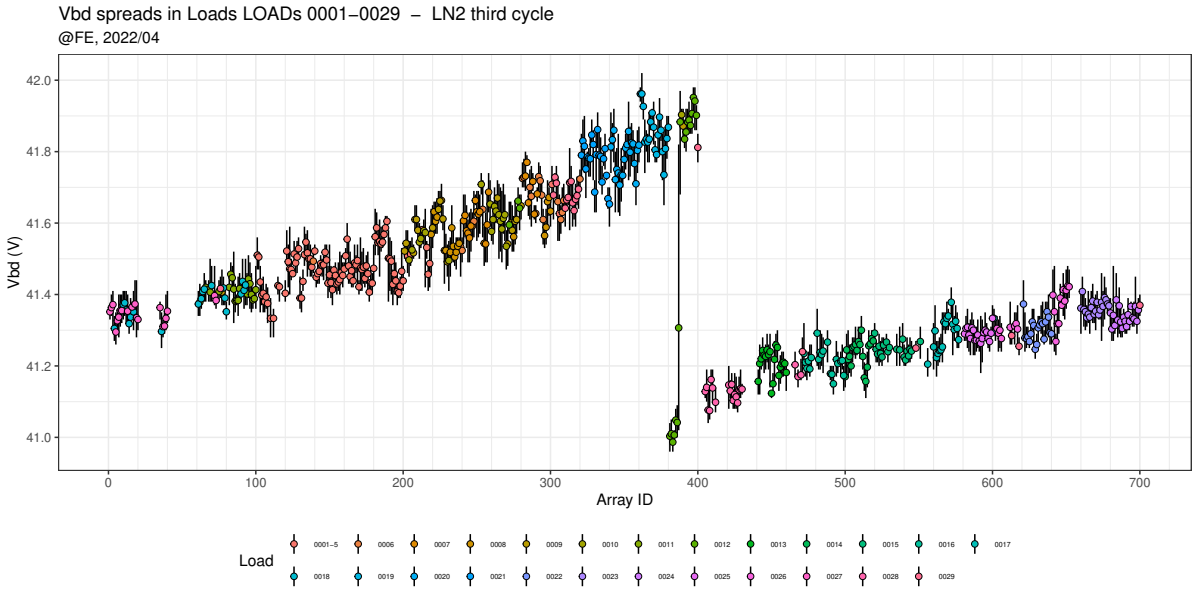

Figure 5.21: Breakdown voltage distributions within the single SiPMs arrays of the HPK model, at LN_2 temperature. For each array ID the plot shows the mean value and the maximum-minimum range of the V_{BD} values. The colors are divided per load, which is the single measurement session described in section 5.3. Each load is related to 30 different SiPM arrays.

As for the FBK case, the team studied the spread of values within single array of SiPMs, to have a better understand of this behaviour and possibly identify the out-of-trend arrays, even if all the sensors are within the DUNE specifications. The resulting distributions are visible in figure 5.21. As visible in the single array distributions, the parameters of the SiPMs inside the same array are consistent with each other, except for a single array which spread almost covers the extrema of the whole distribution.

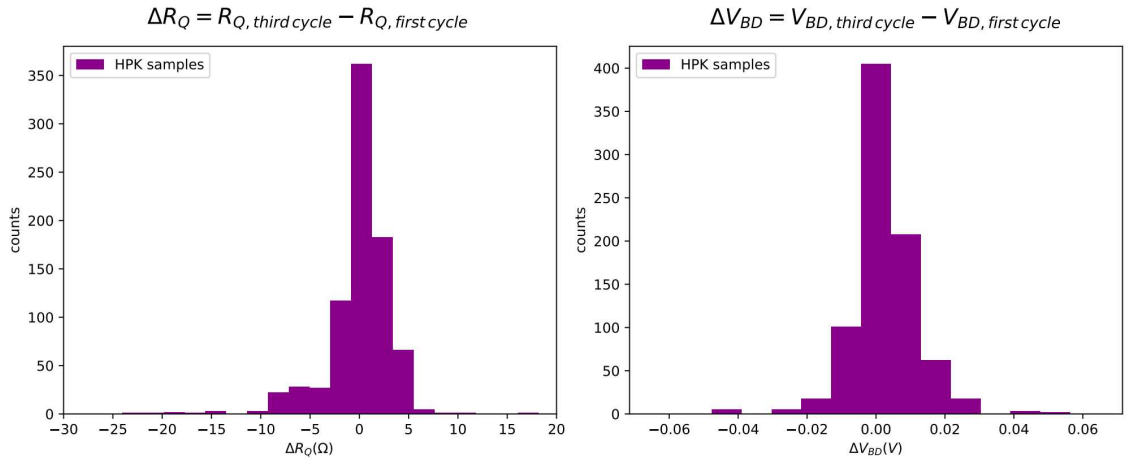

Figure 5.22: Left: distribution of the differences between the R_Q values measured at the third LN_2 immersion and at the first LN_2 immersion for the HPK model. Right: same distribution for the V_{BD} value. These distributions are both compatible with $\Delta = 0$.

Unlike the FBK case, these arrays cannot be classified in categories, but there is an almost linear relation between the V_{BD} value and the array ID which covers almost 1 V range, with an abrupt change in correspondence of the array with large V_{BD} spread.

The last analysis on the IV results involved the distributions of the differences ΔR_Q and ΔV_{BD} as they were defined for the FBK case. These distributions are reported in figure 5.22.

Both the differences ΔR_Q and ΔV_{BD} are compatible with zero, considering the conservative errors of 6% and 0.25% in the R_Q and V_{BD} measurements, respectively.

For what concerns the DCR measurements, the distribution of the results is reported in fig 5.23. The measured DCR values are all within the DUNE specifications for the tested SiPM arrays, but the one with high V_{BD} spread (array ID: 382) must be discarded since it contains SiPMs that cannot be all biased at the same over-voltage in a common cathode configuration.

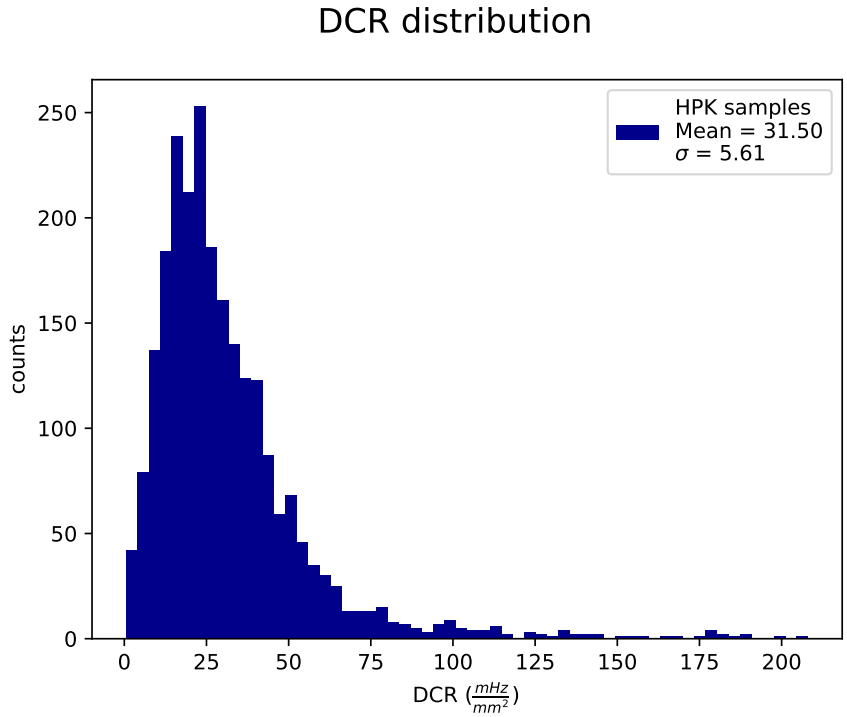

Figure 5.23: Distribution of the measured DCR values for the HPK model. The mean value of this distribution is 31.50 mHz/mm^2.

Conclusions

The main topic of this thesis is the characterization of silicon photomultipliers (SiPM) detectors for the DUNE experiment, in particular for the ProtoDUNE-HD and DUNE-FD1 modules, and the development of novel experimental setups and techniques to perform this task.

The DUNE PDS consortium, responsible for the DUNE and ProtoDUNE PDS design and development, has launched a 3-phase test campaign to down-select and test SiPMs for both the ProtoDUNE-HD and DUNE-FD1, starting from a pool of FBK and HPK SiPM models previously chosen for low-noise properties and cryogenic operation reliability. The main phases are:

- the full characterization of the single SiPM devices (as described in chapter 4);
- the quality assurance test of a large number of SiPMs for the entire ProtoDUNE2-HD and DUNE-FD1 productions (as described in chapter 5).

The first phase ended in 2019 with the down-selection of one model per vendor, starting from a first batch of sensors for the pre-production phase, more precisely 2 models for FBK and 4 models for HPK developed with different initial guess technologies, and divided in 6 splits of 25 sensors for each SiPM model. The characterizations performed in this phase showed that all the tested SiPMs were within the DUNE and ProtoDUNE specifications, in terms of quenching resistance, breakdown voltage, gain and SNR, DCR, AP and CT rates, so the choice felt to the most performing ones in terms of noise and gain.

As mentioned in section 4.4, during the dark noise measurements at LN_2 temperature, the group found an unexpected phenomenon on all the tested SiPMs: the burst phenomenon. These bursts of fast, correlated events are characterized by a higher frequency with respect to the "standard" dark events, and have the net effect of rising the DCR of the device, which still remains within the DUNE specifications, nevertheless, a series of *ad hoc* tests has been developed to study this phenomenon, involving also other members of the PDS Consortium and the two vendors. Neither the cause nor the mechanism of this behaviour are currently understood, but further investigations are currently going on, and the related studies has been shared with the scientific community in talks, posters and a related article [74].

The down-selection led to the choice of two SiPM models as final choice for the DUNE-FD1 and ProtoDUNE-SP2 photon detection systems, selecting one HPK model and one FBK model, together with an ideal working point (V_{OV} value) for both[3]. For the HPK case, the chosen SiPM model is the one with 75 μm pitch, high R_Q, which presents higher Gain and SNR values with respect to the others,

[3] $V_{OV} = 4.5\,V$ for the FBK model, $V_{OV} = 3\,V$ for HPK

while for FBK the chosen model is the triple trench, which presents lower CT and AP percentages with respect to the standard one. This phase ended up in 2020, and was followed by a series of ganging test of 6-unit SiPM arrays (or strips), done by measuring the output of 250 sensors at board level.

The second phase is a massive SiPM test campaign to validate the expected behavior of all the detectors belonging to both the ProtoDUNE and the DUNE productions. The beginning of this phase featured the development of a custom apparatus (CACTUS) to perform fast and automatized characterizations (2021-2022), which was then used for the ProtoDUNE2-HD SiPM characterization campaign (6000 sensors, ended in September 2022) and is currently operating for the DUNEFD1-HD SiPM characterization campaign (288000 sensors).

The results for the ProtoDUNE2-HD SiPM characterization campaign are within the DUNE specifications for almost all the tested sensors, with failure rate below the 0.05% level. More precisely, only two of the 6000 tested sensors showed out-of-specs V_{BD} values, and the spread of the V_{BV} inside single SiPM strips are all below the 100 mV threshold dictated by the DUNE specifications for the HPK model, with the exception of a single strip. This high spread is probably caused by a change in the silicon wafer used as bulk material for the sensors in the strip.

To give a brief estimation of the time gained by the choice of the CACTUS apparatus over traditional characterization techniques, we can estimate 3 minutes to perform an IV curve measurement with a standard source meter (considering both forward and reverse polarization). Such devices have high performances in terms of precision and speed, so the time involved in the measurement is dominated by the human intervention (mount the SiPM, plug the connectors and start the acquisitions). The measurement time duration can be eventually reduced by processing groups of SiPMs with a single algorithm, and in this scenario the results cannot checked after the single IV curve acquisitions. We consider 3 measurements to be done for each SiPM, the first at room temperature, the second at LN_2 temperature and the third still at LN_2 temperature but after the thermal cycles. The thermal cycles could be performed in parallel for all the sensors so they will be not taken into account, even if this would require a parallel of 120 cold-warm connections for the LN_2 temperature measurements. This estimation leads to a total of 18 hours to perform 3 IV curve measurements on 120 SiPMs in series. In contrast, the CACTUS apparatus can perform a parallel IV curve characterization of 120 SiPMs in around 3 minutes in forward polarization and 5 minutes in reverse polarization (for a total of 8 minutes for the set of 3 IV curve measurements), featuring run-time analysis and immediate display of all the results after each characterization. The same logic can be applied to the DCR system, which also works with 120 parallel channels, for these measurements the time duration corresponds roughly to the time window selected for the measurements (120 s in our case).

The CACTUS system is currently installed in two different sites (Bologna and Ferrara Universities), and identical apparatuses are planned to be installed also at the Milano Bicocca, Granada and Prague Universities. These will join the Ferrara and Bologna sites in the DUNEFD1-HD SiPM characterization campaign in 2023.

The CACTUS apparatus is also open for some upgrades: the automatic control of the sensor illumination (LED system), and the FPGA counter, that can be modified to perform multi-threshold analysis (series of acquisitions varying the charge threshold) in relatively short times, together enable the study of the amplitude distribution of events and so the estimation of the SiPM gain and the SNR.

Appendix A

ALIS project

This appendix describes the activities that I carried on during the first year of my PhD course, in parallel with the SiPM characterization mentioned in chapter 4.

These activities are related to the so-called *Advanced Laser Inspection System* (ALIS): an experimental apparatus for fast, non-invasive monitoring of oxygen concentration in pharmaceutical packages (glass vials) of different sizes and shapes. The ALIS system is designed for manufacturers of controlled atmosphere packages, and is meant to be installed at the end of the production line in order to check the O_2 concentration inside each vial through near infrared (NIR) absorption spectroscopy.

The requirements on speed, precision and cost, combined with constraints due to the system geometry, pose a number of technical limitations to the usage of traditional spectroscopy techniques.

The technique used to detect the O_2 concentration is called *Tunable Diode Lased Absorption Spectroscopy* (TDLAS) and it is based on scanning the wavelength of the emitted light across one of the O_2 absorption peaks, by means of a triangular wave [76]. The resulting profile of the transmitted light intensity versus time reflects the spectrum of the absorption peak, and it can be used to study the peak amplitude (after previous calibration), in order to estimate the oxygen concentration inside the sample.

This method have some limitations, the main ones being the distortions due to optical interference (etalon) of the surfaces across the optical path, the noise due to the variation in the transmission of the glass for the different vials, the electrical noise and the $1/f$ noise in general.

To overcome these issues, the system adopts the *Wavelength Modulation Spectroscopy* (WMS) technique, which is a different version of TDLAS (often called TDLAS-WMS)[77]. The procedure is the same as described above, but the triangular wave governing the laser wavelength of the incident light is now added to a fast, sinusoidal modulation. The typical frequency values for the triangular scanner wave are of the order of tens of Hz, while the sinusoidal modulation f_s lies in the kHz range. The procedure then foresees a demodulation of the measured signals at both f_s and $2f_s$, to get the so-called first and second *harmonics* (f_1 and f_2) through lock-in amplification techniques or fast Fourier transformations.

The amplitude of f_1 mainly depends on the absorbed light intensity, so it suffers from variation in the transmission of the optical path, while f_2 mainly depends on the product of oxygen concentration and light intensity. For these reasons, the f_2/f_1 ratio of these two quantities gives a (virtually)

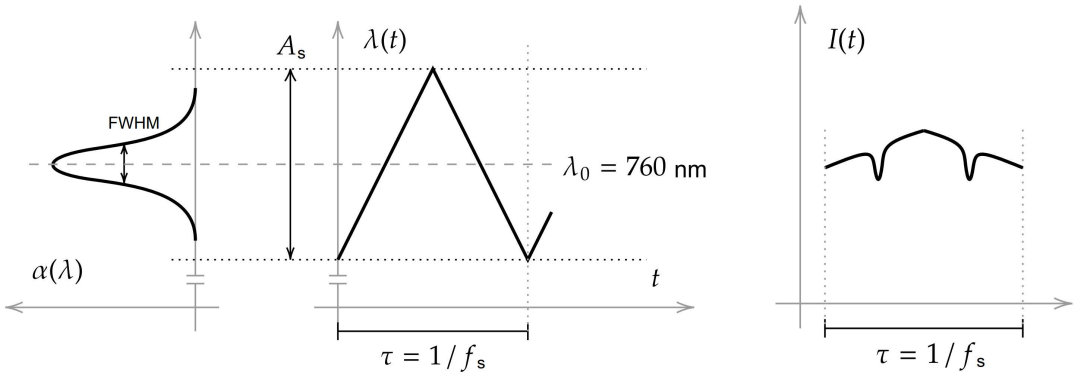

Figure A.1: Example of signals involved in the TDLAS technique. From the left: absorption peak, triangular wave and PD signal. The PD signal shows the absorption peak superimposed to the triangular wave, due to second order effects.

calibration-free estimator of the O_2 concentration in the optical path, which depends on the transmission of the sample only at a second order approximation.

The experimental setup developed for these measurements consists in a *Distributed FeedBack* (DFB) laser[1], controlled by a *Laser Driver and Temperature Controller* (LDTC) module[2], to generate the coherent radiation, a system of optical fiber and lenses to collimate the light beam and point it toward the sample, and a photodiode[3] with integrated front-end electronics to measure the transmitted light. The laser has typically a 2° to 5° vertical (negative) tilt in order to reduce interference effects with the PD window and/or the glass surfaces. The front-end electronic board was designed *ad hoc* for the apparatus, it contains a trans-impedance amplifier with feedback resistor $R_f = 6.8\,k\Omega$ and a high-pass (Butterworth) filter of cutting frequency $f_{cut} = 1\,kHz$.

The LDTC module permits to set and stabilize a fixed temperature value to tune the laser wavelength λ at the 760.9 nm absorption peak (chosen for its high amplitude) with $\sim nm$ level resolution, the LDTC also and governs the driving current I of the laser to change λ at the the level of tens of pm. The first coarse λ tuning is meant to be done before the measurements by setting the laser temperature (because the diode takes some time to stabilize), which remain fixed through all the measurement session, while the driving current signal $I(t)$ is used to change $\lambda(t) = \lambda(I(t))$ reproducing the sum of triangular and sinusoidal waves mentioned before. The laser output is highly responsive to the piloting current $I(t)$, introducing negligible delay for the time scales of ALIS.

It is worth mentioning that also the DFB laser light intensity is influenced by the driving current $I(t)$, this effect introduces non-linearities on the measured PD signal that can compromise the measurements results. For this reason, the dependence of the O_2 concentration estimator on the light intensity is problematic also in absence of variations in the transmission of the optical path. This reinforces the choice of the f_2/f_1 ratio as the estimator of O_2 concentration for the ALIS system.

The LDTC is controlled by a PC interface running a LabVIEW vi, the digital-to-analog conversion is done by a standard input/output board (*PCIe6374*). The board is also used to retrieve the signal

[1] Model *EYP-DFB-0760-00010-1500-BFY02-0002*.
[2] Model *LDTC0520*.
[3] Model *ILX LDC-3724 C* (PD)

from the photodiode, digitize it and send it to the LabVIEW vi for the run-time analysis.

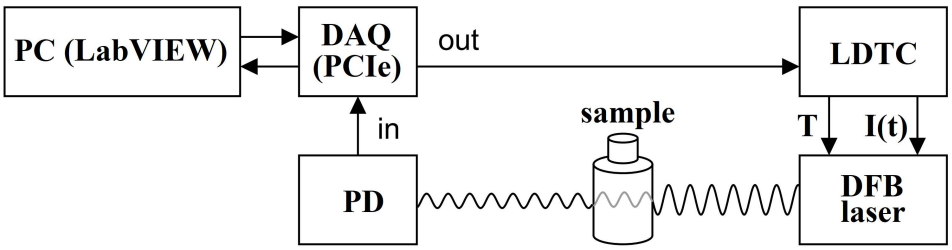

Figure A.2: Sketch of the ALIS experimental setup.

The LabVIEW interface governs all the parameters involved in the measurements and performs the run-time data analysis, which consists of initial signal filtering and demodulation (through digital lock-in techniques), and peak amplitude estimation for the f_2/f_1 function [78]. The actual analysis, which is the result of a series of performance tests, is more complex and takes into account the average of f_1, the integral of $|f_2|$ and the peak-to-peak value of f_1.

The ALIS setup undergone a series of long-term stability tests to check its operations in the industrial environment, finding some drifts in the measured O_2 concentration that introduce systematic errors after few hours of operation. Part of the tests were performed in a climatic chamber to evaluate the role of ambient temperature and humidity in these drifts, finding that the relative standard deviation over 12 h runs drops from 1.5% for the laboratory case to 1.2% in the climate chamber. The long-term stability measurements also show a minimum on the Allan variance for integration times of the order of 10 s, as visible in figure A.3, although the speed requirements impose a maximum integration time of 330 ms.

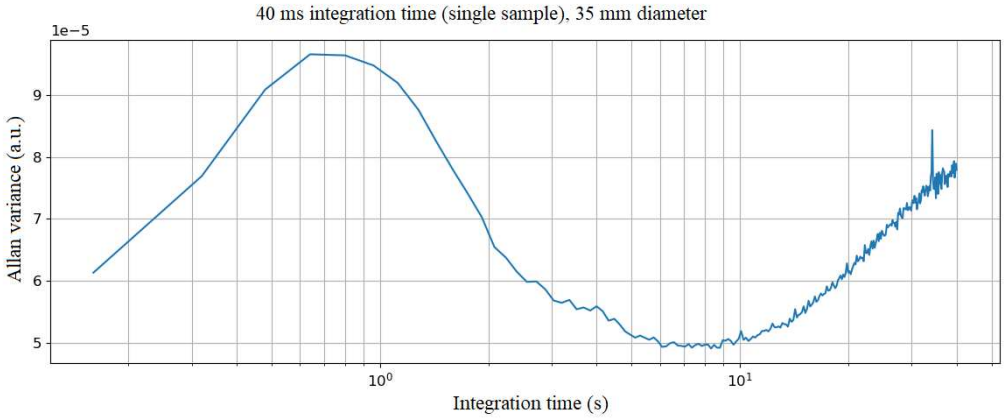

Figure A.3: Example of the Allan variance profile for a 35 mm diameter vial, with single measurement integration time of 40 ms, inside the climatic chamber. The plot shows a minimum around 8 s, which corresponds to the average of 200 measurements.

To reduce these drifts, a correction function was added to the algorithm in order to detect and counter the slow changes in the output signal that are related to the laser temperature variations. Other tests included laser diode characterization, which was studied to check the linearity of the re-

sponse in the range of interest of the driving current, and a number of minor changes in the electronics, optics and analysis algorithm to increase the ALIS performance in terms of speed and precision.

Lastly, is worth mentioning the long test campaign performed in parallel with the development of the final design, aimed to a fine-tuning of the parameters involved in the measurements, and the series of calibration tests that followed the realization of the ALIS final design.

The final version of the ALIS apparatus can reach 9σ discrimination between 0% and 4% O_2 concentration in a single measurement, and up to 2.5σ discrimination on 1% variation in best cases.

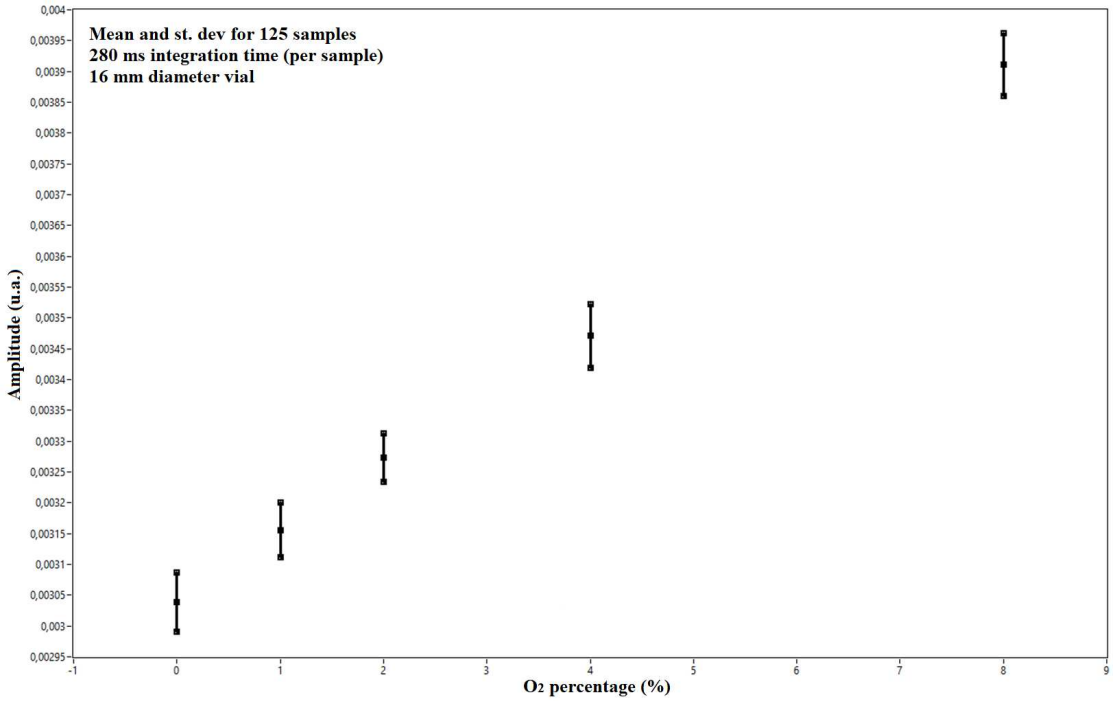

Figure A.4: Plot reporting an example of the ALIS performances for an integration time of 280 ms, measurements on a 35 mm diameter glass vial. The single points are the mean values of a population of 125 samples and the error bars are the related standard deviation (on the sample).

These results are obtained with an integration time of 280 ms in 35 mm diameter glass vials (spec furnished by the company), and a total optical path of ~ 13 cm.

Bibliography

[1] A Abed Abud et al. “Snowmass Neutrino Frontier: DUNE Physics Summary”. In: *arXiv preprint arXiv:2203.06100* (2022).

[2] Peter Siebach. *DUNE at LBNF, Environmental assessment*. URL: https://lbnf-dune.fnal.gov/for-neighbor-and-businesses/environmental-assessment/. Fermilab Website.

[3] aheavey NUS2SURF. *LBNF/DUNE facts and figures*. URL: https://nus2surf.dunescience.org/2018/01/facts-and-figures/. 18/01/2018.

[4] University of Cambridge website. *Professor Mark Thomson elected as co-spokesperson of the Deep Underground Neutrino Experiment (DUNE)*. URL: https://www.phy.cam.ac.uk/news/professor-mark-thomson-elected-as-co-spokesperson-of-the-deep-underground-neutrino-experiment-dune. 18/03/2015.

[5] Babak Abi et al. “Deep underground neutrino experiment (dune), far detector technical design report, volume ii: Dune physics”. In: *arXiv preprint arXiv:2002.03005* (2020).

[6] X. Qian and P. Vogel. “Neutrino mass hierarchy”. In: *Progress in Particle and Nuclear Physics* 83 (2015), pp. 1–30. ISSN: 0146-6410. DOI: https://doi.org/10.1016/j.ppnp.2015.05.002. URL: https://www.sciencedirect.com/science/article/pii/S0146641015000307.

[7] G. Aad et al. “Observation of a new particle in the search for the Standard Model Higgs boson with the ATLAS detector at the LHC”. In: *Physics Letters B* 716.1 (2012), pp. 1–29. ISSN: 0370-2693. DOI: https://doi.org/10.1016/j.physletb.2012.08.020. URL: https://www.sciencedirect.com/science/article/pii/S037026931200857X.

[8] S. Chatrchyan et al. “Observation of a new boson at a mass of 125 GeV with the CMS experiment at the LHC”. In: *Physics Letters B* 716.1 (2012), pp. 30–61. ISSN: 0370-2693. DOI: https://doi.org/10.1016/j.physletb.2012.08.021. URL: https://www.sciencedirect.com/science/article/pii/S0370269312008581.

[9] G. Bellini et al. “Measurement of the solar ^{8}B neutrino rate with a liquid scintillator target and 3 MeV energy threshold in the Borexino detector”. In: *Phys. Rev. D* 82 (3 Aug. 2010), p. 033006. DOI: 10.1103/PhysRevD.82.033006. URL: https://link.aps.org/doi/10.1103/PhysRevD.82.033006.

[10] A. Renshaw et al. “First Indication of Terrestrial Matter Effects on Solar Neutrino Oscillation”. In: *Physical Review Letters* 112.9 (Mar. 2014). DOI: 10.1103/physrevlett.112.091805. URL: https://doi.org/10.1103\%2Fphysrevlett.112.091805.

[11] C. Adams et al. “The Long-Baseline Neutrino Experiment: Exploring Fundamental Symmetries of the Universe”. In: *Snowmass 2013: Workshop on Energy Frontier*. June 2013. arXiv: 1307.7335 [hep-ex].

[12] L. Wolfenstein. “Neutrino oscillations in matter”. In: *Phys. Rev. D* 17 (9 May 1978), pp. 2369–2374. DOI: 10.1103/PhysRevD.17.2369. URL: https://link.aps.org/doi/10.1103/PhysRevD.17.2369.

[13] S. P. Mikheyev and A. Yu. Smirnov. “Resonance Amplification of Oscillations in Matter and Spectroscopy of Solar Neutrinos”. In: *Sov. J. Nucl. Phys.* 42 (1985), pp. 913–917.

[14] Hiroshi Nunokawa, Stephen Parke, and Jose WF Valle. “CP violation and neutrino oscillations”. In: *Progress in Particle and Nuclear Physics* 60.2 (2008), pp. 338–402.

[15] M. Bass et al. “Baseline optimization for the measurement of CP violation, mass hierarchy, and θ_{23} octant in a long-baseline neutrino oscillation experiment”. In: *Phys. Rev. D* 91 (5 Mar. 2015), p. 052015. DOI: 10.1103/PhysRevD.91.052015. URL: https://link.aps.org/doi/10.1103/PhysRevD.91.052015.

[16] D. S. Ayres et al. “The NOvA Technical Design Report”. In: (Oct. 2007). DOI: 10.2172/935497.

[17] K Abe et al. “The T2K experiment”. In: *Nuclear Instruments and Methods in Physics Research Section A: Accelerators, Spectrometers, Detectors and Associated Equipment* 659.1 (2011), pp. 106–135.

[18] Ke Abe et al. “Hyper-Kamiokande design report”. In: *arXiv preprint arXiv:1805.04163* (2018).

[19] Ivan Esteban et al. “Global analysis of three-flavour neutrino oscillations: synergies and tensions in the determination of θ23, δCP, and the mass ordering”. In: *Journal of High Energy Physics* 2019.1 (2019), pp. 1–35.

[20] Pablo Fernández de Salas et al. “Status of neutrino oscillations 2018: 3σ hint for normal mass ordering and improved CP sensitivity”. In: *Physics Letters B* 782 (2018), pp. 633–640.

[21] K Abe et al. “Search for C P Violation in Neutrino and Antineutrino Oscillations by the T2K Experiment with 2.2× 10 21 Protons on Target”. In: *Physical review letters* 121.17 (2018), p. 171802.

[22] K Abe et al. “Atmospheric neutrino oscillation analysis with external constraints in Super-Kamiokande I-IV”. In: *Physical Review D* 97.7 (2018), p. 072001.

[23] MA Acero et al. “First measurement of neutrino oscillation parameters using neutrinos and antineutrinos by NOvA”. In: *Physical review letters* 123.15 (2019), p. 151803.

[24] “Constraint on the matter–antimatter symmetry-violating phase in neutrino oscillations”. In: *Nature* 580.7803 (2020), pp. 339–344.

[25] B. Abi et al. “Neutrino interaction classification with a convolutional neural network in the DUNE far detector”. In: *Physical Review D* 102.9 (Jan. 2020). DOI: 10.1103/physrevd.102.092003. URL: https://doi.org/10.1103\%2Fphysrevd.102.092003.

[26] Babak Abi et al. “Deep Underground Neutrino Experiment (DUNE), Far Detector Technical Design Report, Volume II: DUNE Physics”. In: (Feb. 2020). arXiv: 2002.03005 [hep-ex].

[27] A. Abed Abud et al. *Deep Underground Neutrino Experiment (DUNE) Near Detector Conceptual Design Report*. 2021. DOI: 10.48550/ARXIV.2103.13910. URL: https://arxiv.org/abs/2103.13910.

[28] Matteo Vicenzi. "SAND - System for on-Axis Neutrino Detection - in the DUNE Near Detector Complex". In: *PoS* NuFact2021 (2022), p. 248. DOI: 10.22323/1.402.0248.

[29] M Adinolfi et al. "The KLOE electromagnetic calorimeter". In: *Nuclear Instruments and Methods in Physics Research Section A: Accelerators, Spectrometers, Detectors and Associated Equipment* 482.1 (2002), pp. 364–386. ISSN: 0168-9002. DOI: https://doi.org/10.1016/S0168-9002(01)01502-9. URL: https://www.sciencedirect.com/science/article/pii/S0168900201015029.

[30] Babak Abi et al. "Volume IV. The DUNE far detector single-phase technology". In: *Journal of Instrumentation* 15.08 (Aug. 2020), T08010. DOI: 10.1088/1748-0221/15/08/T08010. URL: https://dx.doi.org/10.1088/1748-0221/15/08/T08010.

[31] C Anderson et al. "The ArgoNeuT detector in the NuMI low-energy beam line at Fermilab". In: *Journal of Instrumentation* 7.10 (Oct. 2012), P10019. DOI: 10.1088/1748-0221/7/10/P10019. URL: https://dx.doi.org/10.1088/1748-0221/7/10/P10019.

[32] R Acciarri et al. "A proposal for a three detector short-baseline neutrino oscillation program in the fermilab booster neutrino beam". In: *arXiv preprint arXiv:1503.01520* (2015).

[33] R. Acciarri et al. "Design and construction of the MicroBooNE detector". In: *Journal of Instrumentation* 12.02 (Feb. 2017), P02017. DOI: 10.1088/1748-0221/12/02/P02017. URL: https://dx.doi.org/10.1088/1748-0221/12/02/P02017.

[34] J. Paley et al. *LArIAT: Liquid Argon In A Testbeam*. 2014. DOI: https://doi.org/10.48550/arxiv.1406.5560. URL: https://arxiv.org/abs/1406.5560.

[35] A.A. Machado et al. "The X-ARAPUCA: an improvement of the ARAPUCA device". In: *Journal of Instrumentation* 13.04 (Apr. 2018), p. C04026. DOI: 10.1088/1748-0221/13/04/C04026. URL: https://dx.doi.org/10.1088/1748-0221/13/04/C04026.

[36] A Abed Abud et al. "Design, construction and operation of the ProtoDUNE-SP Liquid Argon TPC". In: *arXiv preprint arXiv:2108.01902* (2021).

[37] Andrea Falcone. "Deep underground neutrino experiment: DUNE". In: *Nuclear Instruments and Methods in Physics Research Section A: Accelerators, Spectrometers, Detectors and Associated Equipment* 1041 (2022), p. 167217. ISSN: 0168-9002. DOI: https://doi.org/10.1016/j.nima.2022.167217. URL: https://www.sciencedirect.com/science/article/pii/S0168900222005721.

[38] C. E. Aalseth et al. "DarkSide-20k: A 20 tonne two-phase LAr TPC for direct dark matter detection at LNGS". In: *The European Physical Journal Plus* 133.3 (Mar. 2018). DOI: 10.1140/epjp/i2018-11973-4. URL: https://doi.org/10.1140\%2Fepjp\%2Fi2018-11973-4.

[39] V. Golovin. RU 2142175. 1999.

[40] Z. Sadygov. RU 2142175. 1998.

[41] S. Cova et al. “Avalanche photodiodes and quenching circuits for single-photon detection”. In: *Appl. Opt.* 35.12 (Apr. 1996), pp. 1956–1976.

[42] Claudio Piemonte and Alberto Gola. “Overview on the main parameters and technology of modern Silicon Photomultipliers”. In: *Nuclear Instruments and Methods in Physics Research Section A: Accelerators, Spectrometers, Detectors and Associated Equipment* 926 (2019). Silicon Photomultipliers: Technology, Characterisation and Applications, pp. 2–15. ISSN: 0168-9002. DOI: https://doi.org/10.1016/j.nima.2018.11.119. URL: https://www.sciencedirect.com/science/article/pii/S0168900218317716.

[43] Fabio Acerbi and Stefan Gundacker. “Understanding and simulating SiPMs”. In: *Nuclear Instruments and Methods in Physics Research Section A: Accelerators, Spectrometers, Detectors and Associated Equipment* 926 (2019). Silicon Photomultipliers: Technology, Characterisation and Applications, pp. 16–35. ISSN: 0168-9002. DOI: https://doi.org/10.1016/j.nima.2018.11.118. URL: https://www.sciencedirect.com/science/article/pii/S0168900218317704.

[44] Stefan Gundacker and Arjan Heering. “The silicon photomultiplier: fundamentals and applications of a modern solid-state photon detector”. In: *Physics in Medicine and Biology* 65.17 (Aug. 2020), 17TR01. DOI: 10.1088/1361-6560/ab7b2d. URL: https://doi.org/10.1088/1361-6560/ab7b2d.

[45] D. Marano et al. “Silicon Photomultipliers Electrical Model Extensive Analytical Analysis”. In: *IEEE Transactions on Nuclear Science* 61.1 (2014), pp. 23–34. DOI: 10.1109/TNS.2013.2283231.

[46] Claudio Piemonte et al. “Performance of NUV-HD Silicon Photomultiplier Technology”. In: *IEEE Transactions on Electron Devices* 63.3 (2016), pp. 1111–1116. DOI: 10.1109/TED.2016.2516641.

[47] Fabio Acerbi et al. “NUV Silicon Photomultipliers With High Detection Efficiency and Reduced Delayed Correlated-Noise”. In: *IEEE Transactions on Nuclear Science* 62.3 (2015), pp. 1318–1325. DOI: 10.1109/TNS.2015.2424676.

[48] Alessandro Spinelli and Andrea L. Lacaita. “Physics and numerical simulation of single photon avalanche diodes”. In: *IEEE Transactions on Electron Devices* 44.11 (1997), 1931 – 1943. DOI: 10.1109/16.641363.

[49] Max Ludwig Knoetig, Jurgen Hose, and Razmik Mirzoyan. “SiPM avalanche size and crosstalk measurements with light emission microscopy”. In: *IEEE Transactions on Nuclear Science* 61.3 (2014), 1488 – 1492. DOI: 10.1109/TNS.2014.2322957.

[50] S. Cova et al. “Avalanche photodiodes and quenching circuits for single-photon detection”. In: *Appl. Opt.* 35.12 (Apr. 1996), pp. 1956–1976. DOI: 10.1364/AO.35.001956. URL: https://opg.optica.org/ao/abstract.cfm?URI=ao-35-12-1956.

[51] W.G. Oldham, R.R. Samuelson, and P. Antognetti. “Triggering phenomena in avalanche diodes”. In: *IEEE Transactions on Electron Devices* 19.9 (1972), pp. 1056–1060. DOI: 10.1109/T-ED.1972.17544.

[52] Roland H. Haitz. “Model for the Electrical Behavior of a Microplasma”. In: *Journal of Applied Physics* 35.5 (1964), pp. 1370–1376. DOI: 10.1063/1.1713636. URL: https://doi.org/10.1063/1.1713636.

[53] Florian Scheuch et al. “Electrical characterization and simulation of SiPMs”. In: *Nuclear Instruments and Methods in Physics Research Section A: Accelerators, Spectrometers, Detectors and Associated Equipment* 787 (2015). New Developments in Photodetection NDIP14, pp. 340–343. ISSN: 0168-9002. DOI: https://doi.org/10.1016/j.nima.2015.01.066. URL: https://www.sciencedirect.com/science/article/pii/S0168900215000984.

[54] Stefan Seifert et al. “Simulation of silicon photomultiplier signals”. In: *IEEE Transactions on Nuclear Science* 56.6 (2009), 3726 – 3733. DOI: 10.1109/TNS.2009.2030728.

[55] W. Maes, K. De Meyer, and R. Van Overstraeten. “Impact ionization in silicon: A review and update”. In: *Solid-State Electronics* 33.6 (1990), pp. 705–718. ISSN: 0038-1101. DOI: https://doi.org/10.1016/0038-1101(90)90183-F. URL: https://www.sciencedirect.com/science/article/pii/003811019090183F.

[56] Nicola Serra et al. “Experimental and TCAD Study of Breakdown Voltage Temperature Behavior in n^+/p SiPMs”. In: *IEEE Transactions on Nuclear Science* 58.3 (2011), pp. 1233–1240. DOI: 10.1109/TNS.2011.2123919.

[57] D. Renker. “Geiger-mode avalanche photodiodes, history, properties and problems”. In: *Nuclear Instruments and Methods in Physics Research Section A: Accelerators, Spectrometers, Detectors and Associated Equipment* 567.1 (2006). Proceedings of the 4th International Conference on New Developments in Photodetection, pp. 48–56. ISSN: 0168-9002. DOI: https://doi.org/10.1016/j.nima.2006.05.060. URL: https://www.sciencedirect.com/science/article/pii/S0168900206008680.

[58] Kyung Taek Lim et al. “Effect of electric field on primary dark pulses in SPADs for advanced radiation detection applications”. In: *Nuclear Engineering and Technology* 53.2 (2021), pp. 618–625. ISSN: 1738-5733. DOI: https://doi.org/10.1016/j.net.2020.07.006. URL: https://www.sciencedirect.com/science/article/pii/S1738573320302448.

[59] RJ McIntyre. “Theory of microplasma instability in silicon”. In: *Journal of Applied Physics* 32.6 (1961), pp. 983–995.

[60] Roland H. Haitz. “Model for the Electrical Behavior of a Microplasma”. In: *Journal of Applied Physics* 35.5 (1964), pp. 1370–1376. DOI: 10.1063/1.1713636. URL: https://doi.org/10.1063/1.1713636.

[61] K. Yamamoto. JP S49-59585. 1972.

[62] S. Vasile et al. “High gain avalanche photodiode arrays for DIRC applications”. In: *IEEE Transactions on Nuclear Science* 46.4 (1999), pp. 848–852. DOI: 10.1109/23.790690.

[63] M. D. Petroff, M. G. Stapelbroek, and W. A. Kleinhans. “Detection of individual 0.4–28 μm wavelength photons via impurity-impact ionization in a solid-state photomultiplier”. In: *Applied Physics Letters* 51.6 (1987), pp. 406–408. DOI: 10.1063/1.98404. URL: https://doi.org/10.1063/1.98404.

[64] Klaus Pasquinelli et al. “Single-Photon Detectors Modeling and Selection Criteria for High-Background LiDAR”. In: *IEEE Sensors Journal* 20.13 (2020), pp. 7021–7032. DOI: 10.1109/JSEN.2020.2977775.

[65] Rebecca Re et al. “Probe-hosted silicon photomultipliers for time-domain functional near-infrared spectroscopy: phantom and in vivo tests”. In: *Neurophotonics* 3.4 (2016), p. 045004. DOI: 10.1117/1.NPh.3.4.045004. URL: https://doi.org/10.1117/1.NPh.3.4.045004.

[66] Dmitry Kalashnikov and Leonid Krivitsky. “Measurement of photon correlations with multipixel photon counters”. In: *J. Opt. Soc. Am. B* 31.10 (Oct. 2014), B25–B33. DOI: 10.1364/JOSAB.31.000B25. URL: https://opg.optica.org/josab/abstract.cfm?URI=josab-31-10-B25.

[67] K. A. Balygin et al. “A Quantum Random Number Generator Based on the 100-Mbit/s Poisson Photocount Statistics”. In: *Journal of Experimental and Theoretical Physics* 31 (Oct. 2018). DOI: 10.1134/S1063776118060018. URL: https://doi.org/10.1134/S1063776118060018.

[68] Maria Giuseppina Bisogni, Alberto Del Guerra, and Nicola Belcari. “Medical applications of silicon photomultipliers”. In: *Nuclear Instruments and Methods in Physics Research Section A: Accelerators, Spectrometers, Detectors and Associated Equipment* 926 (2019). Silicon Photomultipliers: Technology, Characterisation and Applications, pp. 118–128. ISSN: 0168-9002. DOI: https://doi.org/10.1016/j.nima.2018.10.175. URL: https://www.sciencedirect.com/science/article/pii/S016890021831489X.

[69] Frank Simon. “Silicon photomultipliers in particle and nuclear physics”. In: *Nuclear Instruments and Methods in Physics Research Section A: Accelerators, Spectrometers, Detectors and Associated Equipment* 926 (2019). Silicon Photomultipliers: Technology, Characterisation and Applications, pp. 85–100. ISSN: 0168-9002. DOI: https://doi.org/10.1016/j.nima.2018.11.042. URL: https://www.sciencedirect.com/science/article/pii/S0168900218316176.

[70] Nagy Ferenc et al. “A model based DC analysis of SiPM breakdown voltages”. In: *Nuclear Instruments and Methods in Physics Research Section A: Accelerators, Spectrometers, Detectors and Associated Equipment* 849 (2017), pp. 55–59. ISSN: 0168-9002. DOI: https://doi.org/10.1016/j.nima.2017.01.002. URL: https://www.sciencedirect.com/science/article/pii/S0168900217300025.

[71] A. Nagai et al. “Characterization of a large area silicon photomultiplier”. In: *Nuclear Instruments and Methods in Physics Research Section A: Accelerators, Spectrometers, Detectors and Associated Equipment* 948 (2019), p. 162796. ISSN: 0168-9002. DOI: https://doi.org/10.1016/j.nima.2019.162796. URL: https://www.sciencedirect.com/science/article/pii/S0168900219312379.

[72] Robert Klanner. “Characterisation of SiPMs”. In: *Nuclear Instruments and Methods in Physics Research Section A: Accelerators, Spectrometers, Detectors and Associated Equipment* 926 (2019). Silicon Photomultipliers: Technology, Characterisation and Applications, pp. 36–56. ISSN: 0168-9002. DOI: https://doi.org/10.1016/j.nima.2018.11.083. URL: https://www.sciencedirect.com/science/article/pii/S0168900218317091.

[73] Alberto Gola et al. “NUV-Sensitive Silicon Photomultiplier Technologies Developed at Fondazione Bruno Kessler”. In: *Sensors* 19.2 (2019). DOI: 10.3390/s19020308. URL: https://www.mdpi.com/1424-8220/19/2/308.

[74] M. Guarise et al. “A newly observed phenomenon in the characterisation of SiPM at cryogenic temperature”. In: *Journal of Instrumentation* 16.10 (Oct. 2021), T10006. DOI: 10.1088/1748-0221/16/10/t10006. URL: https://doi.org/10.1088/1748-0221/16/10/t10006.

[75] A. Falcone et al. “Cryogenic SiPM arrays for the DUNE photon detection system”. In: *Nuclear Instruments and Methods in Physics Research Section A: Accelerators, Spectrometers, Detectors and Associated Equipment* 985 (2021), p. 164648. ISSN: 0168-9002. DOI: https://doi.org/10.1016/j.nima.2020.164648. URL: https://www.sciencedirect.com/science/article/pii/S0168900220310457.

[76] Andreas Hangauer. “Detection schemes, algorithms and device modeling for tunable diode laser absorption spectroscopy”. In: 2013.

[77] S. Neethu et al. “Validation of wavelength modulation spectroscopy techniques for oxygen concentration measurement”. In: *Sensors and Actuators B-chemical* 192 (2014), pp. 70–76.

[78] Manish Chandra et al. “Implementation of digital lock-in and concentration measurement for Wavelength Modulation Spectroscopy (WMS) based sensors using MATLAB”. In: *2017 Third International Conference on Sensing, Signal Processing and Security (ICSSS)*. 2017, pp. 350–356. DOI: 10.1109/SSPS.2017.8071619.